Failure of brittle heterogeneous materials, Intermittency, Crackling and Seismicity

Jonathan Barés

École Polytechnique

Failure of brittle heterogeneous materials
Intermittency, Crackling and Seismicity

THÈSE

présentée et soutenue publiquement le 7 Octobre 2013

pour l'obtention du titre de

Docteur de l'École Polytechnique

(spécialité physique)

par

Jonathan Barés

devant le jury composé de :

Coencadrant :	Davy Dalmas
Examinateurs :	Knut Jørgen Måløy Jean-Jacques Marigo Stéphane Roux
Rapporteurs :	Jean-Christophe Géminard Damien Vandembroucq
Directeur de thèse :	Daniel Bonamy

Service de Physique et Chimie des Surfaces et Interfaces — CEA Saclay

Mis en page avec la classe thloria.

Remerciements

Ces trois années de thèse auront vu l'ensemble de mes connaissances, tant sur le plan humain que scientifique s'accroître de façon exponentielle. C'est une période que je clôture par ce manuscrit avec une certaine satisfaction mais aussi avec la grande tristesse d'une aventure passionnante qui se termine.

J'aurais eu pendant ces trois ans l'immense bonheur d'être guidé dans le merveilleux monde de la fracture par le directeur de thèse rêvé de tout étudiant, Daniel Bonamy. Daniel, aucun merci ne suffirait à témoigner de toute la reconnaissance que je te dois pour m'avoir accompagné tout au long de ma thèse avec autant d'humilité, de disponibilité et de confiance. J'espère que ce n'est que le début de notre collaboration.

Toute ma gratitude va également à Davy Dalmas qui en coencadrant ma thèse à su me donner le goût pour les belles expériences. Davy, merci pour ton regard critique, ta sincérité et ta confiance.

Je tiens également à remercier Thierry Bernard qui tout au long de ma thèse, par ces idées et son habileté aura fait de l'ensemble de nos désirs expérimentaux une réalité.

Je remercie vivement l'ensemble des théoriciens du Service de Physique et Chimie des Surfaces et Interfaces (SPCSI), Sylvain Latil, Rémi Zoubkoff, Cyrille Barreteau, Alexander Smogunov, Yannick Dappe pour avoir accueilli mes calculs sur leur cluster et pour m'avoir distillé tout plein de conseils tout au long de ces trois années. Leur aide fut précieuse.

Je remercie très chaleureusement Jean-Christophe Géminard et Damien Vandembroucq pour avoir accepter d'être rapporteur de ma thèse, Knut Jørgen Måløy et Jean-Jacques Marigo pour en avoir été examinateurs et Stéphane Roux pour avoir accepté de la présider.

Je voudrais encore remercier les membres du Service de Physique de l'État Condensé et plus particulièrement Cécile Gasquet, François Daviaud, François Ladieu, Marco Bonetti qui en plus de nous avoir apporté leur aide et leur expertise ont su nous acceuillir, nous et notre expérience, avec beaucoup de respect et de simplicité.

Je remercie pour leur attentive et précieuse relecture du manucrit Cindy Rountree, Daniel Bonamy, Davy Dalmas, Jean-Christophe Géminard et Damien Vandembroucq. Leurs interventions ont grandement apporté à la justesse et à la cohérence de ce manuscrit.

La science n'avance pas sans échanges et sans discussions. Mon travail de thèse doit certainement beaucoup à toutes les personnes avec qui j'ai pu échangé lors de conférences ou avec qui j'ai pu collaborer. Merci donc à Luc Barbier, Tristan Cambonie, Alexander Dobrinevski, Bérengère Dubrulle, Jay Fineberg, Lionel Gélébart, Lamine Hattali, Véronique Lazarus, Laurent Ponson, Carmen Miguel, Naman Recho, Pedro Reis, Cindy Rountree, Alberto Rosso, Stéphane Santucci, Julien Scheibert, Ludovic Vincent et Jérôme Weiss.

Mener à bien une thèse n'est pas une épreuve de tout repos. Je remercie donc les personnes du

SPCSI qui ont su rendre mes journées de travail joviales et agréables tout autant que studieuses. Merci à Cyrille Barreteau, Thierry Bernard, Yannick Dappe, Bruno Delomez, Jérémy Heuille, Catherine Julien, Sylvain Latil, Bruno Lectard, Claire Mathieu, Jean-Baptiste Moussy, Julien Rault, Fabien Silly, Alexander Smogunov et Ludovic Tortech. Je remercie plus particulièrement Marina Barlet qui en tant que collègue de bureau sympathique a su au jour le jour me faire profiter de sa bonne humeur.

Je réserve mes derniers remerciements à ma famille et mes amis qui, tout au long de mes années d'études qui s'achèvent par ce manuscrit, ont su, malgré la distance tant géographique que thématique, rester d'un soutien constant et sincère. Un profond merci à Thierry, Françoise, Aurélien, Camille, Georges, Nazarène, Louis, Nadine, Julien, Anne-Laure et Jérémy. Enfin, le tout dernier merci ira à ma douce à qui je dois énormément. À toi, Lucile.

Sommaire

Context and Motivation

When? Where? and **How?** These are three fundamental questions that orientate the work of scientists when dealing with the fracture phenomenon. From a technological point of view, understanding how materials break has been a fundamental problem for centuries. Some of the first recorded scientists tackling these questions were Leonardo Da Vinci [Vinci (1940)] and Galileo Galilei [Galilei (1958)]. Indeed, Da Vinci's notebooks provides an interesting description of tension tests achieved on metal wires (see figure 1). By attaching and slowly filling a sand bag to the end of the wires, Da Vinci measured their strength to failure. He observed that wires with the same cross-section yet longer lengths failed before their counterparts with shorter lengths. This may appear counterintuitive: A simple analysis based on continuum mechanics shows that wires with same section carry the same stress, irrespectively of their length. Hence, assuming that strength is a material property, one could think that the stress at failure would not depend on the wire's length.

Nevertheless, continuum mechanics considers homogeneous materials. This is not close to the reality, especially for the metal wires forged at the Renaissance! Actually, disorder has a profound impact on the material's strength, since fracture typically originates from the weakest spots like preexisting microcracks or voids. The longer the wire, the easier it is to find a weak spot, and hence, the smaller is the strength. Da Vinci's notebook reports the first experimental verification of size effect in fracture. The difficulty then is to develop a framework being able to address these statistical aspects.

Single crack problem: Continuum fracture theory

For brittle solids broken under tension, Linear Elastic Fracture Mechanics (LEFM) tackles the difficulty by reducing the problem to a destabilization and subsequent growth of

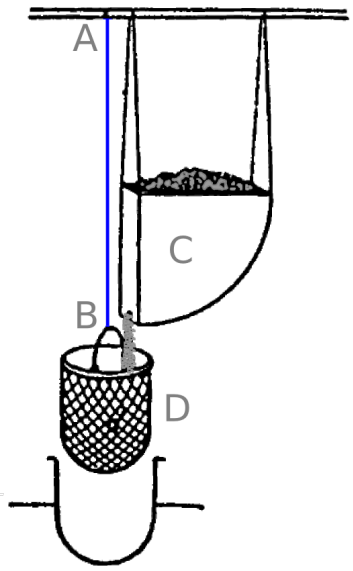

Figure 1: Da Vinci's set-up used to test the strength of metal wire. One end of the cable (in blue) is attached to the roof in A while a basket (D) hangs to the other end in B. Sand is poured from the basket C. See text for more details.

a dominant pre-existing crack. Then, strength statistics and its size dependence are captured by the weakest-link Weibull theory [Weibull (1939)].

A single crack running in a linear elastic solid under tensile loading can be addressed within the elastodynamics framework. As first noted by Orowan [Orowan (1955)] and Irwin [Irwin (1957)], the stress field σ_{ij} is singular in the vicinity of the crack tip (see figure 2). To first order, the following is true:

$$\sigma_{ij}(r,\theta) \approx \frac{K_I}{\sqrt{2\pi r}} f_{ij}(\theta, v), \tag{1}$$

where (r,θ) are the polar coordinates in a frame $(\vec{e}_x, \vec{e}_y$ centered at the crack tip, v is the speed of the tip, $f_{ij}(\theta, v)$ is a dimensionless universal function indicating the angular variation of the stress field and its variations with v, and K_I, *static stress intensity factor*, is the relevant parameter to quantify the macroscopic forcing applying on the crack. It depends on the external loading and specimen geometry only. It is proportional to the externally applied forces, and its dependency with respect to the geometry can be computed (*e.g.* via finite elements methods) in virtually any situations, irrespectively of its complexity.

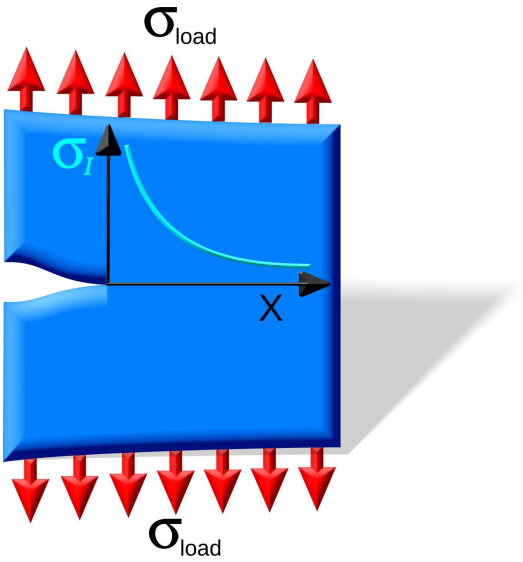

Figure 2: Stress at the crack tip for an ideal material where σ_I stands for σ_{xx}.

This situation of simple tensile loading can be generalized to situations with more complex loadings. Due to the linearity of elastodynamics, these latter loadings can always be decomposed into three independent loading modes:

- Mode I (prying) mode (figure 3-B): This corresponds to the splitting of a crack under tensile stresses.
- Mode II(shearing) mode (see figure 3-B): This corresponds to a shear parallel to the direction of crack propagation.
- Mode III (tearing) mode (see figure 3-C): This corresponds to a shear parallel to the crack front.

For these three cases, the stress field takes a singular form similar to that written in equation 1 with prefactors K_I, K_{II} and K_{III} to be associated with the tensile, shearing and tearing modes, respectively.

The next step is to describe how a crack responds to a given loading. Here, the theory makes use of the singular form of the stress field, which implies arbitrary large stress values as one zooms in on the crack tip. This is physically impossible, so this means that the material stops to be linear elastic around the crack tip. This small zone where linear elasticity stops to be relevant is called the *Fracture Process Zone* (FPZ) and encompass all

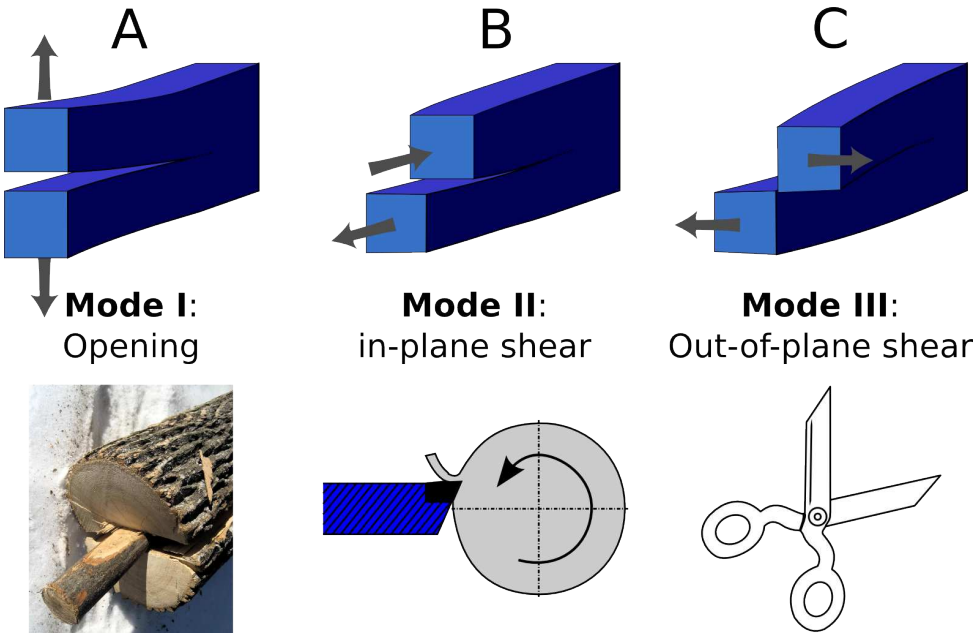

Figure 3: Different modes of fracture and associated illustration taken from the everyday life.

the damage and failure mechanisms. According to the Griffith's theory [Griffith (1920)], the onset of fracture is reached when the amount of elastic energy released by the solid as the crack propagates by a unit length is equal to the energy dissipated within the FPZ during this unity propagation. The form taken by the stress field at the crack tip (see equation 1) relates the mechanical energy release G at the onset of crack propagation (*i.e.* for $v = 0$) to the stress intensity factors. In plane stress, one writes:

$$G = \frac{1}{E}\left(K_I^2 + K_{II}^2 + (1-\nu^2)K_{III}^2\right) \tag{2}$$

Where ν and E are the shear and Young modulus of the material, respectively. The energy dissipated within the FZP as the crack propagates to create two new fracture surfaces of unit area is called the *fracture energy*, Γ, and is considered as a material constant. The Griffith criterion for crack destabilization then is:

$$G > \Gamma \tag{3}$$

Once the crack starts to grow, its velocity is governed by the balance between the

mechanical energy flowing into the FPZ and the dissipation rate $\Gamma \cdot v$, where v the crack tip's speed. For mode I cracks running at speed v, the equation of motion is [Freund (1990)]:

$$\left(1 - \frac{v}{c_R}\right) \frac{K_I^2}{E} = \Gamma \tag{4}$$

where c_R refers to the Rayleigh wave speed in the material. In this Ph.D., slow crack are of interest. To first order in v/c_R. The equation of motion reduces to:

$$\frac{1}{\mu} v = G - \Gamma, \tag{5}$$

with $\mu = c_R/\Gamma$.

To complete the theory, the model requires a criterion to know the crack tip's propagate direction. In homogeneous isotropic solids, the local symmetry principle [Gol'dstein and Salganik (1974)] states that the direction of propagation must locally maintain pure tension (see [Lazarus (2011)] for a careful review on this point). This implies that the direction of propagation is chosen such that:

$$K_{II} = 0 \tag{6}$$

Shortcomings in the continuum theory: Experimental illustrations

The LEFM theory presented above provides a coherent framework to describe crack destabilization and further propagation in brittle solids. Still, numerous observations contradict these predictions. In particular, the equations of motion (equation 5) and of trajectory (equation 6) predict a rather regular, continuous, motion along a smooth trajectory for a slowly loaded and initially smooth crack. This is not always the case.

Several experimental observations reveal that fracture can display complex large-scale fluctuations characterized by scale invariant features [Mishnaevsky (1997); Bonamy

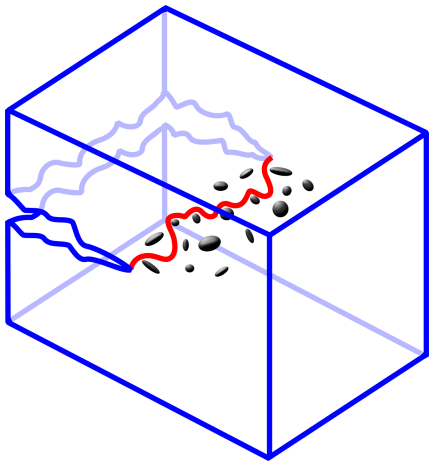

Figure 4: Heterogeneities at the crack tip: non-idealized material.

(2009)]. First, fracture surfaces are found to exhibit roughness the sizes of which are much larger than the typical microstructure scale. These morphologies are characterized by self-affine morphological features [Mandelbrot et al. (1984); Bouchaud et al. (1990); Måløy et al. (1992); Mandelbrot (2006); Bouchaud (1997); Bonamy and Bouchaud (2011); Ponson (2007)]: Topographical profiles $h(r)$ of post-mortem fracture surfaces are statistically invariant through the transformation $(r, h) \to (\lambda r, \lambda h)$, where ζ refers to the roughness exponent. Moreover, the fracturing dynamics can exhibit jerky scale-free dynamics. These intermittent dynamics are evidenced indirectly from the acoustic emission (AE) analysis , which accompany crack growth [Santucci et al. (2004); Salminen et al. (2006); Koivisto et al. (2007); Ramos et al. (2013); Astrom et al. (2006)] or directly in peeling experiments along heterogeneous interfaces [Måløy et al. (2006); Grob et al. (2009)]. Also, they exist in fracture phenomena at the geophysics scale, such as earthquakes and eruptive events and give rise to several empirical laws widely used in the mitigation and assessment of related hazard, *e.g.* the Richter-Gutenberg [Gutenberg and Richter (1944)] law, the Omori law [Omori (1894b)], the Voight law [Voight (1988)], the Utsu law [Utsu (1971)], *etc.*

Possible solutions: Statistical physics approaches

In essence, the above observations cannot be accounted for within homogeneous LEFM framework. Still, the observation of scale-invariant statistics and the fact that the associated exponents are to fair extent universal suggest that some tools issued from statistical physics may be relevant [Herrmann and Roux (1990); Alava et al. (2006); Bonamy (2009)].

Fiber bundle models (FBM) (see [Pradhan et al. (2010)] for review) and random fuse models (RFM) (see [Alava et al. (2006)] for review) were *e.g.* able to reproduce qualitatively, with a minimal set of ingredients, the scale-free microfracturing dynamics [Hansen and Hemmer (1994); Zapperi et al. (1997a)] and self-affine morphological features [Hansen et al. (1991); Zapperi et al. (2005)] of cracks.

The goal of these discrete approaches is not to describe quantitatively solid fracture. They prefer to reproduce qualitatively the scale free statistics keeping only the two main ingredients characterizing material failure: (i) the microstructure randomness and (ii) the long-range coupling due to the redistribution of elastic fields. As a result, they are difficult to conciliate with LEFM framework.

Another approach pioneered by Gao and Rice [Gao and Rice (1989)] takes into account explicitly, within the elastostatics framework, the local distortions of the crack front induced by the material's inhomogeneities. In this context, [Schmittbuhl et al. (1995); Ramanathan et al. (1997)] the fracture problem maps to the depinning problem of an elastic line driven in a random potential. This theory succeeds in reproducing the experimentally observed crackling dynamics [Bonamy et al. (2008)] and self-affine morphological features of crack roughness [Bonamy et al. (2006); Dalmas et al. (2008)]. It can also be used to predict the statistics and size effect of effective toughness [Roux et al. (2003); Patinet et al. (2013)]. Nevertheless, most of the predictions remains qualitative, limited to the reproduction of the scaling laws/scale-free statistics and (eventually) of the associated exponents. They lack experimental data for confirmation.

Goal of the Ph.D. work

The goal of my Ph.D. is to fill this gap. The first part of this manuscript presents an original fracture experiment that permits to test the pinning-depinning theory. It details methods for making a single crack grow in an artificial rock of controlled microstructure (see figure 4) loaded in tension. These experiments captured/measured the time evolution of crack speed, stored and released energy, and acoustic emission with enough accuracy to characterize quantitatively their fluctuations. Part I chapter 2 details some surprising finds; the statistical analysis of AE events displays similarities to seismic activity accompanying earthquakes. The extent at which the time-evolution of speed and stored energy

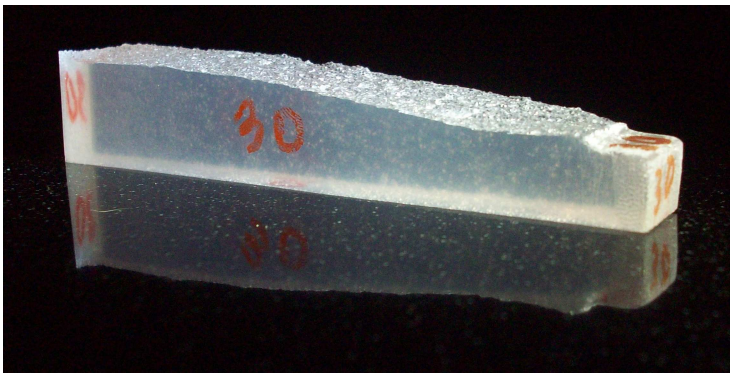

Figure 5: Picture of a broken specimen of our homemade artificial rock (illustration of the work discussed in the first part of the manuscript).

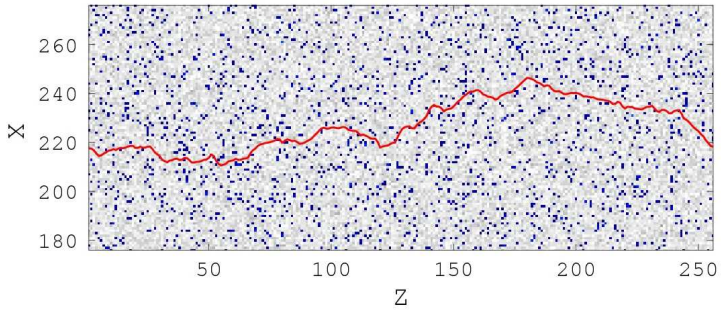

Figure 6: Top view of a crack front simulated numerically (illustration of the work discussed in the second part of the manuscript).

is compatible with depinning-like scenario is presented in Part 1 chapter 3.

Still, intermittent, jerky dynamics is not always observed in fracturing solids (even in presence of heterogeneities), and very often, the LEFM approach gives a correct prediction of the crack growth. To explain this apparent paradox, the second part of this manuscript aids in bridging the gap between the depinning approach and LEFM (see figure 6). Numerical simulations which invoke the equation of motion unravel the conditions (in term of loading rate, specimen geometry, microstructural disorder, material constants) that select continuum-like or crackling dynamics (chapter 2 of part I). Chapter 3 of part II addresses how loading, specimen, and microstructure conditions govern the dynamics in the crackling phase, in which LEFM is not relevant.

Part I

Experimental aspects

Introduction

Contrary to what is predicted by LEFM, crack growth in heterogeneous brittle material sometimes displays jerky dynamics with seemingly random discrete jumps over several length scales. Many fracture experiments reproduce these crackling dynamics via a wide variety of experimental fracture setups (see [Bonamy (2009)] for a review of them). Each time clustering in energy of events, in space and/or in time, is evidenced invoking seismic-like power-laws.

First, since these scale-free distributions are observed universally on Earth independent of the considered area and the time of observation, it is theorized that subjecting laboratory rock specimens to loadings similar to the ones undergone by the Earth's crust should reproduce similar statistical features. In this context, time series of acoustic emission were recorded in various rocks loaded under uniaxial compression up to shear fracture [Mogi (1967); Scholz (1968a,b); Hirata (1987); Davidsen et al. (2007); Baro et al. (2013)]. These loads produce a complex mixing between fracture, damage and friction and manage to reproduce fairly well the statistics observed by Earthquakes. Nevertheless, due to the phenomenon complexity, it is not possible to catch the physics that rule these statistics.

The signature of crackling dynamics is also evidenced via AE which accompanies fracture in simpler situations. Experiments in mode I failure for many brittle materials (rocks [Davidsen et al. (2007)], wood and fiberglass [Garcimartin et al. (1997); Guarino et al. (1998)], polymeric foams [Deschanel et al. (2006, 2009)] and paper [Salminen et al. (2002); Santucci et al. (2004, 2007); Ramos et al. (2013)]) have shown to evidence power-law distributions of energy and silent time between two successive events to what is observed by earthquakes. However, it should be emphasized that the relation between AE energy and released elastic energy remains largely unknown [Minozzi et al. (2003)]. Moreover, power-law exponents vary with the material [Bonamy (2009)] so they do not appear to be universal. It is also worth noting that most of the AE fracture experiments are non-stationary: usually, one starts with an unbroken specimen and loads it to catastrophic failure. In these test, the recorded AE reflects more the micro-fracturing processes preceding the initiation of the macroscopic crack than the growth of the latter. This hierarchy between preceding smaller events and a single main event (*i.e.* crack) is intrinsically different from the case of the earthquakes so both phenomenon can be directly compared from a statistically point of view.

Recently stable crack growth geometries have been used to make the crack front propagate through brittle heterogeneous materials. First, [Salminen et al. (2006); Koivisto et al. (2007)] experimentally investigated the AE statistics in the steady regime of crack propagation of paper peeling. The distribution of AE energy and silent time between events follows a power-law, but the hierarchical organisation between macroscopic events and smaller ones, is not ruled by the same statistic as the one observed for earthquakes. A similar interfacial crack propagation experiment has been set-up by [Måløy and Schmittbuhl (2001); Måløy et al. (2006)] in polymethylmethacrylate (PMMA). They investigate experimentally the dynamics of crack propagation in a simpler configuration, namely the one of planar crack propagating along a weak heterogeneous interface between two sealed heterogeneous transparent PMMA plates. Using a fast camera, they directly observed crack propagation and defined quakes as jump of the crack front (see [Grob et al. (2009)] for more details). The statistical analysis of these quakes [Grob et al. (2009); Tallakstad et al. (2011, 2013)] in terms of surface, duration, time of occurrence and epicenter position were found to be the same in both experimental quakes and real seismicity. Nevertheless no quantitative access to relevant quantities in mechanics (like variation of energy in the system) or acoustics has been studied and the effect of the microstructural texture remains unclear since it is not possible to impose and tune the characteristic size.

Finally, few experiments exists where one breaks materials with a well-defined structure at the nanoscale and still observes crackling dynamics. These experiments are cleavage tests performed on pure crystals such as mica [Marchenko et al. (2006)] and sapphire [Astrom et al. (2006)] and reveal power-law statistics for both the distribution of released energy and silent time between two successive nanofractures. In the case of sapphire, the structure is controlled, but the loading conditions are very complex. Thus, no link is done between the relevant quantities in fracture mechanics such that energy release rate and the statistics predicted by the pinning model

Hence, the goal of my thesis is to bridge the main gaps left by the previous experimental works (*i.e.* to understand the continuity between the complexity of the earthquake physics and the relative simplicity of the pinning model). Therefore, the model fracture experiments invoked herein remain simple enough to be mapped using the theoretical pinning model; but they are rich enough to reproduce the complex statistical features observed by earthquakes. The key objectives of my thesis are:

- Make a 3D crack front propagate in a 3D isotropic material.

- Reduce the fracture to a simple pure mode I propagation mechanism.
- Ensure the propagation is dynamically and geometrically stable.
- Tune the loading rate over several orders of magnitude.
- Fix the microstructure size around a characteristic value and be able to vary it from one sample to another.
- Measure at the same time AE and elastic energies.
- Have quantitative access to the relevant mechanics (energy E, crack speed v) and fracture mechanics (energy release rate G, fracture energy Γ) quantities.
- Ensure the structural integrity of the fracture surfaces for post-mortem analysis (*i.e.* do not destroy the sample during fracture experiments!).

This document details experimental procedures and results obtained. The first chapter describes the experiment, from the preparation of the samples to the computations and filtering of the mechanical and acoustic quantities. Then in the second chapter is dedicated to the analyse of AE with the tools made for earthquake studies to show the statistical richness of fracture in opening mode. The experiment permits access to the elastostatic observables, thus the statistics of their variations are examined in chapter 3.

Chapter 1

Material and method

Introduction

In this chapter, I present the experimental setup that was developed during my PhD, along with the motivation behind its underlined design. The overall goal is to better understand how crackling dynamics form in fracture situations. In this context, we have seen in the introduction that the dynamics observed in some model fracture experiments share statistical similarities with the seismicity associated with Earthquakes.

Below, I detail how to carry out mode I (opening mode) stable fracture propagation in model experiment. These experiments employ tunable heterogeneous brittle materials to recording AE and elastostatic observables in a synchronized manner. The process is explained from sample fabrication to data post processing. Section 1.1 presents the wedge-splitting fracture experiment and its specifications. Then, section 1.2 details the protocol used to fabricate samples. The last section divulges post-processing methods of experimental outputs.

1.1 Fracture set-up: Wedge splitting geometry

The first step is to design a fracture test that permits the growth of slow, stable cracks in pure mode I at various velocities in a controlled manner. The wedge splitting geometry fulfils these requirements [Bruhwiler and Wittmann (1990); Karihaloo and Xiao (2001); Scheibert et al. (2010); Guerra et al. (2012)]. For example, the geometry is perfectly

adapted since the stress intensity factor decreases with crack length. The setup is depicted in figure 1.1. The specimens are first machined to obtain parallelepipeds of dimensions $L \times H \times W$, with $L = 14 \pm 0.4$ cm, $H = 12 \pm 0.4$ cm, and W depending on the material: $W \approx 1.5$ cm for artificial rocks obtained at high sintering pressure, and $W \approx 2$ cm for those obtained at low sintering pressure (see next section). Subsequently, a notch is milled by: (i) cutting a $4.2 \times 3 \times W$ cm^3 rectangle from the middle of one of the 125×15 mm^2 faces; (ii) in the middle of the rectangle a thick groove, 10 mm-long 2 mm, is introduced via a diamond saw ; and (iii) finally a seed crack (~ 0.5 mm long) is formed with a razor blade, a seed crack at the tip of the groove (see appendix B for more details about the sample geometry).

The sample is then loaded by pushing a steel wedge (semi-angle of 15°) into the notch. At a given time, the seed crack destabilizes and starts to grow. Henceforth, the reference frame will coincide with typical conventions in fracture mechanics: (1) $\vec{e}_x$ parallel to the direction of crack propagation (L-direction); (2) $\vec{e}_y$ parallel to the tension loading (H-direction); and (3) $\vec{e}_z$ parallel to the mean crack front (W-direction).

Special attention is given to limit parasitic dissipation sinks (friction or plastic deformation) in the system which can exist outside of the FPZ (*i.e.* dissipation zone located at the crack tip). In this context, the wedge does not push directly into the specimen, but throughout two steel blocks equipped with rollers placed on both sides of notch (see figure 1.1). The opposite side of the specimen lays on a pivot of radius of 3.2 cm. This permits (i) to spread the loading force over a large contact area and prevent any plastic deformation of PMMA at the loading contacts; and (ii) to suppress friction in the system. As a result, the region in the vicinity of the crack tip is assumed to be the sole dissipation source for mechanical energy in the system.

The motion $u(t)$ of the wedge is controlled by a stepper motor (Oriental motor EMP400 Series) allowing incremental displacements from 160 nm to 1.6 nm. In each of the subsequent fracture experiments, the wedge speed ($V = \mathrm{d}u/\mathrm{d}t$) was set to a constant V during a single test. To modify the crack front dynamics between experiments, the wedge's speed varies from 1.6 to 1600 nm/s. During the tests, the force, $f(t)$, applied to the specimen is measured in real-time (acquisition rate of 50 kHz, accuracy of 1 N) via a S-type Vishay load cell connected to the bottom of the sample (see figure 1.1). A camera images the crack propagation at the specimen surface (30 frames per second with a pixel size of 130 μm). Finally, eight acoustic transducers are strategically located on the specimen (four on each

side). They record the acoustic waves generated by the failure (MHz acquisition rate and aJ accuracy) and subsequently pinpoint their emission sources.

A Labview® interface controls the wedge's motion $u(t)$ and records the applied force, $f(t)$, and the specimen's image in a synchronized fashion. On the other hand, the AE is recorded via a dedicated computer. The computers are synchronized at the start of an experiment via a BNC cable and Labview's® interface package. More details on the experimental aspects are provided in appendix B.

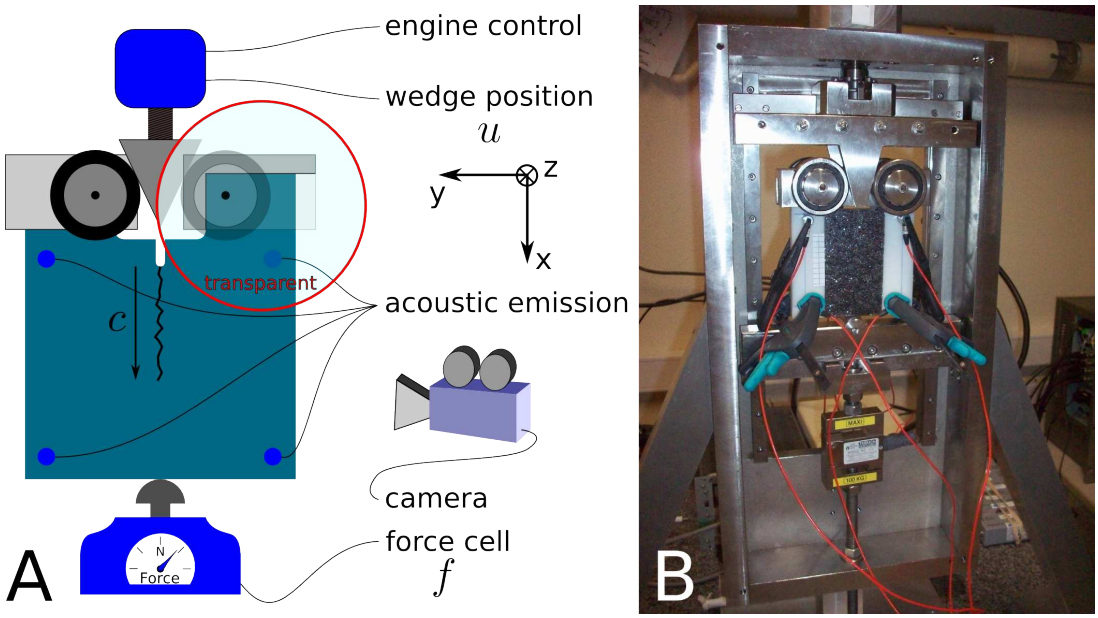

Figure 1.1: Schematic view (A) and picture (B) of the instrumented wedge splitting device. The reference frame is defined so that $\vec{e}_x$ is parallel to the direction of crack propagation , $\vec{e}_y$ is parallel to the tension loading, and $\vec{e}_z$ is parallel to the mean crack front. See text for details.

1.2 Material of study: Artificial rock made of sintered polystyrene beads

The next step is to find the proper material to study. Many experiments reporting intermittent and crackling involve rocks [Mogi (1967); Scholz (1968a,b); Hirata (1987); Davidsen et al. (2007); Baro et al. (2013)]. Hence, rocks appear as promising candidates. Nevertheless, the use of natural rocks suffers from two drawbacks:

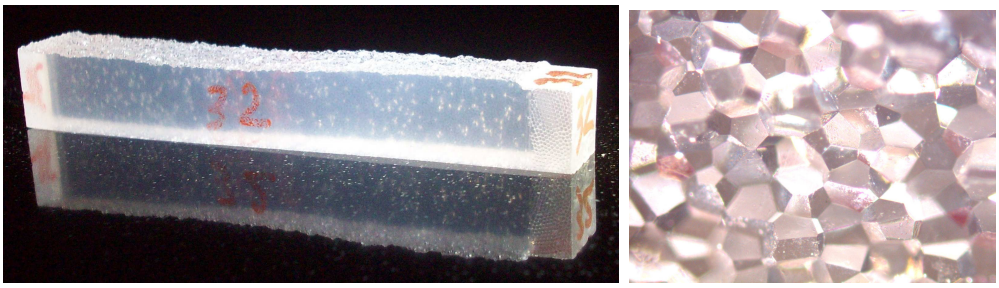

Figure 1.2: Photo of fabricated sample (left) and optical microscope image of the top of the fabricated sample (right) views of the fracture surface of a broken sample (Sa_2: $d = 500$ μm, $V = 160$ nm/s, no porosity).

- They exhibit a complicated polydisperse microstructure, with grain sizes ranging from the μm to the cm and varying porosity, so it is difficult to control their texture and ensure its reproducibility;

- They are stiff materials (Young modulus close to 100 GPa), which makes the experiments sensitive to slight misalignments and inaccuracies in the machining of the experimental setup and of the specimens.

To solve these problems, we chose to mimic the way nature makes rocks (by sintering sand grains at high pressure and high temperature) by replacing the sand grains with a more handy material: polystyrene beads. As a result, artificial polymer rock of reproducible and tunable microstructural texture (modulated by controlling the bead size and the sintering parameters) are obtained. An added advantage to the polystyrene beads is they are significantly softer than rock (Young modulus of 2.7 GPa). Hence, the specimens are much more tolerant to unavoidable misalignments and inaccuracies in the setup and/or specimen machining.

The various stages involved in the sintering process are sketched in figure 1.4-A and detailed in appendix A. First, polymer beads are poured into a rigid metallic mold. The beads are monodisperse and made of polystyrene (see figure 1.3). Second, the filled mold is placed in an oven and heated to 90% of the bead's glassy temperature. When this temperature is reached, prescribed pressure is reached by compressing the polymer beads and the mold between the two jaws of an Instron machine. The system is maintained under these conditions of temperature and pressure for 45 min (figure 1.4-B). The pressure is then relaxed, and the temperature is increased to anneal the specimen (figure 1.4-C). Finally, the sample is cooled down and extracted from the mold (figure 1.4-D). The

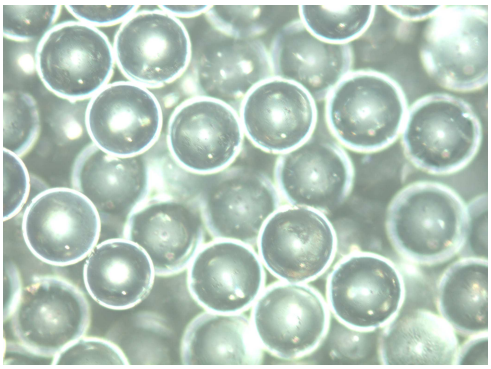

Figure 1.3: Picture of monodisperse 500 μm beads of polystyrene.

temperature and pressure evolutions during the sintering process are detailed in figure 1.5. Over the fracture experiments, the microstructure size is modulated by varying the bead diameter from 20 μm to 500 μm, and the specimen porosity is changed by modifying the sintering pressure from 60 kPa to 5.2 MPa.

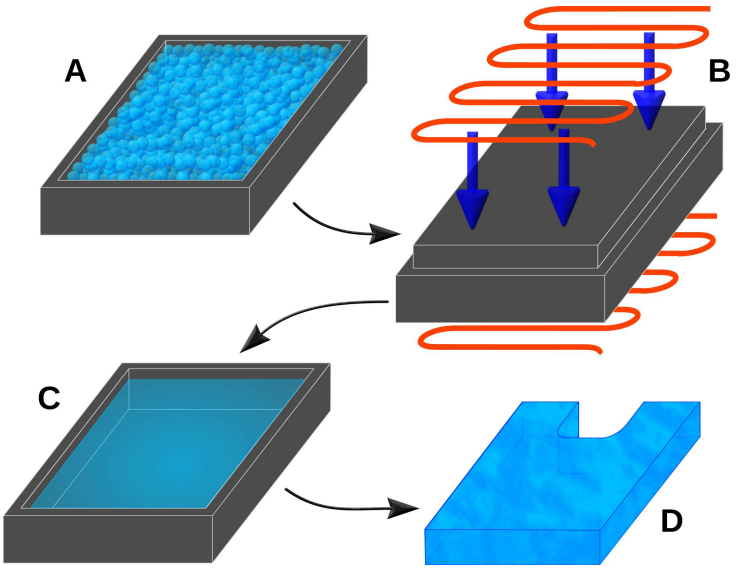

Figure 1.4: Sketch of the various stages involved in the sintering process. See text for details.

The resulting specimens are found to exhibit a tunable, reproducible, and fairly homogeneous microstructural texture. More importantly, the fracture of such materials is found to be intergranular, not transgranular. Indeed, as can be seen from the images of the fracture surfaces presented in figure 1.2 (top view on the right), the crack has propagated between the grains to break the sample, not through them. The table 1.1 gathers the sintering conditions, bead size, density, porosity, and elastic modulus for the various

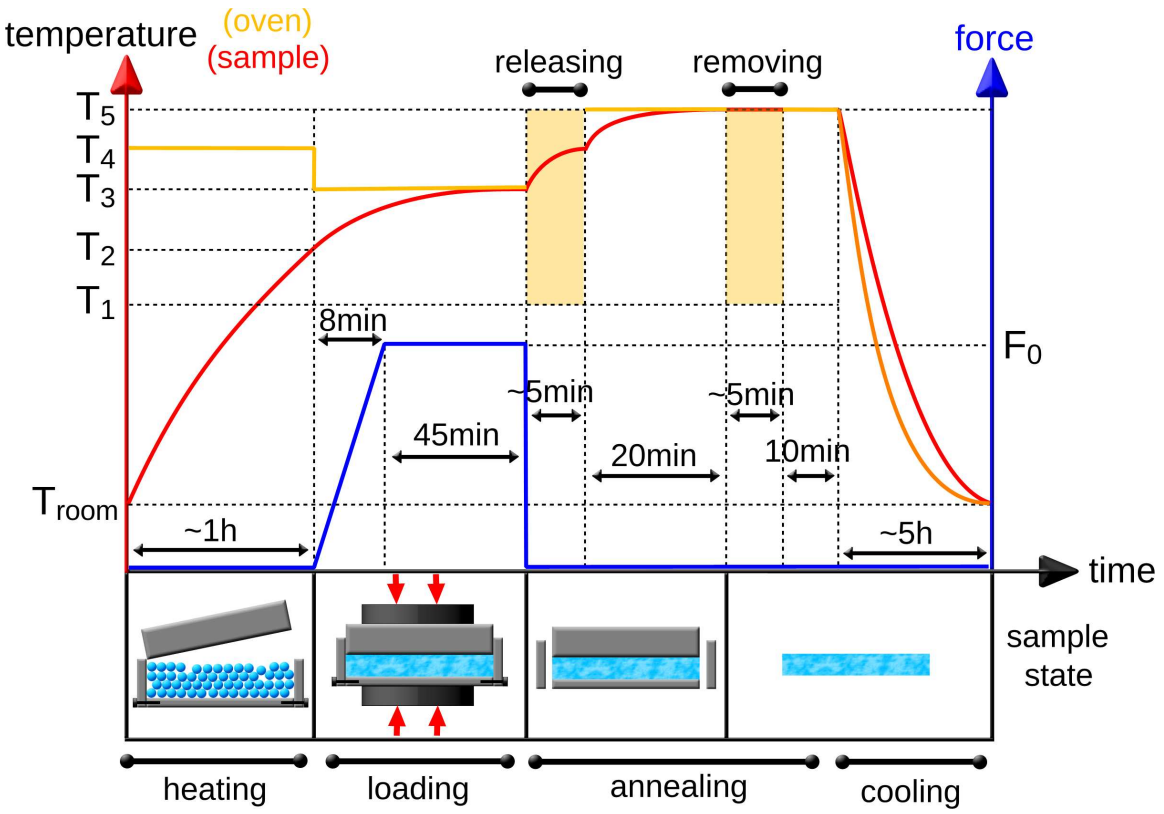

Temperature	500 μm beads	230 μm beads beads	$50-80$ μm beads	20 μm beads
T_1	80°C	80°C	70°C	60°C
T_2	105°C	105°C	105°C	90°C
T_3	115°C	115°C	115°C	100°C
T_4	120°C	120°C	120°C	105°C
T_5	130°C	130°C	130°C	110°C

Force F_0 (N)	$1 \cdot 10^3$	$1 \cdot 10^4$	$2 \cdot 10^4$	$4 \cdot 10^4$	$8 \cdot 10^4$
Pressure (MPa)	0.06	0.6	1.3	2.6	5.2

Figure 1.5: Evolution of the temperature, force and pressure during the sintering protocol. See text for details.

Bead size, d (μm)	F_0 (t)	Material density (kg/m^3)	Material porosity (%)	Young modulus (GPa)	Sample name
500	**8**	**1046**	**0**	**2.4**	Sa_1, Sa_2, Sa_3
500	4	1052	0	2.2	
500	2	1052	0	2.1	
500	1	1014	3	2.2	
500	0.1	802	24		
230	**8**	**1045**	**0**	**2.2**	Sb_1
230	4	1052	0	2.2	Sb_2
230	2	1045	0		Sb_3
230	1	1030	2	2	Sb_4
230	0.1	772	27	0.8	Sb_5
80-50	**8**	**1040**	**0**	**2.1**	Sc_1
80-50	4	1044	0	2.3	Sc_2
80-50	2	1039	0	2.5	Sc_3
80-50	1	1047	0	2.5	Sc_4
80-50	0.1	744	30	0.1	Sc_5
20	**8**	**1019**	**0**	**2.3**	Sd_1
20	0.1	927	12	1.7	Sd_5

Table 1.1: Material properties of the various specimens broken during this PhD. Samples written in blue bold will be studied in detail herein.

specimens synthesized and broken during my PhD. The porosity was deduced from the ratio between the density of the beads and that of the specimens. The Young modulus was obtained via dynamic mechanical analysis (DMA) for specimen Sa_1 (see appendix A). For the other specimens, it was deduced from the ratio between their stiffness prior to crack onset and that of Sa_1.

During my PhD work, I have focused on the samples with the smallest ($\sim 0\%$) porosities. Porosity, indeed, introduces a second characteristic length scale in the microstructure (in addition to that of the bead diameter) and yields an acoustic attenuation that made the characterization of the acoustic events inaccurate. Moreover, crackling dynamics is marked in the specimens with large microstructure length-scales. Thus, most of the statistical analysis presented in the two following chapters will involve the material entitled Sa_1 (bold line in table 1.1) that was obtained from 500 μm beads sintered at a pressure of 5.2 MPa.

1.3 Data post-processing and recorded signals

As outputs for each experiment, we get the wedge position $u(t)$, the applied force $f(t)$, images of the crack propagation at the specimen surface, and the acoustic signals detected at the eight transducers. We need to process and filter these data to compute the relevant fracture mechanics quantities and characterize them. The data processing is detailed in the following subsections

1.3.1 Acoustic measurement

The AE is collected at 8 different locations via 8 piezoacoustic transducers. The signals are preamplified, band filtered, and sent to a powerful PCI-2 acquisition system from Euro Physical Acoustics working at 40×10^6 samples per second. For one transducer, acoustic event i starts at time t_i when the recorded signal $\mathcal{U}(i)$ (in volt) crosses a prescribed threshold (40 dB), and finishes when the signal's oscillation decreases below the threshold. Each event is mainly characterized by two quantities: Time of occurrence and event energy. The former is to be associated to t_i. The latter can be defined either as the integral $\mathcal{U}^2(t)$ over the duration of the event (absolute energy) [Garcimartin et al. (1997); Koivisto et al. (2007); Baro et al. (2013)], or as the maximum square amplitude $\mathcal{U}^2(t)$ for the event duration [Mogi (1967); Davidsen et al. (2007); Mallick (2010)]. As shown in figure 1.6-B both definitions are fairly consistent since they yield proportional quantities, except for the smallest amplitudes. We chose here to follow [Mogi (1967); Davidsen et al. (2007); Mallick (2010)] and define the AE energy as the maximum square amplitude $\mathcal{U}^2(t)$ since, as we will see in the next chapter, the actual duration of an event cannot be attributed to a microfracture event, but rather to the attenuation of the acoustic waves after few reflections within the whole specimen. Note that such a definition is also closer to that proposed by Richter in seismology [i].

The next step is to filter the events collected at each transducer. A single "physical" microfailure event, indeed, will or will not be detected at the various transducers, depending on its intensity as it reaches them. As a result, a raw observation of the collected AE events is counted several (from one to eight) times for each true microfailure event.

[i] The first (and most popular) magnitude scale M to quantify the earthquake energy is the one introduced by Richter [Richter (1935)] that relates M to the logarithm of the maximum amplitude measured on a Wood-Anderson torsion seismometer at a given distance from the earthquake epicenter.

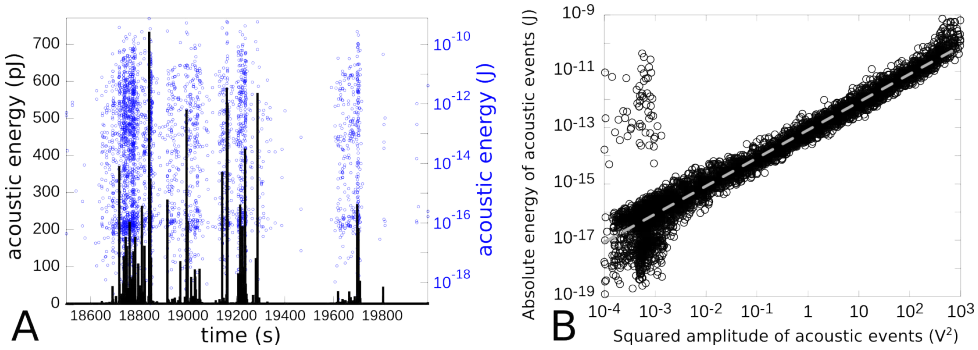

Figure 1.6: A: Energy of acoustic events as a function of time during a typical fracture experiment (sample Sa_1: $d = 500$ μm, $V = 16$ nm/s, no porosity). B: Comparison between maximum squared amplitude ($max(\mathcal{U}^2)$) and absolute energy ($\int \mathcal{U}^2(t)dt$). The axes are logarithmic. The dashed gray line with a slope of 1 is given to guide the eye

We then adopted the following procedure to filter the signals: (i) all the collected events are plotted in a time-energy diagram (figure 1.7); (ii) the points are clustered in groups separated by less than 1 ms (black ellipses in figure 1.7); (iii) all clusters with less than 3 members and more than 8 members are withdrawn (This represent less than 2% of the total); and finally (iv) we only keep the most intense event in each of the remaining clusters, which is assumed to coincide with transducer closest to the emission point (sensor 8 in the given example).

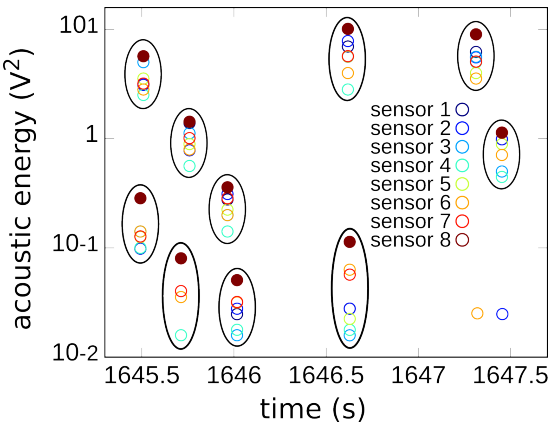

Figure 1.7: Filtering procedure to map a single AE event with each true microfailure event. All the collected events are plotted in a time-energy diagram (different symbols correspond to different sensors). Each cluster (black ellipse) is assumed to correspond to a single true event. In each cluster, only the AE event with the highest energy is kept (filled circle).

The acoustic system can also pinpoint the source of some events[ii]. A first observation of AE location resulting from the system show that few events are localized far from the crack front or even outside the sample (see figure 1.9-A). This is mainly due to the poor location accuracy of events with the lowest energy. We chose to remove these events from our AE catalog. To do so, we begin by removing the events located far ($\sim$ 5mm) from the crack path – This latter being measured in the (y, z) plane as the Tikhonov regularization of the position of all events. The resulting acoustic image is presented in figure 1.8. Then another filtering in time is performed: We consider a sliding group of events (5% of the total number of events) sorted by time and for each time step, we remove the 2% the furthest from the center of mass of the group. Finally a last filtering is space is performed following a similar process: We consider a sliding group of events (5% of the total number of events) sorted by crack length and for each time step, we remove the 2% the furthest from the mean time occurrence in the group. These sequence of filters typically remove between 10% to 20% of the events. In the considered example, the final result is presented in 3D in figure 1.9-B. A movie showing the 3D acoustic imaging obtained from a typical fracture experiments is given in Figure 1.11.

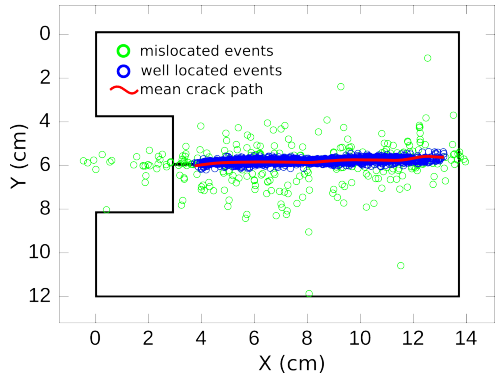

Figure 1.8: Filtering and selection of the localized acoustic events (see text for details on the procedure). All events are projected on the (y, z) plane. These data are recorded while breaking sample Sa_1: $d = 500$ μm, $V = 16$ nm/s, no porosity.

Finally, a last correction can be done to the acoustic data taking into account the energy attenuation of the wave front when propagating from the crack tip to the acoustic sensor. In this context, we aligned the eight transducers. A pulse was emitted by the first one, and received by the seven others. The measured attenuation was found to be around

[ii]Only the AE with the highest energy can be spatially localized by the acoustic software: The number of localized events is always much smaller than (typically one third of) the total number of collected events

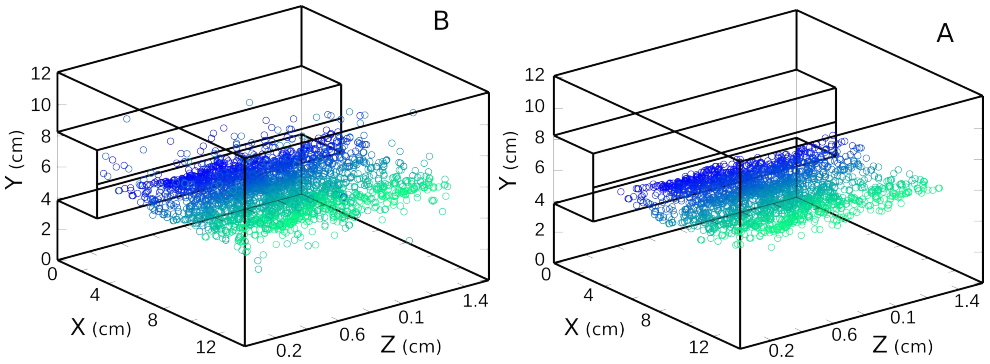

Figure 1.9: A: All localized acoustic events. B: Acoustic events well localised. The blue to green colors stand for the time at which the events take place. These data are recorded while breaking sample Sa_1: $d = 500$ μm, $V = 16$ nm/s, no porosity.

0.1 dB/cm/$\sqrt{\text{MHz}}$. Then, knowing the position of each sensor and the location of the considered event, one can correct the attenuation.

1.3.2 Instantaneous crack velocity, stored energy and energy release rate

The next step is to have access to the quantities relevant for continuum fracture mechanics, namely the crack length ($c(t)$) and the elastic energy release rate ($G(t)$), together with their evolution in time. As we have seen in section 1.2, direct outputs from each fracture experiment include: (i) the variations in the applying force $f(t)$ (figure 1.10); (ii) the wedge position $u(t)$ (figure 1.10); and (iii) a rough measurement of the crack length using the camera $c_{cam}(t)$ (figure 1.11). Processing these outputs signals gives $c(t)$ and $G(t)$ with enough accuracy to characterize their fluctuations!

First, the elastic energy, $E(t)$, stored in the system is directly computed from the applied force and wedge displacement (figure 1.12):

$$E(t) = \frac{1}{2} f(t) \cdot u(t) \tag{1.1}$$

Then, before measuring $G(t)$, we need to measure $c(t)$ precisely. The idea is to relate this quantity to $f(t)$ (measured with high accuracy) rather than measuring it directly on the images (less accurate). Let us assume that we have a rough approximation $c_{cam}(t)$ of

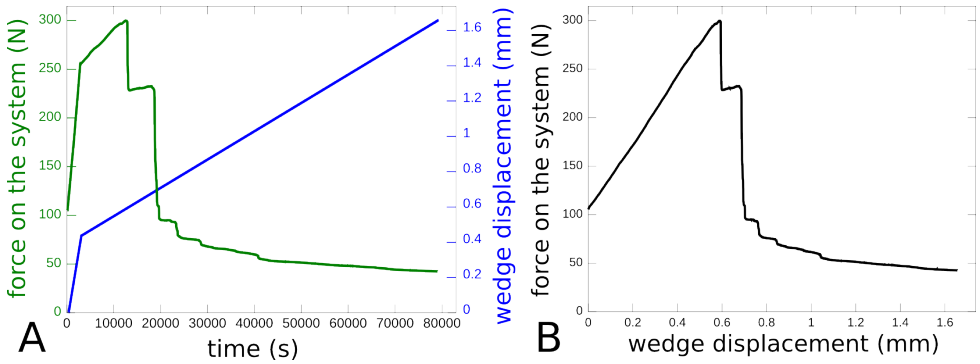

Figure 1.10: A: Evolution of the applied force on the system and of the position of the wedge as a function of the time. B: Force applied on the system as a function of wedge displacement. Those data are recorded when sample Sa_1 (d = 500 μm, V = 16 nm/s, no porosity) is breaking.

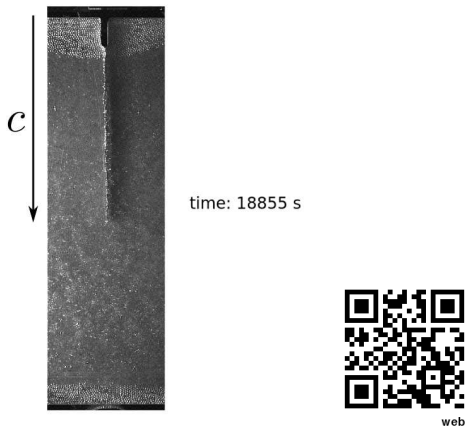

Figure 1.11: Movie of the crack propagation for sample Sa_1 (d = 500 μm, V = 16 nm/s, no porosity). Scan the flash-code with a mobile phone or click http://youtu.be/S46a7tso_Oc with a computer.

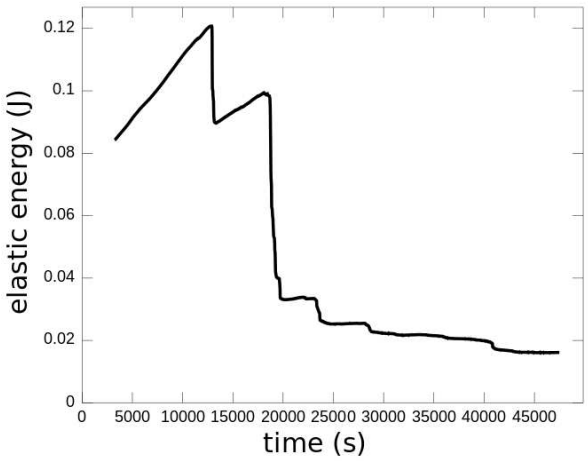

Figure 1.12: Evolution of the elastic energy stored in the system when the sample Sa_1 ($d = 500$ μm, $V = 16$ nm/s, no porosity) is breaking. Each step is a breaking event.

the crack length using the camera pictures. As presented in figure 1.13-A, this permits to plot the sample stiffness $k(t) = \dfrac{f(t)}{u(t)}$ as a function of c_{cam}. This curve is noisy. Still, in a linear elastic material, it should only depend on the specimen geometry and the noise has no physical meaning. Hence, we apply a Tikhonov regularization to smooth the curve. Then, one can use this smoothed curve to infer the crack length $c(t)$ from the values $f(t)$ and $u(t)$: $c(t) = c(f(t)/u(t))$ (figure 1.13-B). The level of noise on the crack length measured this way is significantly smaller than $c_{cam}(t)$ and the accuracy of the curve much better. Finally, simply differentiating this quantity, the crack tip speed $v(t)$ is derived and presented in figure 1.14-A. In this last figure, we see that without this post-processing technique we have far less measurement than with the simple camera. Moreover, to illustrate the considerable denoising effect of this technique, a homogeneous PMMA sample is studied via the same technique in figure 1.14-B. Going back to the case of model rock, we can deduce that the physical noise due to crackling phenomenon is no longer lost in noise measurements.

The next step is to estimate the rate time evolution of energy release rate. We begin by looking at the energy balance of the system at time t_0 in the quasistatic regime [Lawn (1993)]:

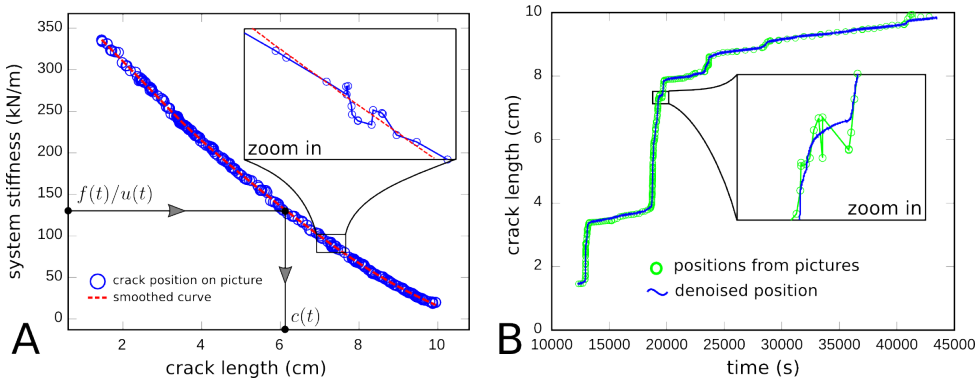

Figure 1.13: A: Stiffness of the sample Sa_1 ($d = 500$ μm, $V = 16$ nm/s, no porosity) as a function of the crack length, c. The dashed red line is the smoothed curve. B: Crack length as a function of time when the crack propagates for the sample Sa_1 ($d = 500$ μm, $V = 16$ nm/s, no porosity) measured from the pictures ($c_{cam}(t)$) and the smoothed $k(c)$ curve ($c(t)$).

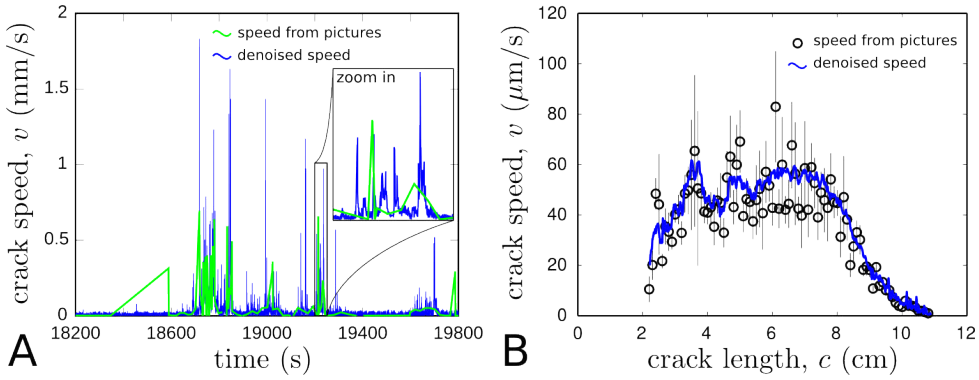

Figure 1.14: A: Crack tip speed as a function of time when the crack propagates for the sample Sa_1 ($d = 500$ μm, $V = 16$ nm/s, no porosity). B: As a complement and to illustrate the gain in term of noise, B shows crack tip speed as a function of the crack length when the crack propagates in homogeneous PMMA. For both graphs, speed is measure from the pictures ($c_{cam}(t)$) and from the smoothed stiffness *vs.* length curve.

$$\underbrace{\int_0^{t_0} f(t)\cdot\frac{du}{dt}dt}_{\text{energy brought to the system}} \quad \underbrace{-W\cdot\int_0^{t_0} G(t)\cdot\frac{dc}{dt}dt}_{\text{energy lost at the crack tip}} = \underbrace{\frac{1}{2}k(t_0)\cdot u^2(t_0)}_{E=\text{energy stored in the system}} \tag{1.2}$$

Where W is the thickness of the sample. Then we derive this relation with respect to time:

$$f(t_0)\cdot\frac{du}{dt}(t_0) - W\cdot G(t_0)\cdot\frac{dc}{dt}(t_0) = \frac{1}{2}\frac{\partial k}{\partial c}\cdot\frac{dc}{dt}(t_0)\cdot u^2(t_0) + u(t_0)\cdot k(t_0)\cdot\frac{du}{dt}(t_0) \tag{1.3}$$

Finally, noting that $f = k\cdot u$ we can simplify and get (see figure 1.15):

$$G(t) = -\frac{1}{2W}\frac{\partial k}{\partial c}u^2(t) \tag{1.4}$$

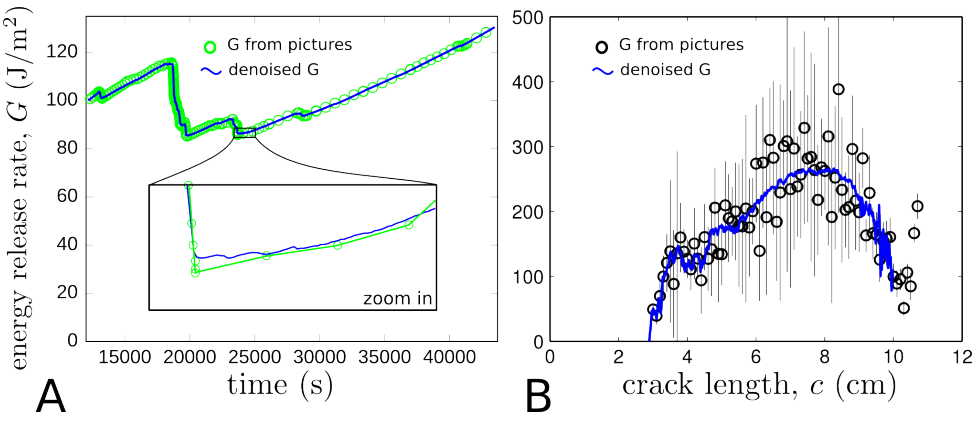

Figure 1.15: A: Energy release rate as a function of time when the crack propagates for the sample Sa_1 ($d = 500$ μm, $V = 16$ nm/s, no porosity). B: As a complement and to illustrate the gain in term of noise, B shows the energy release rate as a function of the crack length when the crack propagates within homogeneous PMMA. Measures are done from the pictures ($c_{cam}(t)$) and the smoothed $k(c)$ curve.

This way to compute the energy release rate G has been compared with a more classical method based on the Digital Image Correlation (DIC) [Sutton et al. (1983); Chu et al. (1985); Hild and Roux (2006)] to check our experimental results and validate the method. A sample with bead size 500 μm and sintering pressure 5.2 MPa is textured with droplets of paint and broken with the loading speed $V = 16$ nm/s (similar to Sa_1). It is filmed

through a lens without distortion while breaking[iii]. Then, following the method described in Roux and Hild (2006), the global translation, global rotation, T-stress and both Stress Intensity Factor (SIF) in mode I and mode II are fitted on a given series of functions. Then the energy release rate G is directly deduced from the SIFs (see equation 2). The results in terms of SIFs are given in figure 1.16-B and the energy release rate is plotted with the one measured from equation 1.4 for sample Sa_1 in figure 1.16. Both methods are in a good agreement.

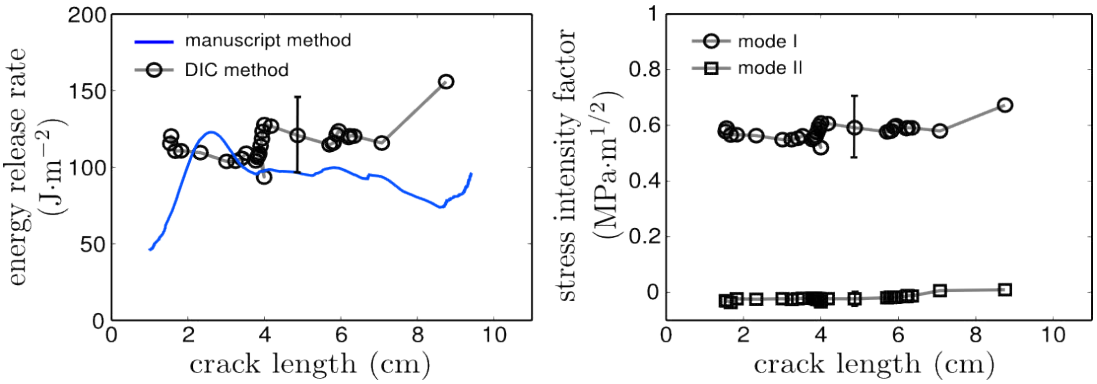

Figure 1.16: A: Energy release rate as a function of the crack length measured from DIC and from u, f and c, when the crack propagates for samples with $d = 500$ μm, $V = 16$ nm/s and no porosity. B: SIF in mode I and mode II for the same sample measured via DIC. The vertical black lines give the error.

Note that, using our method, the camera is not used to directly measure the crack length, but to obtain the curve k *vs.* c. Since AE are emitted in the vicinity of the growing crack tip, we can also use the acoustic localization to derive this curve (see figure 1.17:A). The time evolution of the crack length as deduced in this case coincide with that derived from $c_{cam}(t)$ (see figure 1.17:A). This method can be also applied without any (direct or acoustic-based) measurement of crack length, e.g. by computing the $kvs.c$ curve via finite element simulations.

So finally we get the evolution of both acoustic and mechanical variables, elastodynamic and elastostatic variables in a synchronized manner as presented in figure 1.18.

[iii]The wedge splitting set-up developed at CEA has recently been duplicated at FAST laboratory. This second version has been equipped with a DIC set-up (high resolution camera, telemetric lens and CorreliQ4 software). We borrowed this set-up to measure $K_I(c)$, $K_{II}(c)$ and subsequently $G(c)$.

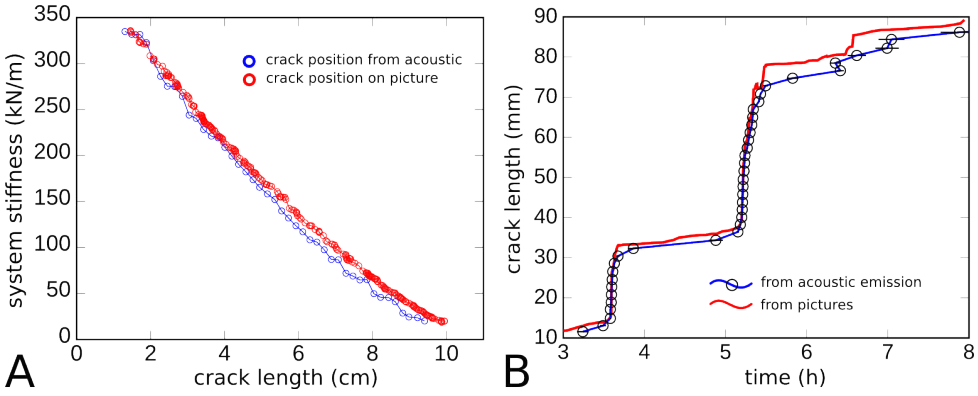

Figure 1.17: A: Decreasing of the system stiffness when the crack propagates for the sample Sa_1 ($d = 500$ μm, $V = 16$ nm/s, no porosity) measured using the camera or from the localisation of AE. B: Resulting time evolution for the crack length, in the sample Sa_1, for each of the two *kvs.c* curves.

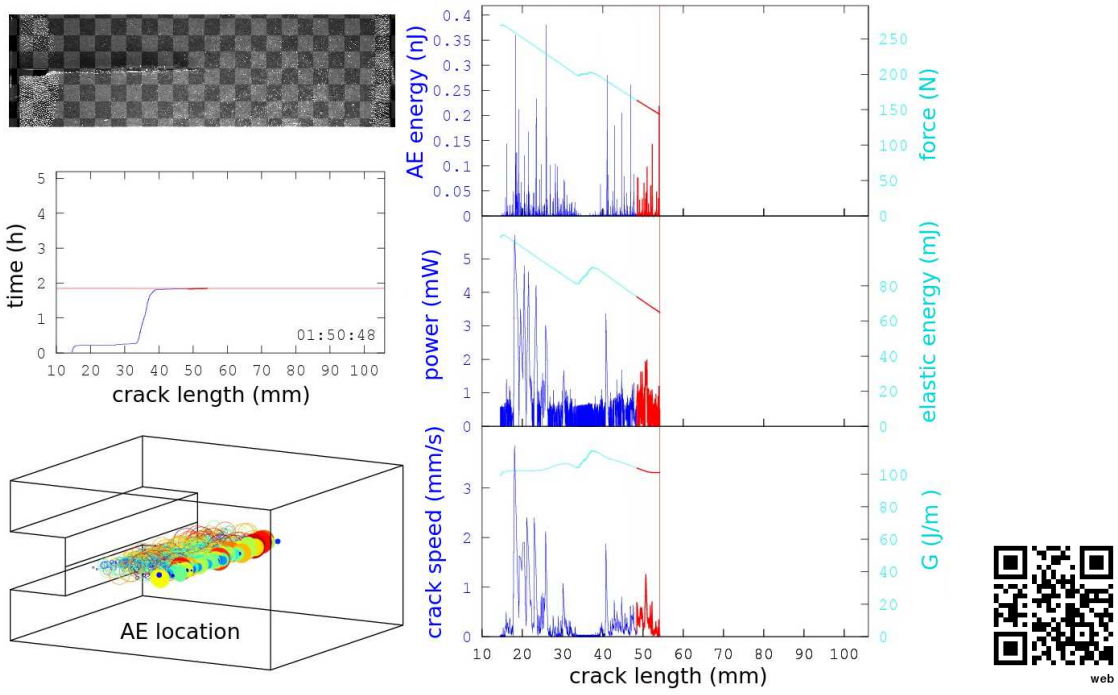

Figure 1.18: Movie showing the synchronized evolution of the mechanical and acoustic parameters when sample Sa_1 ($d = 500$ μm, $V = 16$ nm/s, no porosity) is breaking (http://youtu.be/tSpvZiImq14). See text for details on each curve evolution.

1.3.3 Topography measurement

Finally we examine the morphology of the *post-mortem* fracture surfaces. We used a stylus profilometer (KLA–Tencor® D–120) with a tip radius of 2.5 μm to take various 1D profiles a few centimeters long parallel and perpendicular to the direction of crack propagation. Figure 1.19 presents two surface profiles for different material porosities.

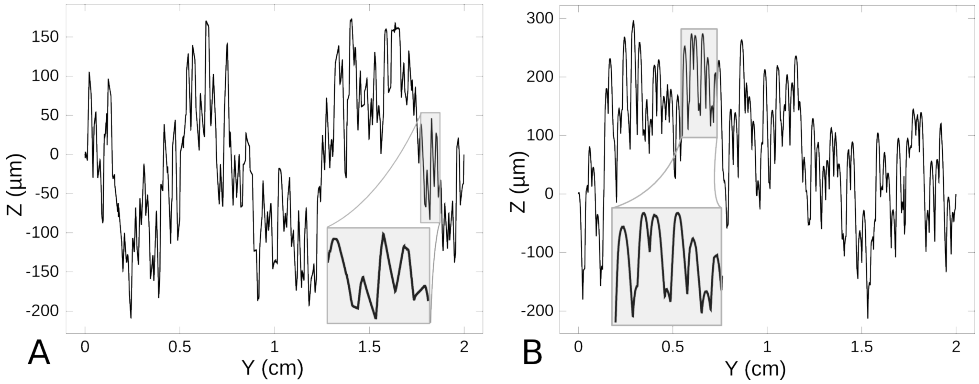

Figure 1.19: Surface profile lines in the direction of propagation of the crack front for a 230 μm beads sample sintered at: A, 5.2 MPa and B, 60 kPa.

1.4 Conclusion

In this chapter, I have presented our sample fabrication and mechanical device. First, the choice to break the sample with the wedge splitting geometry permits the propagation of a 3D crack front in mode I fracture. This crack front has two added advantages; it is both dynamic and geometrically stable. Secondly, the sample material is a model rock fabricated from sintered monodisperse polymer beads. This system fixes, and subsequently tunes, the characteristic length scales of material's macrostructure.

Consequently, and to our advantage, there is not just one big event that breaks the sample all at once, but a step by step propagation. The analyses of the statistics of these steps seen from an acoustic and mechanical view point will occupy the main part of the following chapters. Indeed, post-processing data yields an accurate and synchronized evolution of the acoustical and mechanical observables relevant for fracture.

Main messages of the chapter

◇ A tunable isotropic model rock made from sintered monodisperse polymer beads.

◇ A wedge splitting geometry is invoked to propagate a 3D crack front in a stable manner in mode I for different loading rates.

◇ An original post-processing technique to compute accurately the crack tip speed and the energy release rate

◇ Accurate and synchronized experimental measurement of AE energy and of the relevant quantities of fracture mechanics.

Chapter 2

Acoustic emission and seismicity during crack growth

Introduction

In real life, the crackling dynamics phenomenon that which most people are familiar with is the seismic activity, because it stands out as a huge destructive power. Unforeseen abrupt events in earthquakes or volcanos obey a rich variety of famous robust scaling laws studied for more than a century: Richter-Gutenberg [Gutenberg and Richter (1944)], Omori [Omori (1894b)], Utsu [Utsu (1971)], Voight [Voight (1988)], *etc.*. Most of these laws are also observed in compressive fracture experiments [Davidsen et al. (2007); Baro et al. (2013)], that is why the seismic problem is thought to combine friction and collective nucleation and coalescence of microcracks. This suggest that our single crack propagation experiment will fail to capture the rich statistics of earthquake dynamics.

From a purely physical point of view, there is no argument as to why comparing earthquake activity to the activity of a single fracture propagating in a non-homogeneous brittle material in opening mode (*i.e.* mode I) is feasible. In the first case, the jerky dynamics are mainly generated by material damage and friction [Dieterich (1994); Richter (1958); Nataf and Sommeria (2000)]. In the experiments presented herein, mode I propagation excludes friction, and the grain size is much bigger than the fracture process zone excluding damage at the crack tip. Thus, the nature of both phenomenon is different. However, simple single crack fracture experiments [Måløy and Schmittbuhl (2001); Salminen et al. (2002); Koivisto et al. (2007)] revealing crackling do display an intermittent dynamics.

This is recorded via the acoustic sensors in our experiment and seems to be reminiscent of what is observed for earthquakes. Both figures 2.1 and 2.2 present the evolution of the acoustic energy of fracture and Californian (CA) earthquakes events, respectively, as well as their position. Both evolutions look similar! So, does this model experiment contain the requested ingredients to observe the same statistical richness as seismic activity?

To answer this question, we will post-process experimental mode I fracture data henceforth just like geophysicists do for earthquakes. To compare these two dynamics, when possible, statistical results are compared to results catalogued for all CA earthquakes (*i.e.* including San Andreas, San Jacinto, Santa Monica and Pinto Mountain faults but not limited to these fault lines) over the last twelve years (from 2000 to 2012). The catalogue is available on Southern California Earthquake Data Center's (SCEDC) website [iv].

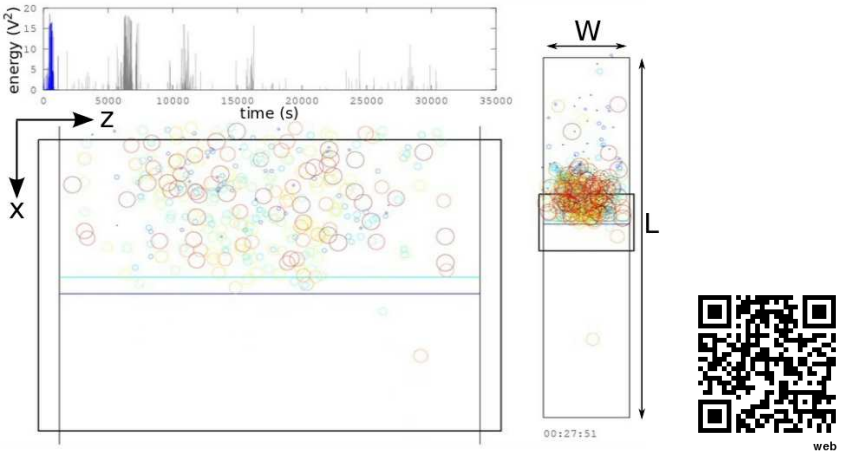

Figure 2.1: Acoustic location of breaking events in the fracture plane and acoustic energy evolution when sample Sa_1 ($d = 500$ μm, $V = 16$ nm/s, no porosity) is breaking. The radius of the circles and their color corresponds with the logarithm of the event energy: the bigger the circle, the higher is the energy. Scan the flash-code with a mobile phone or click http://youtu.be/8jmuUZmEo9s with a computer.

In the first part of this chapter, sections 2.1 - 2.8 present classical tools used by seismologist and compare and contrast the AE of the sample Sa_1 (loading speed 16 nm/s, bead diameter 500 μm and sintering pressure 5.2 MPa) and CA earthquakes. Subsequently, in section 2.9 we examine the generalization of these scaling laws to samples loaded at different rates and fabricated with alternative bead sizes.

[iv] SCEDC website: http://www.data.scec.org/

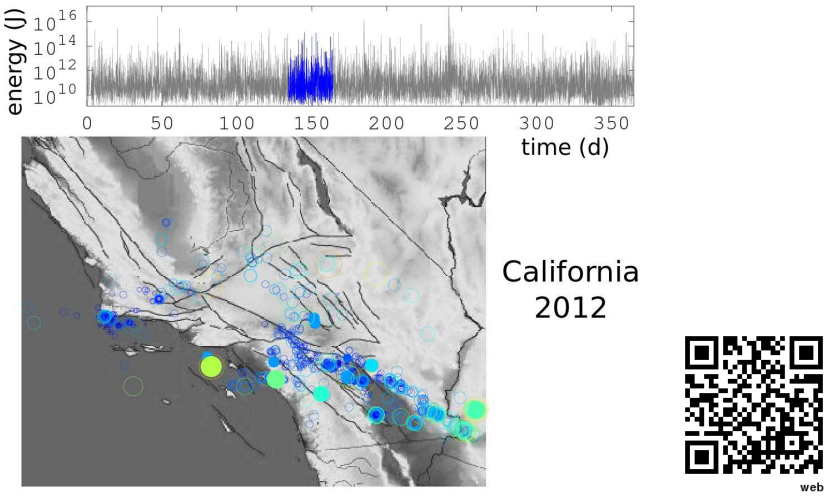

Figure 2.2: Movie showing the location of CA earthquakes in 2012, synchronized with the graph of their energy. The radius of the circles and their color correspond to the logarithm of the event energy: the larger the circle, the higher is the energy (http://youtu.be/ESWU3yIZUVw).

2.1 Distribution in energy of acoustic events: Richter-Gutenberg law in tensile fracture

One of the most well-known laws in the field of seismology is the so-called Richter-Gutenberg law [Gutenberg and Richter (1944, 1954); Richter (1958); Bullen (1985); Nataf and Sommeria (2000)]. This law states that the energy, E, of earthquakes [v] is power-law distributed:

$$P(E) \sim E^{-\beta} \tag{2.1}$$

where the exponent β is found to depend on the zone of observation and the considered period [vi]. It typically varies between 1.3 and 1.9 [Wiemer and Katsumata (1999); Main

[v] The earthquake energy is more commonly quantified by the magnitude M. Different magnitude scales were proposed in the past. The first and most popular one is that introduced by Richter [Richter (1935, 1958); Bullen (1985)], which relates M to the logarithm of the maximum amplitude measured on a Wood-Anderson torsion seismometer at a given distance from the earthquake epicenter. Such a definition combines two advantages: (i) M is relatively easy to measure; and (ii) it is directly useful in the damage hazard mitigation of engineering structures. Magnitude and radiated seismic energy of earthquakes E are usually related via the Kanomori empirical relation [Kanomori (1977)]: $log_{10}(E) = 1.5 \cdot M + 11.8$, with E expressed in Joule.

[vi] Historically, the Richter-Gutenberg law states that the relative number $N(M)/N_{total}$ of earthquakes of

(1996)].

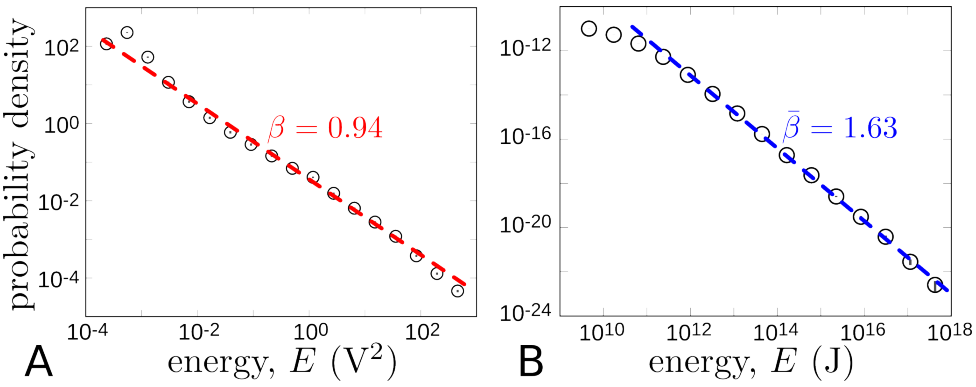

Figure 2.3: A: Probability density function of the energy for AE events going along with the breaking of sample Sa_1 ($d = 500$ μm, $V = 16$ nm/s, no porosity). B: Probability density function of the energy for the earthquakes having occurred in California over a period ranging from 2000 to 2012. In both cases, the axes are logarithmic. In both cases, one observes the Gutenberg-Richter power-law extending over nearly six orders of magnitude. The fitted exponent are found to be $\beta = 0.94 \pm 0.05$ for nominally brittle fracture, and $\bar{\beta} = 1.63 \pm 0.03$ for earthquakes.

To confront this first seismology law, figure 2.3-A depicts the distribution in energy of the AE events. As a complement, figure 2.3-B shows the distribution of the earthquake energy in California over a period ranging from 2000 to 2012. The energy of the AE events going along with the tensile failure of our artificial rocks is found to be power-law distributed over many orders of magnitude (six in figure 2.3). The associated exponent is found to be independent of the loading rate, but significantly depend on the microstructure.

This power-law distributed of the energy for AE events has been reported in numerous fracture experiments (see introduction of this part). It is usually thought to reflect scale-free dynamics for the underlying microfailure events [Garcimartin et al. (1997); Alava et al. (2006); Deschanel et al. (2009)]. This conjecture is supported by observations on the crack growth in 2D sheets of papers [Santucci et al. (2004); Stojanova et al. (2013)] or along heterogeneous interfaces [Måløy et al. (2006); Tallakstad et al. (2011); Lengline et al. (2012)]. In these cases, intermittent dynamics consists of discrete jumps the size of which is power-law distributed. It is also compatible with some models of heterogeneous fracture that map the onset of crack propagation with a depinning transition ([Bonamy

magnitude larger than M goes as $N(M)/N_{total} \approx 10^{-bM}$. The exponent b is related to β via $b = 1.5 \cdot \beta - 1$.

et al. (2008); Bonamy (2009)] and the second part of this manuscript). Still, relations between AE events (elastodynamics quantities) and front jumps (quasi-static motion) remain largely unknown. In particular, the exponents associated with the distributions in size of the front jumps are found to be universal, while those associated with the AE depend on the considered material and the loading conditions. Chapter 3 discuss this point extensively.

2.2 Aftershock sequences in tensile fracture: Omori law

To unravel further analogies with seismology, we characterize the clustering in time of the AE events. In this context, seismologists are very interested in the so-called aftershocks (AS) series that follow big earthquakes [Reasenberg and Jones (1989)]. AS are extremely important as they can lead to catastrophic failure of buildings and structures which were already damaged during the main shock (MS). In 1894, Omori [Omori (1894b,a); Utsu et al. (1995)] showed that in many cases, the AS rate is inversely proportional to time from mainshock. Later, this empirical law was slightly refined [Jeffreys (1938); Utsu (1957)] to:

$$r_{AS}(t_{AS} - t_{MS}) = (t_{AS} - t_{MS} + t_0)^{-p_A} \tag{2.2}$$

where r_{AS} is the time density of AS, t_{AS} and t_{MS} are times corresponding to the AS and MS, respectively, p_A is the exponent characteristic of the algebraic decay, and t_0 is the typical silent time after a MS. The constants t_0 and p_A are not universal, but depend on both the spatial location and the period considered for the analysis.

Omori's law has proven to be very robust. It is central in the implementation of probabilistic forecasting models for seismic hazard [Ogata (1988)]. Still, its origin remains widely debated. Very recently, a similar AS law has been reported at the lab's scale in model experiments of compressive fracture [Baro et al. (2013)]. This yields the following question: Is Omori's law valid in tensile fracture experiments reported herein.

The first step in this context is to identify MS-AS sequences from the AE signal. At first glance, this is not a trivial task. To bypass the problem, we adopt the procedure proposed in [Baro et al. (2013)] and chose to consider as the MS $\{t_{MS}, E_{MS}\}$ all the

events with energies falling into a prescribed energy interval: $E_{MS} \in [E_{min}, E_{max}]$. The AS sequence $\{t_{AS}, E_{AS}\}$ associated to each of these MS contains the series of AE events following this MS, and finishes when an AE event's energy is larger than that of the MS is encountered.

The second step is to plot the AS rate as a function of the time from the MS. This is arrived at by first grouping MS occurrences with similar energies. The relative times $(t_{AS} - t_{MS})$ between the MS in the energy group and the last event of the AS series are binned into intervals uniformly distributed in a logarithmic scale. The variation of the AS rate as a function of time from the MS is plotted in figure 2.4-A, for a typical fracture experiment performed in 500 μm sintered polystyrene beads. In this figure, the different symbols correspond to different energies for the MS. The Omori algebraic decrease is clear for up to 6 decades. Here, the fitted exponent p_A is found to be $p_A = 1.18 \pm 0.07$. It is found to be independent of the loading rate, but dependent on the material.

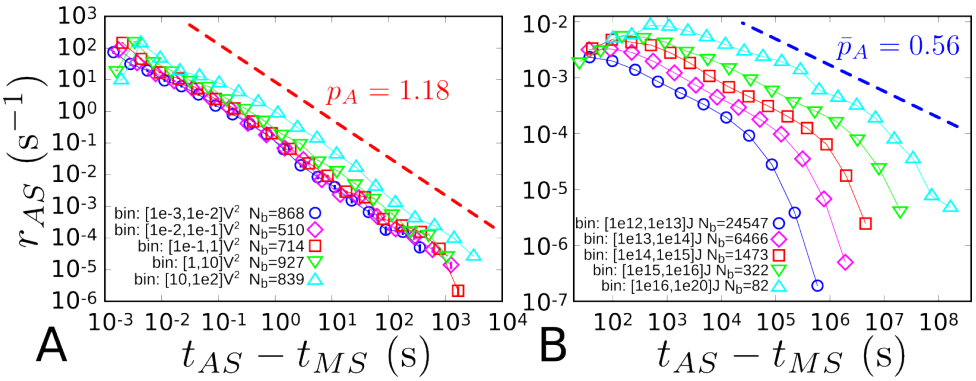

Figure 2.4: A: Time evolution of the AS rate for various MS energies. The analyzed AE signal is that obtained in the breaking of specimen Sa_1 ($d = 500$ μm, $V = 16$ nm/s, no porosity). B: Same analysis performed for the earthquakes having occurred in California over a period ranging from 2000 to 2012. In both cases, the axes are logarithmic. In both cases, one observes the Omori power-law extending over six orders of magnitude. The fitted exponent are found to be $p_A = 1.18 \pm 0.07$ for nominally brittle fracture, and $\bar{p}_A = 0.56 \pm 0.1$ for earthquakes.

As a complement, we performed a similar analysis for the earthquakes having occurred in California from 2000 to 2012. A similar Omori behavior is observed, with an exponent $\bar{p}_A = 0.56 \pm 0.1$. The energy of the considered MS is found to have a direct effect on the cut-offs of the law, which is not the case in our tensile fracture experiments. We will came back on this point later, in section 2.4.

2.3 Foreshock sequences in tensile fracture: Voight law

We also analyzed the foreshock (FS) sequences preceding the MS. Note that such FS sequences are usually very small for earthquakes [Bullen (1985); Utsu et al. (1995)], and major seismic events often occur without detectable warning. But in volcanology, the final eruption (lasting $\sim 1-10$ days) is usually characterized by accelerating rates of seismicity [Kilburn (2003)]. To describe this precursor to an eruption, Voight [Voight (1988, 1991)] proposed that the rate of volcano observables (N: the deformation rate or the seismicity rate) goes as a power-law with the acceleration of this observable[vii]. By identifying the rate r_{FS} of AE events with such observables, one then expects [Bell et al. (2011); Collombet et al. (2003)]:

$$r_{FS}(t_{MS} - t_{FS}) \sim (t_{MS} - t_{FS} + t_0)^{-p_F} \tag{2.3}$$

which is similar to the Omori law for AS.

Thus, FS sequences preceding each MS are identified in the very same manner as AS in section 2.2 (after having inversed time). Subsequently, the time evolution of FS rate is computed. Figure 2.5 shows the resulting curves for fracture experiments on 500 μm sintered polystyrene beads and different MS energies. The fracture data fits very well Voight law (equation 2.3) with an exponent $p_F = 1.22 \pm 0.07$.

In terms of FS, our experimental data share statistical similarities with volcanic eruption (rather than earthquakes). This is consistent with the fact that volcanic eruption are seen as the slow extensions of faults. These continue to grow until they connect a pre-existing array of sub-vertical fractures. This phenomenon so opens a new pathway in which magma can reach Earth's surface [Kilburn (2003); McGuire and Kilburn (1997)]. So the situation approaches the model experiments (without being the same).

Figure 2.6 contains the time evolution of AS and FS rate for three different MS energies. AS and FS curves are found to superimpose fairly well. This translates to a time symmetry for the AE events in fracture experiments: MSs are preceded by FS sequences and followed by AF sequences that share the same time organization. This symmetry, to the very best of our knowledge, is novel! It is neither observed for earthquakes nor for volcanic activity

[vii] Calling N the observable, one gets: $\frac{\mathrm{d}N}{\mathrm{d}t} \sim N^{\delta}$ [Collombet et al. (2003)], with $\delta = \frac{p_F}{p_F - 1}$

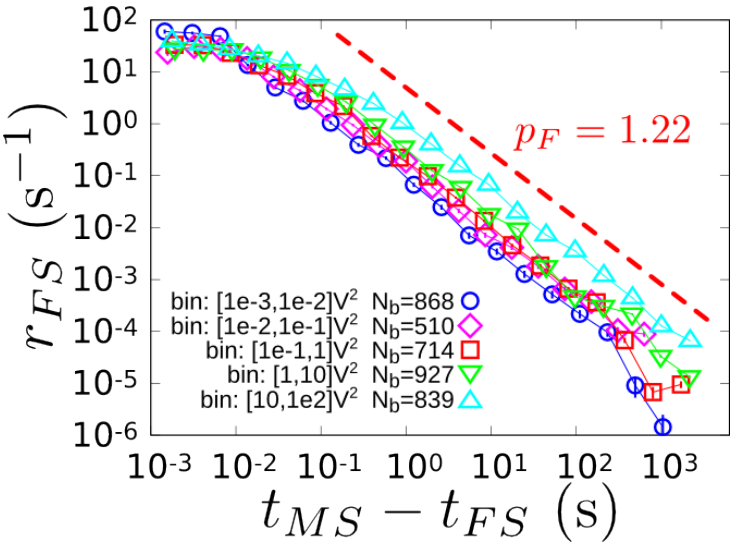

Figure 2.5: Time density of FS preceding a MS (Voight law). The analysed AE signal is that obtained in the breaking of specimen Sa_1 ($d = 500$ μm, $V = 16$ nm/s, no porosity). The axes are logarithmic and one observes the Voight power-law extending over six orders of magnitude. The fitted exponent is found to be $p_F = 1.22 \pm 0.07$.

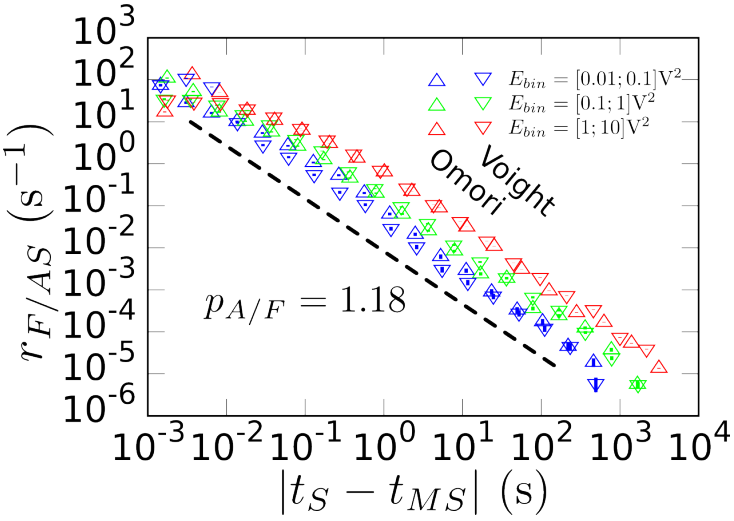

Figure 2.6: Time density of FS and AS around a MS (Voight and Omori laws) when the sample Sa_1 ($d = 500$ μm, $V = 16$ nm/s, no porosity) is breaking. The axes are logarithmic and one observes the Voight law superimposing Omori law over six orders of magnitude.

nor compression fracture experiments. The main difference between our experiments of tensile fracture and the others situations is the following: In our experiments, the AE activity goes along with the propagation of a single crack (at least at the macroscale). This situation is expected to be rather invariant with respect to translation along time. The other situations involved the nucleation, growth and coalescence of many cracks. The crack density is expected to evolve a lot during the fracturing process, and these situations cannot be expected to remain stationary. We conjecture that the symmetry breaking between FS and AS sequences arise from this non-stationarity.

2.4 Aftershock rate *vs.* mainshock energy: Productivity law

The next question asked by geophysicists is: How many AS (/FS) are triggered (/were proceeding) by a MS of given energy E? The answer to this question is given by the productivity law, which states that the rate of AS, $R_{AS}(E)$, scale as a power-law with the MS energy, E, [Utsu (1971); Helmstetter (2003)]:

$$R_{AS}(E) \sim E^{\gamma_A} \tag{2.4}$$

This equation can now be applied to fracture experiments herein. Figure 2.7 presents the results for the AE signal accompanying the breaking of specimen Sa_1. As a complement, $R_{AS}(E)$ for the earthquakes in CA is presented in Figure 2.7-B. Equation 2.4 is fulfilled fairly well in both cases. For the specimen Sa_1 experiment and CA earthquakes, the exponent $\gamma_A = 0.2 \pm 0.1$ and $\bar{\gamma}_A = 0.005 \pm 0.001$ respectively. It is noteworthy that the exponent for CA earthquakes is extremely small.

Similarly thecurve for the FS sequences is fitted by:

$$R_{FS}(E) \sim E^{\gamma_F} \tag{2.5}$$

In the case of fracture, the result is presented in figure 2.8. The fitted exponent is also $\gamma_F = 0.2 \pm 0.1$, so it is a a secondary and novel proof of the symmetry between FS and AS in the case of stable fracture propagation.

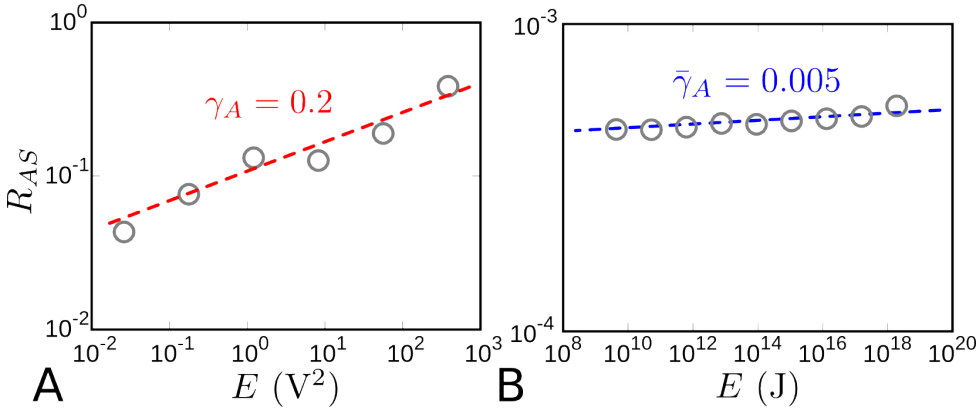

Figure 2.7: A: Rate of AS triggered by a MS of given energy (productivity law) when the sample Sa_1 ($d = 500$ μm, $V = 16$ nm/s, no porosity) is breaking. B: Rate of AS triggered by a MS of given energy for the earthquakes having occurred in California over a period ranging from 2000 to 2012. In both cases, the axes are logarithmic. In the cases of fracture one observes the productivity power-law extending over nearly five orders of magnitude while in the case of earthquake, it is observed over more than eight orders. The fitted exponent are found to be $\gamma_A = 0.2 \pm 0.1$ for nominally brittle fracture, and $\bar{\gamma}_A = 0.005 \pm 0.001$ for earthquakes.

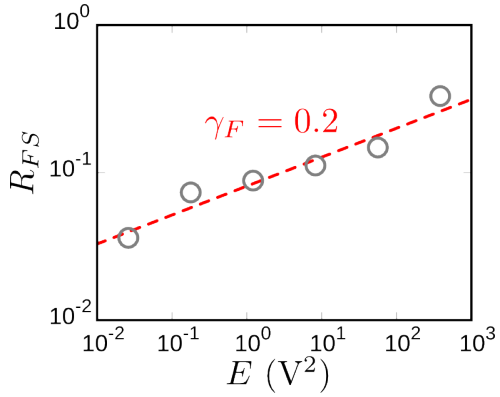

Figure 2.8: Rate of FS triggered by a MS of given energy (productivity law). The analyzed AE signal is obtained from the breaking of specimen Sa_1 ($d = 500$ μm, $V = 16$ nm/s, no porosity). The axes are logarithmic and one observes the productivity power-law for FS extending over nearly five orders of magnitude. The fitted exponent is found to be very close to the one find for AS: $\gamma_F = 0.2 \pm 0.1$.

2.5 Distribution in size of the aftershocks: Utsu law

Another interesting information about the AS is the statistical repartition of their energy. This information is given by the Utsu law [Utsu (1971)] which states that the probability to observe an AS of energy E_{AS} depends on that of the associated MS, and is given by:

$$P\left(\frac{E_{AS}}{E_{MS}}\right) \sim \left(\frac{E_{AS}}{E_{MS}}\right)^{-b_A} \tag{2.6}$$

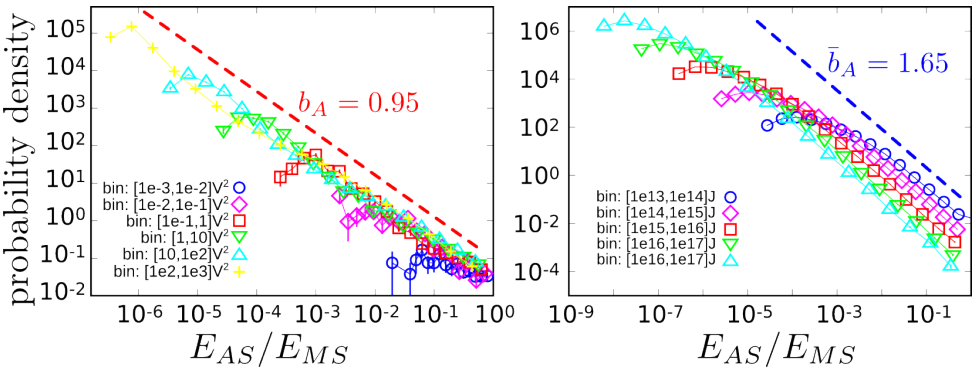

Figure 2.9: A: Utsu law of AS for the sample Sa_1 ($d = 500\,\mu$m, $V = 16$ nm/s, no porosity). B: Utsu law for the earthquakes occurring in California from 2000 to 2012. In both cases, the axes are logarithmic. In the cases of fracture one observes the Utsu power-law extending over five orders of magnitude while in the case of earthquake, it is observed over eight orders. The fitted exponent are found to be $b_A = 0.95 \pm 0.04$ for nominally brittle fracture, and $\bar{b}_A = 1.65 \pm 0.09$ for earthquakes.

As presented in figure 2.9, the data from fracture experiments herein and those for the CA earthquakes fit very well with this law. The measured exponents are found to be $b_A = 0.95 \pm 0.04$ for the fracture case, and $\bar{b}_A = 1.65 \pm 0.09$ for the earthquakes. Note the similarities between these exponents and the Richter-Gutenberg's ones (see section 2.1 and figure 2.3). This means that the statistics of the AS energy are the same as that of any event. The lower cutoff in the curve $P(E_{AS}/E_{MS})$ translates the finite sensitivity of the energy measurement. Finally to check the time symmetry between AS and FS, we computed Utsu law for FS [viii]. The fitted exponent is found to be $b_F = 0.97 \pm 0.04$ which reinforces the idea of a symmetry between FS and AS sequences.

[viii] $P\left(E_{FS}/E_{MS}\right) \sim \left(E_{FS}/E_{MS}\right)^{-b_F}$

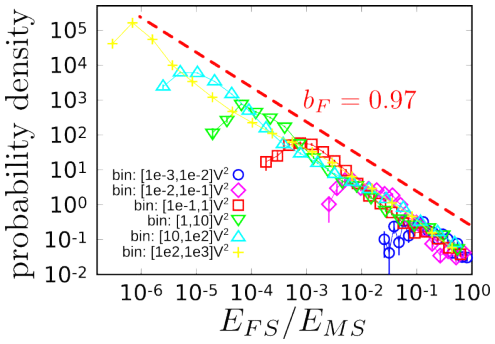

Figure 2.10: Utsu law of FS for the sample Sa_1 ($d = 500$ μm, $V = 16$ nm/s, no porosity). The axes are logarithmic and one observes the Utsu power-law extending over five orders of magnitude. The fitted exponent is found to be very close to the one found with AS: $b_F = 0.97 \pm 0.04$.

2.6 Statistical distribution of silent periods: Waiting time law

We have also computed the distribution of the waiting or inter-event time ΔT between two successive AE events (without seeking to distinguish FS and AS from MS). Similar analysis has indeed been performed on earthquakes [Bak et al. (2002); Corral (2004)] and in experiments of compressive failure [Baro et al. (2013)]. The power-law distribution is:

$$P(\Delta T) \sim \Delta T^{-\pi} \tag{2.7}$$

Note that the Omori law for AS and/or FS naturally implies such a distribution for the waiting time (the reciprocal is not true [Baro et al. (2013)]).

As shown first by [Bak et al. (2002)] and then by [Corral (2004)], it is important to build this law to take into account space, time and energy variability. In experiments herein, the space and time variability may be neglected since the sources of AE events are located along the propagating crack front and the front loading is roughly stationary over most of the fracture experiment. To take into account the energy variability, the distribution $P_{E_{th}}(\Delta T)$ for wait time is computed by maintaining only the energy events larger than a prescribed value E_{th}. Sample Sa_1 results are presented in figure 2.11. The data obeys the expected power-law distribution, as for Earthquakes (plotted as a complement on the left in the same figure). The measured exponent is $\pi = 1.31 \pm 0.03$ for

the fracture experiments, and $\bar{\pi} = 0.94 \pm 0.07$ for earthquakes[ix]. Moreover, just like for the Omori's law the energy threshold E_{th} has a direct effect on the position of the higher cut-off in the case of earthquakes, whereas it seems to only affect the lower cut-off in the case of fracture.

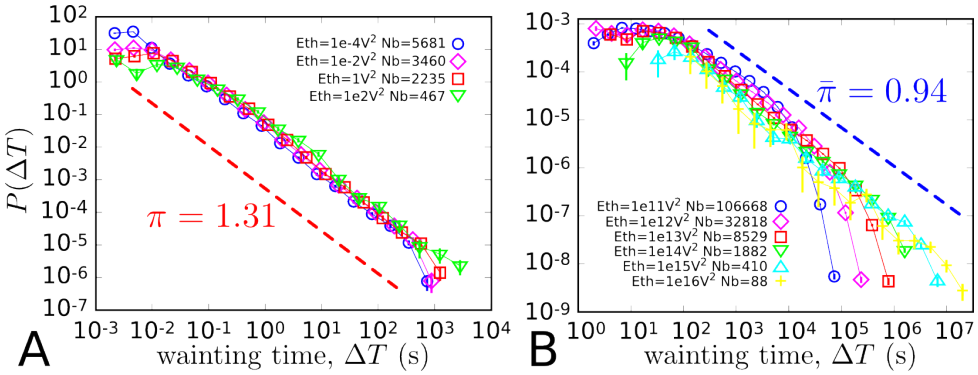

Figure 2.11: A: Probability density function of the inter-event time when the analyzed AE signal obtained when breaking specimen Sa_1 ($d = 500$ μm, $V = 16$ nm/s, no porosity). B: Probability density function of the inter-event time for the earthquakes occurring in California over a period ranging from 2000 to 2012. In both cases, the axes are logarithmic and one observes the waiting time power-law extending over five orders of magnitude. The fitted exponent are found to be $\pi = 1.31 \pm 0.03$ for nominally brittle fracture, and $\bar{\pi} = 0.94 \pm 0.07$ for earthquakes.

2.7 Intensity of the biggest aftershock: Båth law

A last empirical law sometimes mentioned in seismology (but more controversial [Helmstetter and Sornette (2003)] is the Båth law [Bath (1965)]). This law relates the energy of the largest AS with that of the MS. It states that the ratio between the two, $max(E_{AS})/E_{MS}$ is roughly constant, close to 60 [Helmstetter (2003)][x]. Computing this ratio using both earthquakes and fracture data, ratio spreads over a wide range. Consequently, it is not pertinent to compute a mean value. Now let us turning to the probability density function of these ratios which are computed for N_b MS-AS sequences for prescribed MS energy.

[ix] This result is in agreement with [Bak et al. (2002); Baro et al. (2013)]. In [Bak et al. (2002)] a refined study is proposed for earthquakes, taking into account the space and time variability

[x] In terms of magnitudes, the difference between the MS magnitude and the largest AS is 1.2.

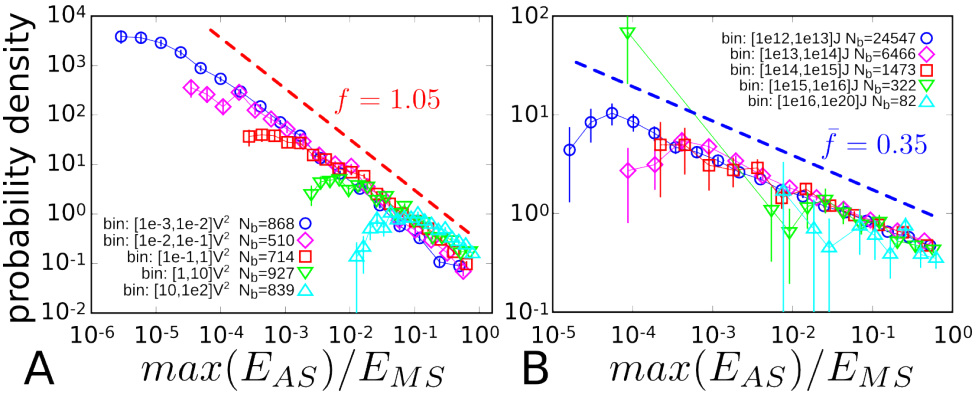

Figure 2.12: A: Probability density function of $max(E_{AS})/E_{MS}$ for the sample Sa_1 ($d = 500$ μm, $V = 16$ nm/s, no porosity). B: The same analysis for the CA earthquakes . In both cases, the axes are logarithmic and one observes the Båth power-law extending over more than four orders of magnitude. The fitted exponent are found to be $f = 1.05 \pm 0.05$ for nominally brittle fracture, and $\bar{f} = 0.35 \pm 0.04$ for earthquakes.

As can be seen in figure 2.12, $max(E_{AS})/E_{MS}$ is found to be power-law distributed:

$$P\left(\frac{max(E_{AS})}{E_{MS}}\right) \sim \left(\frac{max(E_{AS})}{E_{MS}}\right)^{-f} \tag{2.8}$$

With $f = 1.05 \pm 0.05$ for tensile fracture and $\bar{f} = 0.35 \pm 0.04$ for CA earthquakes. It is interesting to note, sequences involving a MS with a high energy (above 10 V^2), the lower cut-off of the power law reaches the higher one and a mean value is approximately 10^{-2}. This is on the order of the value 60 expected by Båth's law.

2.8 Intensity, duration and frequency of an acoustic event: Duration law

One of the last statistics, one cannot leave this section before examining the duration of AE events. Figure 2.13 shows a typical distribution for this duration. One observes a power-law scaling (exponent close to 0.5) between two cut-offs. Special attention should be paid to interpret this quantity and, in particular, its relation with the duration of true fracturing events (analyses in the chapter 3) is difficult to establish. Indeed, the typical frequency of the signals collected at the various transducers is $\sim$ 200 kHz. The

speed of sound in our artificial rocks is $\sim$ 2000 m/s. From the value of this speed and the measured frequency, one can construct a typical length scale $\sim$ 1 cm for the AE events. This corresponds to the thickness (the smallest typical length) of the sample, and is much larger than the typical size (diameter of the sintered beads) expected for the microfailure events. Hence, the duration of the AE events measured at the transducers cannot be identified with the underlying microfailure events. These trigger the mechanical resonance of the whole sample and the duration of the AE events are thought to be the time it takes for this resonance to be dissipated. It is a function of the energy of the event, of the attenuation coefficients, of the system geometry, etc.

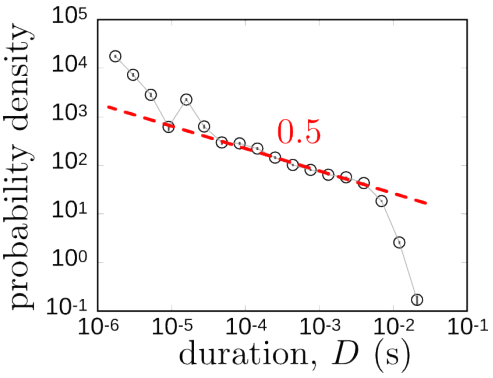

Figure 2.13: Probability density function of the duration of the acoustic events measured via acoustic sensors for sample Sa_1 ($d = 500$ μm, $V = 16$ nm/s, no porosity). The axes are logarithmic. One can fit a power-law exponent with value 0.5.

2.9 Effect of loading rate and microstructure: On the selection of cutoffs and exponents

In the previous sections (2.1-2.8), the AE energy measured during the propagation of a single crack in mode I obeys the same laws as earthquakes with just different universal exponents. This means that the model experiment displays the same statistical richness than the complex phenomenon of geophysical seismicity. In this section, we test the different scalings performed to renormalize those laws. Herein, we will vary the inputs of the statistical problem (wedge speed V and bead size d) and deduce the variations on the power-law cut-offs as the function of the loading rate and the size of the microstructure.

Hence, in the following subsection we present fracture experiments for:

- fixed bead size (500 μm) and varying loading speed (16 nm/s – Sa_1, 160 nm/s – Sa_2, 1600 nm/s – Sa_3)
- fixed loading speed (16 nm/s) and varying bead size (20 μm – Sd_1, 50 – 80 μm – Sc_1, 230 μm – Sb_1, 500 μm – Sa_1).

2.9.1 Richter-Gutenberg law

First, the Richter-Gutenberg law (see section 2.1) is plotted as the probability density function versus the AE energy for different loading rates. Figure 2.14 shows that for the three loading speeds spanned over two orders of magnitude, the statistical regime remains exactly the same: curves superimpose. As we will see in the second part of this manuscript, this is expected from the pinning-depinning model. Moreover, the event intensity clustering is not tuned by the loading rate. In this case, loading rate has no effect on the upper cut-off.

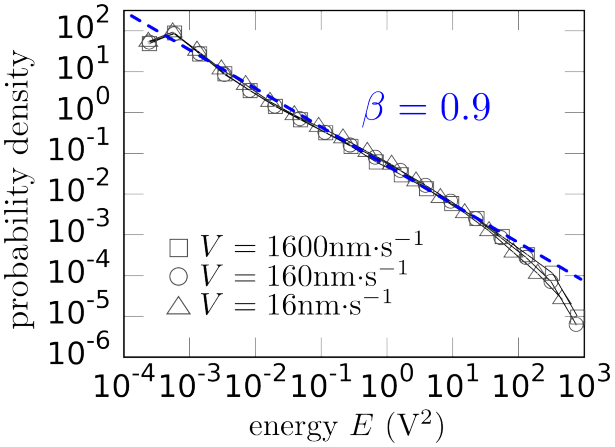

Figure 2.14: Probability density function of the AE for different loading speeds (samples Sa_1, Sa_2 and Sa_3). The axes are logarithmic and all Richter-Gutenberg power-laws collapse over five orders of magnitude. The dashed line with slope $\beta = 0.9$ is given to guide the eye.

Then, to study the effect of the bead size diameter, d, on the clustering in energy, figure 2.15 depicts the Richter-Guttenberg law for different bead sizes. It is reasonable to fit a power-law just for the two experiment with the biggest bead sizes (500 and 230 μm). This parameter clearly has an effect on the regime of propagation of the crack front. This point will be confirmed theoretically in chapter 3: when the bead size is big enough, the crack growths is in the crackling regime.

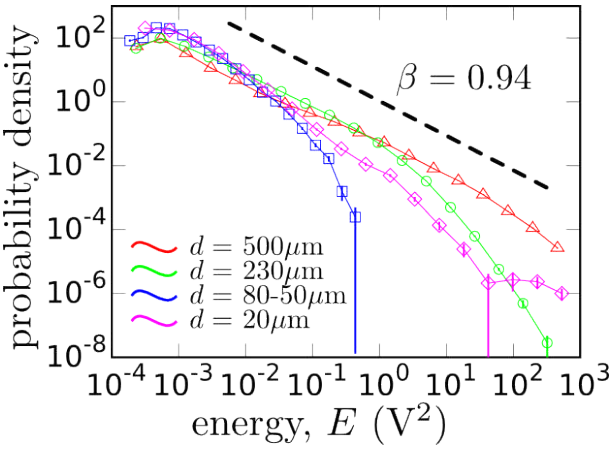

Figure 2.15: Probability density function of the energy of the acoustic events for different bead size (samples Sa_1, Sb_1, Sc_1 and Sd_1, loading speed 16 nm/s without porosity). The dashed line with slope $\beta = 0.9$ is given to guide the eye.

2.9.2 Productivity law

Just like in the previously subsection, the productivity law (see section 2.4) is computed for each wedge speed. As presented in figure 2.16, curves are parallel. This means that the scaling behavior does not depend on the loading rate, the global rate of an AE is a function of the wedge speed. This point was already noted by [Baro et al. (2013)] in compressing rocks.

2.9.3 Omori and Voight laws

First, it is worth noting that one claims [Dieterich (1994); Huang et al. (1998); Scholz (1998)] that the clustering as evidenced by Omori's law, comes from a dependence on the history of the sequence: stressing history, evolution of the matter properties/disorder, underlying fractal structure, or variation of the friction coefficient. Nevertheless, in our single crack propagation case, in opening mode none of these phenomenons intervene. Pinning-depinning model predicts a Poissonian distribution which is also not evidenced. Hence, the origin of this clustering remains an open question.

Returning to section 2.2 and more specially to the variation of the prefactor of Omori law as a function of the energy bin (see figure 2.4), the upward shift of the curves is directly given by the productivity law (see section 2.4): rate of AS triggered by an earthquake for

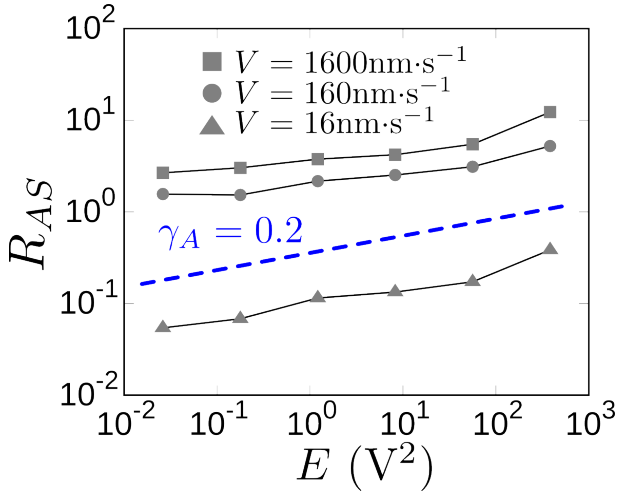

Figure 2.16: Productivity laws for the acoustic energy for different loading speeds (samples Sa_1, Sa_2 and Sa_3, bead size 500 μm without porosity). The axes are logarithmic and all productivity power-laws are parallel over four orders of magnitude. The dashed line with slope $\gamma_A = 0.2$ is given to guide the eye. The prefactor of the power-laws give the global rate of events.

a given energy. Thus, [Baro et al. (2013)] suggests a rescaling of the Omori law's vertical axis $E^{-\gamma}$. Figure 2.17 depicts these results and the collapse is excellent.

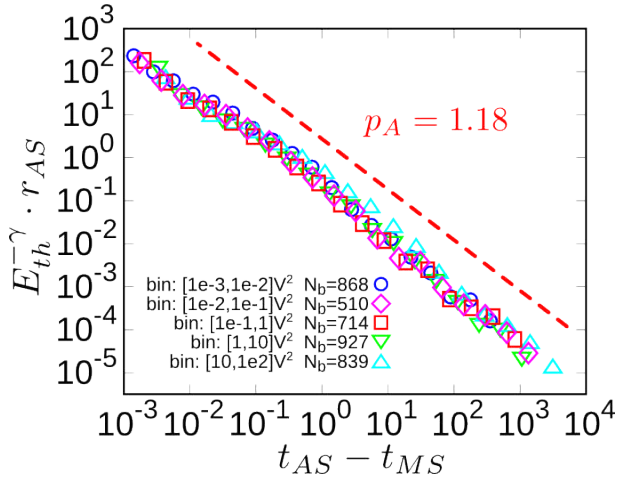

Figure 2.17: Renormalized Omori law for the sample Sa_1 ($d = 500$ μm, $V = 16$ nm/s, no porosity) with $\gamma = 0.2$. The axes are logarithmic and all curves collapse over more than five orders of magnitude. The dashed line has a slope of $p_A = 1.18$ and gives to guide the eye.

Since the exponent of the productivity law does not vary with the loading rate (see section 2.9.2), it is possible to test the renormalization by fixing $\gamma = 0.2$ and collapse the

Omori laws for different wedge speeds. Nevertheless, figure 2.16 shows that the productivity depends on the loading rate via the global rate of event. Thus, to renormalize Omori law for different experiments, it is necessary to take R_S into account, the mean number of events per unit time: the vertical axis is renormalized by $\frac{E^{-\gamma}}{R_S}$ and the horizontal axis by R_S. As presented in figure 2.18-D, it is remarkable to see that this collapse still works with different loading speeds.

Then, to check the time symmetry does not vary with the wedge speed, Omori and Voight laws (see section 2.2 and 2.3) are plotted in figures 2.18-A/B/C for $V = 16/160/1600\text{nm}\cdot\text{s}^{-1}$ respectively. In all cases, the Omori law is equivalent to the Voight's so time symmetry is preserved and as presented in table 2.1 the exponents stay similar.

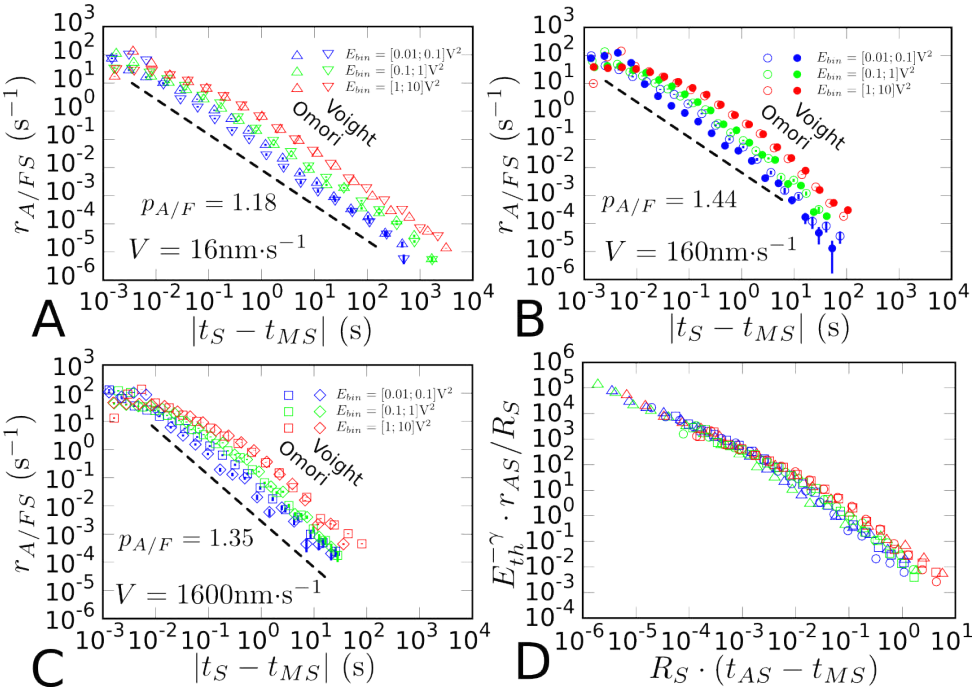

Figure 2.18: Omori and Voight laws for different loading speeds: A: 16 nm·s^{-1} – Sa_1, B: 160 nm·s^{-1} – Sa_2, C: 1600 nm·s^{-1} – Sa_3. D: Collapse of the Omori laws using the productivity law ($\gamma = 0.2$) and the global rate of events R_S. In all graphs the axes are logarithmic.

2.9.4 Utsu law

Then, Utsu law for AS (see section 2.5) is drawn for each loading rate for one significant energy bin. Here again, as presented in figure 2.19 all curves collapse without any

rescaling. Hence, the loading rate has no effect on the amplitude ratio between MS and their AS. This result is reminiscent to the fact that Richter-Gutenberg law also remains unchanged by loading rate variations.

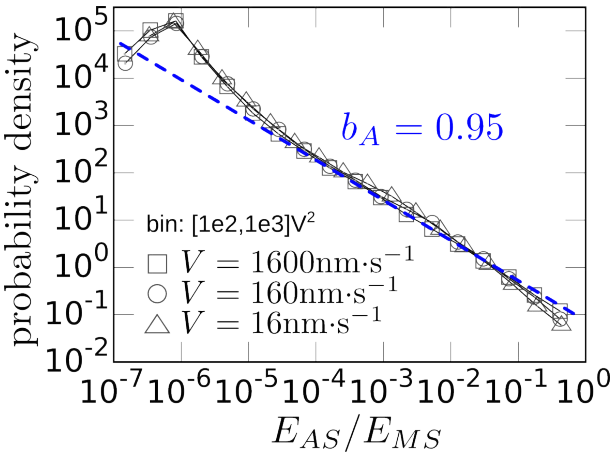

Figure 2.19: Utsu laws for the acoustic energy for different loading speeds (samples Sa_1, Sa_2 and Sa_3, bead size 500 μm without porosity). The axes are logarithmic and all Utsu power-laws collapse over more than four orders of magnitude. The dashed line with slope $b_A = 0.95$ is given to guide the eye.

2.9.5 Waiting time law

[Baro et al. (2013)] proposes a way to unify the waiting time law in energy, space and time for real earthquakes, *i.e.* Epidemic-Type Aftershock Sequences (ETAS) model, and rock compression experiments. Nevertheless it seems this scaling is based on the renormalization by the mean seismic activity rate ($\langle \Delta T \rangle$) and is only valid when $\pi \approx 1$. Below is a generalization of formula with good results for π greater than 1 ($\pi \in]0, 2[$). Following the method explained in [Patinet et al. (2011)], the power-law $P(\Delta T)$ is rewritten with a cut-off ΔT_0 whose shape is given by the function $f(x)$. This function decreases faster than $x^{1-\pi}$ when x goes to infinity:

$$P(\Delta T) = \Delta T^{-\pi} \cdot f(\frac{\Delta T}{\Delta T_0}) \tag{2.9}$$

Then, computing the main seismic activity rate one gets:

$$\langle \Delta T \rangle = \int_0^{+\infty} \Delta T \cdot P(\Delta T) d\Delta T \tag{2.10}$$

Plugging 2.9 into 2.10, one gets:

$$\langle \Delta T \rangle = \int_0^{+\infty} \Delta T^{1-\pi} \cdot f(\frac{\Delta T}{\Delta T_0}) d\Delta T \tag{2.11}$$

Then recasting the variables ($u = \frac{\Delta T}{\Delta T_0}$), one gets:

$$\langle \Delta T \rangle = \Delta T_0^{2-\pi} \underbrace{\int_0^{+\infty} u^{1-\pi} \cdot f(u) du}_{constant} \tag{2.12}$$

Finally, the following relation is reached: $\Delta T_0 \sim \langle \Delta T \rangle^{\frac{1}{2-\pi}}$. This implies that plotting $x = \langle \Delta T \rangle^{\frac{1}{\pi-2}} \cdot \Delta T$ and $y = \langle \Delta T \rangle^{\frac{\pi}{2-\pi}} \cdot P(\Delta T)$ all curves should collapse whatever the value of E_{th}. This scaling is verifed in figure 2.20 for sample Sa_1 and for CA earthquakes. Comparing with figure 2.11, this renormalization collapses both upper and lower cut-offs in the case of fracture but just the upper one in the case of earthquake. In this last case, the gamma distribution mimics what is reported by [Bak et al. (2002); Corral (2004); Davidsen et al. (2006)] and debated by [Touati et al. (2009)][xi].

Then, the waiting law is analyzed as a function of the loading speed. In figure 2.21-A the exponent remains unchanged with V. But the loading rate has an effect on the upper cut-off: the higher the loading speed the lower the cut-off. The rescaling presented in figure 2.20 is also cross-checked with those curves in figure 2.21. It demonstrations a good collapse of the curves for different energy thresholds and different loading rates which enhances the efficiency of this scaling. Moreover, has observed with a simpler renormalization by [Baro et al. (2013)] on compression rock experiments, on ETAS model and on Californian earthquakes and by [Santucci et al. (2007)] on paper tearing, the renormalized curve presents a dogleg shape with a first power-law whose exponent is π

[xi] Based on the so called Epidemic-Type Aftershock Sequences (ETAS) model [Touati et al. (2009)] claims that the gamma distribution found by [Bak et al. (2002); Corral (2004); Davidsen et al. (2006)] is an artifact of their measurements. In our case ETAS model does not suit since it does not take into account the foreshock sequences.

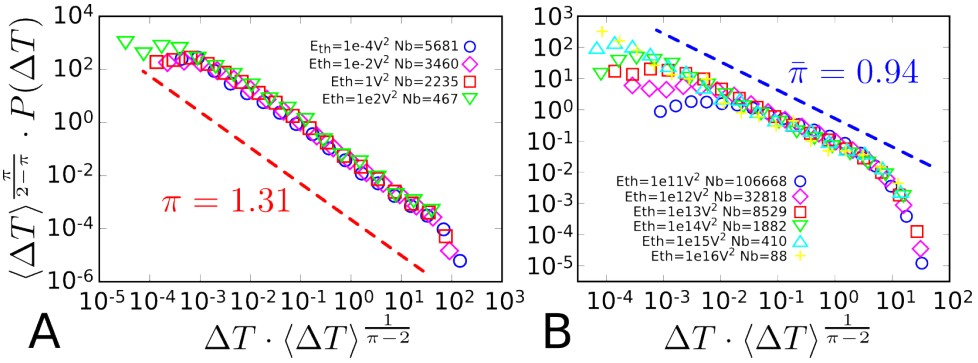

Figure 2.20: A: Renormalized curves for the waiting time probability density function for the sample Sa_1 ($d = 500$ μm, $V = 16$ nm/s, no porosity). Lower and upper cut-offs as well as power-laws collapse on the same curve over six orders of magnitude. B: Renormalized waiting time laws for the CA earthquakes between 2000 and 2012. Both power-law and upper cut-offs collapse on a same curve. In both cases, the axes are logarithmic and dashed lines are given to guide the eyes.

and a second one with an exponent of value close to 2. The exponent of the right part of the law (red dashed line in figure 2.21-B) is highly reminiscent to what is observed in paper by [Santucci et al. (2007)]. This first implies that long silent periods do not follow the same statistical regime as small ones. Secondly, long silent regimes do not require 3D effects to be explained as 2D paper experiments observe them also.

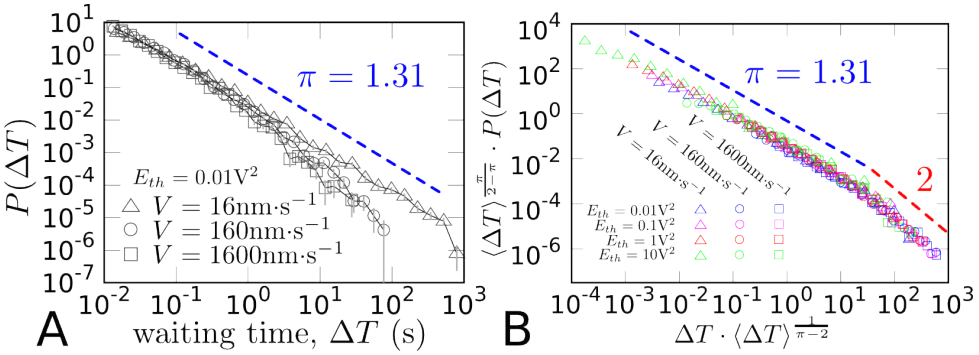

Figure 2.21: A: Probability density function of the time between acoustic events for different loading speeds (samples Sa_1, Sa_2 and Sa_3, bead size 500 μm without porosity). The dashed line with slope $\pi = 1.31$ is a guide for the eye. B: Collapse of these curves. All the waiting time power-laws, for different loading speed and different energy thresholds collapse on a single curve that exhibit two power-law regimes: exponent $\pi = 1.31$ and 2. In both cases, the axes are logarithmic.

Experiments with different bead sizes obtain similar results for waiting time law. Figure 2.22-A illustrates Omori law for the experiments with different bead size. Only experiments with bead size 500 and 230 μm follow a power-law. It is even clearer looking at the rescaling presented in figure 2.22-B. These two experiments give curves that properly collapse on the dogleg shaped curve. Richter-Gutenberg law (section 2.9.1) is in agreement with this point. Moreover, it will be confirmed theoretically in the second part of this manuscript (second chapter).

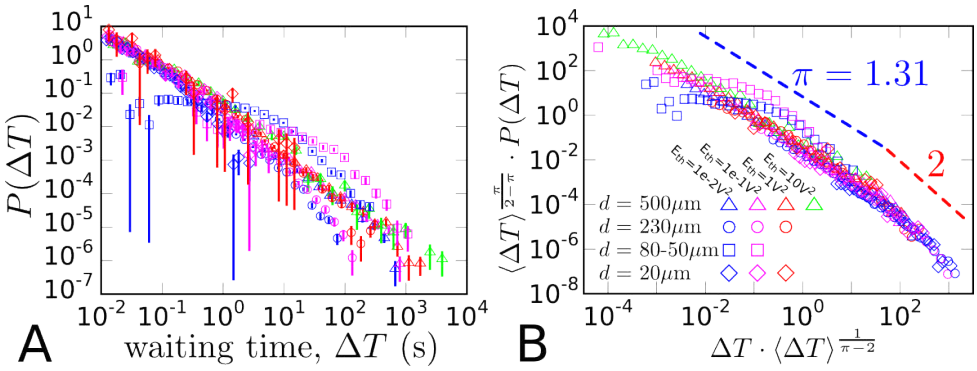

Figure 2.22: A: Probability density function of the time between acoustic events for different bead size (samples Sa_1, Sb_1, Sc_1 and Sd_1) loaded at the same speed (16 nm/s). B: Attempt to collapse them. The curves obtained with the smaller bead sizes do not follow a power-law and do not collapse onto the other curves. For both figures, the axes are logarithmic.

2.9.6 Comparison of the exponents

For sake of simplicity, not all the statistical laws are drawn for each loading rate. Hence, to present results and compare and contrast all exponents, table 2.1 gives the exponent of the different power-laws for the different loading speeds. Most of the exponents are not modified by the loading rate, but there is a higher uncertainty for the exponents with high value V. This originates from the fact that the loading speed has an effect on the propagation regime of the crack tip: in crackling or not (see the second chapter of the second part of this manuscript for more details).

From similarities of the exponent in table 2.1 and from the physical closeness, one can deduce that Omori, Voight and waiting time exponents are the same ($p_A = p_F = \pi$) just like Richter-Gutenberg exponent is the same as Utsu exponent ($\beta = b_A = b_F$).

Exponents for acoustics	$V = 16\text{nm}\cdot\text{s}^{-1}$	$V = 160\text{nm}\cdot\text{s}^{-1}$	$V = 1600\text{nm}\cdot\text{s}^{-1}$
Richter-Gutenberg law: β	0.94 ± 0.05	0.91 ± 0.04	0.91 ± 0.05
Waiting time law: π	1.31 ± 0.03	1.5 ± 0.06	1.55 ± 0.08
Omori law: p_A	1.18 ± 0.07	1.4 ± 0.1	1.35 ± 0.09
Voight law: p_F	1.22 ± 0.07	1.4 ± 0.1	1.5 ± 0.1
Productivity law: γ_A	0.2 ± 0.1	0.2 ± 0.1	0.2 ± 0.1
Utsu law: b_A	0.95 ± 0.04	0.91 ± 0.03	0.99 ± 0.06
Båth law: f	1.05 ± 0.05	1.05 ± 0.06	1.09 ± 0.07

Table 2.1: Measured acoustic exponents of the different power-laws for different loading speeds.

bead size (μm)	event density (ev/cm)
500	730
230	3460
80-50	230
20	940

Table 2.2: Density of acoustic events as a function of the bead size.

2.9.7 Spacial density of events

From a quantitative point of view, It is now interesting to study the link between the material and its ability to produce AE. To study this aspect, one measures the cumulative number of acoustic events received by the acoustic sensors when the crack propagate in the same material (beads of 500 μm and sintering pressure of 5.2 MPa, samples Sa) for different loading speeds (16 nm/s – Sa_1, 160 nm/s – Sa_2 and 1600 nm/s – Sa_3). Figure 2.23 initially depicts transient regime after which the number of acoustic events per unit time remain constant (730 ev.$\cdot\text{cm}^{-1}$). This is independent of the loading speed V and local speed v. This highly non-trivial result, in established regimes, could measure the crack propagation just by counting the number of acoustic events. Moreover, since the mean crack speed is not the same in those three different experiments, this means that the rate of events varies with the loading rate as it was suggested by the scaling in R_S of the Omori law.

The number of events per unit time seems to be a material constant. Table 2.2 presents results on this quantity for different samples varying only the bead size (loading speed is 16 nm$\cdot\text{s}^{-1}$ and sintering pressure 5.2 MPa). Unfortunately, this parameter does not seem to vary simply monotonically with the bead size.

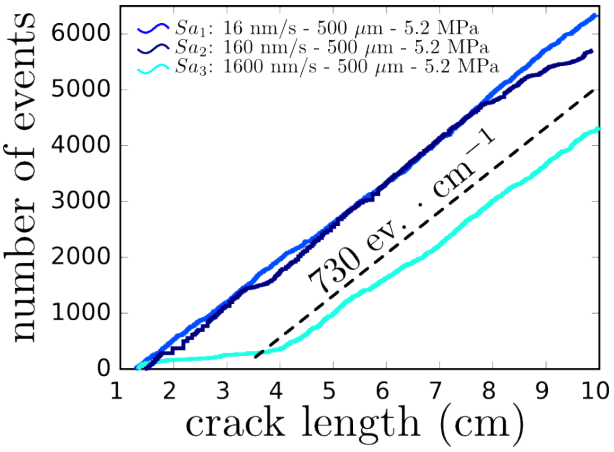

Figure 2.23: Variation in the number of AE as a function of the crack length for a same material but three different loading speeds (samples Sa_1, Sa_2 and Sa_3, bead size 500 μm without porosity). After a transient regime, curves run parallel. The dashed line with slope 720 ev/cm provides a guide for eyes.

2.10 Conclusion

In this chapter, we have demonstrated that the model experiment (whose mechanism is much simpler than earthquake) displays the same statistical richness as the seismic sequences: the Richter-Gutenber, Omori, Voight, productivity, Utsu, Båth and waiting time laws are fitted with universal exponents. More particularly, the unpredicted clustering in time is evidenced with Omori and waiting time laws. The FS-MS-AS sequences are statistically totally symmetric! This is contrary to what is seen for the earthquakes. Besides, the productivity law succeeds in renormalizing the Omori law whatever the loading rate and a generalization of the usual waiting time law renormalization evidence a 2D long silent regime.

Finally one notes that this waiting time law has been wildly observed numerically in the case of friction earthquake models [Scholz (1998); Dieterich (1994)], damage model [Zapperi et al. (1997b)] and Epidemic-Type Aftershock Sequences (ETAS) model [Touati et al. (2009)]; and experimentally in the case of damage [Baro et al. (2013); Davidsen et al. (2006)] and interfacial fracture [Grob et al. (2009); Koivisto et al. (2007)]. However for those different cases the loading conditions, the time dependency and the fundamental physics of the phenomenon are much more complex than in the simple mode I fracture experiments where the law is still valid.

Main messages of the chapter

◇ The statistics of breaking events when a crack is propagating in mode I in a 3D isotropic heterogeneous brittle material are as rich as the ones of seismic events: usual earthquake laws are fitted.

◇ The FS-MS-AS sequence is observed for breaking events with a symmetry between FS and AS.

◇ As long as the propagation stays in the crackling regime, the exponents do not vary with the loading rate nor the microtexture of the material.

◇ Nevertheless the cut-off and prefactors of the Omori and waiting time law scale with the rate of events and energy.

◇ Spatial density of acoustic events is a constant of the material.

Chapter 3

Intermittency and energy release fluctuation during crack growth

Introduction

Contrary to earthquakes and peeling, tearing and rock compression experiments, model fracture experiments herein have synchronized access to the elastodynamics data (AE) and to the elastostatics observables (elastic energy E and crack speed v). The model herein is simple; yet it has paradoxical statistical richness. This leads to link between the complexity of the earthquake mechanism probed by AE and the relevant quantities in fracture mechanics involved in pinning-depinning model. Now the task is to observe and characterize crackling from LEFM quantities for the model experiments herein (*i.e.* nominally brittle 3D solid) and compare results with what is observed in 2D peeling experiments [Grob et al. (2009); Tallakstad et al. (2011, 2013)]. A comparison of the AE statics is also of interest to verify that the difference in nature of both phenomenon cause a difference in the power-law exponents.

In this chapter, first we establish that only one mechanical parameter is free in this fracture problem. So we will study its statistical variations via its probability density function and its power spectrum. Then, with a threshold-based method, we extract its statistical information and analyses it via geophysicist and pinning-depinning model tools.

3.1 Relation between crack velocity and stored elastic energy

LEFM framework relates the growth velocity v of cracks to the variations of elastic energy E in the solid. Figure 1.18 presents the typical time evolution of these two quantities for sample Sa_1 (see table 1.5 for sample details). The crackling dynamics translate in the random large impulses observed in $v(t)$, and in the stair-like aspect of the curve $E(t)$. As expected within LEFM, these two quantities are related. Figure 3.1 presents the variations of radiated power, $\mathcal{P} = \mathrm{d}E/\mathrm{d}t$, as a function of v for different fracture experiments. To first order, both quantities are proportional:

$$v(t) \sim \mathcal{P}(t) \tag{3.1}$$

This proportionality is observed in all our experiments, irrespectively of the specimen microstructure (porosity and diameter of the sintered beads) and of the loading rate (speed of the splitting wedge). It can be interpreted as follow: The radiated power $\mathcal{P}$ is equal to the energy release rate G times the crack speed, v[xii]. Then, by considering a nominally brittle fracture with a small crack speed compared to the Rayleigh speed, G should be equal to the fracture toughness Γ. Within LEFM framework, Γ is a material constant and, hence, $v \sim \mathcal{P}$. The slope of the curve $\mathcal{P}$ *vs.* v is the fracture toughness. Section 3.5 shows that this assumption (*i.e.* constant energy release rate in the middle of the sample to suppress transient regimes) is a reasonable approximation.

This proportionality relationship between v and $\mathcal{P}(t)$ implies that crackling dynamics are fully described by characterizing either v or $\mathcal{P}(t)$. Section 1.3.2 shows that the computation of $v(t)$ is indirect and calls for a smoothening of the curve k *vs.* c (k being the specimen thickness, see section 1.3.2). On the other hand, $E(t)$, and hence $\mathcal{P}(t)$, is directly obtained from force, $f(t)$, measurements and the splitting wedge's displacement, $u(t)$. Logically $\mathcal{P}(t)$ is better to use than $v(t)$ to characterize the dynamics. Henceforth, the focus will be on $\mathcal{P}(t)$ and its variations.

[xii] $\mathcal{P} = -\mathrm{d}E/\mathrm{d}t = -\mathrm{d}E/\mathrm{d}c \times \mathrm{d}c/\mathrm{d}t = G \times v$

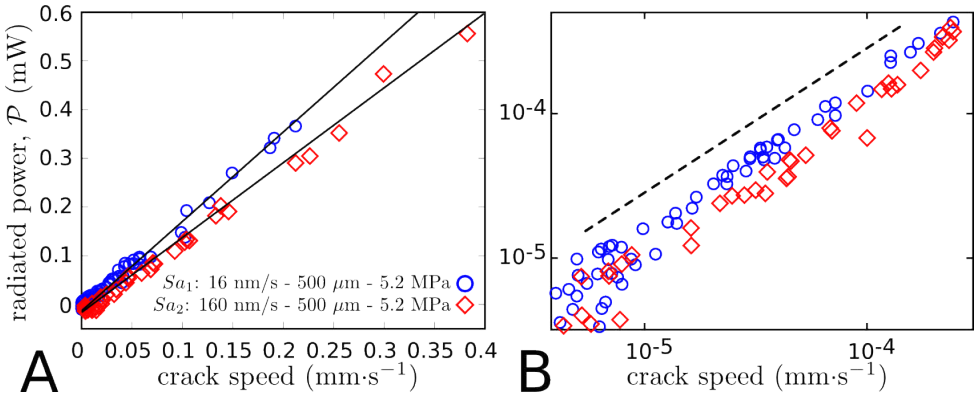

Figure 3.1: Radiated power $\mathcal{P}(t)$ as a function of crack speed $v(t)$ for two different experiments (Sa_1 and Sa_2), the control parameters of which are indicated in the legend: A: linear scales, B: logarithmic scales. In B, the black dashed line with slope 1 is a guide for the eyes.

3.2 Power spectrum of $\mathcal{P}(t)$

The first statistical study of the signal $\mathcal{P}(t)$ is done via its Power Spectrum (PS). This section presents this PS $PS_{\mathcal{P}}(\nu)$ to analyses its statistical variation. To first approximation, $\mathcal{P}(t)$ is (roughly) statistically invariant along time translation. Hence, the power spectrum provides directly a rapid, unbiased, and condensed information on its statistical variation. A typical example of such $PS_{\mathcal{P}}(\nu)$ is presented in figure 3.2. One points out a power-law scaling extending over several orders of magnitudes, reminiscent of crackling dynamics [Sethna et al. (2001); Travesset et al. (2002); Kuntz and Sethna (2000)]:

$$PS_{\mathcal{P}}(\nu) \sim \nu^{1/a}, \tag{3.2}$$

Where notations come from Barkhausen noise and Random Field Ising Model[xiii] and the power-law exponent is $1/a$. The fitted value is $1/a = 0.8 \pm 0.1$. This is significantly different from the one observed for Barkhausen noise or Ising model (exponent = 1.77, [Travesset et al. (2002))]. This indicates that the fracture problem studied here does not belong to the same universality class.

Figure 3.3-A presents the influence of the loading parameters and computed $PS_{\mathcal{P}}(\nu)$ for fracture experiments performed with different splitting wedge speeds V (samples:

[xiii] The sciences of crackling has indeed been pioneered in these fields.

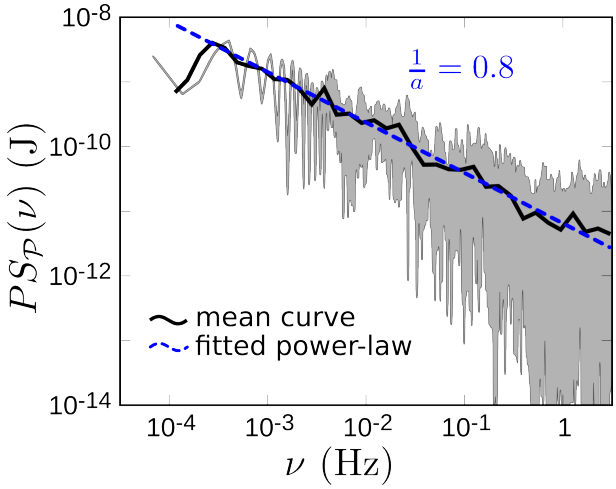

Figure 3.2: Power spectrum of elastic energy derivative signal ($\mathcal{P}$) and its mean curve in logarithmic scale. The blue dashed line represents the fitted power-law. This is computed for sample Sa_1 ($d = 500$ μm, $V = 16$ nm/s, no porosity).

	$V = 16$ nm/s – Sa_1	$V = 160$ nm/s – Sa_2	$V = 1600$ nm/s – Sa_3
PS exponent: $1/a$	0.8 ± 0.1	0.8 ± 0.1	0.6 ± 0.15

Table 3.1: Measured exponents for different loading speeds

16 nm/s – Sa_1, 160 nm/s – Sa_2 and 1600 nm/s – Sa_3). All the curves exhibit a power-law scaling with similar exponents (see table 3.1). On the other hand, the prefactors increase with wedge speed. The the kick up at high frequencies is due to the so-called 50 Hz electrical noise. In other words, the lower the prefactor, the higher the increasing part of the curve is because the regimes intersect for at lower frequencies. By dividing $PS_{\mathcal{P}}(\nu)$ by $V^{1.5}$, one obtains a fairly good collapse of the three curves. Thus, the power-spectrum prefactor scales with the wedge speed. This observation is close to what can be accounted by a statistical model mapping the crack problem with the depinning problem of a 1D elastic manifold (see the last chapter of the following part of this manuscript for more details).

Likewise, $PS_{\mathcal{P}}(\nu)$ is computed in experiments on samples made of sintered beads with different diameters (20 μm – Sd_1, $50 - 80$ μm – Sc_1, 230 μm – Sb_1, 500 μm – Sa_1). The wedge speed was kept constant ($V = 16$ nm/s) in all these experiments. Figure 3.4-A contains results. These results again depict the effect of the 50 Hz electrical noise for the high frequency part of the curves. The PS exponent for The smallest bead size (20 μm) implies only white noise (see table 3.2 for exponents) which is consistent with what we

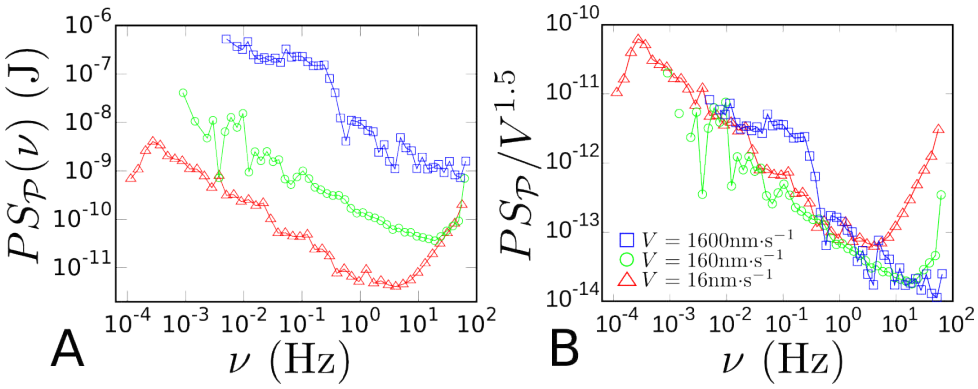

Figure 3.3: A: Power spectrum of radiated power $PS_{\mathcal{P}}$ for different wedge speeds V. B: Collapse obtained by making $PS_{\mathcal{P}} \rightarrow PS_{\mathcal{P}}/V^{1.5}$. The artificial rock broken here is made of sintered beads with $d = 500$ μm and without porosity (Sa_1, Sa_2 and Sa_3). In both case, the axes are logarithmic.

find in the second chapter of the second part of this manuscript. In this following chapter one will see that the pinning-depinning model predicts a scaling of the vertical axis by $1/d$[xiv]. In the experimental case, the result presented in figure 3.4-B shows a good collapse of the curves dividing the vertical axis by d^3.

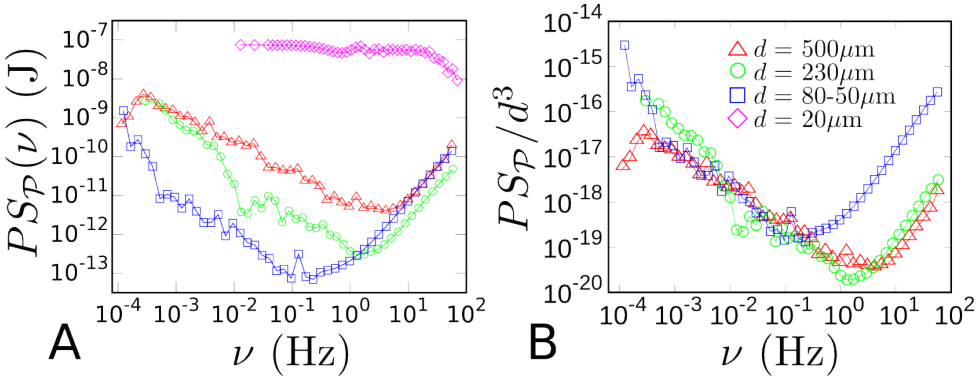

Figure 3.4: A: Power spectrum of the power curves for different bead sizes (samples Sa_1, Sb_1, Sc_1 and Sd_3, wedge speed 16 nm/s, no porosity). B: Collapse obtained by making $PS_{\mathcal{P}} \rightarrow PS_{\mathcal{P}}/d^3$. In both case, the axes are logarithmic.

[xiv] The parameter d of the experimental part is equivalent to $1/N$ in the pinning-depinning model presented in the first chapter of the second part of this manuscript, because the width W of the sample is fixed (for 0% porosity)

	$d = 20\ \mu$m – Sd_1	$d =$ 80-50 μm – Sc_1	$d = 230\ \mu$m – Sb_1	$d = 500\ \mu$m – Sa_1
PS exponent: $1/a$	0 (white noise)	1.0 ± 0.15	1.1 ± 0.12	0.78 ± 0.4

Table 3.2: Measured exponents for different bead sizes

3.3 Distribution of radiated power as a function of time resolution

Another synthetic way to analyze the statistics of an intermittent signal is to compute the probability density function of its values sampled regularly [Planet et al. (2009); Tallakstad et al. (2013)]. Herein, the signal is the radiated power $\mathcal{P}_i$ and the sampling rate is 10 ms. $\mathcal{P}_i$ are the values of the signal denoised with a first order butterworth filter[xv] of cut-off frequency $1/t_{cut}$. Figure 3.5-A presents the results for different cut-offs. According to fiber-bundle model with speed signal [Gjerden (2013)], this probability density function should follow a power-law with an exponent close to 2.5:

$$P(\mathcal{P}) = \mathcal{P}^{-\eta} \tag{3.3}$$

Experimental data herein does not follow this scaling relation. For low power values, the probability density exhibits a plateau and a bump. Nevertheless, plotting the data with linear axes as presented in figure 3.5-B, the mean part of $\mathcal{P}$ statistical behavior follows a Gaussian curve. As emphasize in section 3.2, this Gaussian behavior is due to the 50 Hz electrical noise.

Hence, figure 3.6-A contains the same data with logarithmic axes and add the Gaussian curve fitted in linear scale (see 3.5-B for $t_{cut} = 0.1$ s). It turns out that the plateau and the bump part of the curve match perfectly with the fitted Gaussian. Deconvoluating the signal gives figure 3.6-B. The resulting figure exhibits two different scaling regimes, one with exponent $\eta = 1.6 \pm 0.1$ for low power values and another with $\eta = 2.7 \pm 0.2$ reminiscent to what is observed numerically and experimentally by [Gjerden (2013)] and [Tallakstad et al. (2013)], respectively. However, Tallakstad et al. [Tallakstad et al.

[xv] The gain G of the first order Butterworth low pass filter is given by: $G = \dfrac{1}{\sqrt{1 + \left(\dfrac{\nu}{\nu_c}\right)^2}}$ with ν_c the cut-off frequency

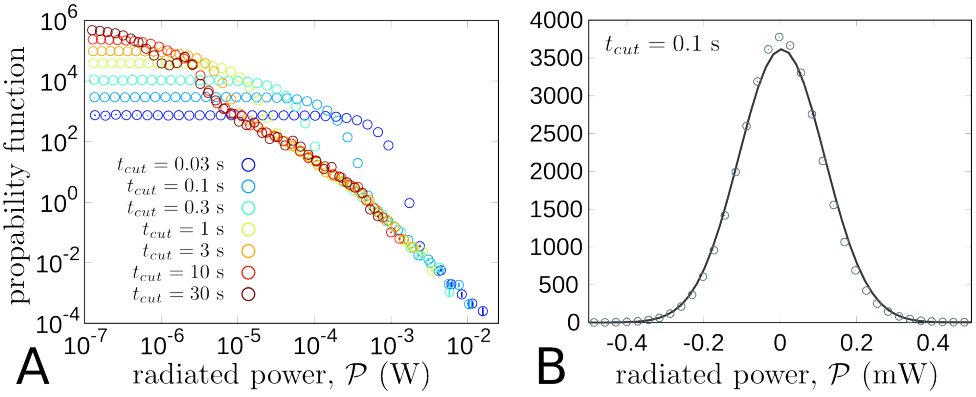

Figure 3.5: A: Probability density function of $\mathcal{P}(t_i) = \mathcal{P}_i$ in logarithmic scale for $\mathcal{P}$ filtered at different cut-off. This is computed from sample Sa_1 ($d = 500$ μm, $V = 16$ nm/s, no porosity). B: Same graph with linear axes for $\mathcal{P}$ filtered at $t_{cut} = 0.1$ s. The plain curve represent a Gaussian fit of the data.

(2013)] fit this probability density function with an alpha stable Levy distribution which is not possible here. Finally, as presented in figure 3.6-B-inset, the maximum value of the denoised signal scale with the value of the filter cut-off as $\mathcal{P} \sim t_{cut}^{-0.5}$ which gives the variation of the upper cut-off of $P(\mathcal{P})$.

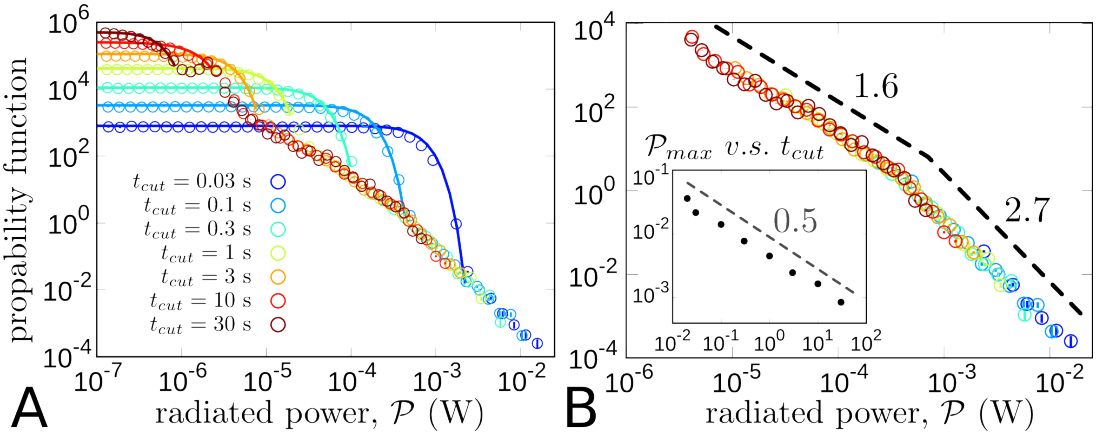

Figure 3.6: A: Probability density function of $\mathcal{P}_i$ in logarithmic scale for $\mathcal{P}$ filtered at different cut-off. This is computed from sample Sa_1 ($d = 500$ μm, $V = 16$ nm/s, no porosity). The plain curves are the Gaussian fitted in linear scale (see figure 3.5-B). B: Same graphs where the parts dominated by the Gaussian regime are removed. The probability density function exhibits two different regime with a crossover around 0.2 mW. B-inset: Maximum value of the denoised power signal as a function of the filter cut-off. All axes are in logarithmic scale.

3.4 Crackling analysis and avalanche statistics

The observations of power-law scaling in the power spectrum, together with that of the scale free features in the power distribution, are strong arguments in favor of crackling dynamics. In this context, the pulses observed in the $\mathcal{P}(t)$ signals result from the depinning avalanches of the crack front [Bonamy et al. (2008); Bonamy (2009)]. The idea is then to isolate these pulses and to study their statistics to get information on the underlying depinning avalanches.

3.4.1 Avalanches identification: Standard threshold-based method

In crackling problems, the standard way to characterize a jerky signal like $\mathcal{P}(t)$ is to introduce a prescribed threshold (expressed as a fraction of the maximum value) and to identify the pulses with the zones where the signal goes above this threshold. Nevertheless, as presented in figure 3.7-A, the curve $\mathcal{P}(t)$ is too noisy to apply directly this method. Noise needs to be filtered first. This is done via a Butterworth low-pass filter (first order) with a cut-off frequency of 1 Hz corresponding to the upper cut-off of the $PS_{\mathcal{P}}(\nu)$ power spectrum (see section 3.2). This filter selection is advantageous because it does not to change the gain below the cut-off (see figure 3.7-B) in the frequency domain. However, in the time domain, the maximum power amplitude scales as $t_{cut}^{-0.5}$ (figure 3.6-B-inset).

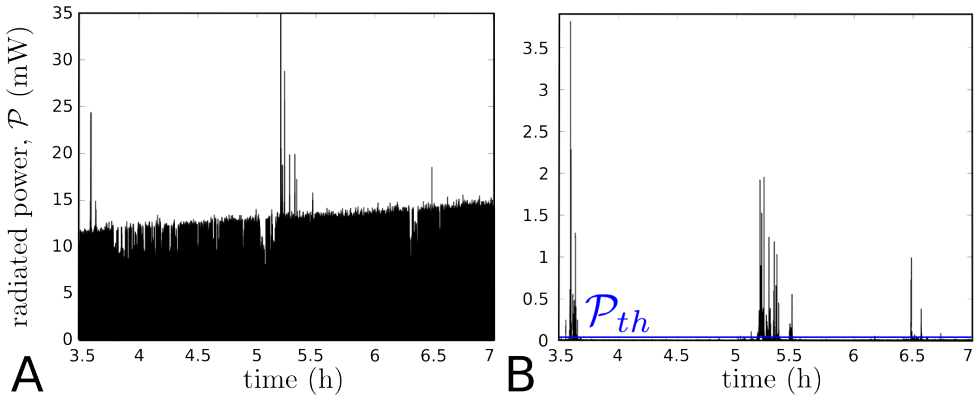

Figure 3.7: A: Raw radiated power signal of sample Sa_1 ($d = 500$ μm, $V = 16$ nm/s, no porosity). B: Denoised power signal. The filter is a 1 Hz Butterworth low-pass filter. As expected from figure 3.6-B-inset the filtering decreases the amplitude of the signal.

In the analyses presented hereafter, the threshold is 1% of the maximum value of

$\mathcal{P}(t)$. Other thresholds have been tried. They give similar results in term of scaling. As presented in the sketch depicted in figure 3.8, for each breaking event i, one extracts the following quantities:

- The event time T_i, *i.e.* first time at which $\mathcal{P}(t)$ goes above the threshold);
- The event duration D_i;
- The maximum speed of the event $\mathcal{P}_{max\text{-}i}$;
- The energy released in the system during the event; E_i;
- The event size S_i, *i.e.* the area swept by the crack front during the event, given by the crack advance during the event times the sample thickness;
- The event position c_i, i.e; the position of the crack front at time T_i;
- The depinning energy release rate $G_{d\text{-}i}$, *i.e.* the energy release rate at the event's initiation;
- The pinning energy release rate $G_{p\text{-}i}$, *i.e.* the energy release rate at the event's death.

One can then characterize the statistics of these quantities and analyze their interrelation. It is worth mentioning that quantity of events is significantly less than the quantity of AE. Hence, the obtained distributions are noisier.

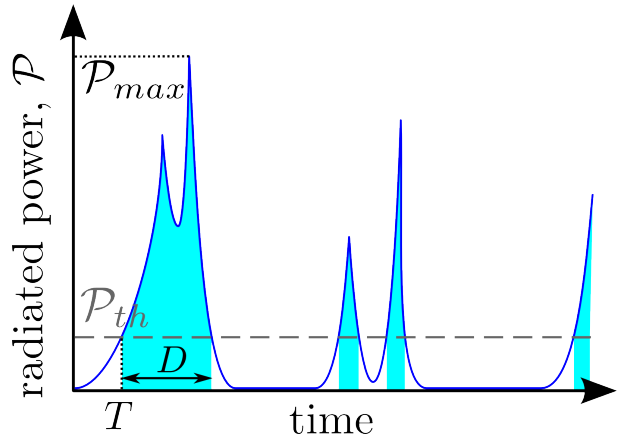

Figure 3.8: The figure depicts a schematic of the radiated power signal and presentation of the threshold-based method to extract breaking events. See text for detail about the notations.

3.4.2 Avalanche statistics

AE-like analysis

This section carries out the same statistical analysis as that proposed in chapter 2. This will shed light on the type of information that can be extracted from AE signals.

Energy distribution ▶ Figure 3.9 presents the distribution in energy of the events. The power-law exponent $\underline{\beta} = 1.4 \pm 0.15$ properly fits the data. This exponent is significantly larger than the one measured on the AE data (see section 2.1). This translates to a fundamental difference between AE and "true" depinning events. The former are elastodynamic quantities while the latter are elastostatic ones. They are not the same objects.

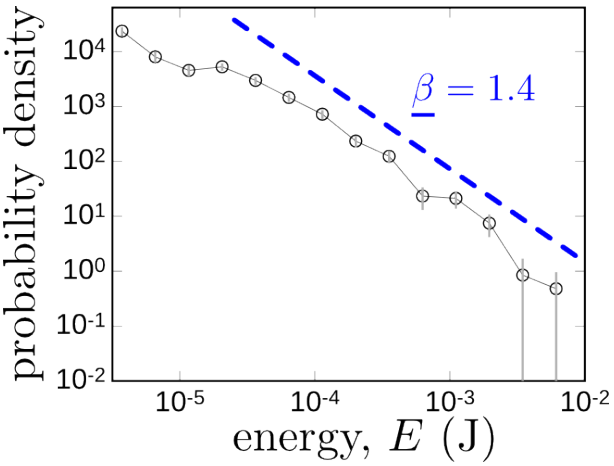

Figure 3.9: Probability density function in logarithmic scale of the energy for events extracted with the threshold-based method applied on the radiated power signal of the sample Sa_1 ($d = 500$ μm, $V = 16$ nm/s, no porosity). One observes the Richter-Gutenberg power-law extending over more than two orders of magnitude, and the fitted exponent is found to be $\underline{\beta} = 1.4 \pm 0.15$.

Distribution of waiting time ▶ Then, as done in section 2.6, one studies the statistics of the time ΔT separating two consecutive events, as detected in the radiated power signal. Figure 3.10 shows that the probability density function of these waiting times, measured for different energy thresholds, obeys the equation 2.7. The associated exponent is $\underline{\pi} = 1.3 \pm 0.15$. This is close to the one measured from AE events. Thus, time clustering seems to be of the same nature. This suggests that AE events result from the depinning of avalanches. Hence, they can be quantitatively located in time.

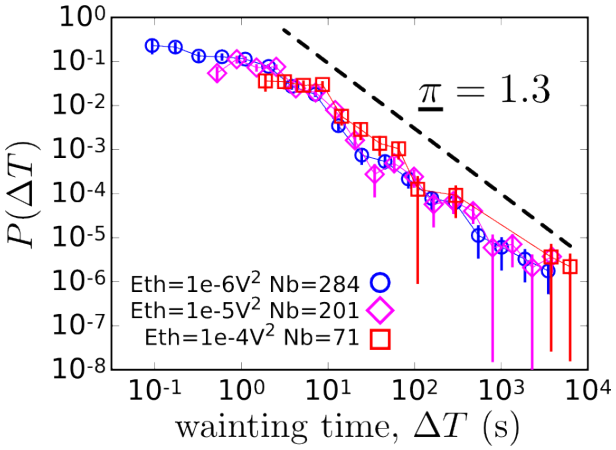

Figure 3.10: Probability density function of the inter-event time in logarithmic scale for the events extracted with the threshold-based method on the radiated power signal for sample Sa_1 ($d = 500\ \mu$m, $V = 16$ nm/s, no porosity). One observes the waiting time power-law extending over three orders of magnitude and the fitted exponent is $\underline{\pi} = 1.3 \pm 0.15$.

Triggering rate for aftershocks ▶ Procedures described in section 2.2 detail how to isolate FS-MS-AS sequences. Figure 3.11 shows the variations for the rate of AS as a function of time from MS, for different values of MS energy. As for AE events, this fulfills the Omori law. The fitted exponent is $\underline{p}_A = 1.3 \pm 0.1$. This corresponds closely with the AE exponent.

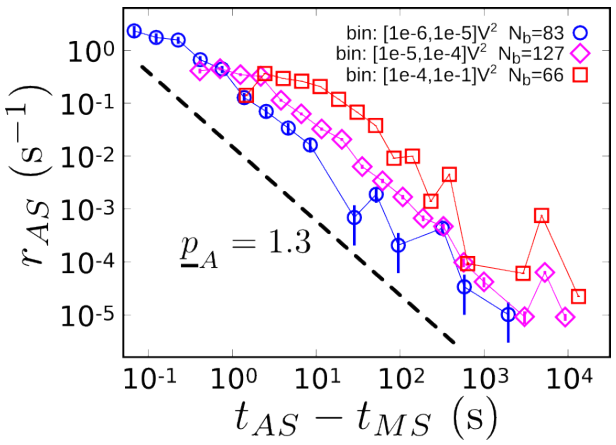

Figure 3.11: Rate of events after a MS in logarithmic scale for the events extracted with the threshold-based method on the radiated power signal for sample Sa_1 ($d = 500\ \mu$m, $V = 16$ nm/s, no porosity). One observes the Omori power-law extending over more than three orders of magnitude and the fitted exponent is $\underline{p}_A = 1.3 \pm 0.1$.

Voight law ▶ The rate of foreshocks has also been computed as function of time (figure 3.12). A Voight law is observed. The exponent fitted from equation 2.3 is $\underline{p}_F = 1.3 \pm 0.1$, *i.e.* very close to that for aftershocks. As for AE events, foreshock-mainshock-aftershock sequences remain statistically invariant along time reversal.

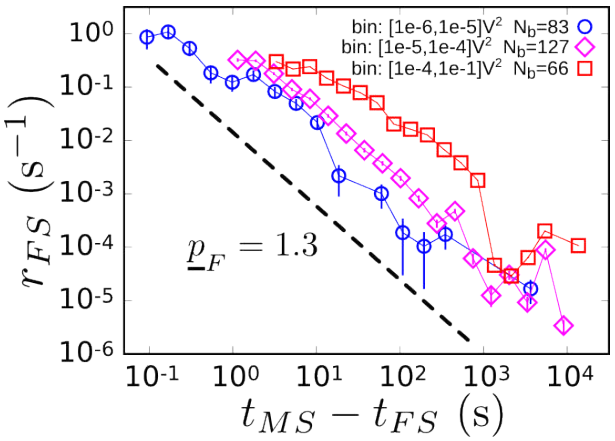

Figure 3.12: Rate of events preceding a MS in logarithmic scale for the events extracted with the threshold-based method on the radiated power signal for sample Sa_1 ($d = 500$ μm, $V = 16$ nm/s, no porosity). One observes the Voight power-law extending over more than three orders of magnitude, and the fitted exponent is very close to the one of Omori law: $\underline{p}_F = 1.3 \pm 0.1$.

Aftershock triggering rate *vs.* **mainshock energy** ▶ Examining the variations of the aftershock rate (prefactor of the curves presented in figure 3.11) as a function of mainshock energy permits the recovery of the productivity law (equation 2.4 presented in section 2.4). Due to a of lack of data, the exponent is fitted by collapsing the curves of Omori law (see figure 3.13) just like the method presented in [Baro et al. (2013)]. This exponent is two times larger than that obtained for AE ($\underline{\gamma}_A = 0.5 \pm 0.1$). Moreover, time symmetry is also observed for this law, and the exponent characterizing the FS productivity is $\underline{\gamma}_F = 0.5 \pm 0.1$.

Utsu law ▶ Finally, Utsu law presented in section 2.5 is also confronted against the events issued from the signal $\mathcal{P}(t)$. Fitting equation 2.6 for both AS and FS gives power-law exponents: $\underline{b}_A = 1 \pm 0.15$ and $\underline{b}_F = 1 \pm 0.15$. Again, time reversal symmetry is observed. Moreover, $\underline{b}_A$ is not equal to the Richter-Gutenberg exponent $\underline{\beta}$ as was verified with acoustic data.

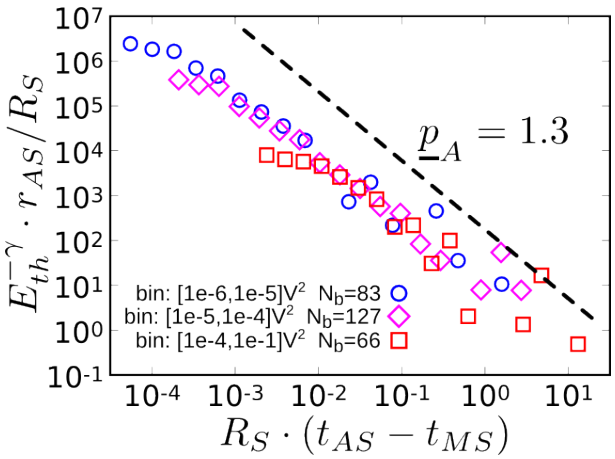

Figure 3.13: Renormalized Omori law in logarithmic scale for the events extracted with the threshold-based method on the radiated power signal for sample Sa_1 ($d = 500$ μm, $V = 16$ nm/s, no porosity), with $\underline{\gamma}_A = 0.5$. The collapse of the curves over more than four orders of magnitude is obtained from productivity law ($\underline{\gamma}_A = 0.5$). A dashed line with slope $\underline{p}_A = 1.3$ guides the eyes.

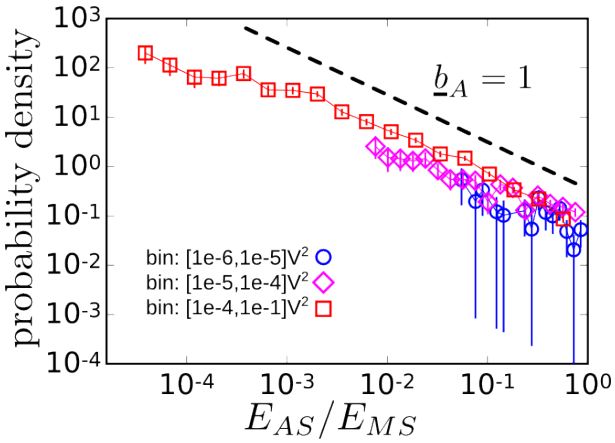

Figure 3.14: Utsu law in logarithmic scale for AS of the events extracted with the threshold-based method on the radiated power signal for sample Sa_1 ($d = 500$ μm, $V = 16$ nm/s, no porosity). A dashed line with slope $\underline{b}_A = 1$ guides the eyes.

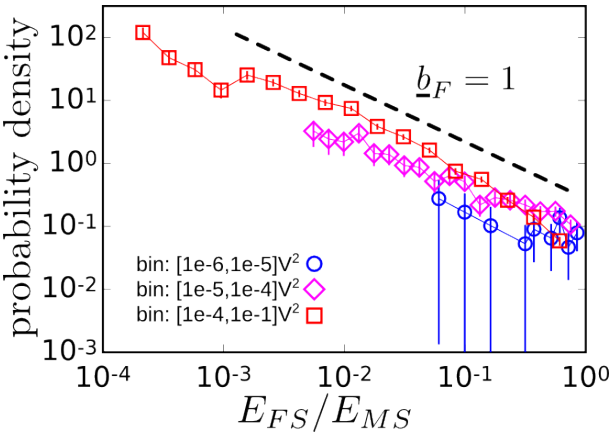

Figure 3.15: Utsu law in logarithmic scale for event FS extracted with the threshold-based method on the radiated power signal for sample Sa_1 ($d = 500$ μm, $V = 16$ nm/s, no porosity).The dashed line with slope $\underline{b}_A = 1$ is given as a guide for the eyes.

Pinning-depinning-like analysis

One now turns to the analysis of the size and duration associated of each burst. The statistics of these two quantities are the ones commonly predicted in the pinning-depinning models [Bonamy et al. (2008); Bonamy (2009)]. This is what is done in this section, keeping in mind that (as shown in section 3.1), the instantaneous released power is proportional to the crack speed.

Distribution of avalanche size ► As we will see in the first chapter of the second part of this manuscript, the pinning-depinning model does not give way energy dissipated in the system during an avalanche E_i. Nevertheless, as explained in section 3.1, $\mathcal{P} \sim v$ and the decrease E_i of elastic energy during an event i is proportional to increment of crack length. After having multiplied this last quantity by the sample width W, the avalanche size S_i which is the surface swept by the crack front during the event is obtained. This quantity is found to be a power-law distributed (figure 3.16). The associated exponent is $\underline{\beta}_S = 1.4 \pm 0.15$, *i.e.* the same as the one found for energy $\underline{\beta}$. This value is just slightly larger than the value $\underline{\beta} = 1.3$ predicted by the depinning approach [Bonamy et al. (2008); Bonamy (2009)].

Distribution of avalanche duration ► The distribution of duration is presented in figure 3.17. It follows the power law:

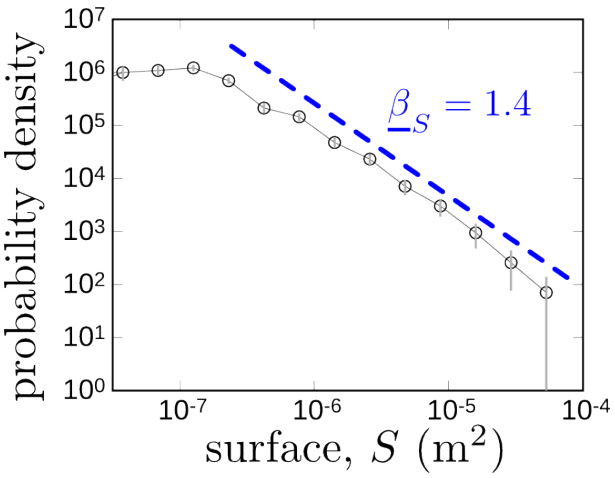

Figure 3.16: Probability density function of the size of an avalanche for the events extracted from power signal with the threshold-based method for sample Sa_1 ($d = 500$ μm, $V = 16$ nm/s, no porosity). The graph is presented in logarithmic scale and one observes the Richter-Gutenberg power-law extending over more than two orders of magnitude. The fitted exponent is very close to the one found with energy instead of surface: $\underline{\beta} = 1.4 \pm 0.15$.

$$P(D) \sim D^{-\kappa} \tag{3.4}$$

With fitted exponent $\underline{\kappa} = 1.8 \pm 0.1$. This value is significantly larger than the value $\underline{\beta} = 1.5$ predicted by the depinning approach [Bonamy et al. (2008); Bonamy (2009)].

Scaling between energy and duration ► Figure 3.18 compares the event duration to their energy. The quantities are plotted by averaging the couples (E, D) of each event along the energy axis. From pinning-depinning approach, the scaling relation follows:

$$D \sim E^{-a} \tag{3.5}$$

The exponent fitted on the first decades is $\underline{a} = 0.7 \pm 0.1$. From pinning-depinning model it is expected that this a corresponds with the exponent of the PS. Nevertheless, we measured $\frac{1}{a} = 0.8$ in section 3.2 for PS, this result significantly differs from that computed here.

Energy release rate at pinning and depinning events ► Another interesting quantity is the value of the energy release rate at the burst initiation (depinning value G_d) and

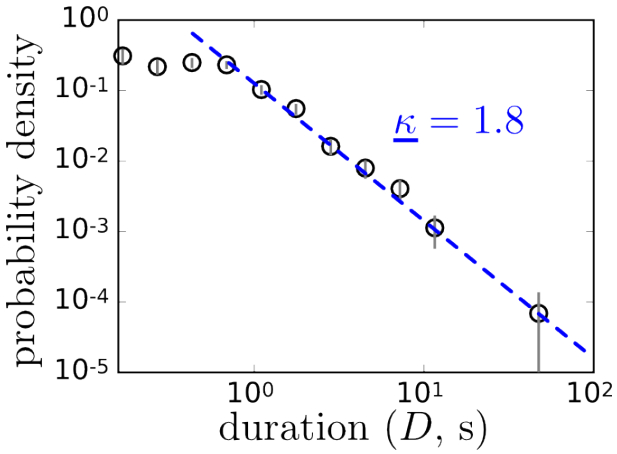

Figure 3.17: Probability density function of event durations for the events extracted from power signal with the threshold-based method for sample Sa_1 ($d = 500$ μm, $V = 16$ nm/s, no porosity). The graph is presented in logarithmic scale and a power-law extends over nearly two orders of magnitude with exponent: $\underline{\kappa} = 1.8 \pm 0.1$.

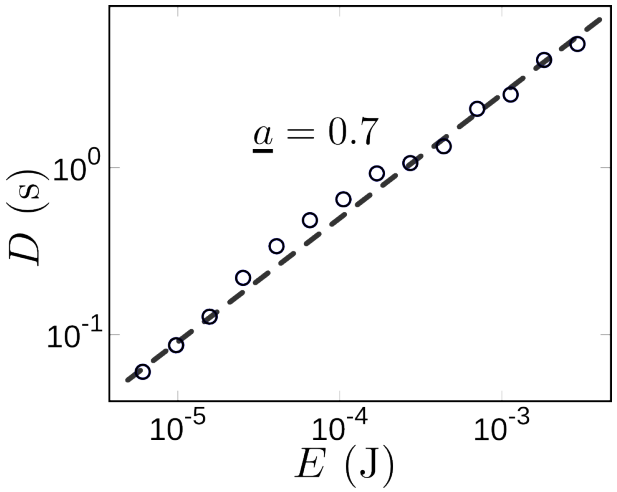

Figure 3.18: Energy *vs.* duration law in logarithmic scale for the events extracted from power signal with the threshold-based method for sample Sa_1 ($d = 500$ μm, $V = 16$ nm/s, no porosity). Each point stands for the average position of several events in the (E, D) plan, logarithmically spread along the x-axis. The fitted exponent is found to be $\underline{a} = 0.7 \pm 0.1$.

at the burst death (pinning value G_p). These two quantities, indeed, inform one on the landscape of effective toughness felt by the front as it propagates, which has been theoretically investigated [Roux et al. (2003); Roux and Hild (2008); Patinet et al. (2013)]. A precise distribution function for these quantities is out of reach, due to the lack of statistics. Still, their cumulative distributions are plotted in figure 3.19-A. The two distributions are fairly narrow (15% around the mean value). To first order, they share similar shapes but with $G_d > G_p$ for all events (see figure 3.19-B). We will come back to this point in section 3.4.2.

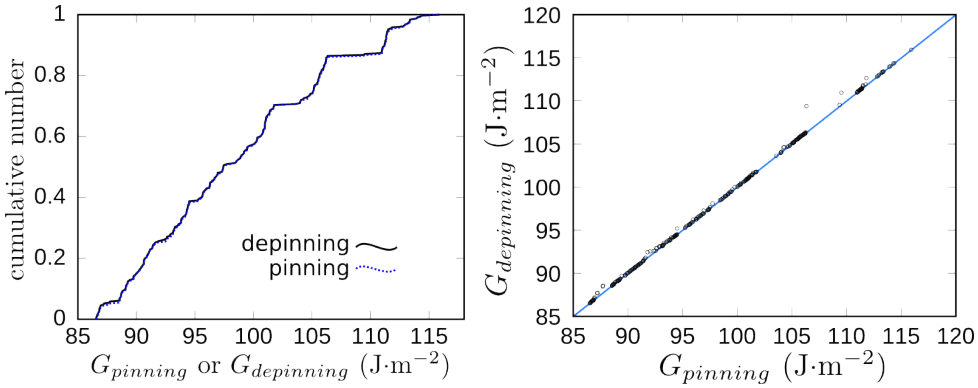

Figure 3.19: A: Cumulative number of energy release rate at the pinning and depinning transition for the events extracted from power thresholding. B: Comparison of both quantities.The data come from the experiment on sample Sa_1 ($d = 500$ μm, $V = 16$ nm/s, no porosity).

Statistics of maxima ▶ Finally, figure 3.20 plots the probability density function for the maximal value $\mathcal{P}_{max\text{-}i}$ of instantaneous radiated power (proportional to the maximal value of front velocity) reached in the events. This follows the power-law:

$$P(\mathcal{P}_{max}) = \mathcal{P}_{max}^{-m} \tag{3.6}$$

With $\underline{m} = 2.4 \pm 0.2$. This value is not far from the one expected theoretically (exponent = 2) within the mean-field theory of the interface depinning transition [Leblanc et al. (2013)].

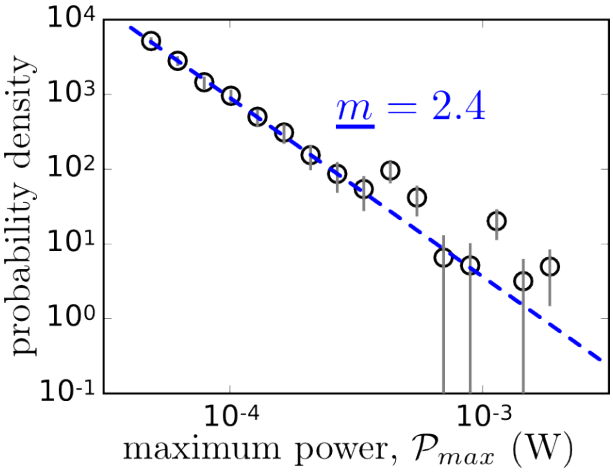

Figure 3.20: Probability density function in logarithmic scale of the maximal power during each events extracted from the threshold-based method for sample Sa_1 ($d = 500$ μm, $V = 16$ nm/s, no porosity). A power law is observed over more than one order of magnitude with exponent: $\underline{m} = 2.4 \pm 0.2$.

Avalanche shape

In pinning-depinning models (see the first chapter of the second part of this manuscript) it is also of interest to characterize the average shape of the pulses and its variation with the size. The procedure to define this shape follows reference [Papanikolaou et al. (2011)]:

- (i) D_0 is the avalanche duration and all the pulses i such that $D_i \in [D_0 - \delta D; D_0 + \delta D]$ are collected.
- (ii) The pulse shape $\mathcal{P}(t)$ at this prescribed value D_0 is computed by averaging $\mathcal{P}_i(t - T_i)$ over all the collected pulse (T_i is the start time of pulse i).

Figure 3.21 presents the normalized pulse shape $\mathcal{P}/\mathcal{P}_{max}$ *vs.* t/D_0 for increasing values D_0. For small D_0, the pulses are roughly symmetric. Depinning models [Papanikolaou et al. (2011); Sethna et al. (2001); Leblanc et al. (2013)] predicts a symmetric shape. But as D_0 increases, the symmetry is lost, and the acceleration phase increases faster than the deceleration phase. This asymmetry in time is of high interest, and as we will see in the last chapter of the second part of this manuscript, it cannot be captured by the pinning-depinning models for crack growth. Its origin remains unsolved. It may result from the viscoelastic nature of the polymer rocks studied here, or be generic in brittle heterogeneous fracture. Answer this question represents an important challenge for future

research!

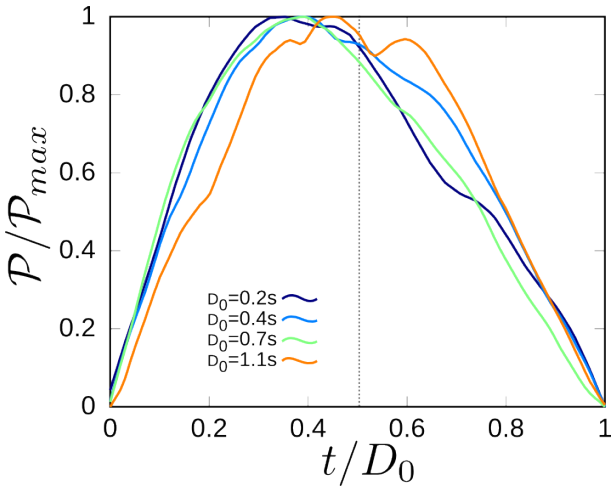

Figure 3.21: Average avalanche shapes for different event duration extracted from the threshold-based method. The shapes are measured from data of the experiment with sample Sa_1 ($d = 500$ μm, $V = 16$ nm/s, no porosity). A vertical dashed line is drawn at $x = 0.5$ to guide the eyes.

3.5 Fracture energy and toughness

This section presents results on the energy release rate G (see equation 1.4) as a function of the crack length in different fracture experiments. Figure 3.22 presents $G(c)$ for sintered beads of diameters 500 μm, 230 μm, $80 - 50$ μm and 20 μm loaded at $V = 16$ nm/s, 160 nm/s and 1600 nm/s. Table 3.3 recaps these experimental parameters and presents the mean value of the energy release rate as computed in the steady part of the curves (*i.e.* over crack length ranging from 2 to the 9 cm.

After propagating a few (necessary to reach the steady state), the energy release rate varies slowly around a mean value with a small amplitude as expected in section 3.1. Then assuming that the whole propagation occurs in the quasistatic regime, one can link G to the fracture toughness of the material Γ. Hence, examining the mean values (given in table 3.3), Γ increases with the crack speed. This point come from the fact that we use an amorphous polymer, polystyrene. In such a material, damage processes at the fracture process zone scale mainly occurs via crazing, and the resulting fracture energy is known to increase with crack speed [Doll (1983); Scheibert et al. (2010)]. Moreover, the material

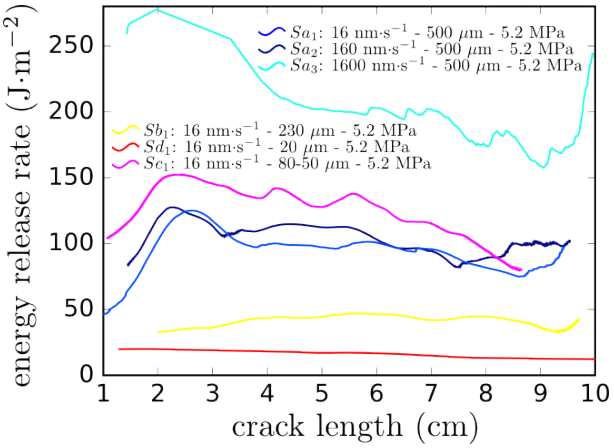

Figure 3.22: Energy release rate as a function of the crack length for model rocks with different bead size and different loading speed (samples Sa_1, Sa_2, Sa_3, Sb_1, Sc_1 and Sd_1; see table 3.3), see text for details.

Sample	Bead size (μm)	Sintering pressure (MPa)	Loading speed (nm/s)	G (J/m^2)
Sa_1	500	5.2	16	110 $\pm$ 15
Sa_2	500	5.2	160	100 $\pm$ 10
Sa_3	500	5.2	1600	210 $\pm$ 15
Sb_1	230	5.2	16	46 $\pm$ 3
Sc_1	80-50	5.2	16	140 $\pm$ 10
Sd_1	20	5.2	16	18 $\pm$ 5

Table 3.3: Mean energy release rate for different experiments.

toughness decreases when the bead size decreases except for sample Sc_1. This may come from the fact that the bead material is not the same, or that the bead mixing (80 and 50 μm beads) induces a toughening effect.

3.6 Fractography

To complete the study, one examines at the *post-mortem* fracture surfaces. This characterization is of interest because their morphology provides keys to unlocking the 3D aspects of crack growth (which, by essence, cannot be access in peeling and interfacial crack propagation experiments). Table 3.4 details the samples which are scanned and analyzed in this section. In this context, topographical profiles are acquired parallel and perpendicular to the direction of crack propagation (see figure 1.19 for height profiles).

This study has been carried out in tight collaboration with Tristan Cambonie[xvi].

Starting from the pioneering work of Mandelbrot et al. [Mandelbrot et al. (1984)], many experiments have revealed that fracture surfaces exhibit self-affine morphological scaling features [Bouchaud et al. (1990); Måløy et al. (1992); Bouchaud (1997)] [Ponson (2007); Bonamy and Bouchaud (2011)]. Recently, it was suggested [Bonamy et al. (2006)] that two distinct scaling regimes can coexist: A small-scale regime characterized by a roughness exponent $\zeta \approx 0.8$ [Mandelbrot et al. (1984); Bouchaud et al. (1990); Måløy et al. (1992); Ponson (2007)] and a large scale regime, with a smaller exponent $\zeta \approx 0.4$ [Bonamy et al. (2006); Ponson et al. (2006)] or logarithmic roughness [Ramanathan et al. (1997); Dalmas et al. (2008)]. The crossover between the two regimes scales with either the size of the fracture process zone [Bonamy et al. (2006)] or with the microstructure scale [Dalmas et al. (2008)].

The self-affinity of the profiles can be *e.g.* revealed by plotting the Fourier spectrum (see figure 3.23-A). This spectrum is then found to decay as a power-law and the associated exponent is given by $1 + 2\zeta$. The height-height also depicts the correlation function $\sigma_{\Delta h}$ for considered profiles $h(r)$. We recall here the definition of this function:

$$\sigma_{\Delta h} = \langle (h(r + \Delta r) - h(r))^2 \rangle_r^{1/2} \tag{3.7}$$

Where the average $\langle \rangle_r$ is taken over all the abscissas r. For a self-affine profile, one expects:

$$\sigma_{\Delta h} \sim \Delta r^{\zeta} \tag{3.8}$$

The samples scanned are presented in table 3.4. Samples made from beads sizes greater than 230 μm are neglected, since the resulting fracture surfaces are too rough for the profilometer (maximum amplitude of 800 μm). Moreover, one only considers materials with no or low porosity (sintering pressure higher than 0.6 MPa), so that the microstructure length-scale is fully set by the bead diameter during sintering. Then, for all these samples, one sketches $\sigma_{\Delta h}$ *vs.* Δr for $h(r)$ parallel (figure 3.24-A) and perpendicular (figure 3.25-B) to the direction of crack propagation. All the curves exhibit a first regime with a roughness exponent $\zeta_1 = 0.9 \pm 0.1$. This is not too far from the universal value $\zeta \sim 0.8$ widely reported in different materials [Bouchaud et al. (1990); Måløy et al.

[xvi] Fluides, Automatique et Systèmes Thermiques laboratory at University of Paris-Sud in Orsay, France

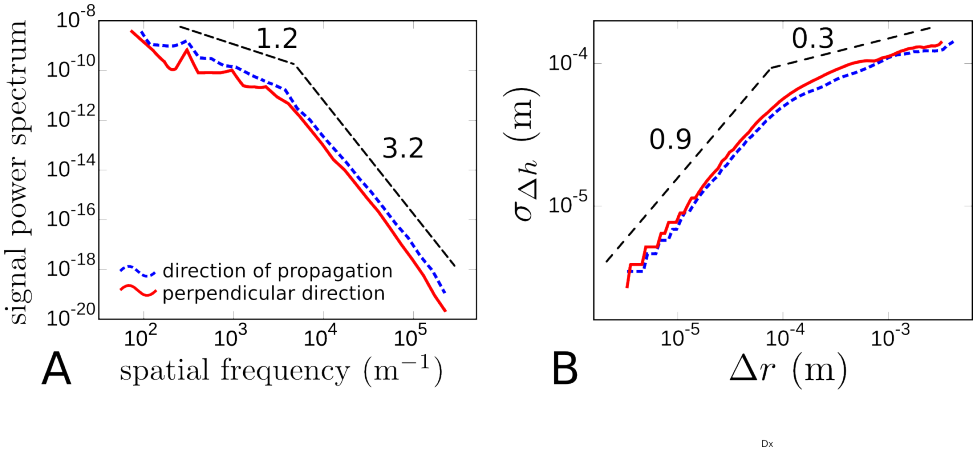

Figure 3.23: A: Fourier spectrum of the height profile extracted on the fracture surface of sample Sb_1 (230 μm, 5.2 MPa) in the direction of crack propagation of the crack (blue) and perpendicularly to the direction (red). B: Height-height correlation functions of these profiles. The results presented in logarithmic scale are averaged on 3 profiles. The dashed lines (slope provided in figure) guide the eyes.

(1992); Ponson (2007)]. At large scales, a second regime is also observed, with a smaller exponent $\zeta_2 = 0.3 \pm 0.15$. This last exponent resides between the $\zeta \sim 0.4$ observed at large scales on rocks and ceramics [Ponson et al. (2006, 2007)] and the logarithmic roughness ($\zeta \sim 0$) observed in nanostructured, partially demixed, vitroceramics [Dalmas et al. (2008)]. The crossover between these two regimes is found to be close to the bead size. Hence, $\sigma_{\Delta h}$ *vs.* Δr curves have been renormalized with an optimized bead size d_{opt} fitted to optimize the collapse. The results and the values of d_{opt} are presented in figure 3.24-A and 3.25-B, for both directions. We observe a fairly good collapse of the curves. The differences between d_{opt} and d can be explained by the fact that when sintering the material, the beads are compressed and deformed so there characteristic length can decrease.

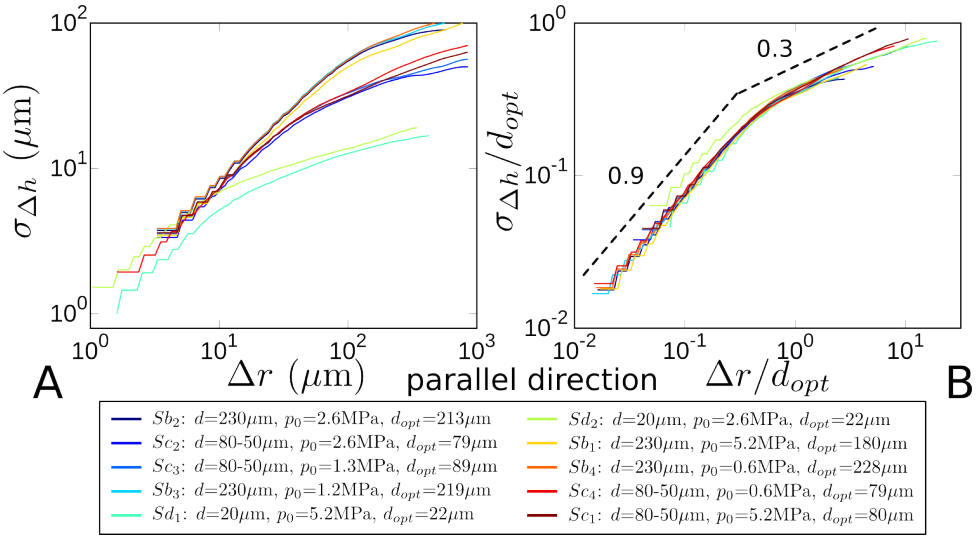

Figure 3.24: A: Height-height correlation function of profiles measured in the direction of propagation of the crack. B: Height-height correlation function curves renormalized with the optimised bead size d_{opt}. All the axes are in logarithmic scale. The dashed line whose slope is a guide for the eyes.

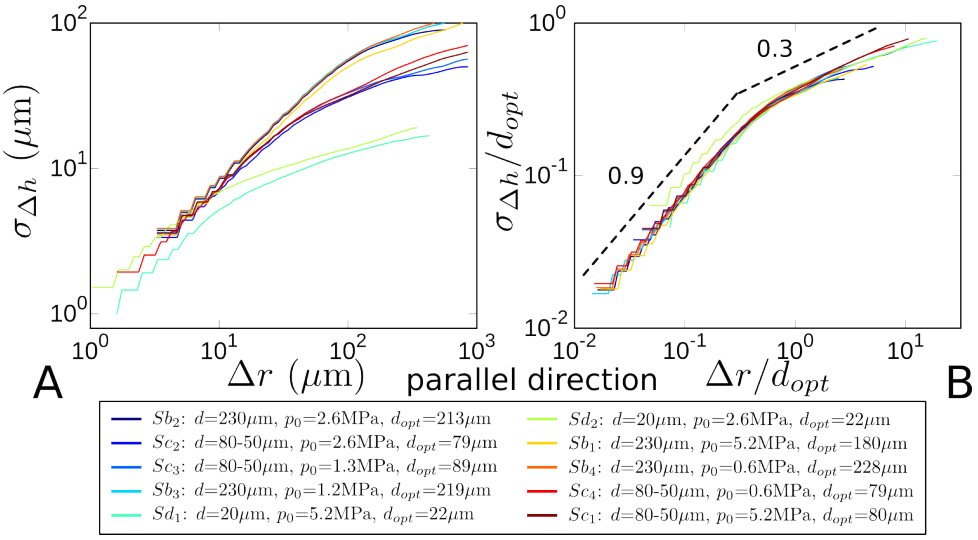

Figure 3.25: A: Height-height correlation function of profiles measured in the direction perpendicular to the direction of propagation of the crack. B: Height-heigh correlation function curves renormalized with the optimized bead size d_{opt}. All the axes are in logarithmic scale. The dashed line whose slope is a guide for the eyes.

Sample name	Bead size (μm)	Sintering pressure p_0 (MPa)
Sb_1	230	5.2
Sb_2	230	2.6
Sb_3	230	1.3
Sb_4	230	0.6
Sc_1	80-50	5.2
Sc_2	80-50	2.6
Sc_3	80-50	1.3
Sc_4	80-50	0.6
Sd_1	20	5.2
Sd_2	20	2.6

Table 3.4: This table lists samples used in the study of fracture surfaces. All these samples have been broken with a loading speed $V = 16$ m/s.

3.7 Conclusion

This chapter studies the evolution and statistical variations of the fracture mechanics observables. The goal is to link the statistical richness of the AE with apparent physical simplicity of the pinning-depinning model. First, we showed that there is just one independent quantity in this problem! This originates from the fact that the crack speed is directly proportional to the power radiated by the system when breaking. Hence, we have chosen to study the statistical variation of the system through the evolution of $\mathcal{P}(t)$. For a direct measurement of the statistical behavior of the system we performed a Fourier spectrum analysis and drown the probability density function of this unfiltered signal. Both studies reveal a power-law behavior expected theoretically. Then for a more complete statistical analysis of the radiated power signal, we extracted avalanches from the denoised signal via a classical threshold-based method. The statistics of these avalanches have been studied in terms of energy, size, duration and inter-event time via statistical earthquake analysis and pinning-depinning tools. Clustering in size, energy and time have been evidenced just like for AE. Nevertheless the power-law exponents are different which means the phenomenon are not physically identical. From this detection of breaking events, we also evidenced an asymmetry in time of the avalanche shape which is not predicted by any theoretical model. The measurement of the energy release rate linked to the fracture energy in steady state regime permitted to confirms that the toughness of the material increases with the crack speed and decreases with the bead size. Finally, a study of the fracture surface evidences that for small scales the roughness regime is closed

to the universal one classically observed and after a cross-over scaling linked to the bead size, a long scale regime appears with a lower roughness exponent.

Main messages of the chapter

◇ Crack tip velocity and radiated power are equivalent quantities.

◇ Power spectrum and probability density function of the radiated power obey a power-law.

◇ Fracture mechanic quantities follow seismic laws with different exponents than AE.

◇ $\mathcal{P}$ signal obeys the main pinning-depinning statistical scaling laws.

◇ Asymmetry in time of the average avalanche shape.

◇ Toughening effect with the increasing of the crack speed and with decreasing of the bead size.

◇ Different small and long scale regimes on the fracture surface roughness.

Part II

Numerical/Theoretical aspects

Introduction

In engineering and more often in physics, the problem of fracture is generally addressed in terms of stability and direction of propagation. This is due to the fact, that fracture is a multiscale problem and the subsequent matching of macroscopic loading and complex microscopic fracture mechanism is not trivial. Thus, its study is reduced to two simple questions treated with the LEFM [Griffith and Waltamn (1924); Lawn (1993)]:

- Will the crack propagate?
- Where will it go?

Hence, the crack's response is idealized as a deterministic response of the applied solicitations. This is an over simplification of the problem as emphasized in the introduction of this manuscript and as evidenced by the experimental part and for many other material [Garcimartin et al. (1997); Deschanel et al. (2006); Salminen et al. (2002); Santucci et al. (2004); Koivisto et al. (2007); Måløy and Schmittbuhl (2001)]. In some of these examples, crack propagation is far from being a continuous answer to the loading excitation: the breaking system responds to a slowly varying external loading trough jerky dynamics, with discrete pulses or avalanches spanning a variety of temporal and spatial length scales.

Thus, in the first part of this manuscript, loading a polymeric material in the wedge-splitting geometry at a constant rate reveals a jerky failure of the sample: the crack speed, or equivalently the radiated power of the system, varies with crackling dynamics (see figure 1.14-A). This kind of behavior occurs in many other systems including ferromagnets [Papanikolaou et al. (2011)], plastically deformed metals [Richeton et al. (2005)], fault seismicity [Rundle et al. (2003)], liquid spreading [Planet et al. (2009)], and fracturing solids [Bonamy (2009); Rosti et al. (2009)]. Each time, system observables unveil universal power-laws just like the ones evidenced experimentally in the first part of this manuscript. There are theoretical explanations to this universality: (i) proximity to an underlying critical point [Sethna et al. (2001)], and (ii) the self-organized criticality (SOC) [Bak et al. (1987, 1988)]. Nevertheless, fracturing homogeneous PMMA (see figure 1.14-B) reveals a smooth dynamic process like what is observed in [Scheibert et al. (2010); Guerra et al. (2012); Ponson (2009)]. Similarly, it seems that when the bead size decreases (or equivalently, when the crack speed increases) the crackling dynamics is less and less obvious. The objective in this part is to characterize both behaviors and identify the

physical parameters that control the failure dynamics: loading rate, geometry, material properties, microstructural texture...

Ferromagnetic systems invoking Barkhausen noise (BN) experience a similar transition [Travesset et al. (2002)]. Nevertheless, ferromagnetic systems focus on the transition from single isolated events to overlapping events without going through the disappearance of crackling dynamics [White and Dahmen (2003)]. Jerky dynamics are always observed! These systems only vary the driving rate. Herein, we would like to take this a step further and identify the ingredients necessary to observe SOC [Dickman et al. (2000)] characterized by crackling noise [Sethna et al. (2001)] in fracture problems.

Characterizing the transition between a continuously propagating crack front and a self-organized jerky one requires numerical systems which overlap both aspects. The pinning-depinning approach pioneered by [Gao and Rice (1989)] is the appropriate tool to reconciliate both fracture dynamics. Invoking LEFM principles at the local scale, this model succeeds in reproducing crackling dynamics at the macroscale [Bonamy et al. (2008)].

In the crackling regime, crackling pulses, evidenced by various methods, result from the depinning of avalanches. Single non-overlapping avalanches exhibit universal scale-free distributions. The scaling relations are characterized by a variety of critical exponents, which can be estimated using renormalization groups (RG) or numerical [Rosso and Krauth (2002); Duemmer and Krauth (2007)] methods. These scale-free features are widely reported for numerical calculations [Tanguy et al. (1998); Alava et al. (2006); Bonamy et al. (2008); Laurson et al. (2010)]. On the other hand, no clear link exists between (i) the cut-offs and prefactors of the power-laws characterizing these free-scale statistics and (ii) the tunable input parameters of the fracture experiments (namely: loading rate, system size, *etc.*). This part of my thesis will aim at resolving this inconsistency.

This numerical/theoretical part begins with a detailed reconstruction of the equation of motion of a crack front stably driven in a heterogeneous isotopic brittle material. Then, just two input parameters are evidenced to command the crackling or continuum-like dynamics of the system (see chapter 2). Finally, chapter 3 investigates the statistical failure as a function of the loading rate, the sample geometry, and the microstructure length scale.

Chapter 1

Brittle failure in heterogeneous solids: the pinning-depinning approach

Introduction

The experiments reported in part I of this manuscript show that crack growth in presence of microstructural disorder can exhibit crackling dynamics. This is incompatible with continuum fracture mechanics. This Chapter shows how to extend continuum fracture mechanics to *explicitly and in a self-consistent manner* account for the presence of microstructural disorder.

In this context, the approach taken herein was pioneered by [Gao and Rice (1989)] and later extended by [Schmittbuhl et al. (1995); Ramanathan et al. (1997); Charles et al. (2004); Vandembroucq et al. (2004); Ponson and Bonamy (2010)]. The idea is to map the crack's propagation to an elastic[xvii] manifold driven in a random potential. This chapter reveals that the elastic line model for crack growth can be rigorously derived within elasticity theory by considering a random field of fracture energy. The study herein is limited to the case of perfectly brittle linear elastic materials with weakly heterogeneous local properties, in the quasi-static limit.

Section 1.1 reveals the equation of motion for the elastic line. The resulting equation is

[xvii] The term "elastic" here is to be taken in its statistical physics meaning rather that within its continuum mechanics meaning. An elastic manifold is characterized by an energy cost per unit length/area/volume (depending on its dimension) which tends to smooth deform under the action of disorder.

parameterized by a variety of parameters that encode the material properties, microstructural texture, sample geometry and loading rate. All these parameters are expressed in term of experimentally measurable quantities. Dimensional analysis allows then reducing the number of independent parameters. The boundary conditions and sample specifications are finally given (section 1.2) to specify the numerical resolution.

1.1 Derivation of the equation of propagation

1.1.1 Ideal homogeneous brittle material: Conventional fracture mechanics

Since Griffith's pioneering works [Griffith (1920)] lead to a coherent theoretical framework (namely the linear elastic fracture mechanics, LEFM). LEFM describes the destabilization and further propagation of brittle cracks in homogeneous linear elastic media (see introductory chapter of the manuscript). Within LEFM framework, crack velocity, v, (if small enough) is proportional to the excess energy released locally:

$$\frac{1}{\mu} v = G - \Gamma, \tag{1.1}$$

Where G is the energy release rate, Γ is the fracture energy, and μ is the effective mobility of the crack front. To first order in v/c_R with c_r the Rayleigh wave speed, $\mu = c_R/\Gamma$.

As Γ is constant, equation 1.1 predicts that initially straight crack fronts are translated without deformation. Additionally, since G is a linear function of the external loading, equation 1.1 predicts regular dynamics for the front. Thus, LEFM cannot account for the crackling dynamics studied experimentally in part I. Nevertheless, the mechanical loading provides forces to the system at the macroscopic scale, yet dissipation processes (due to plasticity, cavitation, chemical reactions...) remain confined to a tiny zone at the crack tip (specifically the fracture process zone, FPZ). This separation in length scales, intrinsic to fracture mechanics, makes the failure properties observed at the continuum length scale extremely sensitive to the microstructural disorder of the material [Bonamy (2009)]. This macroscale sensitivity to microscale is the mechanism responsible for the large scale fluctuations and crackling observed in the crack dynamics. It is then necessary

to include explicitly material disorder in this equation.

1.1.2 Microstructural disorder and front distortion

The simplest way to capture the presence of material inhomogeneities at the microstructural scale is to introduce spatial fluctuations in the fracture energy. This will yields distortions in the crack front: The crack front will preferentially propagate along the zone of lower fracture energy. These crack front distortions will yield mixed mode loading (see introductory chapter of the manuscript for more details about this point) and limit the amount of prying forces at the crack tip. Herein the dynamics and path of cracks is a balance between these two.

Figure 1.1-A depicts how the problem is parameterized. The front is described by its in-plane ($f(z,t)$) and out-of-plane ($h(x = f(z,t), z)$) deviations. As a result, a point on the front is defined by its coordinates ($x = f(z,t), y = h(f,z), z$). Herein (as in part I), the coordinated system follows the standard frame of fracture mechanics:

- $\vec{e}_x$ parallel to the mean direction of crack propagation.
- $\vec{e}_y$ parallel to the mean direction of tension loading.
- $\vec{e}_z$ parallel to the mean direction of the crack front (along specimen thickness W).

Even in the presence of material inhomogeneities, a perfectly brittle material obeys equation 1.1 for the local speed at each point on the crack front. Hence, the complexity of the problem arrives in expressing G and Γ.

To capture the presence of material inhomogeneities, the fracture energy will now contain a spatially distributed component:

$$\Gamma(x,y,z) = \overline{\Gamma} + \gamma(x,y,z) \tag{1.2}$$

Where $\overline{\Gamma} = \langle \Gamma(x,y,z) \rangle_{x,y,z}$ (operator $\langle \bullet \rangle_{x,y,z}$ means averaging over space) is the mean value of fracture energy and γ is a random field. This random term is characterized by the probability density function ($p(\gamma)$) and the spatial correlation ($C(\vec{r}) = \langle \gamma(\vec{r_0} + \vec{r})\gamma(\vec{r_0}) \rangle_{r_0}$). Henceforth, several assumptions are made: (i) a Gaussian distribution p

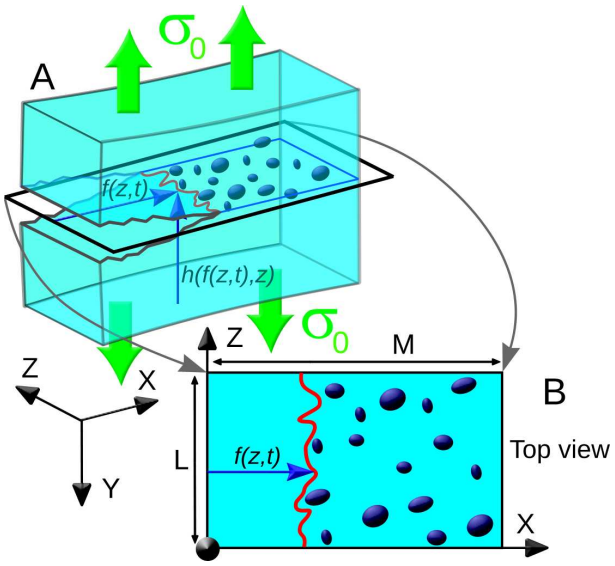

Figure 1.1: Schematic view of a perfectly brittle single crack growing in a heterogeneous material. A: 3D view of the crack. B: 2D projection on the mean crack plane.

with standard deviation $\tilde{\gamma}$; and (ii) an isotropic correlation function C which decreases linearly with $|r|$ over a distance ℓ beyond which $C = 0$. ℓ defines a correlation length for the disorder landscape. This simply means that, the fracture energy between two points of the specimen separated by a distance larger than ℓ are uncorrelated. (Note that according to [Vandembroucq et al. (2004)] scaling properties are expected to remain unaffected by changing the shapes of $p(\gamma)$ and $C(|r|)$). Thus, the microstructural disorder is fully characterized by $\tilde{\gamma}$ and ℓ. This simply means that fracture energy in two points of the specimen separated by a distance larger than ℓ are uncorrelated.

The second step is to relate G to frontal distortions $\{f\}$ and $\{g\}$. It turns out that to the first order, $G(z,t)$ depends on the in-plane component f only[xviii] [Ball and Larralde (1995); Movchan et al. (1998)]. This reduces the 3D problem (see figure 1.1-A) to the simpler 2D situation after a projection on the $(\vec{e}_x\vec{e}_z) - plane$ (see figure 1.1-B). In this 2D equivalent problem, the fracture energy depends on two space variables only: $\Gamma(x,y,z) \longrightarrow \Gamma(f(z,t),z)$. One can then use Rice's analysis [Rice (1985); Lazarus (2011)] to relate the local $G(z,t)$ to in-plane front distortions $f(z,t)$:

[xviii]The out-of-plane distortions h play on the mode II and mode III components which, in a tensile experiments, are of second order in G

$$G(z,t) = G_0(\overline{f}(t),t) + \frac{\overline{\Gamma}}{\pi} \times \int_{front} \frac{f(\zeta,t) - f(z,t)}{(\zeta - z)^2} d\zeta \tag{1.3}$$

Where the integral is defined in the principal value meaning. The quantity G_0 is the energy release rate for a straight crack at $\overline{f}(t) = \langle f(z,t) \rangle_z$ (where the operator $\langle \bullet \rangle_z$ means averaging over z coordinate only) everything else remains the same. $G_0(\overline{f}(t),t)$ here depends explicitly on the crack length and the time. This dependency translates the relations between energy release rate and both the specimen geometry (that evolves when the crack length changes) and external loading (that can evolve with time).

Substituting equations 1.2 and 1.3 in equation 1.1 results in an equation of motion for the crack front as follows:

$$\frac{1}{\mu} \frac{\partial f(z,t)}{\partial t} = G_0(\overline{f}(t),t) - \overline{\Gamma} + \frac{\overline{\Gamma}}{\pi} \times \int_{front} \frac{f(\zeta,t) - f(z,t)}{(\zeta - z)^2} d\zeta - \gamma(f(z,t),z) \tag{1.4}$$

This gives the general equation for a crack in an infinite material with sufficiently weak heterogeneities. Futhermore, Rice's formula (equation 1.3), derived for a slightly perturbed crack, remains valid for the effect of a larger perturbation (for more details see [Adda-Bedia et al. (2006)]). This approach is expected to be valid as long as (i) the slope $\partial f/\partial z \ll 1$; and (ii) $\partial f/\partial t \ll c_R$. In particular, f does not need to be small with respect to a characteristic geometrical dimension.

Variants of equation 1.4 with a constant force $F = G_0(\overline{f}(t),t) - \overline{\Gamma}$ have been extensively studied in the past to model crack propagation in solids [Schmittbuhl et al. (1995); Ramanathan et al. (1997)]. They are also used to describe other diverse systems such as interfaces in disordered magnets [Bertotti et al. (1994); Durin and Zapperi (2000)] or contact lines of liquid menisci on rough substrates [Ertas and Kardar (1994); Rolley et al. (1998)]. A key feature for the crack front is the depinning transition. In other words, the crack front remains stationary (*i.e.* pinned by the heterogeneities) for F less than a well-defined threshold value F_p, and it starts to move with a finite speed when $F > F_p$. This depinning transition at F_p [Ertas and Kardar (1994)] belongs to the critical phenomena realm. This realm is characterized by universal scale-invariant features and scaling laws. In particular, at F_p, the interface moves through scale-free avalanches reminiscent of the

crackling dynamics observed in the part I.

1.1.3 Stable growth, external forcing and resulting equation of motion

To go further into the analysis, the equation of motion requires more continuum mechanics and the driving force $F = G_0(\overline{f}(t), t) - \overline{\Gamma}$ needs to be modelled more accurately. For stable crack growth conditions, the crack is loaded by imposing an external displacement that grows with time t. For sake of simplicity, the displacement rate is assumed to be a constant henceforth (as *e.g.* for the experiments discussed in part I of this manuscript). In parallel, the prying force is expected to decrease with crack length, $\overline{f}$, since the specimen stiffness decreases with $\overline{f}$. Without loss of generality, we consider the crack immobile at $t = 0$ and the x-axis origin is at the crack tip ($\overline{f}(t = 0) = 0$). Then one gets: $G(\overline{f} = 0, t = 0) = \overline{\Gamma}$. Considering the subsequent variations of f small enough with respect to the initial crack length, one can write:

$$F(\overline{f}, t) = \dot{G}_0 \cdot t - G'_0 \cdot \overline{f} \tag{1.5}$$

Where $\dot{G}_0 = \partial G/\partial t$ (driving rate) and $G'_0 = -\partial G/\partial \overline{f}$ (unloading factor) are positive constants set by the imposed displacement rate and the specimen/loading geometry, respectively.

As a result, the driving force of the crack is an effective quadratic potential. Moreover, it moves at the velocity $v_m = G'_0/\dot{G}_0$. After a short transient regime, the velocity of the mean crack position is also v_m. Gathering equations 1.5 and 1.4 via relation $F = G_0(\overline{f}(t), t) - \overline{\Gamma}$, one gets:

$$\frac{1}{\mu}\frac{\partial f(z,t)}{\partial t} = \dot{G}_0 \cdot t - G'_0 \cdot \overline{f} + \frac{\overline{\Gamma}}{\pi} \times \int_{front} \frac{f(\zeta,t) - f(z,t)}{(\zeta - z)^2} d\zeta - \gamma(f(z,t), z) \tag{1.6}$$

This equation describes the motion of a brittle crack slowly driven in a brittle heterogeneous material. As first established in [Bonamy et al. (2008)], this equation predicts crackling dynamics for $\dot{G}_0 \to 0$ and $G'_0 \to 0$. Section 1.2 presents the precise conditions

yielding crackling.

1.2 Numerical aspects

Equation 1.6 requires numerical schemes to be solved. According to equation 1.6 seven parameters select the crack front dynamics: μ, $\overline{\Gamma}$, $\dot{G}_0$, G'_0, $\tilde{\gamma}$, ℓ and the system size W (specimen thickness along z axis as shown in figure 1.1). Yet, the spatial distribution of inhomogeneities require only two parameters: The disorder contrast $\tilde{\gamma}$ and the disorder length scale ℓ [Vandembroucq et al. (2004)]. The introduction of dimensionless time ($t \rightarrow t/(\ell/\mu\overline{\Gamma})$) and length ($\{x, z, f\} \rightarrow \{x/\ell, z/\ell, f/\ell\}$) reduces the number of independent parameters. One gets:

$$\frac{\partial f}{\partial t} = ct - k\overline{f} + \frac{1}{\pi} \times \int_{front} \frac{f(\zeta,t) - f(z,t)}{(\zeta - z)^2} d\zeta + \eta(z, x = f(z,t)) \tag{1.7}$$

Where $c = \dot{G}_0\ell/\mu\overline{\Gamma}^2$ is the dimensionless driving rate, $k = G'_0\ell/\overline{\Gamma}$ is the dimensionless unloading factor, and η is the Gaussian random term with standard deviation $\sigma = \tilde{\gamma}/\overline{\Gamma}$ and an unit spatial correlation length. As a result, 4 independent parameters define the front dynamics: c, k, σ, and the scale ratio $N = W/\ell$.

Subsequent chapters will explore, the front dynamics described by equation 1.7 and its variations with respect to $\{c, k, \sigma, N\}$. Each set of parameters has an associated $N \times p \cdot N$ random Gaussian map $\eta(z, x)$, with zero average and σ variance. At time $t = 0$, the crack front position is a straight line located at $x = 0$: $f(z, t = 0) = 0\ \forall z \in [0, N]$. The space-time evolution of $f(z, t)$ is then solved using a fourth order Runge-Kutta scheme. Periodic boundary conditions are chosen along z: $f(z = 0, t) = f(z = N, t)\ \forall t \in \mathbb{R}$. This speeds up the computation time as the integral term in equation 1.7 can be solved in the Fourier domain.

Herein, c ranges from 10^{-6} to 10^{-4}. The minimum value maintains a reasonable computation time (less than 40 days on a 2 GHz CPU). Its maximal value keeps a sufficient scale separation between the depinned front velocity and the loading rate. The other parameters k, σ, and N were respectively varied from 10^{-8} to 1, 10^{-1} to 4, and 32 to 2048. This permits a wide exploration of phase diagram.

1.3 Conclusion

In this chapter (following pioneer works [Gao and Rice (1989); Schmittbuhl et al. (1995); Ramanathan et al. (1997); Bonamy et al. (2008)]), we developed the equation of motion for a line propagating in a random potential. This line propagation model maps to the first order a crack front's propagation when driven in a heterogeneous material. The inputs of the problem reduce to 4 independent parameters. Moreover, these parameters are computed from mechanical measurements. This model reproduces crackling dynamics observed in the experimental part of this manuscript. Moreover, it provides access to the local propagation of the front which is unavailable via current experimental techniques. This access gives way to more accurate statistical analysis.

These numerical tools are wildly explored in the following chapters. Chapter 2 uses them to characterize when crackling dynamics are observed and when continuous propagation is observed. Then, a more specific analysis examining the variation of the statistical answer in crackling regime *vs.* the input parameters is studied.

Finally, it is worth mentioning that equations similar to the equation of motion of a crack (1.7) are involved in many physical situations where elastic systems are embedded in a material containing random impurities, such as vortex lines, magnetic domain walls, or charge density waves. As a result, this kind of equations has been largely studied both from a numerical point of view [Rosso and Krauth (2002); Duemmer and Krauth (2007)] and using an approximated analytical approach based on renormalization group theory [Ertas and Kardar (1994); Chauve et al. (2001)]. Hence, subsequent results can be applied to different physical view points and lead to different interpretations.

Main messages of the chapter

◇ An equation of motion for a crack front slowly driven within a random heterogeneous brittle material.

◇ Just 4 independent parameters are required to describe the inputs of the problem.

Chapter 2

Brittle failure: Continuum-like or crackling?

Introduction

Chapter 1 presents how to derive a description for brittle crack growth taking into account explicitly the microstructural disorder. In this framework, the crack front is modeled with a long-range elastic spring [Gao and Rice (1989); Schmittbuhl et al. (1995); Ramanathan et al. (1997)] propagating in a 2D random potential. The onset for crack destabilization can be mapped to a depinnning transition [Ertas and Kardar (1994); Roux et al. (2003); Ponson (2009); Bonamy (2009)]. Stable crack geometries yield a self-adjustment in the driving force around its depinning value [Bonamy et al. (2008)]. Under some conditions, this can exhibit crackling dynamics similar to experimental results observed in part I herein and reported in some interfacial experiments [Måløy et al. (2006); Bonamy et al. (2008)]. Still, many situations involving a variety of disordered brittle solids (structural glasses, brittle polymers, ceramics, *etc.*) with stable crack growth do not exhibit crackling. Rather they experience continuous dynamics compatible with LEFM predictions (see *e.g.* the velocity profiles presented in chapter 1 for homogeneous PMMA broken using our experimental device).

Here, we broach the question of the when, where and why crackling versus continuum-like dynamics are observed in heterogeneous brittle failure. In this context, we solve the elastic line model given by equation 1.7, and looked at the dynamics selected as a function of its parameters $\{c, k, \sigma, N\}$. One will see that either continuum-like or crackling

dynamics are observed. A transition line is found to separate the two regimes and defines a phase diagram within a space defined by two reduced variables.

2.1 Different types of fracture dynamics

To begin, when simulating crack propagation with the equation of motion 1.6 (in all cases), the front is pinned until the external loading reaches a critical force F_p called depinning force. Then, two kinds of behavior can be observed while the front goes through the $N \times p \cdot N$ random map looking at the mean speed signal $\overline{v}(t) = \langle v(z,t) \rangle_z$. In the first case, it keeps going without stopping: after a transient regime, the $\overline{v}(t)$ signal fluctuates over the mean value c/k expected from LEFM (*i.e.* with $\eta = \gamma \equiv 0$), without going back to 0. This case is shown in figure 2.1-A_1, for a low value of k. In the second case (after a very short transient regime), the mean signal of the speeds becomes very jerky and exhibits crackling dynamics with distinct pulses separated by silent periods where the whole front is trapped in a pinning position. This regime characterized by avalanche dynamics and universal scale-free behaviors was observed by [Ertas and Kardar (1994); Bonamy (2009); Ponson and Bonamy (2010)]. Such a $\overline{v}(t)$ signal is shown in figure 2.1-A_3 for a high k value. The signal presented in figure 2.1-A_2 is a transitional regime between both regimes.

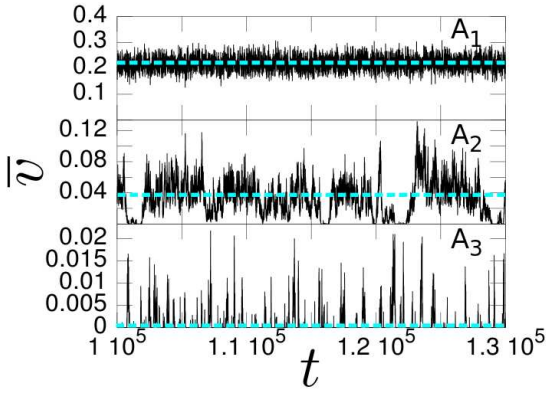

Figure 2.1: Qualitative transition from crackling to LEFM-like dynamic regime seen from the point of view of the mean speed $\overline{v}(t)$. Several mean speed curves for different k values are presented: A_1: in the LEFM-like regime – A_3: in the crackling regime – A_2: the transition between both.

The signal $\overline{v}(t)$ is the one accessible (and of interest) in experiment. Still the qualitative characterization of both LEFM-like and crackling regimes can also be seen at the local

scale from the crack front position frozen at different time. For LEFM-like dynamics, two fronts are perfectly distinct (*i.e.* independent of the time interval between the 2 fronts) as presented in figure 2.2-A. On the contrary, in the crackling regime, it is possible to find a time interval between two frozen fronts such that the fronts are partially or totally overlapping. In this last case, presented in figure 2.2-B, the area swept by the non-overlapping part of the curve represents a breaking event also called an avalanche. It is also worth mentioning that even if those figures (2.2) are reminiscent to the pinning-depinning transition [Roux et al. (2003)], this case is not valid since the mechanical loading is not the same: the front is driven in stable conditions, the loading force (see equation 1.5) varies around F_p.

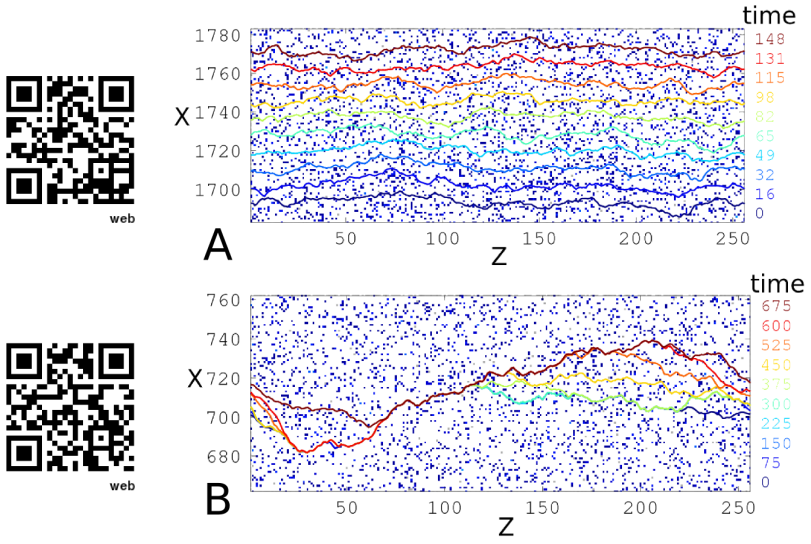

Figure 2.2: A: Crack front frozen at different times on the random map in the LEFM-like regime and movie of the evolution. B: Crack front frozen at different times on the random map in the crackling regime and movie of the evolution. Scan the flash-code for movies depicting the different senarii or go to the Youtube sites for the movies: LEFM-like regime http://youtu.be/Fut-JKJYCUs and crackling regime http://youtu.be/v8NdKVgyW7I.

Finally to merge both local and global points of view, figure 2.3 in the continuum and crackling regimes presents the evolution of local front speed in space (z-coordinate) as well as its mean value over a short time. For LEFM-like dynamics, the speed vanishes for any point of the front at any time. On the contrary for crackling dynamics, the crack speed is nearly zero everywhere with the exception of several small places for short durations, the avalanches or pulses. Thus classifying these two regimes gives way to detecting the transitions between them:

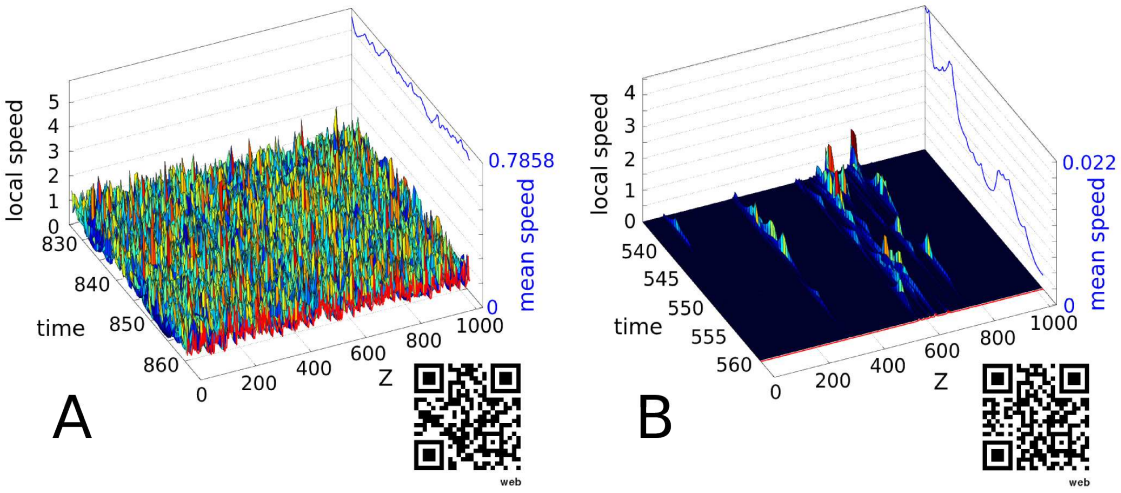

Figure 2.3: A: Evolution of the local and global speed in LEFM-like regime: http://youtu.be/RWhLu4-8Wbo B: Evolution of the local and global speeds in crackling regime: http://youtu.be/V4JJtZYcnSw.

- The transition from a global point of view: "the mean crack speed never vanishes" $(\forall t \rightarrow \overline{v}(t) > 0)$ *vs.* "the mean crack speed sometimes vanishes" $(\forall t_0, \exists t > t_0 \rightarrow \overline{v}(t) = 0)$

- The transition from a local point of view: "none of the front points are pinned" $(\forall t, \forall z \rightarrow v(z,t) > 0)$ *vs.* "at some instances in time, one or more crack front points are pinned" $(\forall t_0, \exists t > t_0, \exists z \rightarrow v(z,t) = 0)$.

Invoking these rules, the transitions are tested for different loading conditions herein and by [White and Dahmen (2003)].

Strictly speaking the transitions are not exactly the same. Defining the transition from crackling to LEFM-like regime as the moment when avalanches begin to overlap one each other gives two different scenarii. The first transition constitutes an overlapping in time only. The second is an overlapping both in time and space of the avalanches. Nevertheless, the study of the differences between these transitions is beyond the scope of this thesis project. Hence, this study will focus on the first transition. On a side note, work is currently underway to map these transitions with a percolation transition problem.

Next it is important to discriminate in a quantitative way the transition between both regimes (*i.e.* crackling and LEFM-like) and build a phase diagram. The phase diagram

should distinguishes each point via the 4 parameters (see section 1.2). The quantitative criterions originate from the definitions above. Figure 2.4 depicts the minimum value $\overline{v}_{min}$ of mean crack speed after the transient regime as a function of k for 15 simulations for c, σ and N. A sharp variation in this curve occurs at k_c, *i.e.* a critical value of the unloading factor. As presented in figure 2.1-A_1, LEFM-like regime comes about when $k < k_c$. In this region $\overline{v}_{min} > 0$, thus the mean crack speed never vanishes. For $k > k_c$, the crackling regime transpires (see figure 2.1-A_3). Hence $\overline{v}_{min} = 0$, and the mean crack speed always goes back to zero. Using $\overline{v}_{min}(c, k, \sigma, N)$ is a convenient and quantitative way to know in which regime the propagation takes place.

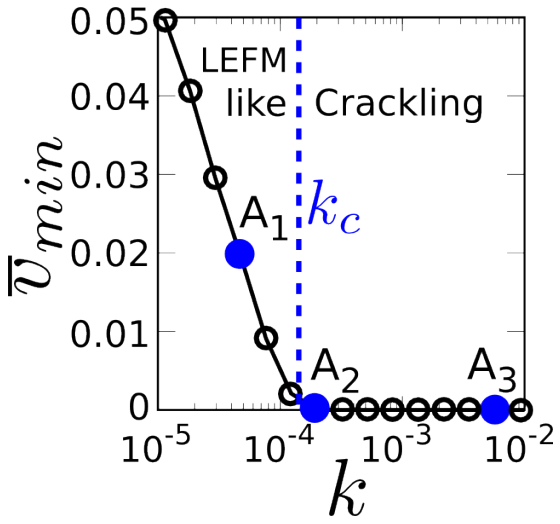

Figure 2.4: Evolution of the minimum mean speed when k increases and evidences of the transition. The points A_1, A_2 and A_3 correspond to the mean speed signal presented in figure 2.1.

2.2 Identification of the phase diagram for the dynamic

Now invoking the $\overline{v}_{min}$ measurement, one can define the crackling/continuum-like regimes in the $\{c, k, \sigma, N\}$ space diagram. In this context, $\{\sigma, N\}$ remains constant, and the transition value for the unloading factor k_c as a function of the loading rate c is calculated. For each series of parameters, several simulations were performed with independent random disorder maps $\eta(z, x)$ (from $\sim$ 40 simulations for $N = 64$ to $\sim$ 3 simulations for $N = 1024$). Averaging over these simulations gives the transition value k_c, and the error bars correspond to a 95% confident interval (figure 2.5).

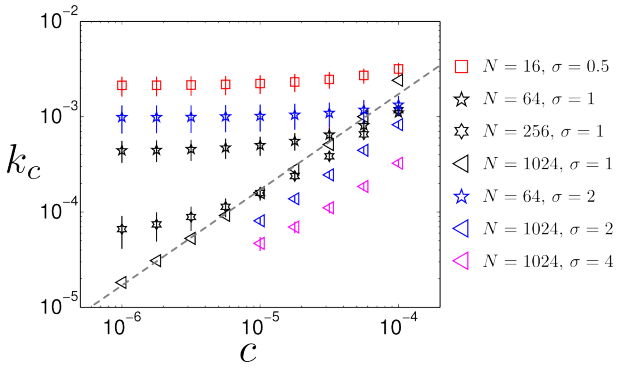

Figure 2.5: Depicts how k_c varies with c for different input values of $\{\sigma, N\}$. The dashed grey line with slope 1 is given to guide the eye. Axes are in logarithmic scale.

Figure 2.5 shows different $k_c vs. c$ curves obtained for different sets of $\{\sigma, N\}$. For the larger N ($N = 1024$), k_c is roughly proportional to c, with a prefactor A that depends on N and σ. For smaller N, the curves can be decomposed into two pieces: A plateau $k_{c\ Sat}$ for small c and a $k_c \propto c$ for large c.

As the crack propagates throughout the disordered landscape, the profile $\eta^{eff}(x)$ (*i.e.* effective pinning force) gives clues to the form of the k_c *vs.* c:

$$\eta^{eff}(x) = \left\langle \int_{front} \frac{f(\zeta,t) - f(z,t)}{(\zeta - z)^2} d\zeta + \eta(z, x = f(z,t)) \right\rangle_z \tag{2.1}$$

Figure 2.6 depicts a typical profile. The value k_{csat} observed for $c \to 0$ is set by the relative positions of the maximum ($S_1 = \{x_1, \eta_1\}$) and the next-to-maximum ($S_2 = \{x_2, \eta_2\}$) peaks over the travelled distance ($k_{c\ Sat} = (\eta_1 - \eta_2)/(x_2 - x_1)$). Indeed, if k is less than k_c, the front (once depinned from S_1) will continue to propagate with a driving force always larger than $\eta^{eff}(x)$. On the contrary, if k is greater than k_c, the front (once depinned from S_1) will (at least) be pinned again by the S_2 peak and the velocity $\overline{v}(t)$ will vanish for at least one point. The linear variation of $\{\eta^{eff}\}$ with σ yields $k_{csat} \propto \sigma$.

For finite c, the front earns an extra driving force during its depinning jump (duration τ_{12}) from S_1 to S_2 yielding $k_c = k_{c\ Sat} + Ac$ with $A = \tau_{12}/(x_2 - x_1)$. Thus, one expects $k_c \approx k_{c\ Sat}$ for $c \ll k_{c\ Sat}/A$ and $k_c \approx Ac$ for $c \gg k_{c\ Sat}/A$. In this scenario, the jerky dynamics observed for $c \ll k_{c\ Sat}/A$ are dominated by a single large avalanche (from S_1 to S_2). Truly steady self-sustained crackling dynamics transpire for only $c \gg k_{c\ Sat}/A$.

The simple argument above demonstrates that $k_{c\ Sat}$ is directly proportional to σ. One

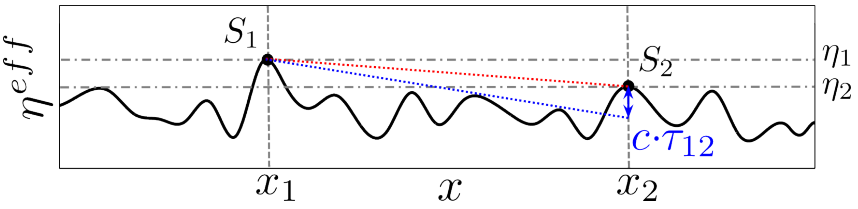

Figure 2.6: Sketch of the variation of the effective pinning force applying on the front as it quasistatically propagates throughout the disordered landscape (see *e.g.* [Tanguy et al. (1998)] for implementation of such a propagation algorithm). Points $S_1 = \{x_1, \eta_1\}$ and $S_2 = \{x_2, \eta_2\}$ locate the maximum and subsequent next-to-maximum peaks over the travelling distance.

now has to infer its variations with N. In this context, figure 2.7 plots $k_{c\ Sat}/\sigma$ *vs.* N for different value of σ. It turns out that this obeys a power law with exponent $\alpha_3 = 1.65 \pm 0.05$. Hence, $k_{c\ Sat} \sim \sigma N^{-\alpha_3}$.

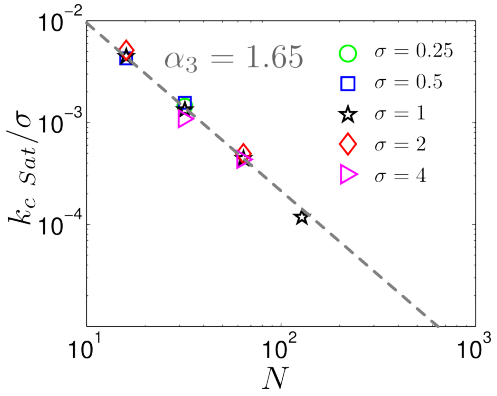

Figure 2.7: Value of the plateau of figure 2.5 $k_{c\ Sat}$ as a function of the system size N for different heterogeneity amplitudes σ. Exponent $\alpha_3 = 1.65 \pm 0.05$ is fitted on this curve and given with the grey dashed line. Axes are in log-log scale.

The final step is to unravel the dependencies of the proportionality constant A with respect to σ and N. The raw plot presented in figure 2.8-A shows that A decreases with both σ and N. To quantify the scaling,the exponent α_2 yields a good collapse of the curves A/N *vs.* σ (see figure 2.8-B). This later is obtained for $\alpha_2 = 0.38 \pm 0.05$, and the resulting curve is found to decrease as $\sigma^{-\alpha_1}$ with a fitted value $\alpha_1 = 1.15 \pm 0.05$.

In summary, the various k_c *vs.* c curves presented in figure 2.5 reduce to 2 regions:

- A c-independent plateau $k_{c\ Sat}$ for small c, small N, and large σ.
- A linear increasing k_c with c (slope A) for large c, large N, and small σ.

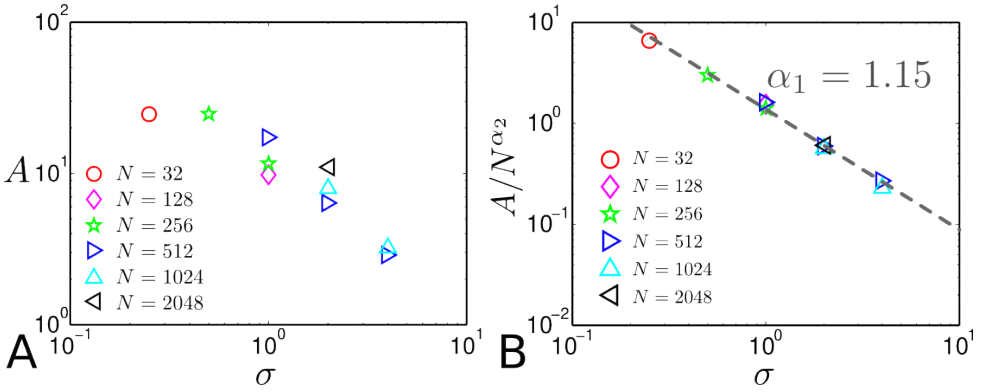

Figure 2.8: A: Proportionality constant A for the regime $c \gg 1$ of figure 2.5, as a function of σ for different values of N. B: Collapse obtained by making $A \to A/N^{\alpha_2}$ with $\alpha_2 = 0.38$. The grey dashed line indicates a power-law of exponent $\alpha_1 = 1.15$. The axes are logarithmic.

Then by making the following variable changes $k_c \to k_c^* = k_c/k_{c\ Sat}$ and $c \to c^* = A \cdot c/k_{c\ Sat}$, all curves collapse. Both A and $k_{c\ Sat}$ go as a power-law with N and σ: $A \approx \sigma^{-\alpha_1} N^{\alpha_2}$ with $\alpha_1 = 1.15 \pm 0.05$ and $\alpha_2 = 0.38 \pm 0.05$, and $k_{c\ Sat} \approx \sigma \cdot N^{-\alpha_3}$ with $\alpha_3 = 1.65 \pm 0.05$. These relations collapse all curves on a single master curve, plotted in figure 2.9:

$$k_c^* = f(c^*) \quad \text{with} \quad f(c^*) \approx \begin{cases} k_{c\,sat}^* & \text{if } c^* \ll k_{c\,sat}^* \\ c^* & \text{if } c^* \gg k_{c\,sat}^* \end{cases} \tag{2.2}$$

by making $c^* = /c \times N^{\alpha_2+\alpha_3}/\sigma^{1+\alpha_1}$ and $k_c^* = k_c \times N^{\alpha_3}/\sigma$. The plateau value $k_{c\,sat}^*$ decreases with p. This curve separates LEFM-like and crackling dynamics.

Recall that the jerky dynamics observed for $c \ll k_{c\ Sat}/A$ is dominated by a single large avalanche (mainly driven by the positions of the maximum and next-to-maximum peaks in the $\eta^{eff}(x)$ profiles, see figure 2.6), while a true steady self-sustained crackling dynamics can only be observed for $c \gg k_{c\ Sat}/A$.

Figure 2.9 and equation 2.2 reveal that large disorder (contrast $\tilde{\gamma}$ or length-scale ℓ), large unloading factor G_0', small specimen size L and small driving rate $\dot{G}_0$ yield crackling dynamics, and the opposite yields a LEFM-like dynamics. These tendencies can now be discussed. A continuum description is naturally expected to be relevant as disorder is weak. Also, a larger specimen size with respect to disorder scale allows coarse-graining; hence, a continuum description for large sample is more relevant than for small specimen

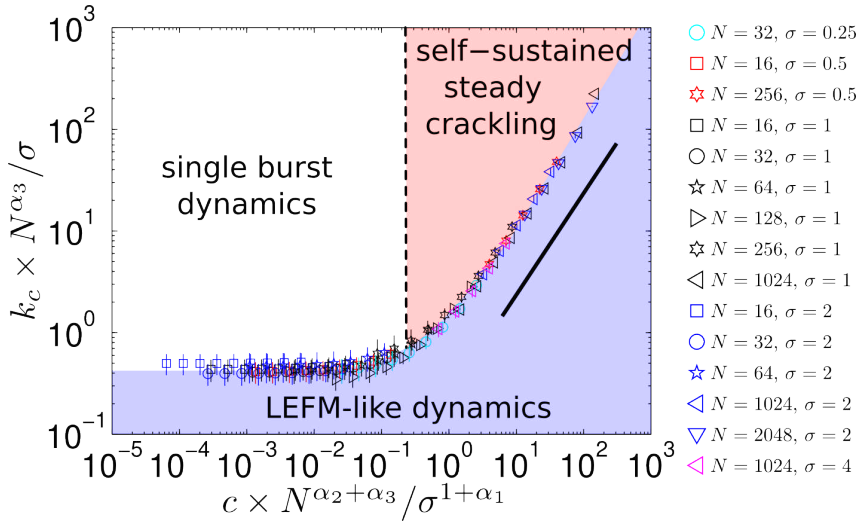

Figure 2.9: Main image depicts the phase diagram of the crack dynamics. Inset: variation of k_c as a function of c for different N and σ. Each point results from averaging over many simulations and errorbars correspond to a 95% confidence interval. Main panel: Collapse obtained with $\alpha_1 = 1.15$, $\alpha_2 = 0.38$ and $\alpha_3 = 1.65$. Straight line indicates proportionality.

sizes. A small unloading factor yields larger avalanches and a large driving rate decreases the silent time between two avalanche nucleation. These two effects favor avalanche overlapping and favor continuum dynamics by averaging the avalanches. The phase diagram unraveled here is compatible with this intuition. It allows its rationalization. This can inform technological relevant fracture processes, *e.g.* implementation in future rationalized design methodologies to prevent (or to limit) inopportune crackling (and induced indetermination) in cutting-edge technologies like nano-technologies where the relative microstructural size is very high.

Finally to link this theoretical study to experiments presented in the previous part, one can check, at least qualitatively, that when the loading speed of the system increases (sample Sa_3: $d = 500$ μm, $V = 1600$ nm·s^{-1}, no porosity) or similarly when the bead size decreases (sample Sd_1: $d = 20$ μm, $V = 16$ nm·s^{-1}, no porosity), the crack dynamics pass from crackling to LEFM-like.

2.3 Nature of separation line between continuum and crackling regime: Simple crossover or true transition?

Finally, this chapter concludes with a study on how the dynamics change as the crack goes from the LEFM-like regime to the crackling one. Hence, the keys to unlock this are in the evolution of the signal $\overline{v}(t)$ within the steady regimes as it progresses from the first regime to the second one. One way to characterize its fluctuations is to compute its power spectrum (PS). Such an analysis has two advantages with respect to the standard statistical analysis (see following chapter and part I of the manuscript for further discussion) of pulse size and duration developed to analyze crackling signals [Travesset et al. (2002)]: (i) It allows a full exploration of the phase diagram (both crackling and LEFM-like); (ii) in the crackling part, it does not call for any additional criteria (threshold setting) to filter single pulses in presence of overlapping avalanches.

Figure 2.10 presents the evolution of $PS_{\overline{v}}(\nu)$ for increasing k and constant other parameters. Below k_c, all curves overlap except at the lowest frequencies. This is precisely what is requested in a classical mechanics description (*i.e.* the continuum-level scale controls the parameter k and should affect the system at large scales only). Conversely, above k_c, the PS curves are clearly distinct, showing that *all* scales are affected by k. One points out that power-law behavior is characteristic of a crackling dynamics [Kuntz and Sethna (2000); Travesset et al. (2002); Durin and Zapperi (2005)]. The power-law exponent $1/a$ is independent of k, whereas the prefactor decreases with k (see section 3.1 for further analysis). The dramatic change observed as k crosses k_c is a signature that the LEFM-crackling transition line is a true transition and not simply a crossover phenomenon.

The precise nature of this transition has not been uncovered. On-going work with Alberto Rosso[xix] and Alexander Dobrinevski[xx] aims at filling this gap. The idea is to look at the space-time distribution of the avalanches during the propagation. In such a space-time diagram, the unloading factor k controls the typical size of avalanches: the larger is k, the smaller are the avalanches. On the other hand, the driving rate c plays

[xix] Laboratoire Physique Theorique et Modeles Statistiques (LPTMS), University of Paris Sud in Orsay, France

[xx] Laboratoire de Physique Théorique (LPT), École Normale Supérieure in Paris, France

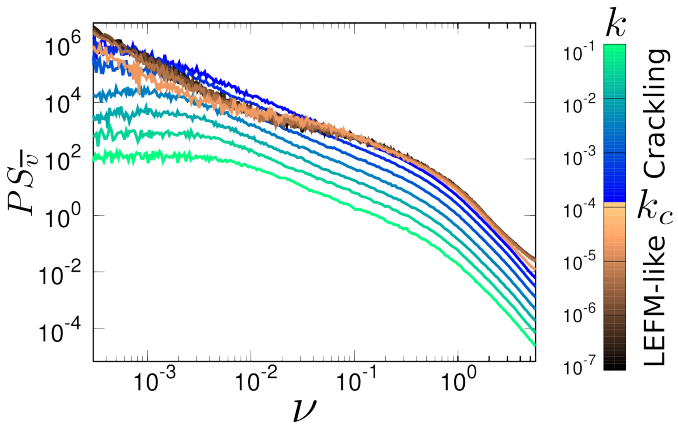

Figure 2.10: Qualitative transition from crackling to LEFM-like dynamic regime seen from the point of view of the mean speed Fourier spectrum.

on the density of avalanches: the larger is c, the smaller is the time distance between two neighbouring avalanches. Hence, one expects interplay between c and k to control the overlap between avalanches and, for some conditions, an infinite avalanche percolates throughout the space-time diagram. In this scenario, the LEFM-like cracking transition may be mapped to a percolation driven problem. This may lead to a way to explain the values of the critical exponents α_i at play in setting the phase diagram (figure 2.9).

2.4 Conclusion

In this chapter, we used statistical models developed in chapter 1 to see how a brittle crack selects its propagation dynamics in presence of microstructural disorder. Two different regimes are evidenced: LEFM-like and crackling dynamics. Large disorder (contrast or length-scale), large unloading factor, small specimen size and small driving rate favor crackling while the opposite favor continuum-like dynamics. A detailed parametric study of the equation of motion (equation 1.7 in chapter 1) gives way to rationalize the phase diagram. This latter is found to be fully controlled by two reduced variables (see figure 2.9). The separation line between LEFM-like and crackling regimes is a true transition, not a simple crossover. Indeed, the dynamics dramatically change as the system crosses the separation line.

This result sheds light on experimental conditions required to observe crackling in brittle fracture. As such, it can inform technological relevant fracture processes, *e.g.* in the future development of rationalized design methodologies to prevent (or to limit) inopportune crackling (and induced indetermination) in cutting-edge technologies. Beyond solid failure, this analysis directly extends to a number of others systems described by the same long-range string model, such as contact line dynamics in wetting problems [Ertas and Kardar (1994)] and domain walls dynamics in ferromagnets [Durin and Zapperi (2000)] (field sweep rate and demagnetization factor then playing the role of c and k). As such, it may be relevant in other fields that face similar problematic, *e.g.* nanofluidic or nanomagnetism technologies.

In the next chapter, we will focus on the dynamics in the crackling regime, and see how they depend on the parameter series $\{c, k, \sigma, N\}$.

Main messages of the chapter

◇ A physical transition is uncovered between the regimes where the crack propagates with free-scale statistic and a regime where it growth continuously.

◇ A two dimensionless parameters phase diagram to control if the crack growth in LEFM-like or crakling regime.

◇ The phase diagram is in accordance with experimental results.

Chapter 3

Dynamic selection in the crackling phase

Introduction

Chapter 2 revealed that an elastic line approach derived from LEFM can reproduce crackling dynamics under certain parametrical conditions. This section characterizes the crackling dynamics. Publications over the last twenty years contain a multitude of theoretical and numerical works [Tanguy et al. (1998); Durin and Zapperi (2000); Rosso et al. (2009)] [Papanikolaou et al. (2011); Dobrinevski et al. (2012)]. Avalanching dynamics are extracted from space-space activity maps [Måløy et al. (2006); Bonamy et al. (2008); Laurson et al. (2010)], space-time activity maps [Tanguy et al. (1998)], bursts exhibited by spatially-averaged front velocity filtered out via threshold based methods [Leblanc et al. (2013)], or directly studied from the Fourier spectrum of this spatially averaged velocity [Lopez et al. (2010); Travesset et al. (2002)].

Analyses herein unravel universal scale-free statistics of avalanches and determine the associated exponents. Nevertheless, few of them deal with the relations between the non-universal parameters of these scaling laws (cut-offs, prefactors,*etc.*) and the non-universal parameters at play in the equation of motion. Furthermore, most of them focused on the adiabatic limit, *i.e.* a vanishing driving rate ($c \to 0$ in equation 1.7). Herein we examine the effects of these input parameters (c, k, N and σ in equation 1.7) on the exponents, prefactors and cut-offs associated to the crackling statistics. Moreover, since the computation and the comparison of the exponents can lead to inaccurate conclusion

[Clauset et al. (2007)], as emphasized by [Papanikolaou et al. (2011)], for the statistical study of each dynamical observable, we focus on the scaling phenomena.

This chapter details each way to extract the statistical information from jerky dynamics of fracture simulations in the crackling steady state regime. Then for each observable (avalanche duration, surface, *etc.*), we analyze how the statistical distribution (exponents, prefactors and cut-offs) varies as a function of the input parameters of the system.

Simulations herein concern thirty independent numerical simulations with varying parameters sets c, k, N and σ (see position in the phase diagram in figure 3.1). Each simulation lasted 30 days on a 2 GHz CPU ($\sim 10^7$ time steps). Special attention is given to vary the parameters one-by-one (see table 3.1 and figure 3.1).

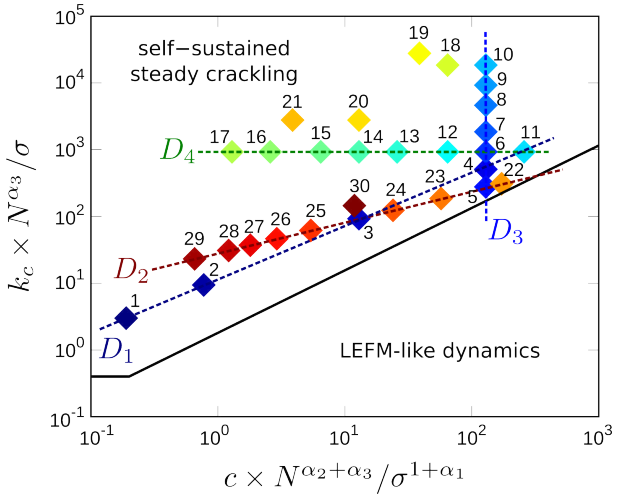

Figure 3.1: Location of the simulations in the phase diagram evidenced in the previous chapter (figure 2.9). The parameters of the simulations correspond with the ones given in table 3.1. The straight lines correspond to 1D cuts obtained by varying one parameter only, while keeping the others constant: D_1 (N varies), D_2 (σ varies), D_3 (k varies), D_4 (c varies).

3.1 Fourier spectrum

3.1.1 Signal analysis

Recalling section 3.2 for experimental signals, a good way to obtain global statistical information of a signal invariant with respect to time translation is to compute its power

Simulation number $\mathcal{N}$	c	k	σ	N
1	10^{-5}	10^{-3}	1	128
2	10^{-5}	10^{-3}	1	256
3	10^{-5}	10^{-3}	1	1024
4	10^{-4}	$5.5 \cdot 10^{-3}$	1	1024
5	10^{-4}	$3 \cdot 10^{-3}$	1	1024
6	10^{-4}	$1 \cdot 10^{-2}$	1	1024
7	10^{-4}	$2 \cdot 10^{-2}$	1	1024
8	10^{-4}	$5 \cdot 10^{-2}$	1	1024
9	10^{-4}	$1 \cdot 10^{-1}$	1	1024
10	10^{-4}	$2 \cdot 10^{-1}$	1	1024
11	$2 \cdot 10^{-4}$	$1 \cdot 10^{-2}$	1	1024
12	$5 \cdot 10^{-5}$	$1 \cdot 10^{-2}$	1	1024
13	$2 \cdot 10^{-5}$	$1 \cdot 10^{-2}$	1	1024
14	$1 \cdot 10^{-5}$	$1 \cdot 10^{-2}$	1	1024
15	$5 \cdot 10^{-6}$	$1 \cdot 10^{-2}$	1	1024
16	$2 \cdot 10^{-6}$	$1 \cdot 10^{-2}$	1	1024
17	$1 \cdot 10^{-6}$	$1 \cdot 10^{-2}$	1	1024
18	$5 \cdot 10^{-5}$	$2 \cdot 10^{-1}$	1	1024
19	$3 \cdot 10^{-5}$	$3 \cdot 10^{-1}$	1	1024
20	$1 \cdot 10^{-5}$	$3 \cdot 10^{-2}$	1	1024
21	$3 \cdot 10^{-6}$	$3 \cdot 10^{-2}$	1	1024
22	$1 \cdot 10^{-5}$	$1 \cdot 10^{-3}$	0.3	1024
23	$1 \cdot 10^{-5}$	$1 \cdot 10^{-3}$	0.5	1024
24	$1 \cdot 10^{-5}$	$1 \cdot 10^{-3}$	0.75	1024
25	$1 \cdot 10^{-5}$	$1 \cdot 10^{-3}$	1.5	1024
26	$1 \cdot 10^{-5}$	$1 \cdot 10^{-3}$	2	1024
27	$1 \cdot 10^{-5}$	$1 \cdot 10^{-3}$	2.5	1024
28	$1 \cdot 10^{-5}$	$1 \cdot 10^{-3}$	3	1024
29	$1 \cdot 10^{-5}$	$1 \cdot 10^{-3}$	4	1024
30	$1 \cdot 10^{-5}$	$1 \cdot 10^{-3}$	2	2048

Table 3.1: Parameters invoked for numerical simulations. The different colors stand for the different lines in the phase diagram (see figure 3.1): D_1 in blue (N varies), D_2 in red (σ varies), D_3 in green (k varies) and D_4 in magenta (c varies).

spectrum PS. Hence, the PS[xxi] ($PS_{\overline{v}}(\nu)$) concerns the spatially-averaged velocity front ($\overline{v}(t)$), equation 1.7 describes the frontal motion. Even if it condenses the information, such a curve accurately describes the statistics of propagation, yet the information is limited. Figure 3.2 is a typical spectrum and gives way to the following information:

- The Fourier spectrum amplitude of the plateau at low frequency.
- The pre-factor and exponent ($1/a$) of the power-law.
- The lower (ν_{min}) and upper (ν_{max}) frequency cut-offs of this power-law.

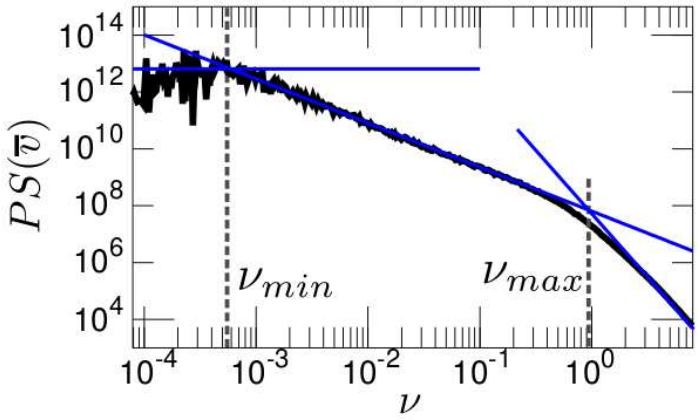

Figure 3.2: The image depicts the Fourier spectrum of a mean speed signal in the crackling regime. ν_{min} and ν_{max} represent the lower and upper cut-offs of the power-law respectively.

3.1.2 Effects of the loading rate c

First, we analyze the variation of the PS of the crack's mean speed $PS_{\overline{v}}(\nu)$ as a function of the loading rate c. Figure 3.3-A presents these PS. They follow a power-law with exponent $1/a = 1.55 \pm 0.1$ (fitted on simulation $\mathcal{N}6$) between two cut-offs. These cut-offs do not vary with c, but the prefactor of the power-law increases with the loading speed. To be more precise, figure 3.3-B shows that the prefactor is almost proportional to the loading rate since the exponent of the scaling between c and the prefactor is 0.9 ± 0.1.

[xxi] Computing the squared value of the signal's Fast Fourier Transform (FFT) and renormalizing it with the Parseval identity gives the Fourier spectrum.

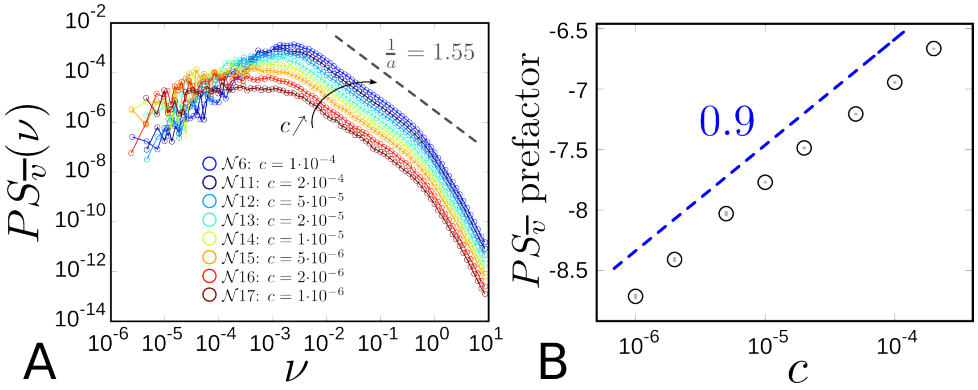

Figure 3.3: A: Fourier spectrum of the crack front's mean speed for different loading rates ($k = 1 \cdot 10^{-2}$, $\sigma = 1$, $N = 1024$). For the simulation $\mathcal{N}6$ one observes a power-law extending over more than two orders of magnitude, and the fitted exponent is $1/a = 1.55 \pm 0.1$. B: Relation between the prefactor of the PS power-law and the loading rate. One observes a scaling relation between these two quantities over more than two orders of magnitude. The fitted exponent is 0.9 ± 0.1. In both cases the axes are logarithmic.

3.1.3 Effects of the unloading factor k

Then, $PS_{\overline{v}}(\nu)$ is studied as a function of the unloading factor, k. One continues to observe a power-law scaling between $PS_{\overline{v}}$ and ν (Figure 3.4-A), with an exponent of $1/a = 1.55 \pm 0.1$. Here, the prefactor decreases as the unloading factor increases. To be more precise, figure 3.4-B shows that the prefactor is almost inversely proportional to the unloading factor since the exponent of the scaling between k and the prefactor is -0.95 ± 0.1. Moreover, the lower cut-off increases with k while the upper cut-off stays constant. Figure 3.4-C shows that this lower cut-off scale with k: $\nu_{min} \sim k^{\Delta}$, with $\Delta = 0.35 \pm 0.2$.

3.1.4 Effects of the disorder σ

$PS_{\overline{v}}(\nu)$ is also studied as a function of the disorder amplitude σ. Figure 3.5-A demonstrations that the prefactor of the power-law increases with σ. As shown in figure 3.5-B, this increase takes the form of a power-law of exponent $2\lambda = 1.5 \pm 0.2$. Finally, the lower cut-off is independent of σ, while the upper one goes as $\nu_{max} \sim \sigma^{2\lambda}$ with the same exponent as previously $\lambda = 0.75 \pm 0.1$.

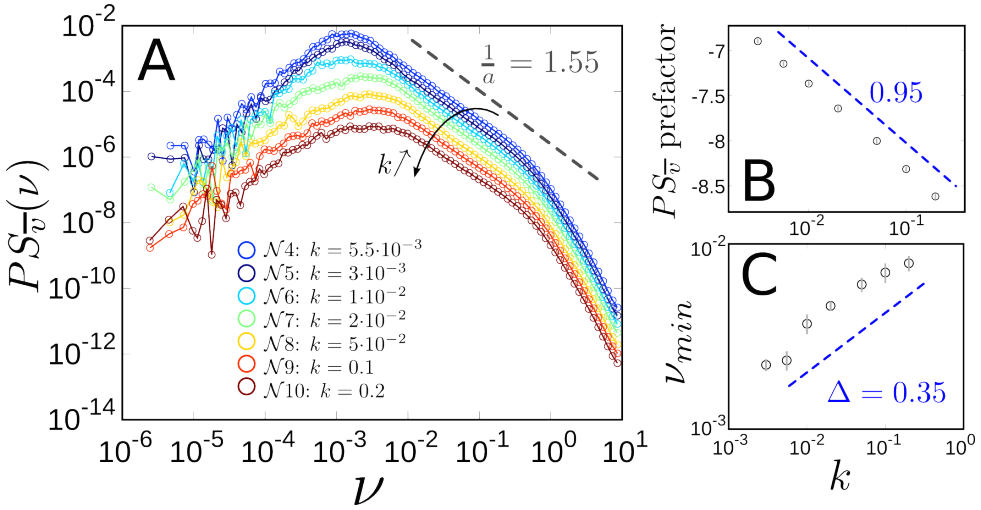

Figure 3.4: A: Fourier spectrum of the fracture's mean speed for different unloading factors ($c = 1 \cdot 10^{-4}$, $\sigma = 1$, $N = 1024$). For the simulation $\mathcal{N}4$ one observes a power-law extending over nearly three orders of magnitude, and the fitted exponent is $1/a = 1.55 \pm 0.1$. B: Relation between the prefactor of the PS power-law and the unloading factor. One observes a scaling relation between these two quantities for more than two orders of magnitude. The fitted exponent is -0.95 ± 0.1. C: Relation between the lower cut-off of the PS power-law and the unloading factor. One observes a scaling relation between these two quantities over more than one order of magnitude. The fitted exponent is $\Delta = 0.35 \pm 0.2$. In all cases the axes are logarithmic.

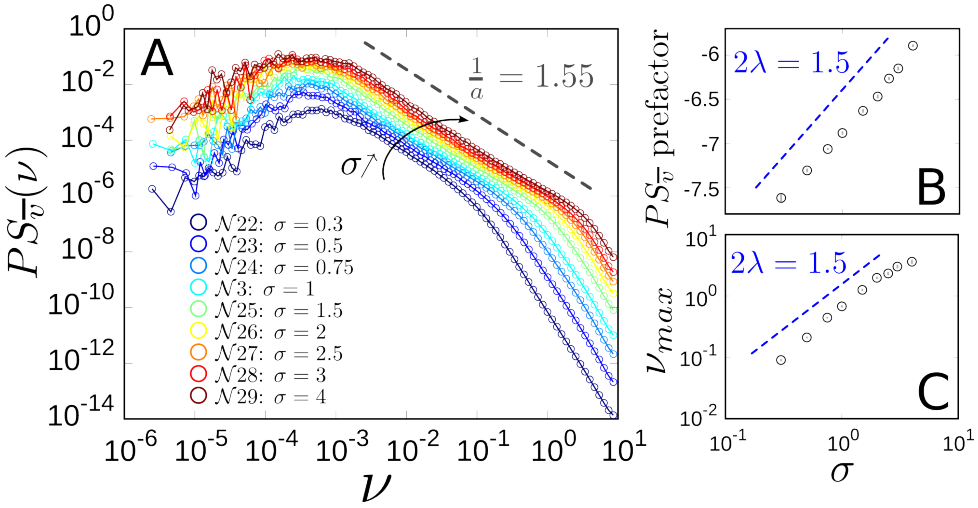

Figure 3.5: A: Fourier spectrum of the fracture mean speed for different heterogeneity amplitudes ($c = 1 \cdot 10^{-5}$, $k = 1 \cdot 10^{-3}$, $N = 1024$). For the simulation $\mathcal{N}29$ one observes a power-law extending over three orders of magnitude, and the fitted exponent is $1/a = 1.55 \pm 0.1$. B: Relation between the prefactor of the PS power-law and the unloading factor. One observes a scaling relation between these two quantities over more than one order of magnitude. The fitted exponent is $2\lambda = 1.5 \pm 0.2$. C: Figure depicts the relationship between the upper cut-off of the PS power-law and the heterogeneity amplitude. One observes a scaling relation between these two quantities over more than one order of magnitude. The fitted exponent is $2\lambda = 1.5 \pm 0.2$. In all cases the axes are logarithmic.

3.1.5 Effects of the size N and discussions

Last but not least, $PS_{\overline{v}}(\nu)$ dependence on the system size, N, is studied. As presented in figure 3.6-A, changing N does not alter the power-law scaling between $PS_{\overline{v}}$ and ν nor the value of the exponent $1/a = 1.55 \pm 0.1$. Hence, neither ν_{min} nor ν_{max} vary with N, but the prefactor of the power-law decreases as the system size increases. To be more precise, figure 3.6-B shows that the prefactor is almost inversely proportional to the system size. The scaling exponent between N and the prefactor is -0.95 ± 0.2.

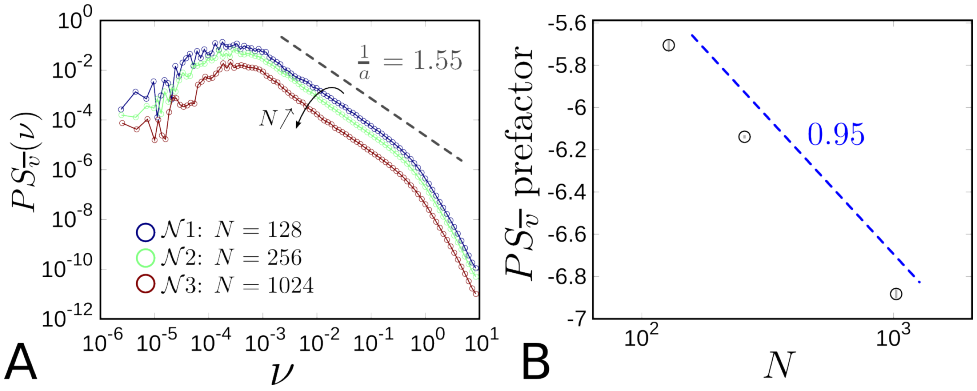

Figure 3.6: A: Fourier spectrum of the fracture's mean speed for different system sizes ($c = 1 \cdot 10^{-5}$ $k = 1 \cdot 10^{-3}$, $\sigma = 1$). For the simulation $\mathcal{N}1$ one observes a power-law extending over more than two orders of magnitude, and the fitted exponent is $1/a = 1.55 \pm 0.1$. B: Relation between the prefactor of the PS power-law and the loading rate. One observes a scaling relation between these two quantities over one order of magnitude. The fitted exponent is -0.95 ± 0.25. In both cases the axes are logarithmic.

To summarize, the power spectrum of the mean crack speed is a power-law; the prefactor of which scale with c, k, σ and N as:

$$PS_{\overline{v}} \approx \frac{\sigma^{2\lambda}}{N}\frac{c}{k}\nu^{-1/a}. \tag{3.1}$$

Its lower cut-off only varies with k, while the upper one depends on σ only:

$$\nu_{max} \sim \sigma^{2\lambda}, \nu_{min} \sim k^{\Delta}. \tag{3.2}$$

Fitting exponents are: $\lambda = 0.75 \pm 0.1$ and $\Delta = 0.35 \pm 0.15$.

To illustrate the accuracy of the rescaling presented in equation 3.1, figure 3.7-A plots all the $PS_{\overline{v}}(\nu)$ for all the simulations. Figure 3.7-B shows the rescaling. All the power laws collapse on a single straight line.

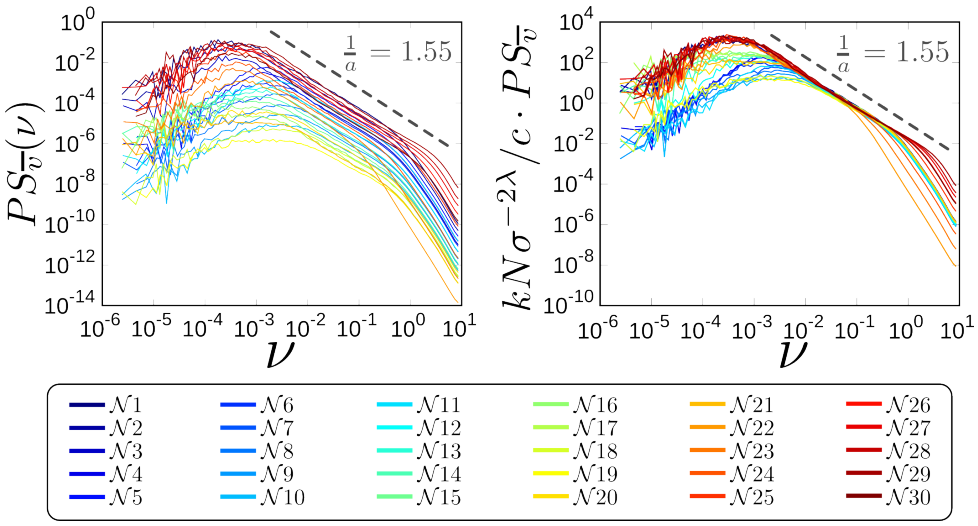

Figure 3.7: A: Fourier spectrum of the fracture's mean speed for all the simulations. B: Renormalization of the power spectrum using equation 3.1. In both figures the axes are logarithmic.

These scaling and the meaning of the exponents are now discuss (and partially interpret). The crackling pulses evidenced in the $\overline{v}(t)$ signal results from the depinning of avalanches. Single non-overlapping avalanches exhibit universal scale-free distributions. They also display scaling relations characterized by a variety of critical exponents, which can be estimated via renormalization groups (RG) or numerical methods [Rosso and Krauth (2002); Duemmer and Krauth (2007)]. These scale-free features only hold for length-scales larger than the Larkin length [Larkin (1979)], $\mathcal{L}$, which scales as $\mathcal{L} \approx 1/\sigma^2$ for the model herein. Then $\nu_{max} \approx 1/\mathcal{L}^{\lambda} \approx \sigma^{2\lambda}$ is expected, where $\lambda = 0.770(5)$ [Duemmer and Krauth (2007)] refers to the dynamic exponent. This value agrees with the measurements herein. For the adiabatic limit ($c \to 0$), there is a one-to-one relation between the $\overline{v}(t)$ pulses and the single depinning avalanches. Then, the PS exponent a_{ad} in equation 3.1 ('ad' index stands for 'adiabatic limit') defines [Kuntz and Sethna (2000)] the scaling ($D \propto S^{a_{ad}}$) between avalanche size (S) and duration (D): $a_{ad} = \lambda/(1+\zeta)$ [Bonamy (2009)], where $\zeta = 0.385(5)$ [Rosso and Krauth (2002); Duemmer and Krauth (2007)] refers to the roughness exponent. As a result, one expects $1/a_{ad} = 1.80(2)$. The exponent Δ_{ad} in equation 3.2 defines the scaling between the upper cut-off in time for scale-free features and the unloading factor k. Reference [Bonamy (2009)] gives $\Delta_{ad} = \lambda/2$ yielding

$\Delta_{ad} = 0.385(5)$. This is very close to the one found herein. Nevertheless, a_{ad} (=0.55) is significantly different from the value of a (=.65) measured here.

It should also be noted that by yielding some overlap between avalanches, a finite driving rate c alters [White and Dahmen (2003)] the PS shape.

3.2 Statistics of pulse $\overline{v}(t)$: threshold-based method

3.2.1 Extraction of the statistics

We will now analysis the pulses of $\overline{v}(t)$, as was achieved on the experimental signals $\mathcal{P}(t)$ in the first part (chapter 3) of this manuscript. Classically, these pulses are dug out from the $\overline{v}(t)$ signal by introducing a threshold value $\overline{v}_{th}$ expressed as a percentage of the maximum mean speed. Their statistics are subsequently characterized. Herein, the threshold tests invoke 3 different percentages of the maximum mean speeds: 5%, 10% and 20%. In each simulation, a set of parameters identify each threshold and breaking events (cartoon in figure 3.8). The parameters are (cartoon in figure 3.8):

- The time at which the event occur (beginning of the event: T_i).
- The event's duration (D_i).
- The maximum mean speed during the event ($V_{max\text{-}i}$).
- The size of the event (the area swept by the crack front during the event, which is nothing but the area below the $\overline{v}(t)$ curve: S_i).
- The mean position of the event (mean position of the crack front at time T_i: H_i).
- The depinning force of the front (force applied on the elastic line at the beginning of the event: $F_{d\text{-}i}$).
- The pinning force of the front (force applied on the elastic line at the end of the event: $F_{p\text{-}i}$).

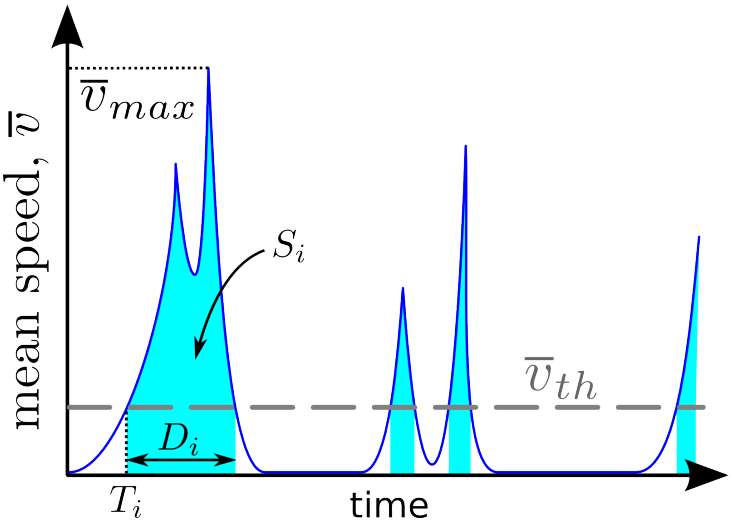

Figure 3.8: Sketch depicting a schematic view of the mean speed signal and the threshold-based method used to extract statistics. See text for details.

3.2.2 Statistical analysis of the avalanche sizes S

Effects of the loading rate c ▶ Statistical analysis of the avalanche sizes, S, begins by looking at the variation of the probability density function $P(S)$ of S as a function of the loading rate, c. Figure 3.9-A exposes that the prefactor and exponent $\tilde{\beta} = 1.3 \pm 0.1$ (fitted on simulation $\mathcal{N}6$) are independent of c. This exponent is different from that measured experimentally in the first part (section 3.4.2) of the manuscript. On the other hand, it is very close to the universal value $\beta = 1.280 \pm 0.010$ [Bonamy (2009)] expected at the depinning transition of a long-range elastic line propagating in a 2D uncorrelated random potential. This would mean that the experimental case corresponds with tha short-range kernel case.

The upper cut-off increases as c increases (see figure 3.9-B-inset). This may appear surprising since the correlation length (and hence the avalanche size) is expected to increase (diverge algebraically) as the system approaches the transition (*i.e.* when c decreases). Theories behind this counterintuitive observation hypothesize an avalanche overlapping effect: The avalanche density increases as c increases and favors avalanche overlapping. By coalescence, small avalanches yield larger ones. Figure 3.9-B invokes the average value of $\langle S \rangle$ (see section 2.9.5 of part I) to collapse the $P(S)$ curves on a single power-law. The fairly good collapse proofs that beyond the value of the exponent β the scaling function's form does not depend on c.

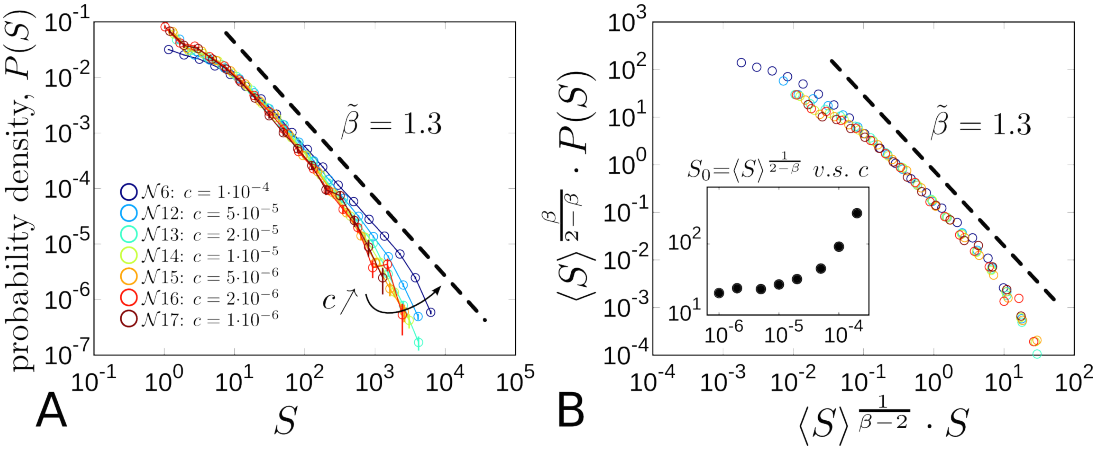

Figure 3.9: A: Probability density function of the avalanche size detected via threshold based method as a function of the loading rate, c (here, $k = 1 \cdot 10^{-2}$, $\sigma = 1$, $N = 1024$). For the simulation $\mathcal{N}6$ one observes a power-law extending over more than two orders of magnitude, and the fitted exponent is $\tilde{\beta} = 1.3 \pm 0.1$. B: Collapse of the curves using the mean size value. Inset: Evolution of the upper cut-off measured via the mean avalanche size as a function of the loading rate. In all cases the axes are logarithmic.

Effects of the unloading factor, k ► This section analyzes the probability density function $P(S)$ dependence on the unloading factor, k. Figure 3.10-A shows that the prefactor and exponent $\tilde{\beta} = 1.3 \pm 0.1$ (fitted on the simulation $\mathcal{N}4$) remain independent of k. On the other hand, the upper cut-off decreases as the unloading factor increases following a scaling relation with exponent 1.1 ± 0.15 as presented in figure 3.10-B-inset. This means the avalanche relevance decreases as the system's stiffness increases, which is consistent with the mechanical view point. Figure 3.10-B illustrates the collapse of $P(S)$ curves for different k onto a single master curve employing $\langle S \rangle$.

Effects of the disorder σ ► Finally, how the probability density function $P(S)$ varies with the heterogeneity amplitude σ is examined. Figure 3.9-A establishes that the prefactor and exponent $\tilde{\beta} = 1.3 \pm 0.1$ (fitted on the simulation $\mathcal{N}29$) remain independent of σ. Nevertheless, the lower cut-off decreases with the heterogeneity amplitude while the upper one remains constant. This means that the smaller σ, the smaller the avalanches are. Here again, and looking at figure 2.6 in the previous chapter, this seems consistent.

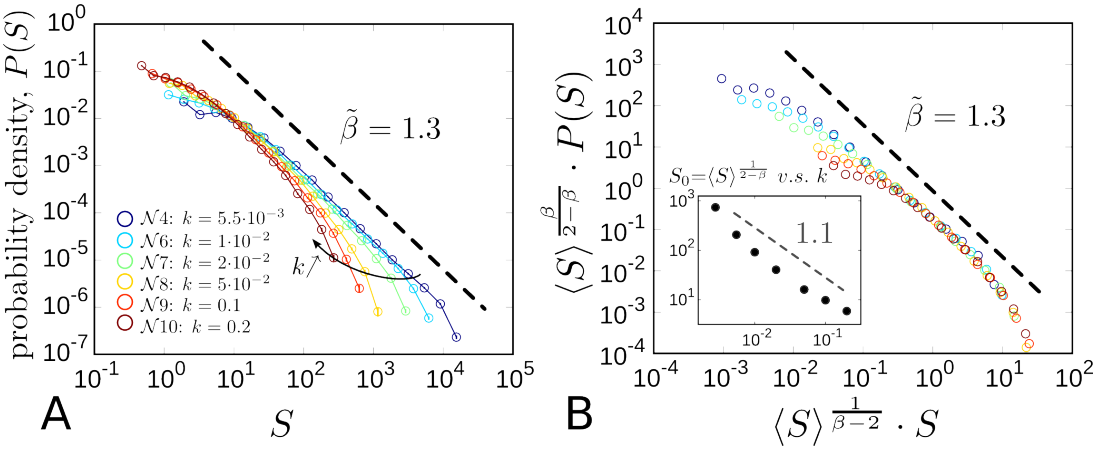

Figure 3.10: A: Probability density function of the avalanche size detected via threshold based method as a function of k (here, $c = 1 \cdot 10^{-4}$, $\sigma = 1$, $N = 1024$). For the simulation $\mathcal{N}4$ one observes a power-law extending over nearly three orders of magnitude. The fitted exponent is $\tilde{\beta} = 1.3 \pm 0.1$. B: Collapse of the curves using the mean size value. Inset: Evolution of the upper cut-off measured via the mean avalanche size as a function of the unloading factor. This relation turns out to be a power-law with exponent -1.1 ± 0.15. In all cases the axes are logarithmic.

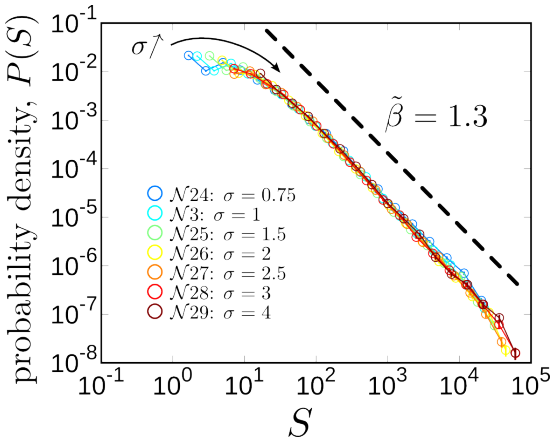

Figure 3.11: Probability density function of the avalanche size detected via the threshold based method as a function of the heterogeneity amplitude ($c = 1 \cdot 10^{-5}$, $k = 1 \cdot 10^{-3}$, $N = 1024$). For the simulation $\mathcal{N}29$ one observes a power-law extending over three orders of magnitude. The fitted exponent is $\tilde{\beta} = 1.3 \pm 0.1$. The axes are logarithmic.

3.2.3 Statistical analysis of the avalanche durations D

Effects of the loading rate, c ▶ Another quantity classically analyzed in crackling dynamics is the duration of an avalanche, D. Here the variation of the probability density function, $P(D)$, as a function of c is examined. Figure 3.12-A reveals that the prefactor and exponent $\tilde{\kappa} = 1.5 \pm 0.1$ (fitted on the simulation $\mathcal{N}6$) remain independent of c. This exponent differs from experimental measurements in part I (section 3.4.2) of this manuscript. On the other hand, it is very close to the universal value $\kappa = 1.50 \pm 0.01$ [Bonamy (2009)] expected at the depinning transition of a long-range elastic line propagating in a 2D uncorrelated random potential.

The upper cut-off increases with c (see figure 3.12-B-inset). Once again, this may appear counterintuitive: The correlation length (and hence the avalanche duration) is expected to increase as the system gets closer to the transition (*i.e.* when c decreases). As before, hypotheses behind this counterintuitive observation postulate an avalanche overlapping effect. Thus, all the $P(D)$ curves collapse various c by making $D \to D/\langle D \rangle^{1/2-\kappa}$ and $P(D) \to P(D) \times \langle D \rangle^{\kappa/2-\kappa}$ (see figure 3.12-B).

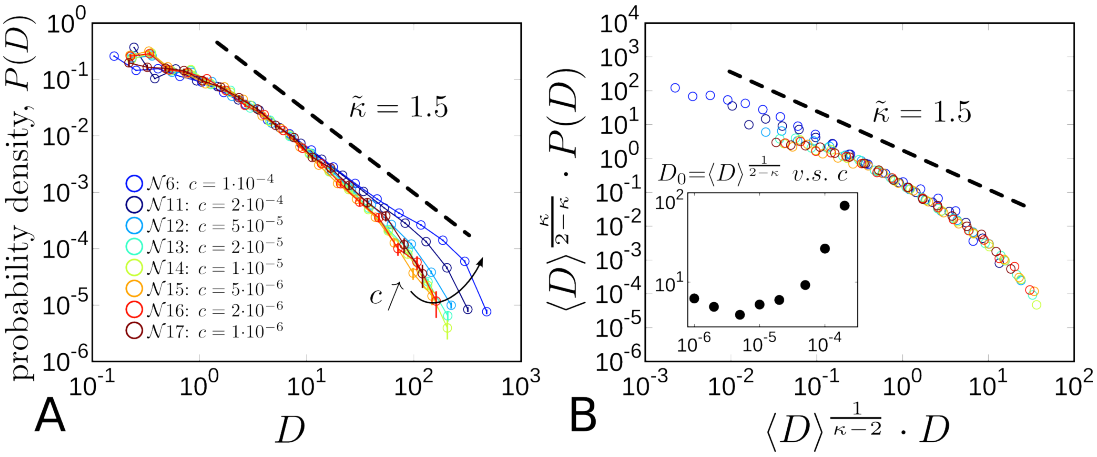

Figure 3.12: A: Probability density function of the avalanche duration detected via threshold based methods as a function of the loading rate ($k = 1 \cdot 10^{-2}$, $\sigma = 1$, $N = 1024$). For simulation $\mathcal{N}6$, the power-law extends over more than two orders of magnitude. The fitted exponent is $\tilde{\kappa} = 1.5 \pm 0.1$. B: Collapse of the curves using the mean size value. Inset: Evolution of the upper cut-off measured via the mean avalanche duration as a function of the loading rate. In all cases the axes are logarithmic.

Effects of the unloading factor, k ▶ The variation of $P(D)$ as a function of the unloading factor, k, is examined. The exponent remains the same $\tilde{\kappa} = 1.5 \pm 0.1$, irre-

spectively of k (figure 3.13-A). The prefactor also remains constant. However, the upper cut-off decreases as k increases in a seemingly scaling relation with exponent 1.1 ± 0.3 (see 3.13-B-inset). This means on average, the avalanches duration reduces as the system's stiffness increases, which sounds consistent from a mechanical view point.

Figure 3.13-B invokes the same scaling as previously to collapse the $P(D)$ curves on a single power-law. A fairly good collapse of the upper cut-off proofs that it is the only thing that varies with the unloading factor.

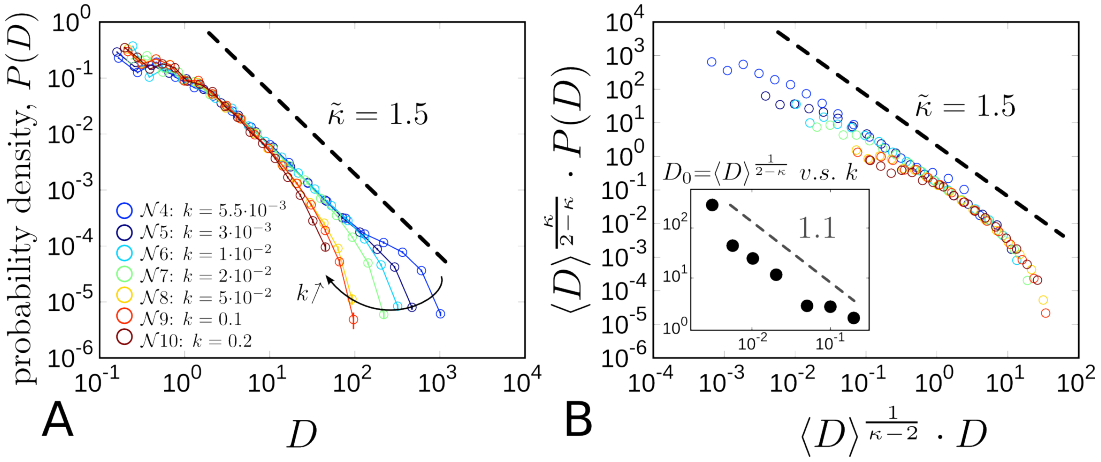

Figure 3.13: A: Probability density function of the avalanche duration detected via the threshold based method as a function of the unloading factor ($c = 1 \cdot 10^{-4}$, $\sigma = 1$, $N = 1024$). For the simulation $\mathcal{N}4$ one observes a power-law extending over more than two orders of magnitude, and the fitted exponent is $\tilde{\kappa} = 1.5 \pm 0.1$. B: Collapse of the curves using the mean size value. Inset: Evolution of the upper cut-off measured via the mean avalanche size as a function of the unloading factor. This relation turns out to be a power-law with exponent -1.1 ± 0.15. In all cases the axes are logarithmic.

Effects of the disorder σ ▶ Finally, how $P(D)$ evolves as the heterogeneity amplitude σ increases is examined. Figure 3.14-A reveals the exponent $\tilde{\kappa} = 1.5 \pm 0.1$ (fitted on the simulation $\mathcal{N}29$) remains constant for all σ. Nevertheless, the lower cut-off and the prefactor increase as the heterogeneity amplitude decreases. This means that on average, the duration of the avalanches increases when σ decreases. Once again this make sense by looking at figure 2.6.

The increasing lower cut-off, σ, is reminiscent of the Fourier spectrum's upper cut-off in section 3.1. Hence, these curves collapse via a renormalization of the x and z axes by the Larkin time: $\mathcal{T} = 1/\sigma^{2\lambda}$, with $\lambda = 0.75 \pm 0.1$. Figure 3.11-B presents the result

of this renormalization. This gives a fairly good collapse (more particularly of the lower cut-offs).

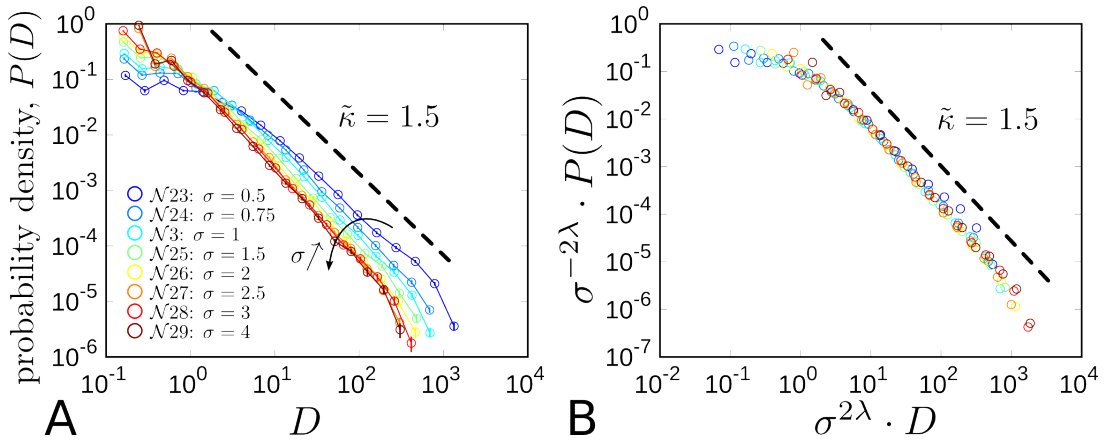

Figure 3.14: A: Probability density function of the avalanche duration detected via the threshold based method as a function of the heterogeneity amplitude ($c = 1 \cdot 10^{-5}$, $k = 1 \cdot 10^{-3}$, $N = 1024$). Simulation $\mathcal{N}29$ reveals a power-law extending over more than two orders of magnitude. The fitted exponent is $\tilde{\kappa} = 1.5 \pm 0.1$. B: Collapse of the curves using the Larkin time: $2\lambda = 1.5$. In both cases the axes are logarithmic.

3.2.4 Analysis of the avalanche shape

Then to emphasize the peculiarity of the shape asymmetry observed for experimental data in section 3.4.2 of the previous part (figure 3.21), figure 3.15 plots the mean avalanche shape for different characteristic durations. Recalling the protocol to arrive at this average shape, the first step defines D of interest for the avalanche duration. Then, all the pulses (i), such that $D_i \in [D - \delta D, D + \delta D]$, are collected. Subsequently, the pulse shape $\overline{v}(t)$ at D is computed by averaging $\overline{v}_i(t - T_i)$ over all the collected pulse (T_i is the initiation time of each pulse). Figure 3.15 presents the normalized pulse shape $\overline{v}/\overline{v}_{max}$ as a function of t/D for increasing D. As emphasized by [Papanikolaou et al. (2011); Sethna et al. (2001); Leblanc et al. (2013)] the avalanche shape is perfectly symmetric in time, and its width increases with D. This symmetry is not observed for large D in the experiments presented in section 3.4.2 of the first part of this manuscript. Thus, the long-range elastic line model proposed herein to describe heterogeneous fracture still misses some features of the model experiment.

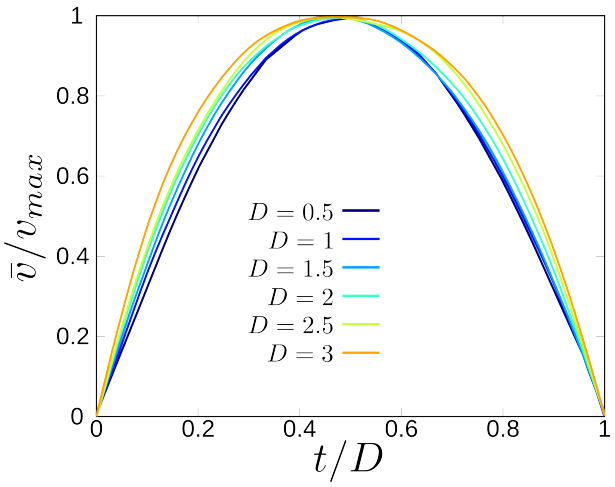

Figure 3.15: Average avalanche shapes for different durations, D, of events extracted via the threshold-based method. The shapes are measured from simulation $\mathcal{N}1$: $c = 1 \cdot 10^{-5}$, $k = 1 \cdot 10^{-3}$, $\sigma = 1$ and $N = 128$.

3.3 Statistics of pulse $v(z,t)$: space-time activity map

3.3.1 Extraction of the statistics

Figure 2.3 shows the local speed $v(z,t)$ of the crack front (accessible only from simulations). Extraction of breaking events occurs directly from this local information and not from global quantities like the spatially averaged front speed. Tanguy et al. [Tanguy et al. (1998)] pioneered this method to extract breaking event. To do so, the time-space activity map (time, z-space, $v(z,t)$) is used to isolate non connected time-space areas where the local speed $v(z,t)$ is above the background numerical noise. One notes, avoiding any side effects requires periodic boundary conditions when isolating avalanches. Figure 3.16 presents the map. In this example, the space-time activity map would detect a single event, while analyzing the $\overline{v}(t)$ signal gives two events.

Figure 3.17 presents a a cartoon on how to analyze events in the (time, z-space, $v(z,t)$) map as well as in the (x-space,z-space) plan. Thus, each event detected in the time-space activity map yields (Note this is repeated for every simulations):

- The time at which the event occur (beginning of the event: T_i).
- The event duration (D_i).

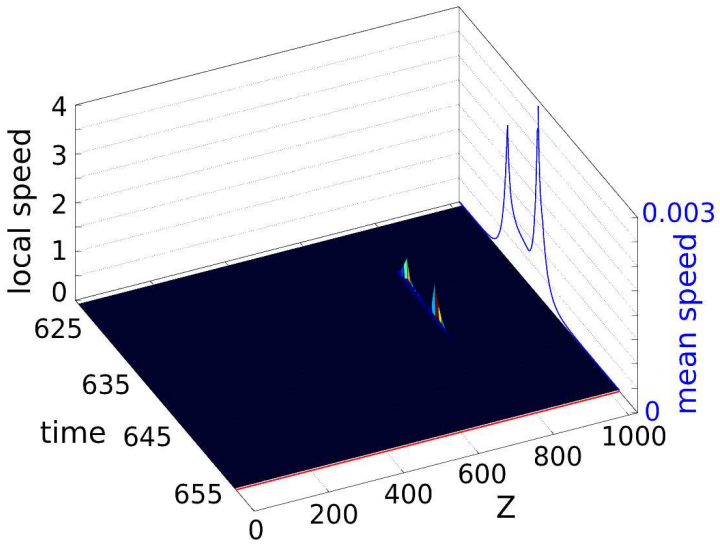

Figure 3.16: The image depicts an isolated avalanche in the time-space map. This 3D graph presents the speed profile of each point of the crack front as a function of the time. The blue line on the right hand side is the spatially averaged speed $\overline{v}(t)$. In this simple case, because the avalanche is isolated in space and time, both have the same shape.

- The maximum local speed during the event ($v_{max\text{-}i}$).
- The size of the event (the area of the cluster in the X-Y space: S_i).
- The X-Y position of the event (This corresponds to the first point of the cluster where the local speed exceeds a threshold): ($X_{begin\text{-}i}$,$Z_{begin\text{-}i}$)).
- The depth of the cluster (Lx_i).
- The height of the cluster (Lz_i).
- The front depinning force (force applied on the elastic line at the beginning of the event: $F_{d\text{-}i}$).
- The front pinning force (force applied on the elastic line at the end of the event: $F_{p\text{-}i}$).

Figure 3.17 is a schematic view of these different quantities. A single avalanche appears on both the (t-time,z-space) and (x-space,z-space) maps. It shows that this method is the most complete one to detect events since it localizes events via three degree of freedom,

two in space and one in time. Thus, the threshold based analysis of $\overline{v}(t)$ is similar to the way one detects events from the variations of the elast(ostat)ic energy in the experiments presented in chapter 3 of the first part of this manuscript. Yet, the method may be closer to the events detected from the AE analysis (Part I chapter 2 presents methods used for acoustical detection of events). To illustrate the type of results given by this method, figure 3.18 presents a zoom of the (t-time,z-space) and (x-space,z-space) maps. Figure 3.19 presents similar maps for a longer simulation, without giving the exact avalanche shape but the area. Clustering in space and time appears clearly in these maps.

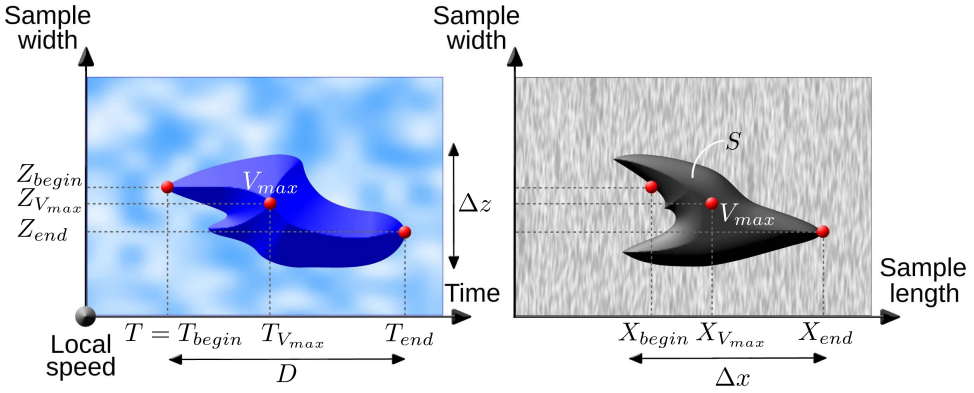

Figure 3.17: Schematic representation of an avalanche in the (t-time,z-space) plane (left) and counterpart representation in the (x-space,z-space) plane (right). See text for details.

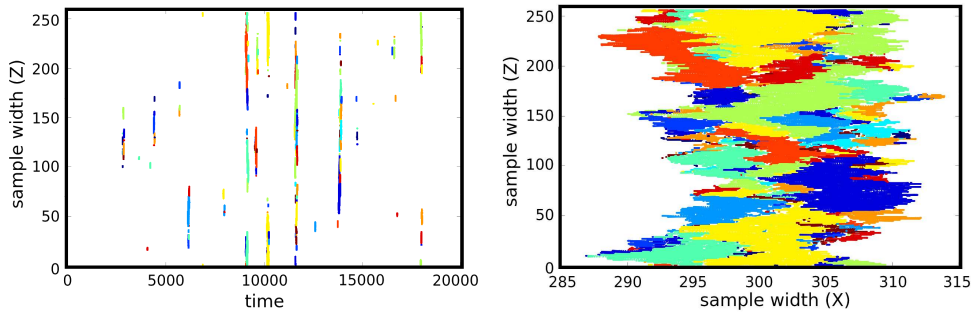

Figure 3.18: Zooming in on a small part of simulation $\mathcal{N}2$ ($c = 1 \cdot 10^{-5}$, $k = 1 \cdot 10^{-3}$, $\sigma = 1$ and $N = 256$) reveals: avalanches detected in the time-space plane (left) and the space-space plane (right). A single color characterizes each, which is the same for the space-space map and the time-space one.

Now, it is interesting to compare both local and global methods to detect avalanches: the one based on the threshold of the signal $\overline{v}(t)$ (see section 3.2.1); and the one where events are directly extracted from $v(z,t)$. For a given short crack propagation simulation

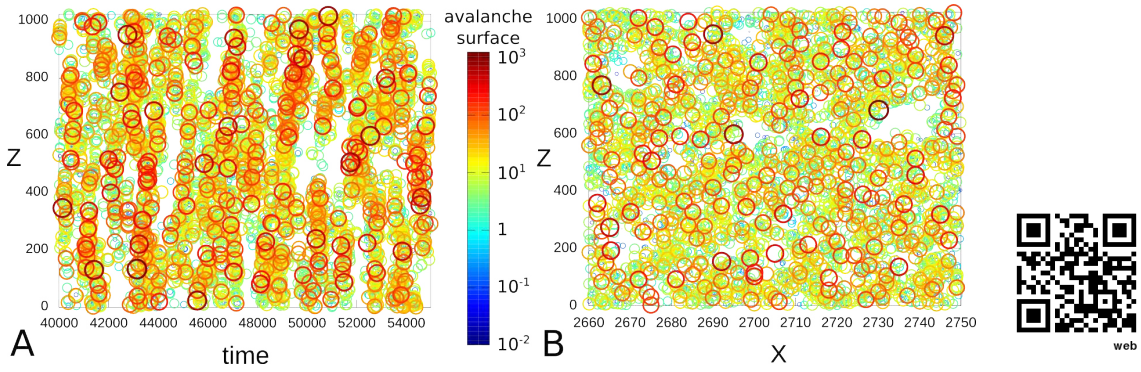

Figure 3.19: A: Positions of the avalanches detected in the time-space activity map and presented in the (t-time,z-space) plane. B: Positions of the avalanches detected in the time-space activity map and presented in the (x-space,z-space) plane. In both cases, the circles' radius represents the area swept out by an avalanche (S) and is in log scale. The color also changes with respect to this size. A movie showing the time evolution of these maps is also presented: Scan the flash-code with a mobile phone or click http://youtu.be/dcsPalGLAw4.

in the crackling regime, one extracts the avalanches via both methods. Results in terms of occurrence times and avalanche surfaces are summed-up in figure 3.20. This comparison shows that the two methods yield significantly different results. As expected, the detection from the time-space activity card gives the most accurate results whereas the threshold method causes many events to overlap. In this sense, the first method compares to AE used in the experimental part of this manuscript. The second one equivalent to the threshold-based method applied on the radiated power signal. These two methods are not directly comparable since they give different results from a statistical point of view (see the following section and [Laurson et al. (2010)] for more information).

In the rest of this section, (for sake of brevity and simplicity) the focus is on the statistical variation of S as measured via the space-time activity map method. This shows the accuracy of the method and the fact that it does not give the same statistical information as the one used previously.

3.3.2 Statistical analysis of the avalanche sizes S

Effects of the loading rate, c ▶ First of all, one is interested in the probability density function of the avalanche size $P(S)$ measured on the space-time activity map, and its

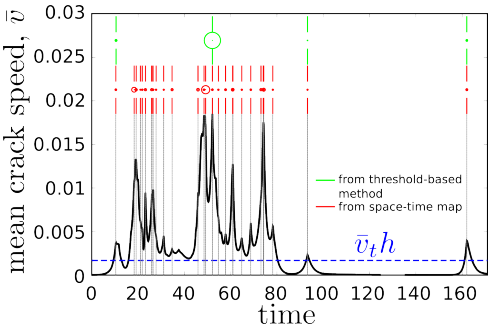

Figure 3.20: Simulated mean crack speed signal $\overline{v}(t)$ and comparison in terms of occurrence time and avalanche size of detected events. Events are detected via the threshold based method and time-space activity card. For each method, the centers of the circles give the position of the events; and their areas correspond to the surface swept out during the avalanche. $\overline{v}_{th}$ is the threshold used for the first method.

variation as a function of the loading rate c. Figure 3.21-A shows that the prefactor and exponent $\hat{\beta} = 1.5 \pm 0.1$ (fitted on the simulation $\mathcal{N}16$) do not depend on c. The values measured here differ values obtained from the $\overline{v}(t)$ analysis. This difference between $\tilde{beta}$ measured from spatially averaged signals and $\hat{\beta}$ measured from space-time/space-space activity maps has already been observed [Bonamy et al. (2008); Laurson et al. (2010)]. Simulation results herein and by [Bonamy et al. (2008); Laurson et al. (2010)] do correspond. It is also interesting to note that it coincides with the one observed experimentally in peeling experiments [Måløy et al. (2006)].

In figure 3.21-B-inset, the upper cut-off decreases with c. This behavior is the contrary to what is observed when the avalanches are extracted from the spatially averaged velocity. This suggests that the overlapping effect is less pronounced when one looks at the time-space/space-space activity map. Figure 3.21-B uses the scaling explained in the section 2.9.5 to collapse all $P(S)$ curves onto a single master curve. The very good collapse proofs that just the upper cut-off varies with the loading speed, emphasizing the fact that the exponent remain constant. Then, using the relation $S_0 \sim \langle S \rangle^{1/(2-\beta)}$ computed in section 2.9.5, one gets a scaling between the upper cut-off S_0 and the loading rate with an exponent equal to 1 ± 0.2. In other words, $S_0 \sim 1/c$ (see figure 3.21-B-inset).

Effects of the unloading factor, k ▶ Now, the variations of $P(S)$ as a function of k are examined. The exponent and prefactor remain unchanged (figure 3.22-A). The upper cut-off increases with k. Once again this opposes observations for avalanches defined using the

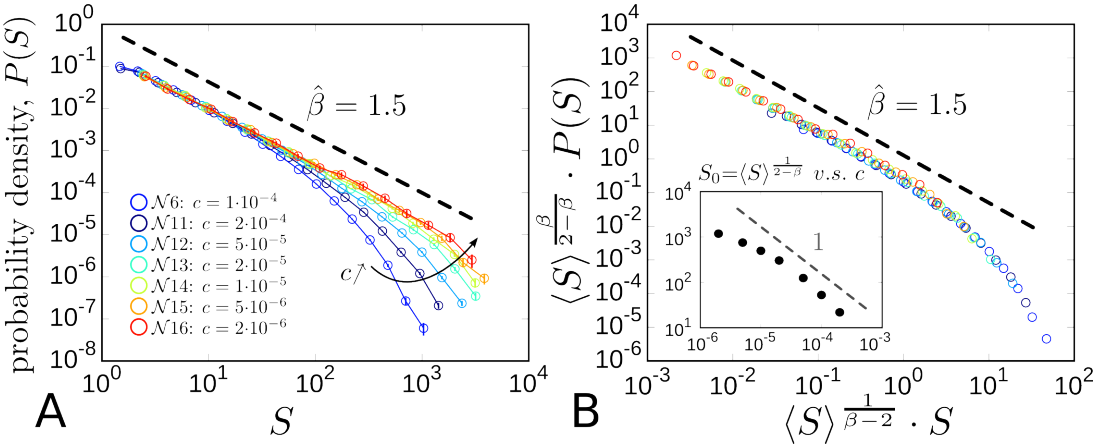

Figure 3.21: A: Probability density function of the avalanche size as detected in the space-time activity maps. Its varies as a function of the loading rate ($k = 1 \cdot 10^{-2}$, $\sigma = 1$, $N = 1024$). For the simulation $\mathcal{N}16$ one observes a power-law extending over nearly three orders of magnitude. The fitted exponent is $\hat{\beta} = 1.5 \pm 0.1$. B: Collapse of the curves using the average value $\langle S\rangle$. Inset: Scaling of the upper cut-off S_0 (proportional to $\langle S\rangle^{1/(2-\beta)}$) as a function of c. The straight dashed line with slope -1 is given as a guide for the eyes. In all cases the axes are logarithmic.

spatially averaged signal $\overline{v}(t)$. As before, all curves collapse by making $S \to S/\langle S\rangle^{1/(2-\beta)}$ (figure 3.22-B:Main). Like in the previous section, the upper cut-off value S_0 is plotted as a function of k. Figure 3.22-B-inset shows that S_0 scales as a power-law with k, with an exponent close to 1.2 (± 0.2): $S_0 \sim k^{1.2}$.

Effects of the disorder, σ ▶ To finish this section, how $P(S)$ evolves with the heterogeneity amplitude σ is studied. Figure 3.23-A shows that the prefactor and exponent $\hat{\beta} = 1.5 \pm 0.1$ (fitted on the simulation $\mathcal{N}29$) remain independent of σ. Nevertheless, the upper cut-off increases with σ while the lower one remains constant. This means smaller avalanches yield smaller σ. This is reminiscent of $\overline{v}(t)$ analysis. Invoking this method to measure the avalanche size, the upper cut-off moves while the lower one is fixed contrary to what is observed with the other method.

Figure 3.23-B uses the same method invoked when k or c vary to collapse the upper cut-offs of the $P(S)$ power-law. One obtains a very good collapse of the upper cut-off which is a proof that it is the only thing that varies with the heterogeneity amplitude. Moreover, like in the previous section, figure 3.23-B-inset plots the upper cut-off value S_0 measured from the mean avalanche size as a function of σ. As presented in this figure, S_0

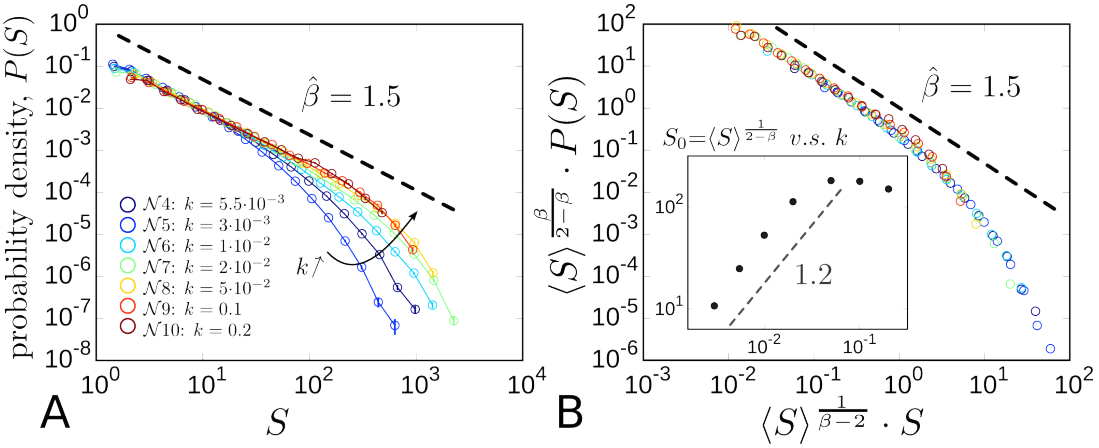

Figure 3.22: A: Probability density function of the avalanche size detected via the space-time activity card method as a function of the unloading factor ($c = 1 \cdot 10^{-4}$, $\sigma = 1$, $N = 1024$). Simulation $\mathcal{N}8$ evidences a power-law extending over two orders of magnitude. The fitted exponent is $\hat{\beta} = 1.5 \pm 0.1$. B: Collapse of the curves using the average value $\langle S\rangle$. Inset: Scaling between the upper cut-off S_0 and k. A straight dashed line with slope 1.2 is given to guide the eyes. In all cases the axes are logarithmic.

scales with σ with an exponent close to 1.7 (± 0.1): $S_0 \sim \sigma^{1.7}$.

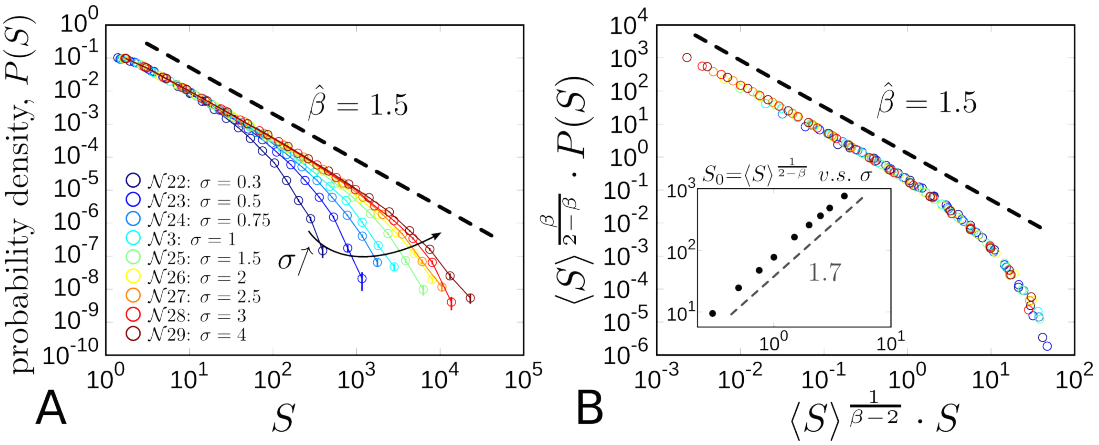

Figure 3.23: A: Probability density function of the avalanche size detected on the space-time activity map, as a function of the heterogeneity amplitude σ ($c = 1 \cdot 10^{-5}$, $k = 1 \cdot 10^{-3}$, $N = 1024$). For the simulation $\mathcal{N}29$ one observes a power-law extending over three orders of magnitude. The fitted exponent is $\hat{\beta} = 1.5 \pm 0.1$. B: Collapse of the curves using the average value $\langle S\rangle$. Inset: Scaling between the upper cut-off S_0 and σ. A straight dashed line with slope 1.7 guides the eyes. In all cases the axes are logarithmic.

3.4 Statistics of pulse $v(z,x)$: space-space activity map

3.4.1 Extraction of the statistics

The last common way to extract the avalanche statistics from crackling signals is the one pioneered by [Måløy et al. (2006)]. It consists of building waiting-time or spatial activity maps $W(x,z)$ which represents the time spent by the crack front at each location (x,z) in the observation zone. Figure 3.24-A depicts a typical example of a spatial activity map.

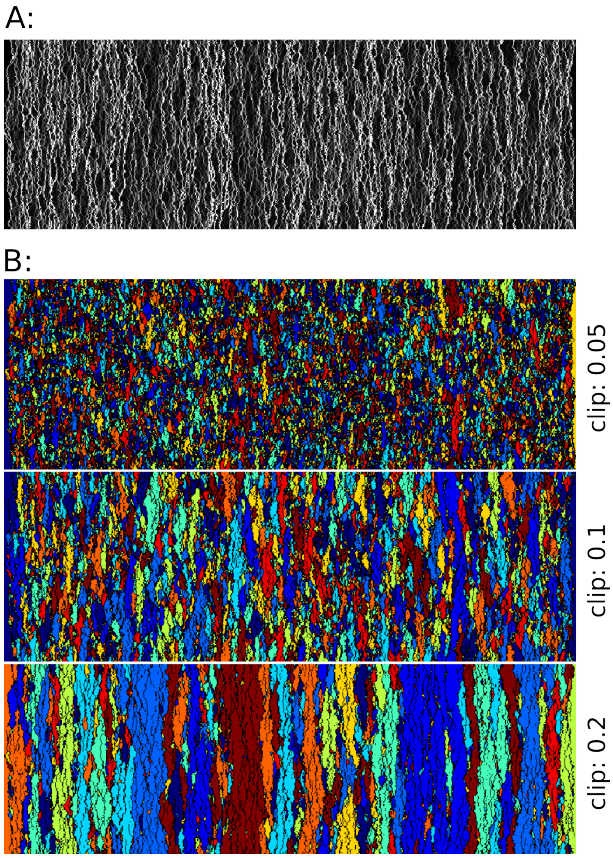

Figure 3.24: A: Gray scale image of the activity card for numerical simulation $\mathcal{N}2$ ($c = 1 \cdot 10^{-5}$, $k = 1 \cdot 10^{-3}$, $\sigma = 1$ and $N = 256$). B: Spatial clustering measured from this activity card for different value of clip. Colors mark separated avalanches.

The first step in this method is to identify a cartograph ($\mathcal{V}(x,z)$) of the local velocities where $\mathcal{V}(x,z) = 1/W(x,z)$. At the same time, a threshold value ($\mathcal{V}_{th}$) is defined via a clip value, C: $\mathcal{V}_{th} = C \cdot \langle \mathcal{V}(x,z) \rangle_{x,z}$. Clusters extracted from this map are isolated islands and reside above $\mathcal{V}_{th}$. Clustering is done by taking into account the periodic

boundary conditions and 3 different clip values: $C = 0.05$, 0.1 and 0.2. Figure 3.24-B shows clustering for the different clip values. Hence, repeating techniques used in the time-space activity card; cluster events for each simulation and clip value in the activity map provide the following information:

- The event duration (D_i).
- The cluster size (the area of the cluster: S_i).
- The cluster depth (Lx_i).
- The cluster height(Lz_i).

The rest of this section focuses on the statistical variation of the avalanche dimensions as a function of the different input parameters of the system. The clip value is fixed to $C = 0.1$.

3.4.2 Statistical analysis of the avalanche sizes S

Effects of the loading rate, c ▶ As before, the probability density function dependence on avalanche size and c is studied. Figure 3.25-A shows that the prefactor and exponent $\check{\beta} = 1.5 \pm 0.1$ (fitted on simulation $\mathcal{N}14$) remain constant whatever c. This exponent corresponds to the one obtained from the space-time activity map. The upper cut-off decreases with c (see figure 3.25-B-inset). In other words, it seems obvious that the statistics of the avalanches extracted from the space-space activity map coincides with those from the time-space map (see previous section). Finally, one can collapse all $P(S)$ curves by making $S \to s/\langle S\rangle^{1/(2-\beta)}$.

Effects of the unloading factor, k ▶ The variations of $P(S)$ with k are the same as that observed in the previous section. The prefactor and exponent ($\check{\beta} = 1.5 \pm 0.1$) are independent of k, yet the upper cut-off decreases with k following a scaling law with exponent 1.6 ± 0.2 (figure 3.26-B inset).

Effects of the disorder σ ▶ Finally, one looks at how $P(S)$ depends on σ. Figure 3.27-A illustrates that the prefactor and exponent $\check{\beta} = 1.5 \pm 0.1$ (fitted on simulation $\mathcal{N}25$) remain constant whatever σ. Nevertheless, the upper cut-off increases with the heterogeneity amplitude while the lower one remains constant. This means on average for

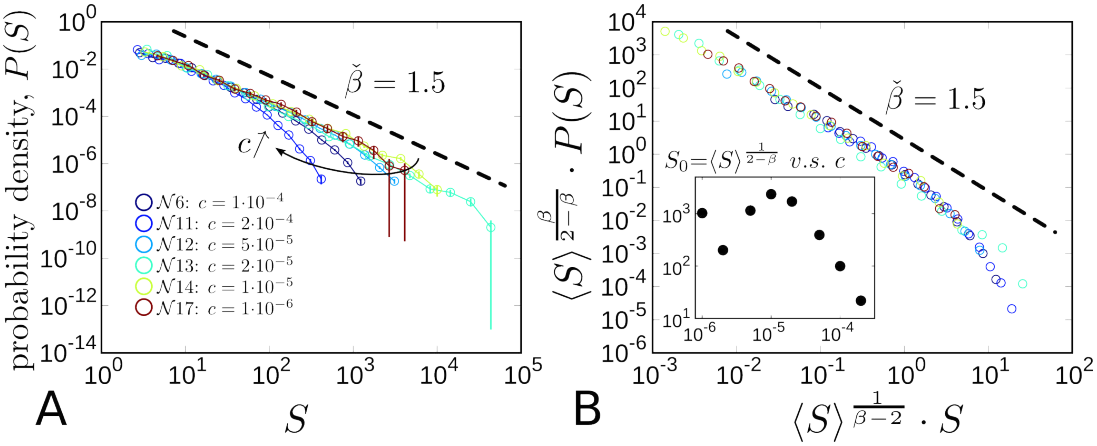

Figure 3.25: A: Probability density function of the avalanche size detected via the activity map as a function of c ($k = 1{\cdot}10^{-2}$, $\sigma = 1$, $N = 1024$). Simulation $\mathcal{N}14$ gives a power-law extending over more than two orders of magnitude. The fitted exponent is $\check{\beta} = 1.5 \pm 0.1$. B: Collapse of the curves using the average value $\langle S\rangle$. Inset: Evolution of the upper cut-off measured via the mean avalanche size as a function of the loading rate. In all cases the axes are logarithmic.

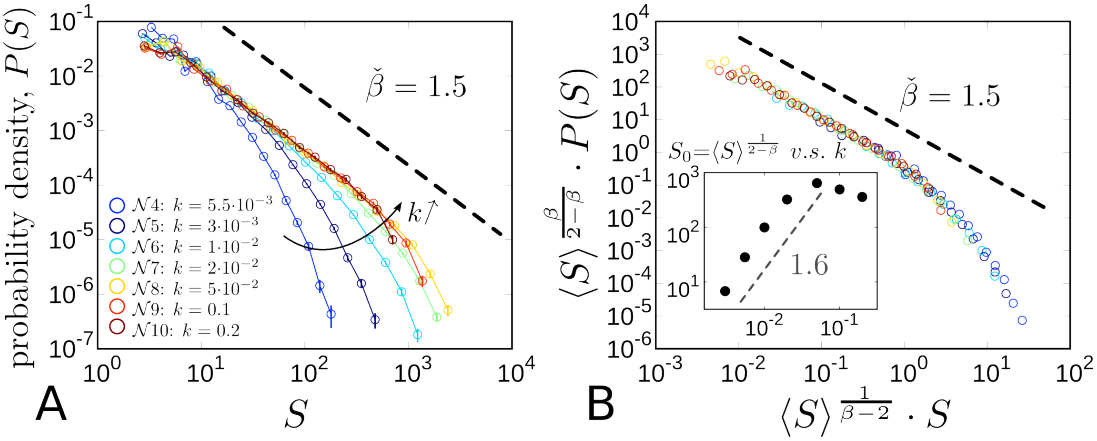

Figure 3.26: A: Probability density function of the avalanche size detected via the activity map method as a function of k ($c = 1 \cdot 10^{-4}$, $\sigma = 1$, $N = 1024$). Simulation $\mathcal{N}9$ yields a power-law extending over nearly three orders of magnitude. The fitted exponent is $\check{\beta} = 1.5 \pm 0.1$. B: Collapse of the curves using the average value $\langle S\rangle$. Inset: Evolution of the upper cut-off measured via the mean avalanche size as a function of the unloading factor. This relation turns out to be a power-law with exponent 1.6 ± 0.2. In all cases the axes are logarithmic.

small σ yield small avalanches, which is reminiscent of the other two methods. However, with this way to measure the avalanche size, just like the one using the space time activity map, the upper cut-off moves while the lower one remains fixed.

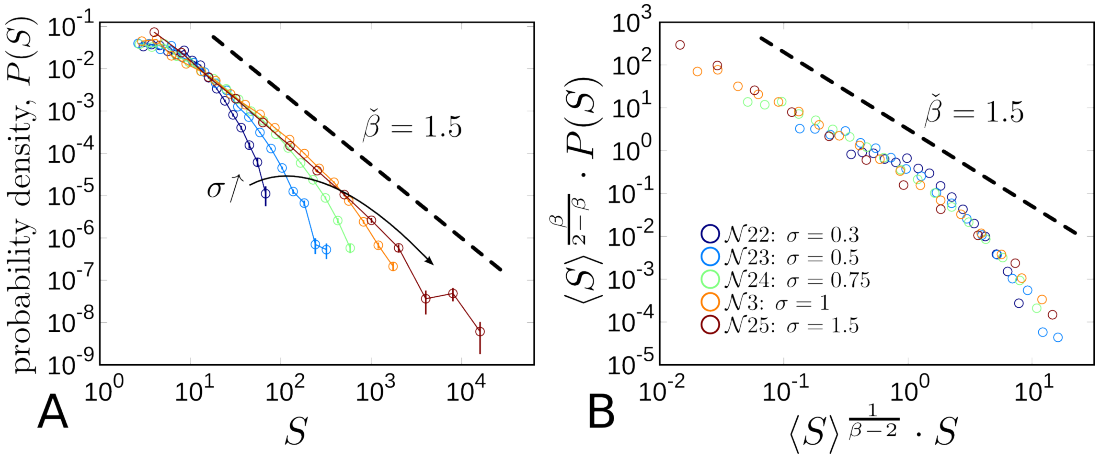

Figure 3.27: A: Probability density function of the avalanche size detected via the activity card method as a function of the heterogeneity amplitude ($c = 1 \cdot 10^{-5}$, $k = 1 \cdot 10^{-3}$, $N = 1024$). Simulation $\mathcal{N}25$ yields a power-law extending over three orders of magnitude and the fitted exponent is found to be $\check{\beta} = 1.5 \pm 0.1$. B: Collapse of the curves using the average value $\langle S \rangle$. In both cases the axes are logarithmic.

3.4.3 Statistical analysis of the avalanche width Lx measured along the direction of crack propagation

Effects of the loading rate, c ▶ Now the spatial avalanche shape is examined. This is obtained by first computing $P(Lx)$ of the avalanche width (Lx) along x for avalanches extracted from the space-space activity map, and secondly, examining its variations as a function of c. Figure 3.28-A shows that the prefactor and exponent $\check{\tau}_x = 2.4 \pm 0.25$ (fitted on the simulation $\mathcal{N}13$) remain independent of the loading conditions. The upper cut-off decreases as c increases, which is consistent with the observed decrease of avalanche size S with respect to c.

Collapsing the curves requires the scaling explained in the section 2.9.5. Still, this method has to be adapted. Indeed, since $\check{\tau}_x > 2$ causes the integral $\langle Lx \rangle = \int_0^\infty LxP(Lx)\,\mathrm{d}Lx$ to diverge as $Lx \to \infty$, the second moment $\langle Lx^2 \rangle = \int_0^\infty Lx^2 P(Lx)\,\mathrm{d}Lx$ is invoked which is properly defined. It relates to the upper cut-off value via $Lx_0 \sim \langle Lx^2 \rangle^{1/(3-\tau_x)}$.

Renormalization occurs by multiplying the abscissa by $\langle Lx^2\rangle^{1/(\tau_x-3)}$ and the ordinate by $\langle Lx^2\rangle^{\tau_x/(3-\tau_x)}$. Figure 3.28-B presents the results. The fairly good collapse proofs that just the upper cut-off varies with the loading speed, emphasizing the fact that the exponent remains constant.

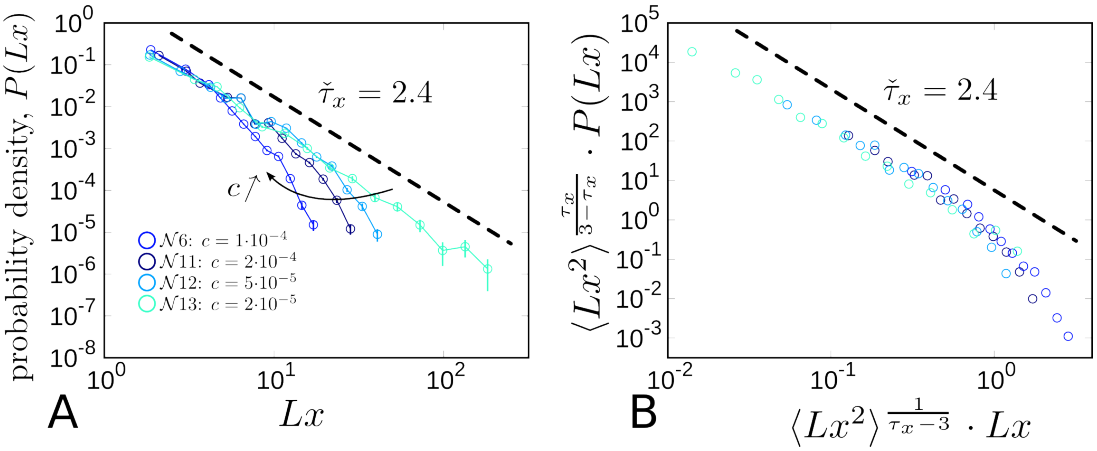

Figure 3.28: A: Probability density function of the avalanche depth detected via the activity card as a function of the loading rate ($k = 1 \cdot 10^{-2}$, $\sigma = 1$, $N = 1024$). Simulation $\mathcal{N}13$ one observes a power-law extending over two orders of magnitude. The fitted exponent is $\check{\tau}_x = 2.4 \pm 0.25$. B: Collapse of the curves using the second moment of the avalanche depth. In both cases the axes are logarithmic.

Effects of the unloading factor, k ▶ Then, one analyzes the variations of $P(Lx)$ as a function of k. Figure 3.29-A shows that the prefactor and exponent $\check{\tau}_x = 2.4 \pm 0.25$ (fitted on simulation $\mathcal{N}8$) remains independent of k. The upper cut-off decreases with k. All curves collapse by normalizing Lx by $\langle Lx^2\rangle^{1/(\tau_x-3)}$ (figure 3.29-B).

Effects of the disorder, σ ▶ Now, one turns to the effect of σ on $P(Lx)$. Figure 3.30-A shows that the prefactor and exponent $\check{\tau}_x = 2.4 \pm 0.25$ (fitted on the simulation $\mathcal{N}25$) remain constant whatever σ. Nevertheless, the upper cut-off increases with the heterogeneity amplitude while the lower one remains constant. This means on average smaller σ implies a smaller depth. Figure 3.30-B uses the second moment method to collapse all the $P(Lx)$ curves.

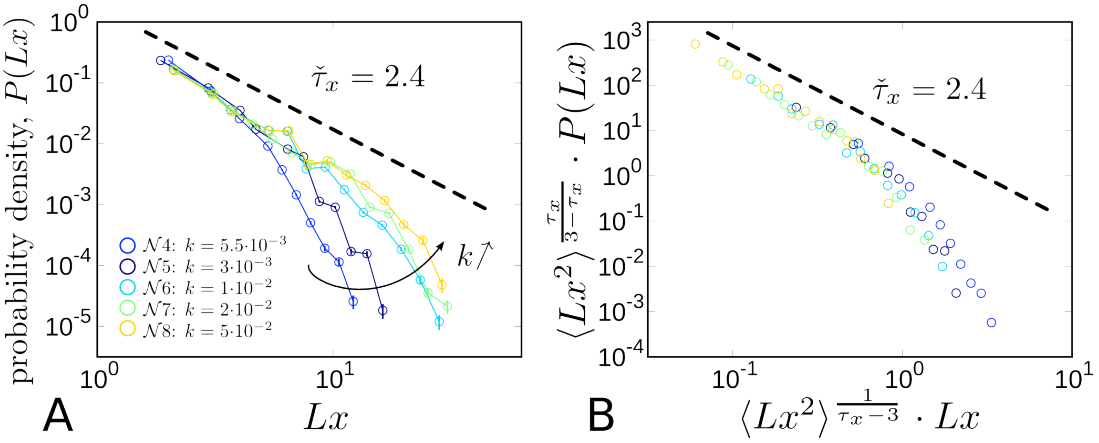

Figure 3.29: A: Probability density function of the avalanche depth detected via the activity card as a function of the unloading factor ($c = 1{\cdot}10^{-4}$, $\sigma = 1$, $N = 1024$). For the simulation $\mathcal{N}8$ one observes a power-law extending over more than one order of magnitude. The fitted exponent is $\check{\tau}_x = 2.4 \pm 0.25$. B: Collapse of the curves using the second moment of the avalanche depth. In both cases the axes are logarithmic.

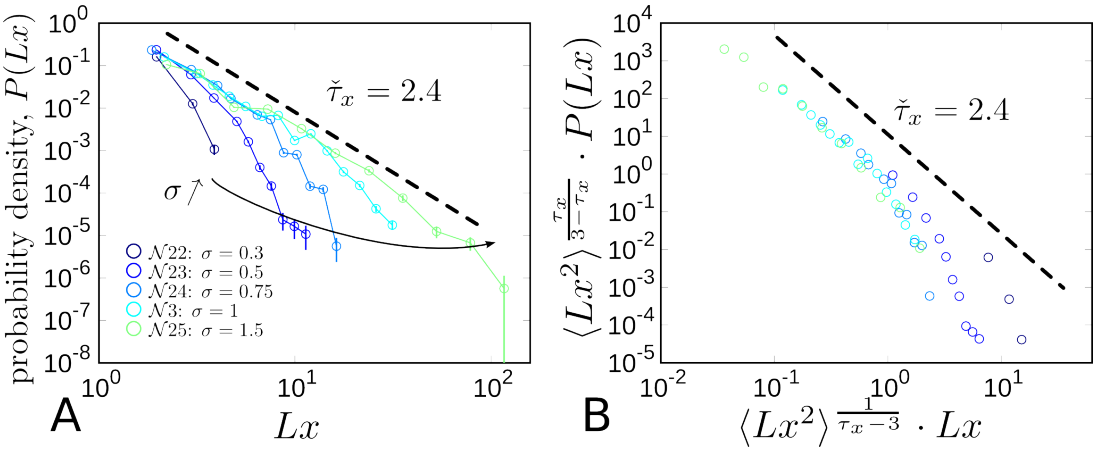

Figure 3.30: A: Probability density function of the avalanche depth detected via the activity card as a function of the heterogeneity amplitude ($c = 1{\cdot}10^{-5}$, $k = 1{\cdot}10^{-3}$, $N = 1024$). Simulation $\mathcal{N}25$ yields a power-law extending over nearly two orders of magnitude. The fitted exponent is $\check{\tau}_x = 2.4 \pm 0.25$. B: Collapse of the curves using the second moment of the avalanche depth. In both cases the axes are logarithmic.

3.4.4 Statistical analysis of the avalanche height Lz

Effects of the loading rate, c ▶ Next, one analyzes the statistics of the avalanche dimensions in terms of size perpendicular to the direction of propagation (z axis). For varying values of c, the activity map provides an estimate of the probability density function of the avalanche height $P(Lz)$. Figure 3.31-A gives way to a prefactor and exponent $\check{\tau}_z = 1.9 \pm 0.15$ (fitted on the simulation $\mathcal{N}14$) which are independent of c. Nevertheless, the upper cut-off decreases when c increases, which is consistent with observations relating to S.

Using the first moment scaling explained in the section 2.9.5 of the first part, curves collapse since $\check{\tau}_z < 2$. Figure 3.31-B depicts the excellent collapse. Moreover this proofs that just the upper cut-off varies with the loading speed, emphasizing the fact that the exponent remain constant.

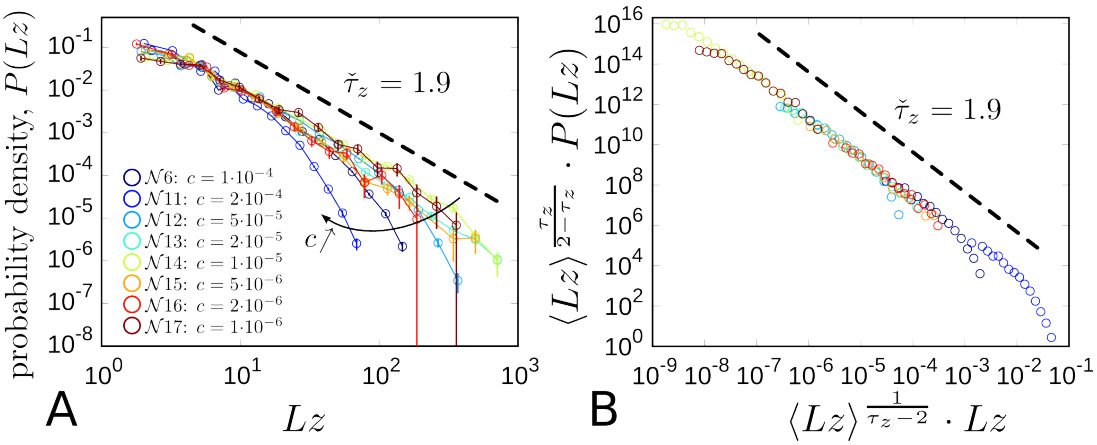

Figure 3.31: A: Probability density function of the avalanche depth detected via the activity map as a function of the loading rate ($k = 1 \cdot 10^{-2}$, $\sigma = 1$, $N = 1024$). Simulation $\mathcal{N}14$ reveals a power-law extending over two orders of magnitude. The fitted exponent is $\check{\tau}_z = 1.9 \pm 0.15$. B: Collapse of the curves using the second moment of the avalanche depth. In both cases the axes are logarithmic.

Effects of the unloading factor, k ▶ Then, the activity map unmasks $P(Lz)$ dependence on k. Figure 3.32-A reveals that the prefactor and exponent $\check{\tau}_z = 1.9 \pm 0.15$ (fitted on the simulation $\mathcal{N}9$) remain constant with varying k. However, the upper cut-off decreases with the unloading factor. This means that on average, the smaller k the thinner the avalanches.

Figure 3.29-B calls upon the first moment scaling, previously used to collapse the $P(Lz)$ curves on a single power-law. the upper cut-off collapses proving $P(Lz)$ only depends on k.

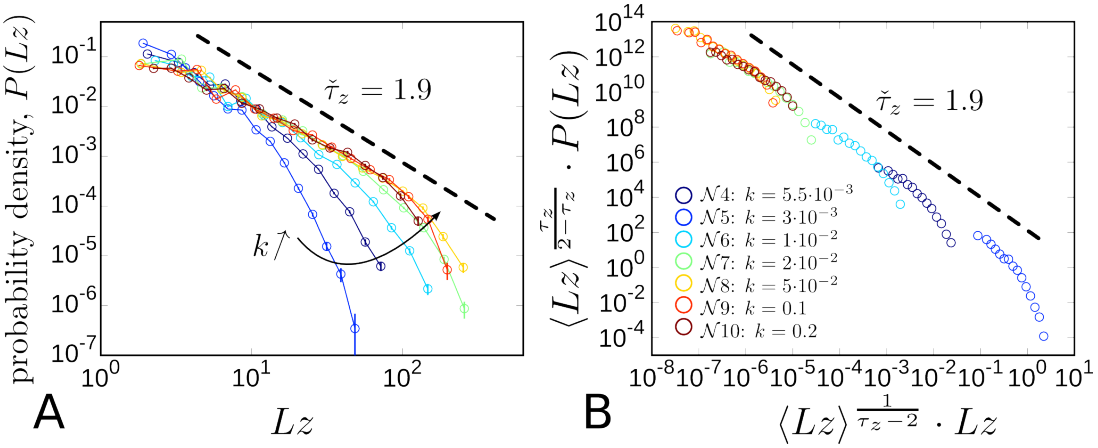

Figure 3.32: A: Probability density function of the avalanche depth detected via the activity map as a function of the unloading factor ($c = 1{\cdot}10^{-4}$, $\sigma = 1$, $N = 1024$). Simulation $\mathcal{N}9$ uncovers a power-law extending over nearly two orders of magnitude. The fitted exponent is found to be $\check{\tau}_z = 1.9 \pm 0.15$. B: Collapse of the curves using the second moment of the avalanche depth. In both cases the axes are logarithmic.

3.4.5 Analysis of the 3D avalanche shapes

Next the mean avalanche shape needs to be studied, which is extracted from the speed map $\mathcal{V}(x,z)$ (see subsection 3.4.1). One of the first things to verify is if the symmetry in time of the avalanche shape as evidenced in section 3.2.4 is also evidenced in the x and z directions. To compute this average shape, one first notes that $\mathcal{V}(x,z) = 1/W(x,z)$ is the local normal velocity around (x,z). Next, an avalanche size (S) of interest is identified. Then, all the avalanches i such that $S_i \in [S - \delta S, S + \delta S]$ are collected. The coordinates of these avalanches i correspond to $X_{i\ min}$ (respectively $Z_{i\ min}$) the smaller avalanche coordinate in the X direction and $X_{i\ max}$ (respectively $Z_{i\ max}$) the highest avalanche coordinate in the X direction. Hence $Lx_i = X_{i\ max} - X_{i\ min}$ and $Lz_i = Z_{i\ max} - Z_{i\ min}$. Then the avalanche mean shape at S is computed by averaging $\mathcal{V}(x - X_i, z - Z_i)$ over all the collected pulse; where X_i (respectively Z_i) is equal to $X_{i\ max} + X_{i\ min}/2$ (respectively $Z_{i\ max} + Z_{i\ min}/2$). Finally figure 3.33 presents the normalized pulse shape $\mathcal{V}/\mathcal{V}_{max}$ as a function of $(x/Lx, z/Lz)$ for two values S.

We see that in both directions x and z, for small and big avalanches, the mean shapes are symmetric. Nevertheless as we could expect from the two previous section, because their probability density function are not the same, the shape in the x direction is not the same as the one in the z direction. Moreover, just like the 1D shape in time (see figure 3.15), when the avalanche surface S increases (or equivalently the duration D), the shape is broader.

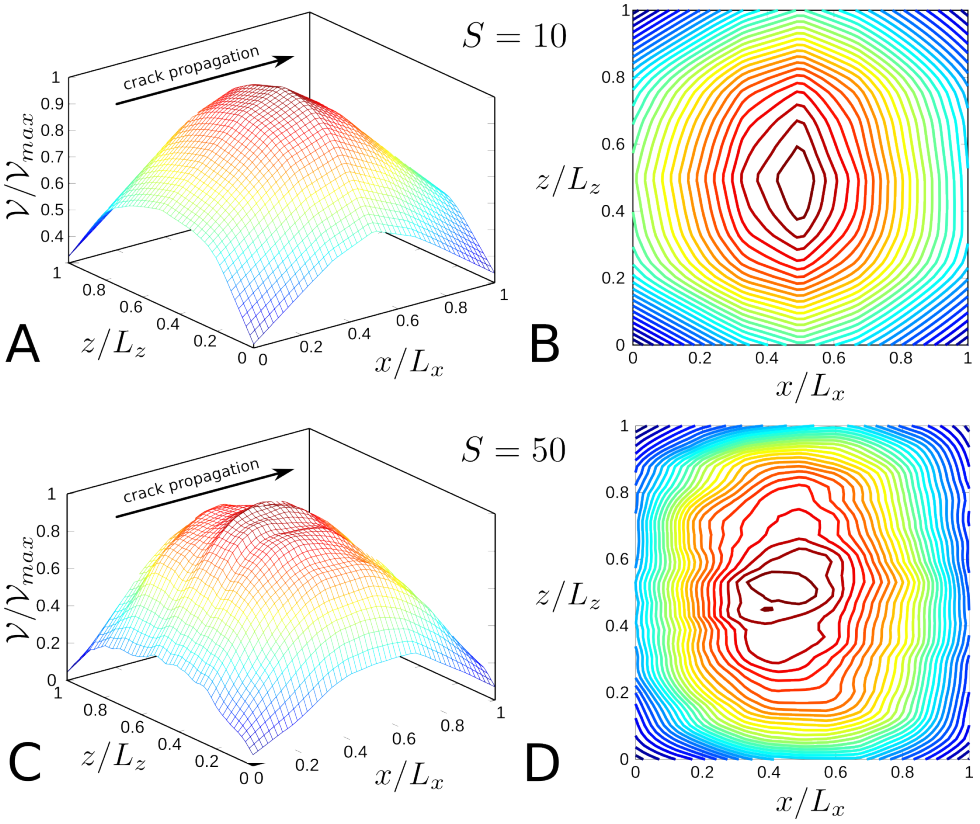

Figure 3.33: A: Average avalanche shapes for $S = 10$ in the x-z plane. B: Top view. C: Average avalanche shapes for $S = 50$ in the X-Z plane. D: Top view. The shapes are measured from simulations $\mathcal{N}2$: $c = 1 \cdot 10^{-5}$, $k = 1 \cdot 10^{-3}$, $\sigma = 1$ and $N = 256$. See text for details.

3.5 Fore/Main/After-shock organization of avalanches

3.5.1 Exploration of the time clustering

As already mentioned in part I chapter 2 of this manuscript, a model that maps crack growth with a depinning elastic line model, *a priori*, is not expected to yield time clustering for the avalanches. Indeed, for a front driven at constant force just above the depinning threshold, the probability density function of the waiting time between events $P(\Delta T)$ is expected to be Poissonian. Still, the model fracture simulations developed in the first chapter of this numerical part (see equation 1.7) is not exactly equivalent to this situation. Indeed, the driving force goes as $ct - k\overline{f}$ (*i.e.* it is not constant); hence, it includes a feedback term that keep it close to the depinning value F_p. How does this affect $P(\Delta T)$?

To answer this question, one computes $P(\Delta T)$ for different values of the equation parameters. The avalanches extracted come from the spatially averaged signal $\overline{v}(t)$ using the threshold based method: threshold value $\overline{v}_{th}$ equals 10% of the maximum. The top 10% largest avalanches in size are examined, all remaining avalanches are ignored. Then using these avalanches the time probability density function is calculated between these fracture events.

Figure 3.34-A presents different $P(\Delta T)$ curves obtained for different loading rates, c. In the case of high c vales (simulations $\mathcal{N}$6,11,12), a power-law exists between two cut-offs: a lower one independent of c and an upper one increasing with c. In other words, increasing c increases the power-law range. For extremely high c, in the phase diagram (see figure 3.1 and 2.9) approaches the single burst regime. Figure 3.34-A reveals for simulation $\mathcal{N}$16 and 17 the appearance of a peaked component in the distribution for the longest waiting times.

Figure 3.34-B plots $P(\Delta T)$ for different unloading factors k. For small value of k (simulation $\mathcal{N}$4 for instance), it is possible to observe a power-law between a fixed lower cut-off and an upper cut-off which decreases when k increases. When k becomes too large, the two cut-offs become too close with respect to one another and the power-law is lost (see simulations $\mathcal{N}$8,9 or 10 for instance).

As a first (preliminary) conclusion, it seems that equation 1.7 (derived to describe crack grow) can reproduce time clustering provided several conditions:

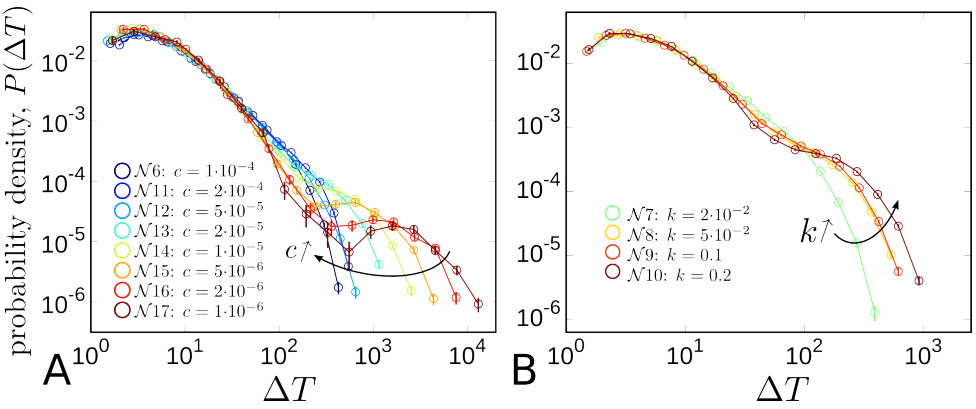

Figure 3.34: A: Probability density function of the time between avalanches computed from the threshold-based method for different loading rates ($k = 1{\cdot}10^{-2}$, $\sigma = 1$, $N = 1024$). B: Probability density function of the time between avalanches computed from threshold-based method for different unloading factors ($c = 1 \cdot 10^{-4}$, $\sigma = 1$, $N = 1024$). In both cases the axes are logarithmic.

- (i) The simulation should stay in the crackling regime.
- (ii) k should not be too high otherwise the upper cut-off comes too close to the lower one and the power-law vanishes.
- (iii) c should not be too high for the same reasons.
- (iv) c must not be too small otherwise the simulation is too close to the single burst regime and the statistics are Poissonian.

In summary, the best place to observe time clustering, in the phase diagram (figure 2.9), is close to the transition line between the self-sustained steady state crackling zone and the LEFM-like one, but not too close!

Thus, it seems that along the straight line, D_2, of the phase diagram (see figure 3.1), there is a good chance to observe time clustering. That is why figure 3.35-A plots $P(\Delta T)$ for various disorder amplitudes, σ. For all these simulations, a power-law extending over at least 1.5 orders of magnitude exists. It is noted that for simulations close to the single burst regime area of the phase diagram (simulation $\mathcal{N}29$ for instance) the Poissionian regime begins to appear near the upper cut-off. Also, the lower cut-off increases when σ decreases. Once again, herein the hypothesis is that this is due to a variation in the Larkin time. Figure 3.35-B presents the results of a curve collapse invoking $\Delta T \rightarrow \Delta T \times \sigma^{2\lambda}$. As presented in figure 3.35-B, the collapse is excellent, which confirms the hypothesis.

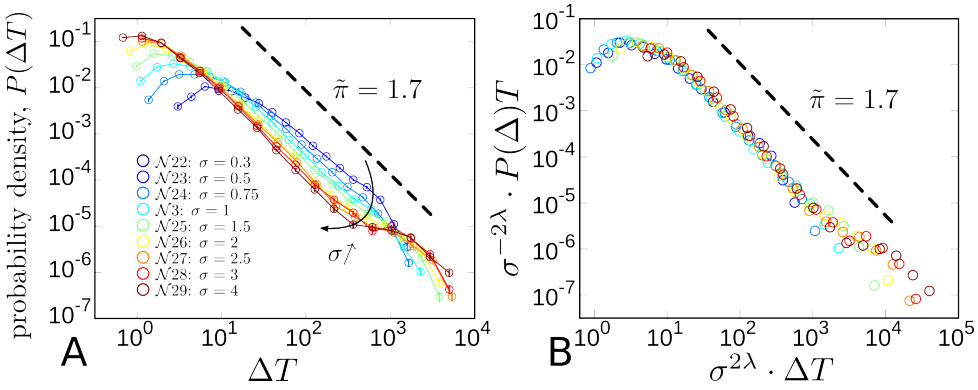

Figure 3.35: A: Probability density function of the time between avalanches computed from threshold-based method for different heterogeneity amplitudes ($c = 1 \cdot 10^{-5}$, $k = 1 \cdot 10^{-3}$, $N = 1024$). Simulation $\mathcal{N}29$, the power-law extends over two orders of magnitude. The fitted exponent is $\tilde{\pi} = 1.7 \pm 0.15$. B: Collapse of the curves using the Larkin time. In both cases the axes are logarithmic.

3.5.2 Waiting time laws

Now, one considers a single point in the phase diagram domain where time clustering is observable (simulation $\mathcal{N}3$) and perform a complete analyze of $P(\Delta T)$ and its dependence on an event size threshold, S_{th}, (in the spirit of what has been done in section 2.6 of the experimental part). Figure 3.36-A, plots the probability density function of the waiting time ΔT between two consecutive avalanches the size of which is greater than S_{th}. The expected power-law distribution is obtained; and the measured exponent is $\tilde{\pi} = 1.7 \pm 0.15$. This exponent differs from those measured experimentally in chapters 2 and 3. To collapse these laws onto a single curve, the scaling presented by [Baro et al. (2013)] is invoked which consists in dividing the horizontal axis by the mean waiting time $\langle \Delta T \rangle$ and multiplying the vertical axis by the same quantity. This provides a fairly good collapse of the lower and upper cut-offs.

3.5.3 Omori law

According to [Baro et al. (2013)], the Omori law implies a power-law distribution for ΔT, but the contrary is not true. So, since the numerical simulations exhibit a power-law statistics, Omori law needs to be verified. Hence, Figure 3.37-A, for the data from simulation $\mathcal{N}3$, depicts the Omori law for different size bins. The power-law extends

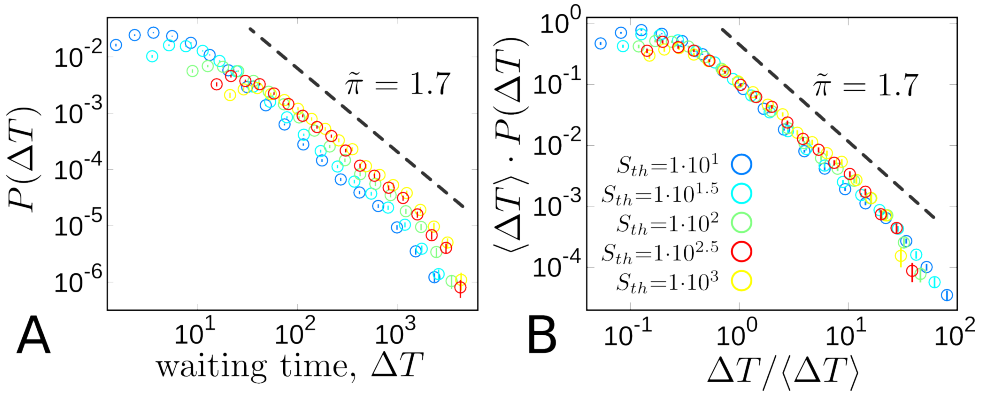

Figure 3.36: A: Probability density function of the waiting time between two consecutive avalanches whose size is higher than S_{th} for simulation $\mathcal{N}3$ ($c = 1 \cdot 10^{-5}$, $k = 1 \cdot 10^{-3}$, $sigma = 1$ and $N = 1024$). Avalanches are detected via threshold based method. The waiting time power-law extends over two orders of magnitude. The fitted exponent is $\tilde{\pi} = 1.7 \pm 0.15$. B: Collapse of the curve via the mean time scaling. In both cases the axes are logarithmic.

over two orders of magnitude with exponent $\tilde{p_A} = 1.5 \pm 0.15$. Moreover, figure 3.37-B shows a collapse of this law using the productivity law ($\tilde{\gamma} = 0.8 \pm 0.1$) as explained in the experimental part of this manuscript (subsection 2.9.3): all curves collapse over three orders of magnitude.

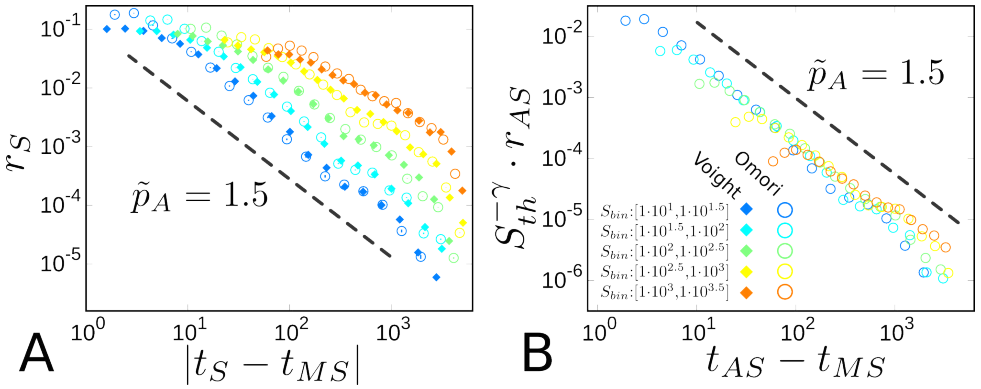

Figure 3.37: A: Omori and Voight laws for simulation $\mathcal{N}3$ ($c = 1 \cdot 10^{-5}$, $k = 1 \cdot 10^{-3}$, $sigma = 1$ and $N = 1024$). Avalanches are detected via threshold based method. One observes the waiting time power-law extending over two orders of magnitude. The fitted exponent is $\tilde{p_A} = 1.5 \pm 0.15$. B: Renormalized Omori law with $\gamma = 0.2$. In both cases the axes are logarithmic.

To verify the time symmetry between AS and FS observed in our fracture experiment is still observable in these numerical simulations, we compute the Voight law presented

in the first part of this manuscript (see section 2.3). This law is equivalent to the Omori law for the FS. Figure 3.37-A presents both Omori and Voigth law. The curves collapse except for small relative time. This means that contrary to the experimental case, both laws are not perfectly equivalent: t_0 the typical silent time after a MS for Omori law and before for Voight law is not the same, it is smaller for Voight law.

Finally, it is worth recalling that [Dieterich (1994); Huang et al. (1998); Scholz (1998)] claim the clustering evidenced by Omori law, would come from a history dependent sequence. Moreover, pinning-depinning model predicts a Poissonian distribution for the Omori or waiting time laws, yet line propagation model herein differs from the pinning-depinning model by the fact that the loading permits a steady state propagation of the crack front. The dependency of the effective driving force *vs.* time and front position (driving force given by $ct - k\overline{f}$ in equation 1.7) can be the ingredient that recovers Omori-like clustering in the front dynamics.

3.6 Conclusion

This chapter characterizes the crackling dynamics produced by equation 1.7 (PS of the spatially averaged front velocity $\overline{v}(t)$, burst statistics and clustering in $\overline{v}(t)$, statistics of the avalanches identified in the space-time and space-space activity maps). As presented in table 3.2, this analysis tested the various scale-free and scaling features expected close to the depinning transition. Is also showed which extent the scaling laws empirically observed in seismology (and in our experiments, see chapter 2) can be reproduced in a theoretical framework.

The use of thirty simulations judiciously located along different places in the phase diagram (figure 3.1) uncovered the role of the various parameters (loading rate, unloading factor, disorder amplitude) on the selection of these dynamics.

More importantly under certain conditions, it is possible to observe clustering in time for this line propagation model. It is thought that this time dynamics is ruled by the feed-back loop involved in the driving force $ct - k\overline{f}$ applying on the propagating front as this term can introduce additional time scales in the problem (see [Papanikolaou et al. (2012)] for recent developments in this direction).

scaling laws	Space activity map: D, T, S, Lx, Lz	Space-time activity map: D, T, S, Lx, Lz, H, V_{max}, F_p, F_d, (X_{begin},Z_{begin})	Threshold-based me D, T, S, Lx, H, $V_$ F_p, F_d, X_{begin}
Richter-Gutenberg: $P(S)$	**x**	**x**	**x**
Waiting-time: $P(\Delta T)$		x	**x**
Duration: $P(D)$	x	x	**x**
Avalanche depth: $P(Lx)$	**x**	x	x
Avalanche heigth: $P(Lz)$	**x**	x	
Maximum speed: $P(V_{max})$		x	x
Omori: $r_{AS}(T_{AS} - T_{MS})$		x	**x**
Voight: $r_{FS}(T_{MS} - T_{FS})$		x	**x**
Utsu: $P(S_{A\text{-}FS}/S_{MS})$		x	x
Productivity: $R_{A\text{-}FS}(S_{MS})$		x	x
Båth: $P(max(S_{AS})/S_{MS})$		x	x
Lx *vs.* Lz	x	x	
D *vs.* V_{max}		x	x
D *vs.* S	x	x	x
Lx *vs.* S	x	x	x
Lz *vs.* S	x	x	
F_p *vs.* F_d		x	x
Depinning-pinning force: $F_{p\text{-}d}$		x	x
Avalanche shape	**x**	x	**x**
Space density of events	x	x	x
Time density of events		x	x

Table 3.2: Statistical laws studied for each extraction method. In bold and blue we give the laws that are presented in this manuscript.

Main messages of the chapter

◇ Four methods to extract statistical data from simulations: (i) Fourier spectrum, (ii) Threshold based method, (iii) spatial activity card, and (iv) space-time activity card.

◇ The main pinning-depinning statistical laws as a function of the different loading paramters and rescaling of these laws are analyzed.

◇ Time-clustering invoking Omori and waiting time laws in the simulations are observed.

Conclusion

This manuscript concentrates on the statistical aspects associated with the propagation of a brittle crack within a heterogeneous solid. A two-step approach addresses this problem: (i) an experimental approach in Part I, and (ii) theoretical and numerical investigation of the phenomenon in Part II.

The model experiment (see Part I) designed during my Ph.D. consists in making a single crack grow in artificial rocks made of sintered polymer beads. The crack is broken in opening mode via a wedge splitting geometry. During the breaking process, the acoustic emissions (AE), stored and released mechanical energy and crack speed are monitored in real time and in a synchronized manner. Analyzing acoustic data in the same manner as geophysicists process seismic signals reveals that most of the empirical laws defining earthquake dynamics are relevant in our simple experiments. For example, AE events accompanying a single crack's propagation self-organizes in time. These break into foreshock-mainshock-aftershock (FS-MS-AS) sequences and obey the Richter-Gutenberg, the Omori, the Voight, the waiting time, and the Utsu laws just like in seismic problems. This observation was unexpected. In particular, the depinning line models yield a Poissonian statistics for the fracturing events of which is incompatible with FS-MS-AS-like clustering, yet it seems to be relevant in describing brittle heterogeneous fracture. Note however that FS-MS-AS sequences of a single crack propagating, herein, are symmetric in time. Earthquakes (more AS than FS) and volcanic eruptions (more FS than AS) do not experience this symmetry. The asymmetry of these two geophysical situations is then conjectured to result from the non-stationarity of the underlying fracturing process.

Model experiments herein revealed the time evolution of the relevant observables in fracture mechanics (stored mechanical energy and crack speed). These observables permitted the initial verification that the spatially-averaged crack speed and the power (time derivative of energy) released in the solid are proportional. A depinning line model derived

from continuum fracture mechanics expects this. Thus, the statistics of the power dynamics is characterized. Sudden bursts (*i.e.* avalanches) make up these dynamics. They are power-law distributed in size and duration, as expected in depinning line models. Conversely, the avalanche shapes are asymmetric at large scales, which is incompatible with the predictions of depinning line models. Also, these avalanches organize in time to form FS-MS-AS sequences, as the AE events. Finally, the fracture surfaces' roughness is analyzed as well as their evolution with respect to the microstructure scale and the crack velocity.

Part II of this manuscript addresses the problem of brittle heterogeneous fracture theoretically and numerically. These simulations invoke elastic line models in random potential and depinning transition. Invoking this framework, a novel equation of motion for a propagating crack comes about. Paying special attention during the development of these equations gives way to relating quantitatively the parameters of this equation to quantities that can be measured/controlled experimentally. The four main parameters are the loading rate (time derivative of energy release), the unloading factor (derivative of energy release as a function of crack length), the disorder amplitude, and the relative system size (specimen thickness over microstructure length-scale). Depending on these parameters, either continuum-line or crackling dynamics can be observed. The phase diagram associated with these two regimes is ruled by only two independent dimensionless parameters.

Finally, a numerical exploration of the equation of motion relates the statistics characterizing the crackling dynamics to the input parameters of the model. Microfracturing event detection uses two different procedures for different length scales: (i) At the continuum-level: The method invokes the threshold tests of the spatially-average speed signal (like in the model experiments) or (ii) at the local scale: directly from time-space or activity map of the crack growth. Each time, the distributions in size, dimensions and durations of the avalanches are computed and found to be power-law distributed with universal exponents between non-universal cut-offs. The scaling between these latter and the loading rate, unloading factor and disorder amplitude are uncovered. Some specific values of the input parameters exhibit avalanche events which organize to form FS-MS-AS events with Omori-like clustering as observed experimentally. Note that the scaling exponents observed in these numerical explorations of a depinning line model of crack growth are not the same as those observed experimentally for artificial rocks.

Via this work, I illustrated experimentally and theoretically the richness of the dynamics followed by a simple propagating crack growing in a disordered solid. Experimentally and theoretically the framework provided by continuum fracture mechanics provides a suitable model to address this problem. As such, brittle heterogeneous fracture problems may be a prototype system to study the complexity in other systems (more difficult to access). Relevant systems need to be driven by similar competitions between random localized dissipative events and overall large-scale coupling via elastic-like redistribution. Applicable systems range from biology [Ito et al. (2000); Huss and Holme (2007); Smith et al. (2003)] to bibliometry [Redner (1998)] via sociology of violence [Turcotte and Roberts (1998); Small and Singer (1982)] or network technology [Newman (2005); Willinger and Paxson (1998)] (see [Clauset et al. (2007)] for a revue).

Appendices

Appendix A

Polymer bead sintering protocol

In this appendix, we present the sintering protocol to make the constitutive material of our samples. A detail method to get the material is necessary in order to have reproducible experiments. This material is considered as a model rock because the process for the Nature to make rocks is the one we mimic to prepare our samples: a granular material undergoes high temperature and pressure conditions and when brought back to room environment it becomes a solid. In our case, to be in a more easily accessible temperature and pressure sintering domains, we do not use mineral materials but a polymer powder. In this way we can vary most of the material parameters of the rock such that the size of the microstructure (varying the bead size), the toughness (varying the sintering duration temperature) and the porosity (varying the pressure, but keeping it low).

A.1 Material

For our experiments, we have used five different kinds of monodisperse polystyrene bead powders: Microbeads® Dynoseeds® TS 500, 230, 140, 80-50 and 20. The number at the end of the name stands for the size of the beads in μm. We precise that for the 80-50 powder, it is an equimassic mix of 80 and 50 μm beads. Moreover, the material properties of the polystyrene constitutive of the beads are different for each bead size. For example, the molecular weight vary and so the the glassy temperature does. These beads are all sold by Microbeads® AS - Vestvollveien 3A - P.O. Box 256 2019 Skedsmokorset - Norway. (see figure A.1)

To apply controlled pressure and temperature, we used an Instron® machine and its oven as presented in figure A.2.

The mold has been done in our lab in bulk cast iron. Its geometry is roughly presented in figure A.3.

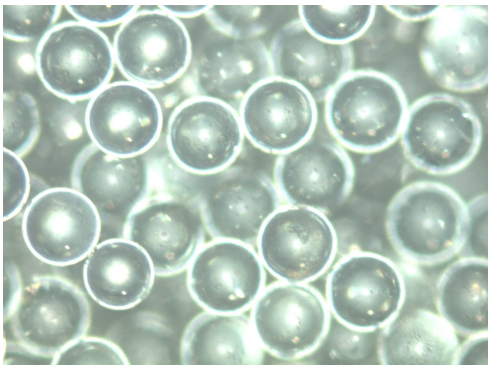

Figure A.1: Picture of Microbeads® Dynoseeds® TS 500

A.2 Protocol

Here is given the detailed protocol we used to sinter our samples. In figure A.4 is presented a schematic view of this protocol.

1. Preliminaries for mold and bead powder:
    - Clean each pieces of the iron mold with a clean piece of rag and spray Teflon®lubricant over the whole inner surfaces.
    - Screw together the different pieces of the mold paying attention there is a sufficient play to insert the free top piece.
    - Fill in the mold with 250 g of beads of the chosen size and gently press inserting the top piece to make the free surface of the beads flat. Remove this top part.
2. Thermo-mechanical sintering:
    - Adapt the oven on the Instron® machine and install the appropriate force sensor (in our case we used the $100kN$ sensor)

Figure A.2: Instron® machine and its oven

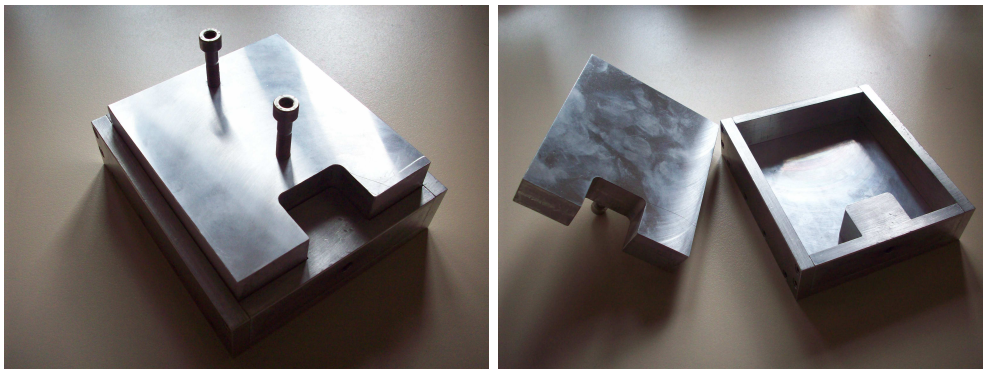

Figure A.3: Cast iron mold used to sinter samples

- Put both part of the mold and beads in the hot oven at T_4. During this operation take care that the free surface of the powder keeps flat.
- Slip the probe of a thermocouple in the middle of the bead powder (few millimeters below the free surface, far from the sides). This will permit to follow the evolution of the bead temperature during the heating up step. This corresponds with the 'heating' step presented in figure A.4.
- When the temperature inside the powder reaches T_2 (after approximatively 1 hour, depending on the bead size), remove the temperature probe, turn the oven temperature down to T_3 and engage the top part of the mold inside the bottom one.
- Via the Instron® machine, apply a linearly increasing force on the system to reach the nominal force F_0 after 8 minutes. Then keep this force constant during 45 minutes. This corresponds with the 'loading' step presented in figure A.4.
- Unload slowly the system to free the mold while turning the oven temperature up to T_5.
- Paying attention that the oven temperature does not go below T_1, unscrew the different parts of the mold without taking it to pieces: sample must be free to expand but all its faces must be in contact with the mold to avoid thermal-shock when opening the oven. This corresponds with the 'releasing' step presented in figure A.4.
- When the mold is loosened, wait some time for the temperature to reach T_5 and let the sample anneal during 20 minutes. This corresponds with the 'annealing' step presented in figure A.4.
- Paying attention that the oven temperature does not go below T_1, remove the different parts of the mold. This step is not easy because the sample could be stick on some pieces of the mold. Nevertheless it is important to remove them without damaging the sample. It corresponds with the 'removing' step presented in figure A.4.
- Finally, let the temperature of the oven rising up to T_5 and wait 10 minutes. Then turn the oven off and let the temperature slowly decrease to the room temperature, this could take 5 to 6 hours. This corresponds with the 'cooling' step presented in figure A.4.

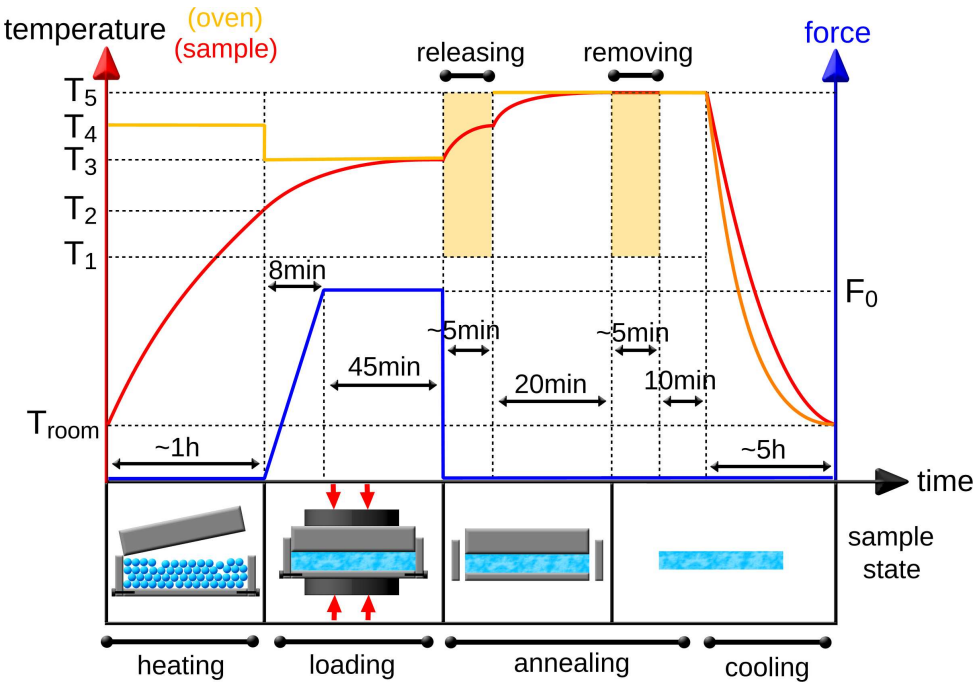

Figure A.4: Protocol to sintered sample material

Temperature	500 μm beads	230 μm beads	140 μm beads	$50-80$ μm beads	20 μm beads
T_1	80°	80°	70°	70°	60°
T_2	105°	105°	100°	105°	90°
T_3	115°	115°	110°	115°	100°
T_4	120°	120°	115°	120°	105°
T_5	130°	130°	120°	130°	110°

Table A.1: Temperatures of the sintering protocol for the different sort of bead used

A.3 Parameters

Because of the variation of the material properties when varying the bead size, it is necessary to adapt the sintering temperatures. We sump-up here in table A.1 the temperatures we used.

To tune the intergranular toughness and porosity of the material, we varied the force (F_0 in figure A.4) applied by the Instron® machine on the mold. We give in table A.2 the different forces we applied and the the corresponding pressure inside the material.

Force F_0 (N)	$1 \cdot 10^3$	$1 \cdot 10^4$	$2 \cdot 10^4$	$4 \cdot 10^4$	$8 \cdot 10^4$
Pressure (MPa)	0.06	0.6	1.3	2.6	5.2

Table A.2: Forces and pressures of the sintering protocol

N^o	F_0 (t)	Bead size (μm)	Volume (mm^3)	Weight (g)	Density (kg/m^3)	Name
46	0.1	20	18.27	16.948	927.7	
18	2	500	18.24	19.184	1052	
23	1	50-80	18.00	18.836	1047	
47	0.1	230	22.01	16.573	753.1	
36	8	20	17.64	17.981	1019	Sd_1
21	2	230	18.30	19.132	1045	
17	0.1	230	21.97	16.968	772.3	
19	4	50-80	17.19	17.943	1044	
24	1	500	17.52	17.768	1014	
39	0.1	500	22.02	17.663	802.0	
43	8	230	17.07	17.831	1045	Sb_1
48	8	50-80	17.05	17.651	1040	Sc_1
20	2	50-80	18.47	19.181	1039	
16	1	230	17.73	18.253	1030	
33	8	500	17.67	18.481	1046	Sa_1
13	4	230	16.58	17.440	1052	
15	4	500	17.07	17.958	1052	
	0.1	50-80	23.92	17.808	744.5	

Table A.3: Density of some samples for different forces and pressures of the sintering protocol

A.4 Material Density

It seems interesting and important to characterize the material got from this protocol to measure its density for different sintering parameters. This as been done for different bead sizes and different sintering forces (F_0) measuring precisely the volume and the mass of some samples. The results are reported in table A.3 and plotted in figure A.5.

A.5 Mechanical properties of the material

Similarly, it is important to characterize the mechanical properties of the sound material to interpret the results we get when the sample is breaking. Since, we mainly analyzed

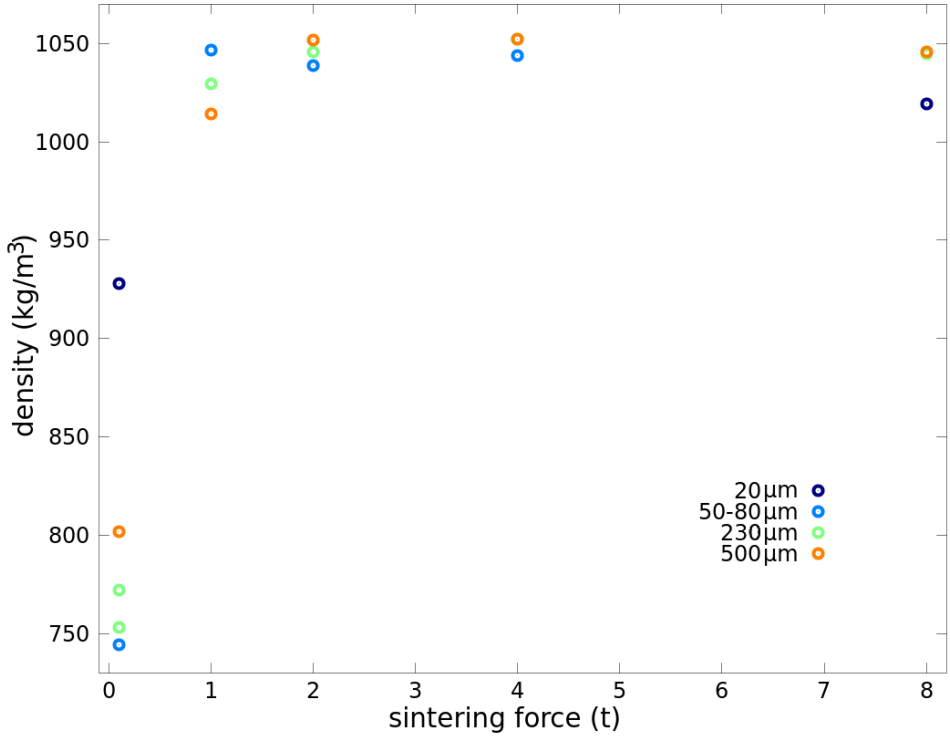

Figure A.5: Density of the sintered material as a function of the sintering force (F_0) for different bead sizes

results from samples sintered at high pressure ($F_0 = 8$t) and big bead size ($d = 500$ μm) and since the analyze is very time consuming, we focus on the material of sample Sa_1. To characterize the static and dynamic properties of this material, we performed Dynamical Mechanical Thermal Analysis (DMTA) at the Surface des Verres et Interfaces lab (SVI)[xxii] on a 2mm thin plate of matter. The analyze frequency has been varied from 0.1Hz to 10Hz at the room temperature. The results are presented in figure A.6. We see that the Young modulus E is almost constant for this frequency range and that the loss modulus varies less than 20%. Hence, since the temperature is fixed in our experiments (18°C) we can consider that the material keeps the same properties during the failure.

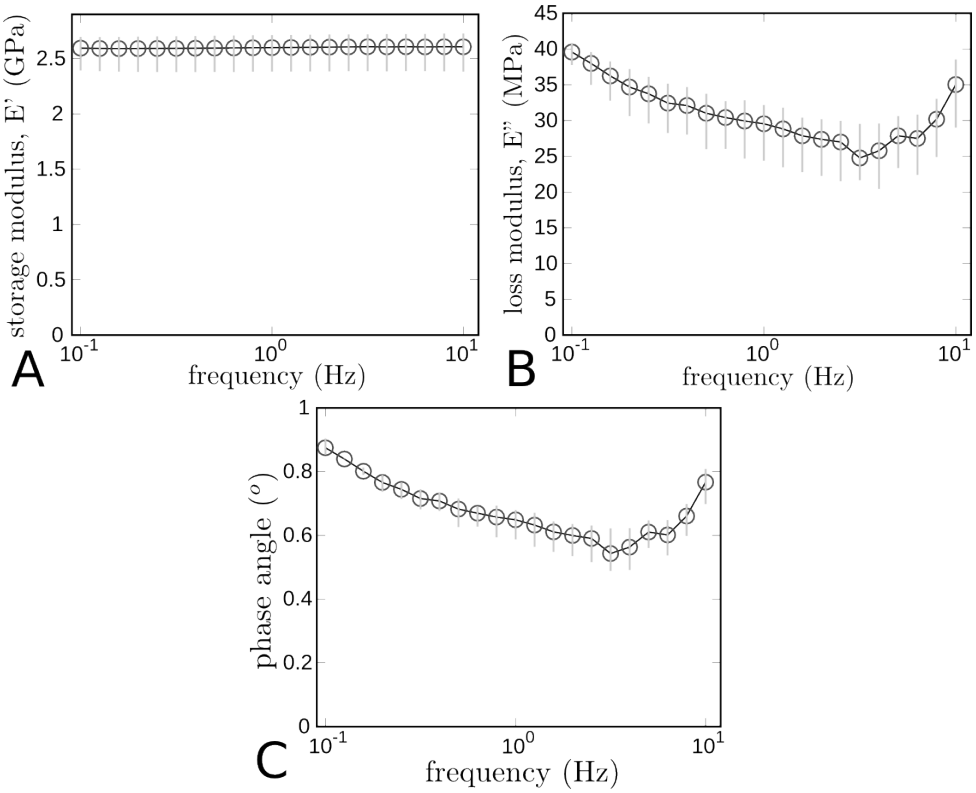

Figure A.6: Variation of the storage (A) and loss (B) moduli as a function of the excitation frequency for the material of sample Sa_1. The variation of the phase angle is given in C. The circles and barres stand for the average, minimum and maximum values of 4 tests

[xxii] in Unité Mixte de Recherche with Centre National de la Recherche Scientifique (CNRS) & Saint-Gobain

Appendix B

Model rock breaking experiment

In this appendix, we present the experimental protocol to break our model rock samples in opening mode recording mechanical and acoustic variables on a synchronized time. Details on the way to drive an experiment are given from the sample preparation to the software monitoring. We give a lot of details for each step to get reproducible as well as comparable results.

B.1 Sample preparation: geometry and acoustic sensor location

When the model rock material is get from the sinter process described in Appendix A, its shape is close to the sample geometry but not exactly. To be sure that there is no friction or plastic deformation of the material where it is in contact with the rest of the system (wedges and pivot), it is important that all edges remain plane and parallel to their opposite counterpart. This is done cutting edges with a classical milling machine. A diamond disk grinder is also used to add a 8 mm pre-crack (2 mm wide). Hence, the dimensions are not the same for all specimens, but for each of them, edges are accurately oriented as shown in figure B.1.

To process the acoustic signal (energy attenuation) and extract the location of the events it is necessary to know the position of the acoustic sensors. So, not to measure the position of the sensor a posteriori we have chosen to locate them at the same place on all

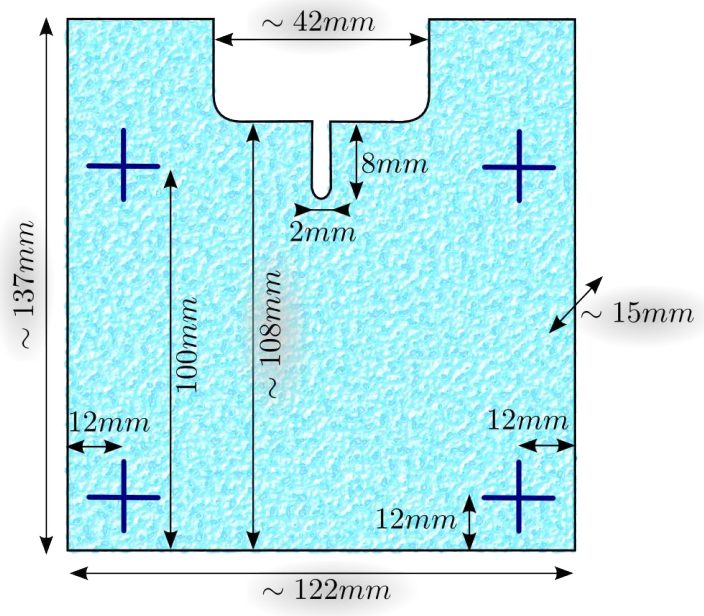

Figure B.1: Model rock sample geometry and acoustic sensor locations (blue crosses): exact dimensions are given in black whereas approximative ones are in a grey cloud

specimens as shown in figure B.1 (blue crosses).

B.2 Crack initiation: pre-crack breaking

The goal of the experiment is to make the crack propagating in quasi-static steady-state regime. So it is necessary not to store a big amount of energy in the system before the crack initiation. To do so, the pre-crack must be as sharp as possible. The one done with the disk grinder has a 1 mm radius of curvature so it does not suit. To reduce it, this pre-crack is propagated pushing a cutter blade with a soft hammer in the bottom of the former crack. This new pre-crack is now approximatively 1.5 cm long and sharp.

B.3 Sample putting on the breaking device

The next step is to put the sample on the breaking device. First, both jaws are put down on the sample paying attention that the space between their edges and the sample faces

are the same for both sides. It is possible to use cardboard wedges to make it sure. This is done to ensure the loading is symmetric. Then, the sample with the jaws are installed in the breaking device on the pivot. The pivot is risen up until the jaws are in contact with the wedge by screwing the nut down the sensor force. The nut must be screw to slightly load the whole system (few N measured with the force cell). At the end of this step it is import to check that the bottom of the specimen is perfectly horizontal.

B.4 Acoustic sensor setting-up

All the eight acoustic sensors must be connected to their 40 dB hardware filters which are connected to the AE computer in-puts. Each of them are clipped or clamped at the location given in figure B.1 adding acoustic gel between the sensor and the sample. Similarly, a coaxial cable must be plugged from an output of the mechanical data computer to the acoustic computer to send a synchronization signal.

B.5 Mechanical and acoustic software preparation

First the recording of the acoustic emission is prepared. The file are saved with a name following this format: 'EA_vWWWnms_dXXX_Yt_nZZ.txt', where WWW is the wedge speed in nm/s, XXX is the bead size in μm, Y is the sintering force in 10^4 N and ZZ is the number of the sample. The position of the sensor on the sample are given in figure B.1. To check that all the sensors are properly connected to the sample and to measure the speed of sound in the material, one by one, a pulse is send from each sensor and recorded by the others. Hence, if a sensor is not properly connected, it will detected a weaker signal than the others. From the delay between emission and reception, the speed of the sound (for the transverse wave) in the material. This speed is given by the AE software to compute the position of the events. On the other hand, the monitoring of the motor and the recording of the mechanical are prepared on the other computer. The wedge engine has to be switched on before the *LabView*® code *Fract4.exe* is executed. The periods of force and picture acquisition are given in the tab 'Experiment Settings' as shown in figure B.2.

In the same tab, the force cell and the corresponding calibration are chosen as given

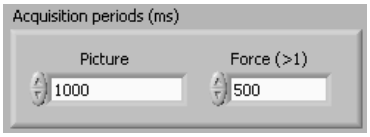

Figure B.2: Choice of the periods of force and picture acquisition

in figure B.3.

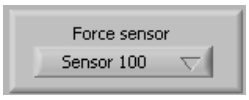

Figure B.3: Choice of the force cell

Then, the files in which mechanical data and pictures are saved in streaming as well as the prefix of the picture and text files are given as shown in figure B.4. These names are build following this rule '/meca/dat_XXXX' for the mechanical data and '/image/img_XXXX' for the pictures ('XXXX' is given automatically by the software).

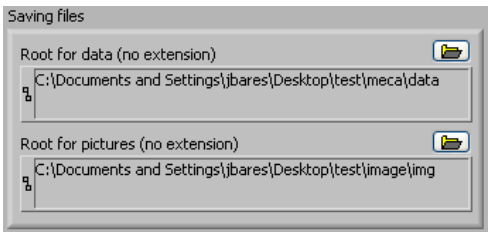

Figure B.4: Saving files

Playing with lighting (from the rear of the sample is better to detect the crack) and camera settings, the quality of the image on the right side of the 'Experiment Settings' tab is adjusted. Then pressing button 1 ('Take Reference Picture'), a new windows appear to select the Region Of Interest (see figure B.5). This region is the only one that the camera will send to the computer during the experiment. It permits to reach an higher frequency.

Now both acoustic emission and mechanics management software's are ready to go. The first one must be started pressing 'OK' few seconds before the second one, pressing button 2 ('Time Start'). This permits to detect the time mark sent via coaxial cable to the acoustic emission computer. This time mark is used during the post processing to synchronize data. From this point, the acoustic emission is recorded. We note that it is possible to send other time marks to the acoustic emission computer to mark some special events.

Figure B.5: Selection of the Region Of Interest

B.6 Monitoring the fracture

Few adjustments are still necessary before breaking the sample. First in the tab 'Image', the quality of sample picture is tunable thank to a panel as the one presented in figure B.6: different filters can be applied.

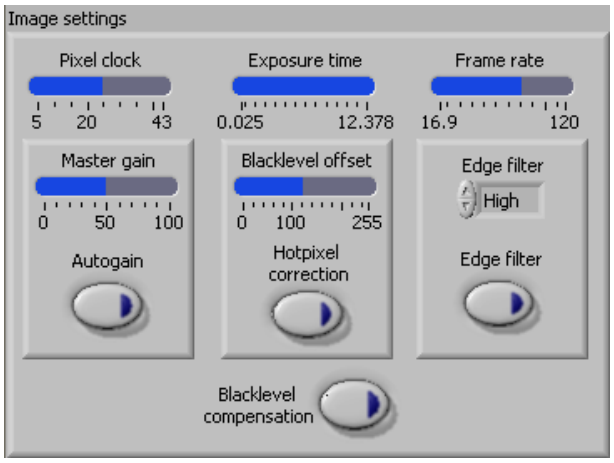

Figure B.6: Picture tuning

Then, in the tab 'Engine', to control the engine, the step angle (SA), the speed (V), the initial speed (VS) and the direction (H) must be given before pressing 'Send Command' to activate the wedge. These command parameters can be changed at any time later. Pressing 'Save Images' and 'Save Force' in tab 'Image' and 'Force' respectively permits to save the data.

Finally, when the sample is broken, pressing 'Stop Experiment' stop the engine and shut the *LabView*® program down. Similarly, the acoustic emission software can be shut down.

B.7 Output files

Both mechanical and acoustic software outputs are text file and png pictures. Here is a list of these data:

1. Mechanical data:
    - dat_force.dat: Force measured by the force cell (unit: N).
    - dat_time_force.dat: Time from the 'time start' when force is saved (unit: s).
    - dat_position.dat: Position of the wedge given by the engine control (unit: m).
    - dat_time_postion.dat: Time from the 'time start' when wedge position is saved (unit: s).
    - dat_time_picture.dat: Time from the 'time start' when each picture is saved (unit: s).
    - dat_engine_marks_events.txt: History of the commands sent to the engine and time marks (time in ms and commands).
    - XXXXXX.png: Pictures of the sample at the $XXXXXX^{th}$ time of dat_time_picture.dat.
2. Acoustic data:
    - EA_vXXXnms_dXXX_Xt_nXX.txt: Matrix with the data attached with each events (time, energy, amplitude...).
    - Localisation.txt: Matrix with the data attached with the event which have been localised (time, position, energy...)

B.8 Table of broken samples

Table B.1 gives the input parameters of each experiments performed during our study.

Sample Number	Wedge speed (nm/s)	Bead size (μm)	Sintering force ($10^4 \cdot N$)	Sample Name
13	16	230	4	
15	16	500	4	
16	16	230	1	
17	16	230	0.1	
18	16	500	2	
19	16	80-50	4	
20	16	80-50	2	
21	16	230	2	
22	16	80-50	0.1	
23	16	80-50	23	
24	16	500	1	
25	16	500	0.1	
26	1600	500	8	Sa_3
30	1.6	500	8	
32	160	500	8	Sa_2
33	16	500	8	Sa_1
35	4	20	4	
36	16	20	8	Sd_1
41	16	20	4	
43	16	230	8	Sb_1
44	16	20	8	
46	16	20	0.1	
47	16	230	0.1	
48	16	80-50	8	Sc_1

Table B.1: Inputs of the experiments

Bibliography

Adda-Bedia, M., Katzav, E., and Vandembroucq, D. (2006). Second-order variation in elastic fields of a tensile planar crack with a curved front. *Physical Review E*, 73:035106.

Alava, M. J., Nukala, P. K. V. V., and Zapperi, S. (2006). Statistical models of fracture. *Advances in Physics*, 55(3-4):349–476.

Astrom, J., Stefano, P. D., Probst, F., Stodolsky, L., Timonen, J., Bucci, C., S, S. C., Cozzini, C., Feilitzsch, F., Kraus, H., Marchese, J., Meier, O., Nagel, U., Ramachers, Y., Seidel, W., Sisti, M., S, S. U., and Zerle, L. (2006). Fracture processes observed with a cryogenic detector. *Physics Letters A*, 356:262–266.

Bak, P., Christensen, K., Danon, L., and Scanlon, T. (2002). Unified scaling law for earthquakes. *Physsical Review Letter*, 88(17):178501.

Bak, P., Tang, C., and Wiesenfield, K. (1987). Self-organized criticality: an explanation of 1/f noise. *Physical Review Letters*, 59:381–384.

Bak, P., Tang, C., and Wiesenfield, K. (1988). Self-organized criticality. *Physical Review A*, 38:364.

Ball, R. C. and Larralde, H. (1995). 3-dimensional stability analysis of planar straight cracks propagating quasi-statically under type-i-loading. *International Journal of Fracture*, 71:365–377.

Baro, J., Corral, A., Illa, X., Planes, A., Salje, E. K. H., Schranz, W., Soto-Parra, D. E., and Vives, E. (2013). Statistical similarity between the compression of a porous material and earthquakes. *Physical Review Letters*, 110:088702.

Bath, M. (1965). Lateral inhomogeneities of the upper mantle. *Tectonophysics*, 2(6):483 – 514.

Bell, A. F., Naylor, M., Heap, M., and Main, I. (2011). Forecasting volcanic eruptions and other material failure phenomena: An evaluation of the failure forecast method. *Geophysical Research Letters*, 38(15):n/a–n/a.

Bertotti, G., G, G. D., and Magni, A. (1994). Scaling aspects of domain wall dynamics and barkhausen effect in ferromagnetic materials. *Journal of Applied Physics*, 75:5490–5492.

Bonamy, D. (2009). Intermittency and roughening in the failure of brittle heterogeneous materials. *Journal of Physics D: Applied Physics*, 42(21):214014.

Bonamy, D. and Bouchaud, E. (2011). Failure of heterogeneous materials: A dynamic phase transition? *Physics Report*, 498:1–44.

Bonamy, D., Ponson, L., Prades, S., Bouchaud, E., and Guillot, C. (2006). Scaling exponents for fracture surfaces in homogeneous glass and glassy ceramics. *Physical Review Letters*, 97:135504.

Bonamy, D., Santucci, S., and Ponson, L. (2008). Crackling dynamics in material failure as the signature of a self-organized dynamic phase transition. *Phys. Rev. Lett.*, 101(4):045501.

Bouchaud, E. (1997). Scaling properties of cracks. *Journal of Physics: Condensed Matter*, 9:4319–4344.

Bouchaud, E., Lapasset, G., and Planès, J. (1990). Fractal dimension of fractured surfaces: A universal value? *Europhysics Letters*, 13.

Bruhwiler, E. and Wittmann, F. H. (1990). The wedge splitting test: A method for performing stable fracture mechanics tests. *Engineering Fracture Mechanics*, 35:117–125.

Bullen, K. E. (1985). *An Introduction to the Theory of Seismology*. Cambridge University Press.

Charles, Y., Vandembroucq, D., Hild, F., and Roux, S. (2004). Material-independent crack arrest statistics. *Journal of the Mechanics and Physics of Solids*, 52:1651–1669.

Chauve, P., Doussal, P. L., and Wiese, K. J. (2001). Renormalization of pinned elastic systems: how does it work beyond one loop? *Physical Review Letters*, page 1785.

Chu, T., Ranson, W., and Sutton, M. (1985). Applications of digital-image-correlation techniques to experimental mechanics. *Experimental Mechanics*, 25(3):232 – 244.

Clauset, A., Shalizi, C. R., and Newman, M. E. J. (2007). Power-law distributions in empirical data. *ArXiv e-prints*.

Collombet, M., Grasso, J., and Ferrazzini, V. (2003). Seismicity rate before eruptions on piton de la fournaise volcano: Implications for eruption dynamics. *Geophysical Research Letters*, 30(21):n/a–n/a.

Corral, A. (2004). Long-term clustering, scaling, and universality in the temporal occurrence of earthquakes. *Phys. Rev. Lett.*, 92:108501.

Dalmas, D., Lafarge, A., and Vandembroucq, D. (2008). Crack propagation through phase separated glasses: effect of the characteristic size of disorder. *Physical Review Letters*, 101:255501.

Davidsen, J., Grassberger, P., and Paczuski, M. (2006). Earthquake recurrence as a record of breaking process. *Geophysical Research Letters*, 33:L11304.

Davidsen, S., Stanchits, S., and Dresen, G. (2007). Scaling and universality in rock fracture. *Phys. Rev. Lett.*, 98:125502.

Deschanel, S., Vanel, L., Godin, N., Vigier, G., and Ciliberto, S. (2009). Experimental study of crackling noise: conditions on power law scaling correlated with fracture precursors. *Journal of Statistical Mechanics: Theory and Experiment*, page P01018.

Deschanel, S., Vanel, L., Vigier, G., Godin, N., and Ciliberto, S. (2006). Statistical properties of microcracking in polyurethane foams under tensile test, influence of temperature and density. *International Journal of Fracture*, 1:87–98.

Dickman, R., Munoz, M. A., Vespignani, A., and Zapperi, S. (2000). Paths to self-organized criticality. *Brazilian Journal of Physics*, 30:27 – 41.

Dieterich, J. (1994). A constitutive law for rate of earthquake production and its application to earthquake clustering. *Journal of Geophysical Research: Solid Earth*, 99(B2):2601–2618.

Dobrinevski, A., Doussal, P. L., and Wiese, K. J. (2012). Nonstationary dynamics of the alessandro-beatrice-bertotti-montorsi model. *Physical Review E*, 85:031105.

Doll, W. (1983). Optical interference measurements and fracture mechanics analysis of crack tip craze zones. *Advanced in Polymer Sciences*, 52/53:105–168.

Duemmer, O. and Krauth, W. (2007). Depinning exponents of the driven long-range elastic string. *Journal of Statistical Mechanics*, 1:01019.

Durin, G. and Zapperi, S. (2000). Scaling exponents for barkhausen avalanches in polycrystalline and amorphous ferromagnets. *Physical Review Letters*, 84:4705–4708.

Durin, G. and Zapperi, S. (2005). The barkhausen effect. In Bertotto, G. and Mayergoyz, I., editors, *The Science of Hysteresis*, page 181. Academic, New York.

Ertas, D. and Kardar, M. (1994). Critical dynamics of contact line depinning. *Physical Review E*, 49:R2532.

Freund, L. B. (1990). *Dynamic Fracture Mechanics*. Cambridge University Press.

Galilei, G. (1958). *Discorsi e Dimostrazioni Matematiche Intorno a due Nueve Scienze*. Boringhieri, Torino.

Gao, H. and Rice, J. R. (1989). A first order perturbation analysis on crack trapping by arrays of obstacles. *Journal of Applied Mechanics*, 56:828.

Garcimartin, A., Guarino, A., Bellon, L., and Ciliberto, S. (1997). Statistical properties of fracture precursors. *Physical Review Letters*, 79:3202–3205.

Gjerden, K. S. (2013). *Role of quenched disorder in fracture front propagation*. Thesis.

Gol'dstein, R. V. and Salganik, R. (1974). Brittle fracture of solids with arbitrary cracks. *International journal of Fracture*, 10:507–523.

Griffith, A. A. (1920). The phenomena of rupture and flow in solids. *Philosophical Transaction of the Royal Society of London*, A221:163.

Griffith, A. A. and Waltamn, J. (1924). The theory of rupture. In Biezeno, C. B. and Burgers, J. M., editors, *Proc. First Internat. Congr . Appl. Mech.*, page 55.

Grob, M., Schmittbuhl, J., Toussaint, R., L.Rivera, Santucci, S., and Maloy, K. J. (2009). Quake catalogs from an optical monitoring of an interfacial crack propagation. *Pure and Applied Geophysics*, 166:777–799. 10.1007/s00024-004-0496-z.

Guarino, A., Garcimartin, A., and Ciliberto, S. (1998). An experimental test of the critical behaviour of fracture precursors. *European Physical Journal B*, 6:13–24.

Guerra, C., Scheibert, J., Bonamy, D., and Dalmas, D. (2012). Understanding fast macroscale fracture from microcrack post mortem patterns. *Proceedings of the National Academy of Sciences USA*, 109:390–394.

Gutenberg, B. and Richter, C. F. (1944). Frequency of earthquakes in california. *Bulletin of the Seismological Society of America*, 34:185–188.

Gutenberg, B. and Richter, C. F. (1954). *Seismicity of the earth and associated phenomena.* Princeton University Press.

Hansen, A. and Hemmer, P. C. (1994). Burst avalanches in bundles of fibers - local versus global load-sharing. *Physics Letters A*, 184:394–396.

Hansen, A., Hinrichsen, H., and Roux, S. (1991). Roughness of crack interfaces. *Physical Review Letters*, 66(19):2476–2479.

Helmstetter, A. (2003). Is earthquake triggering driven by small earthquakes ? *Physical Review Letter*, 91.

Helmstetter, A. and Sornette, D. (2003). Bath's law derived from the gutenberg-richter law and from aftershock properties. *Geophysical Research Letters*, 30(20):n/a–n/a.

Herrmann, H. J. and Roux, S. (1990). *Statistical model for the fracture and breakdown for disordered media.* North Holland, Amsterdam.

Hild, F. and Roux, S. (2006). Digital image correlation: from displacement measurement to identification of elastic properties – a review. *Strain*, 42(2):69–80.

Hirata, T. (1987). Omori's power law aftershock sequences of microfracturing in rock fracture experiment. *Journal of Geophysical Research*, 92:6215–6221.

Huang, Y., Saleur, H., Sammis, C., and Sornette, D. (1998). Precursors, aftershocks, criticality and self-organized criticality. *Europhysics Letters*, 41(1):43.

Huss, M. and Holme, P. (2007). Currency and commodity metabolites: their identification and relation to the modularity of metabolic networks. *IET Systems Biology*, 1:280 – 285.

Irwin, G. R. (1957). Analysis of stresses and strains near the end of a crack traversing a plate. *Journal of Applied Mechanics*, 24:361.

Ito, T., Tashiro, K., Muta, S., Ozawa, R., Chiba, T., Nishizawa, M., Yamamoto, K., Kuhara, S., and Sakaki, Y. (2000). Toward a protein–protein interaction map of the budding yeast: A comprehensive system to examine two-hybrid interactions in all possible combinations between the yeast proteins. *Proceedings of the National Academy of Sciences*, 97(3):1143–1147.

Jeffreys, H. (1938). Aftershocks and periodicity in earthquakes. *Gerlands Beitrage zur Geophysik*, 56:111–139.

Kanomori, H. (1977). The energy release in great earthquakes. *Journal of Geophysical Research*, 82:2981–2987.

Karihaloo, B. L. and Xiao, Q. Z. (2001). Higher order terms of the crack tip asymptotic field for a wedge-splitting specimen. *International Journal of Fracture*, 112:129.

Kilburn, C. (2003). Multiscale fracturing as a key to forecasting volcanic eruptions. *Journal of Volcanology and Geothermal Research*, 125(3–4):271–289.

Koivisto, J., Rosti, J., and Alava, M. J. (2007). Creep of a fracture line in paper peeling. *Phys. Rev. Lett.*, 99:145504.

Kuntz, M. C. and Sethna, J. P. (2000). Noise in disordered sytems: The power spectrum and dynamic exponents in avalanche models. *Physical Review B*, 62:11699.

Larkin, A. I. (1979). Pinning in type-ii superconductors. *Journal of the low temperature physics*, 34:409–428.

Laurson, L., Santucci, S., and Zapperi, S. (2010). Avalanches and clusters in planar crack front propagation. *Phys. Rev. E*, 81(4):046116.

Lawn, B. (1993). *fracture of brittle solids*. Cambridge solide state science.

Lazarus, V. (2011). Perturbation approaches of a planar crack in linear elastic fracture mechanics: A review. *JMPS*, 59:121.

Leblanc, M., Angheluta, L., Dahmen, K., and Goldenfeld, N. (2013). Universal fluctuations and extreme statistics of avalanches near the depinning transition. *Physical Review E*, 87:022126.

Lengline, O., Elkhoury, J. E., Daniel, G., Schmittbuhl, J., Toussaint, R., Ampuero, J. P., and Bouchon, M. (2012). Interplay of seismic and aseismic deformations during earthquake swarms: An experimental approach. *Earth and Planetary Science Letters*, 331:215–223.

Lopez, J. M., Pradas, M., and Hernandez-Machado, A. (2010). Activity statistics, avalanche kinetics, and velocity correlations in surface growth. *Physical review E*, 82(3, Part 1).

Main, I. (1996). Statistical physics, seismogenesis, and seismic hazard. *Reviews of Geophysics*, 34(4):433–462.

Mallick, N. (2010). *Exemples d'invariances d'échelle dans la fracture des matériaux fragiles désordonnés*. PhD thesis, Université Lyon 1.

Måløy, K. J., Hansen, A., Hinrichsen, E. L., and Roux, S. (1992). Experimental measurements of the roughness of brittle cracks. *Physical Review Letters*, 68:213–215.

Måløy, K. J., Santucci, S., Schmittbuhl, J., and Toussaint, R. (2006). Local waiting time fluctuations along a randomly pinned crack front. *Physical Review Letters*, 96:045501.

Måløy, K. J. and Schmittbuhl, J. (2001). Dynamical event during slow crack propagation. *Physical Review Letters*, 87:105502.

Mandelbrot, B. (2006). Fractal analysis and synthesis of fracture surface roughness and related forms of complexity and disorder. In Carpinteri, A., Mai, Y.-W., and Ritchie, R., editors, *Advances in Fracture Research*, pages 13–17. Springer Netherlands.

Mandelbrot, B. B., Passoja, D. E., and Paullay, A. J. (1984). Fractal character of fracture surfaces of metals. *Nature*, 308:721–722.

Marchenko, A., Fichou, D., Bonamy, D., and Bouchaud, E. (2006). Time resolved observation of fracture events in mica crystal using scanning tunneling microscope. *Applied Physics Letters*, 89:093124.

McGuire, W. J. and Kilburn, C. R. J. (1997). Forecasting volcanic events: some contemporary issues. *Geologische Rundschau*, 86(2):439–445.

Minozzi, M., Caldarelli, G., Pietronero, L., and Zapperi, S. (2003). Dynamic fracture model for acoustic emission. *European Physical Journal B*, 36:203–207.

Mishnaevsky, L. (1997). Methods of the theory of complex systems in modelling of fracture: A brief review. *Engineering Fracture Mechanics*, 56(1):47 – 56.

Mogi, K. (1967). Earthquakes and fractures. *Tectonophysics*, 5(1):35 – 55.

Movchan, A., Gao, H., and Willis, J. (1998). On perturbations of plane cracks. *International Journal of Solids and Structures*, 35(26-27):3419 – 3453.

Nataf, H. C. and Sommeria, J. (2000). *La physique de la terre*. Belin.

Newman, M. (2005). Power laws, pareto distributions and zipf's law. *Contemporary Physics*, 46(5):323 – 351.

Ogata, Y. (1988). Statistical models for earthquake occurrences and residual analysis for point processes. *Journal of the American Statistical Association*, 83(401):9–27.

Omori, F. (1894a). On after-shocks of eartquakes. *Journal of the College of Science of the Imperial University of Tokyo*, 7:111–200.

Omori, F. (1894b). On aftershocks. *Rep. Imp. Earthquake Invest. Comm.*, 2:103–109.

Orowan, E. (1955). Energy criteria of fracture. *The Welding Journal Research Supplement*, 34:157–160.

Papanikolaou, S., Bohn, F., Sommer, R. L., Durin, G., Zapperi, S., and Sethna, J. P. (2011). Universality beyond power laws and the average avalanche shape. *Nature Physics*, 7:1745–2473.

Papanikolaou, S., Dimiduk, D. M., Choi, W., Sethna, J. P., Uchic, M. D., Woodward, C. F., and Zapperi, S. (2012). Quasi-periodic events in crystal plasticity and the self-organized avalanche oscillator. *Nature*, 490:517.

Patinet, S., Bonamy, D., and Proville, L. (2011). Atomic-scale avalanche along a dislocation in a random alloy. *Physical Review B*, 84:174101.

Patinet, S., Vandembroucq, D., and Roux, S. (2013). Quantitative prediction of effective toughness at random heterogeneous interfaces. *Phys. Rev. Lett.*, 110:165507.

Planet, R., Santucci, S., and Ortín, J. (2009). Avalanches and non-gaussian fluctuations of the global velocity of imbibition fronts. *Phys. Rev. Lett.*, 102:094502.

Ponson, L. (2007). Crack propagation in disordered materials: how to decipher fracture surfaces. *Annales de Physique*, 32:1.

Ponson, L. (2009). Depinning transition in the failure of inhomogeneous brittle materials. *Physical Review Letters*, 103(5):055501.

Ponson, L., Auradou, H., Pessel, M., Lazarus, V., and Hulin, J.-P. (2007). Failure mechanisms and surface roughness statistics of fractured fontainebleau sandstone. *Physical Review E*, 76:036108.

Ponson, L. and Bonamy, D. (2010). Crack propagation in brittle heterogeneous solids: Material disorder and crack dynamics. *International Journal of Fracture*, 162(1-2):21–31.

Ponson, L., Bonamy, D., and Bouchaud, E. (2006). 2d scaling properties of experimental fracture surfaces. *Physical Review Letters*, 96:035506.

Pradhan, S., Hansen, A., and Chakrabarti, B. K. (2010). Failure processes in elastic fiber bundles. *Review of Modern Physics*, 82:499.

Ramanathan, S., Ertas, D., and Fisher, D. S. (1997). Quasistatic crack propagation in heterogeneous media. *Physical Review Letters*, 79:873.

Ramos, O., Cortet, P. P., Ciliberto, S., and Vanel, L. (2013). Experimental study of the effect of disorder on subcritical crack growth dynamics. *Physical Review Letters*, 110:165506.

Reasenberg, P. A. and Jones, L. M. (1989). Earthquake hazard after a mainshock in california. *Science*, 243(4895):1173–1176.

Redner, S. (1998). How popular is your paper? an empirical study of the citation distribution. *The European Physical Journal B - Condensed Matter and Complex Systems*, 4(2):131 – 134.

Rice, J. R. (1985). 1st-order variation in elastic fields due to variation in location of a planar crack front. *Journal of Applied Mechanics*, 52:571–579.

Richeton, T., Weiss, J., and Louchet, F. (2005). Breakdown of avalanche critical behaviour in polycrystalline plasticity. *Nature Materials*, 4:465.

Richter, C. F. (1935). An instrumental magnitude scale. *Bulletin of the Seismicological Society of America*, 25:1–32.

Richter, C. F. (1958). New dimensions in seismology: Earthquakes are characterized by geographical position, instant of occurrence, depth, and magnitude. *Science*, 128(3317):175–182.

Rolley, E., Guthmann, C., Gombrowicz, R., and Repain, V. (1998). Roughness of the contact line on a disordered substrate. *Physical Review Letters*, 80:2865–2868.

Rosso, A., Doussal, P. L., and Wiese, K. J. (2009). Avalanche-size distribution at the depinning transition: A numerical test of the theory. *Physical Review B*, 80:144204.

Rosso, A. and Krauth, W. (2002). Roughness at the depinning threshold for a long-range elastic string. *Physical Review E*, 65(2):025101.

Rosti, J., Illa, X., and Alava, J. K. M. J. (2009). Crackling noise and its dynamics in fracture of disordered media. *Journal of Physics D: Applied Physics*, 42:214013.

Roux, S. and Hild, F. (2006). Stress intensity factor measurements from digital image correlation: post-processing and integrated approaches. *International Journal of Fracture*, 140(1-4):141 – 157.

Roux, S. and Hild, F. (2008). Self-consistent scheme for toughness homogenization. *International Journal of Fracture*, 154(1-2):159–166.

Roux, S., Vandembroucq, D., and Hild, F. (2003). Effective toughness of heterogeneous brittle materials. *European Journal of Mechanics A/Solids*, 22:743–749.

Rundle, J. B., Turcotte, D. L., Shcherbakov, R., Klein, W., and Sammis, C. (2003). Statistical physics approach to understanding the multiscale dynamics of earthquake fault systems. *Review of Geophysics*, 41:1019.

Salminen, L. I., Pulakka, J. M., Rosti, J., Alava, M. J., and Niskanen, K. J. (2006). Crackling noise in paper peeling. *EPL*, 73:55.

Salminen, L. I., Tolvanen, A. I., and Alava, M. J. (2002). Acoustic emission from paper fracture. *Physical Review Letters*, 89(18):185503.

Santucci, S., Vanel, L., and Ciliberto, S. (2004). Subcritical statistics in rupture of fibrous materials: Experiments and model. *Physical Review Letters*, 93:095505.

Santucci, S., Vanel, L., and Ciliberto, S. (2007). Slow crack growth: models and experiments. *European Physical Journal -Special Topics*, 146:341.

Scheibert, J., Guerra, C., CÃ©lariÃ©, F., Dalmas, D., and Bonamy, D. (2010). Brittle-quasibrittle transition in dynamic fracture: An energetic signature. *Physical Review Letters*, 104(4).

Schmittbuhl, J., Roux, S., Vilotte, J. P., and Måløy, K. J. (1995). Interfacial crack pinning: effect of nonlocal interactions. *Physical Review Letters*, 74:1787–1790.

Scholz, C. H. (1968a). Frequency-magnitude relation of microfracturing in rock and its relation to earthquakes. *Bulletin of the Seismicological Society of America*, 58:399.

Scholz, C. H. (1968b). Microfractures aftershocks and seismicity. *Bulletin of the Seismicological Society of America*, 58:1117.

Scholz, C. H. (1998). Earthquakes and friction laws. *Nature*, 391:37–42.

Sethna, J. P., Dahmen, K. A., and Myers, C. R. (2001). Crackling noise. *Nature*, 410:242–250.

Small, M. and Singer, J. (1982). *Resort to arms: International and civil wars, 1816-1980*. Sage Publications.

Smith, F., Lyons, S., Ernest, S., Jones, K., Kaufman, D., Dayan, T., Marquet, P., Brown, J., and Haskell, J. (2003). Body mass of late quaternary mammals. *Ecological*, 84:3403 – 3403.

Stojanova, M., Santucci, S., Vanel, L., and Ramos, O. (2013). Statistical analysis of subcritical crack growth by acoustic emission vs. direct imaging. submitted to Physical Review Letters.

Sutton, M., Wolters, W., Peters, W., Ranson, W., and McNeill, S. (1983). Determination of displacements using an improved digital correlation method. *Image and Vision Computing*, 1(3):133 – 139.

Tallakstad, K. T., Toussaint, R., Santucci, S., and Maloy, K. J. (2013). Non-gaussian nature of fracture and the survival of fat-tail exponents. *Physical Review Letter*, 110:145501.

Tallakstad, K. T., Toussaint, R., Santucci, S., Schmittbuhl, J., and Maloy, K. J. (2011). Local dynamics of a randomly pinned crack front during creep and forced propagation: An experimental study. *Physical Review E*, 83:046108.

Tanguy, A., Gounelle, M., and Roux, S. (1998). From individual to collective pinning: Effect of long-range elastic interactions. *Physical Review E*, 58(2):1577–1590.

Touati, S., Naylor, M., and Main, I. (2009). Origin and nonuniversality of the earthquake interevent time distribution. *Physical Review Letter*, 102:168501.

Travesset, A., White, R. A., and Dahmen, K. A. (2002). Crackling noise, power spectra, and disorder-induced critical scaling. *Physical Review B*, 66:024430.

Turcotte, D. and Roberts, D. C. (1998). Fractality and self-organized criticality of wars. *Fractals*, 06(04):351 – 357.

Utsu, T. (1957). Magnitude of earthquakes and occurrence of their aftershocks. *Zisin*, 10:35–45.

Utsu, T. (1971). Aftershocks and eartquakes statistics (iii). *Journal of the Faculty of Science, Hokkaido University, Serie VII*, 3:380–441.

Utsu, T., Ogata, Y., and Matsu'ura, R. (1995). The centenary of the omori formula for dacay law of aftershock activity. *Journal of Physical Earth*, 43:1–33.

Vandembroucq, D., Skoe, R., and Roux, S. (2004). Universal depinning force fluctuations of an elastic line: Application to finite temperature behavior. *Physical Review E*, 70:051101.

Vinci, L. D. (1940). *I libri di Meccanica*. Hoepli, Milano.

Voight, B. (1988). A method for prediction of volcanic eruptions. *Nature*, 332:125–130.

Voight, B. (1991). Prospects for eruption prediction in near real-time. *Nature*, 350:695 – 698.

Weibull, W. (1939). *A Statistical Theory of the Strength of Materials*. Generalstabens Litografiska Anstalts Förlag, Stockholm.

White, R. A. and Dahmen, K. A. (2003). Driving rate effects on crackling noise. *Physical Review Letter*, 91:085702.

Wiemer, S. and Katsumata, K. (1999). Spatial variability of seismicity parameters in aftershock zones. *Journal of Geophysical Research: Solid Earth*, 104(B6):13135–13151.

Willinger, W. and Paxson, V. (1998). Where mathematics meets the internet. *Notice of the American Mathematical Society*, 45:961.

Zapperi, S., Nukala, P. K. V. V., and Simunovic, S. (2005). Crack roughness and avalanche precursors in the random fuse model. *Physical Review E*, 71(2 Pt 2):026106.

Zapperi, S., Purusattam, R., Stanley, H. E., and Vespignani, A. (1997a). First-order transition in the breakdown of disordered media. *Physical Review Letters*, 78:1408.

Zapperi, S., Vespignani, A., and Stanley, H. E. (1997b). Plasticity and avalanche behaviour in microfracturing phenomena. *Nature*, 388:658–660.

Résumé

Prévoir où, quand et comment les matériaux cassent est une problématique qui occupe scientifiques et ingénieurs depuis des siècles. Ce problème est rendu complexe par le fait que la concentration des contraintes en pointe de fissure lie intimement le comportement observé à l'échelle macroscopique aux inhomogénéités de microstructure à des échelles très fines. Ceci induit une dynamique de fissuration erratique, composée d'événements d'endommagement rapides et imprévisibles séparés de périodes calmes (*e.g.* dynamique des tremblements de terre le long des failles). Par essence, ces aspects statistiques ne peuvent pas être traités avec l'approche de la mécanique des milieux continus traditionnels. Dans un premier temps, nous tentons d'appréhender ce problème au travers d'une expérience modèle qui consiste à faire propager une fissure dans une roche artificielle dont nous contrôlons la microstructure. La vitesse de chargement du système de fracture est réglable sur une large gamme de valeurs. La vitesse de fissuration et l'énergie mécanique sont enregistrées en temps réel. En parallèle, l'émission acoustique associée aux événements de fracture ainsi que leur localisation sont mesurées via des capteurs piézoélectriques, puis analysées comme cela est communément fait en sismologie. Ces expériences nous permettent de caractériser quantitativement la dynamique intermittente de la fissuration. Elles montrent qu'un certain nombre des lois empiriques observées en géophysique sur la sismicité (loi de Richter-Gutenberg, d'Omori, de Voight, d'Utsu...) se retrouvent dans notre système modèle. Dans un deuxième temps, nous adressons ce problème théoriquement et numériquement, en identifiant le phénomène de fracture dans les matériaux hétérogènes avec celui de la propagation d'une ligne élastique sur un potentiel aléatoire 2D. Ceci permet de déterminer quantitativement, en termes de vitesse de chargement, de tailles des hétérogénéités, de propriétés du matériau, et de géométrie de structure, quand la dynamique de fissuration est régulière et compatible avec l'approche ingénieur des milieux continus, et quand elle devient erratique et nécessite une approche statistique. Dans ce dernier cas, nous caractérisons la statistique de de cette dynamique et relions celle-ci aux paramètres de l'expérience.

Mots-clés: fracture, matériau hétérogène, clustering, crakling, sismologie, transition de

phase et phénomènes critiques

Abstract

The problem of the solid fracture has occupied scientists and engineers for centuries. This phenomenon is classically addressed within the framework of continuum mechanics. Still, stress enhancement at crack tips makes the failure behavior observed at the continuum-level scale extremely dependent on the presence of microstructure inhomogeneities down to very small scales. This yields statistical aspects which, by essence, cannot be addressed using the conventional engineering continuum approaches. I addressed this problem from two different points.

First, I designed an experimental setup that allows growing well-controlled tensile cracks in brittle heterogeneous solids of tunable microstructure, over a wide range of loading speed. The crack dynamics and the evolution of stored and released mechanical energy are monitored in real time. In parallel, the acoustic emission going along with crack growth is recorded via a series of acoustic transducers, and analyzed in a way similar to that develop by geophysicists to process seismic signals. The experiments allowed me to characterize quantitatively the crackling dynamics of cracks, also to evidence intriguing statistical similarities between the seismicity associated with this simple situation of a single running crack under tension and the much more complex situation of multicracking in compressive fracture and in earthquakes.

In parallel, I addressed the problem numerically. The simulations invoke a recent statistical model mapping heterogeneous fracture with the depinning transition of an elastic manifold in a random potential. The numerical exploration of the parameter space allowed me to unravel when (i.e. which loading conditions, microstructure material parameters, material constants...) regular dynamics compatible with continuum approaches are expected to be observed, and when crackling dynamics calling for statistical approaches are observed. In this latter case, we have characterized quantitatively the dynamics statistic and its variations as a function of the input parameters.

Keywords: fracture, heterogeneous material, clustering, crackling, seismology, phase

transition and critical phenomena